

8-AR

COMPUTER-AIDED ANALYSIS OF FORMATION PRESSURE
INTEGRITY TESTS USED IN OIL WELL DRILLING

A Dissertation

Submitted to the Graduate Faculty of the
Louisiana State University and
Agricultural and Mechanical College
in partial fulfillment of the
requirements for the degree of
Doctor of Philosophy

in

The Petroleum Engineering Department

by

Maurício de Aguiar Almeida
B.S., Fundacao Tecnico-Educacional Souza Marques, 1978
M. S., Louisiana State University, 1985

August 1986

TABLE OF CONTENTS

	Page
Acknowledgements	ii
List of Figures	vii
List of Tables	xii
Abstract	xiii
INTRODUCTION	1
LITERATURE REVIEW	12
Factors Affecting Fracture Initiation Pressure	12
Subsurface Stress Field	13
Hydraulic Fracturing Mechanism	16
Cylindrical Borehole Effect	18
Overburden Stress	21
Penetrating Versus Nonpenetrating Fracturing Fluids	25
Tensile Strength of Rock	30
Joints and Faults Near the Well Bore	32
Formation Pore Pressure	35
Correlations for Fracture Pressure Prediction	36
Fracture Expansion	49
System Overall Compressibility	61
Mud Compressibility	63
Drill Pipe and Drill Collar Expansion	65
Casing Expansion	65
Casing Not Cemented	67
Casing Cemented	68
Filtration	69
Borehole Expansion	72
Non-Newtonian Fluid Flow Effects	74
Fracture Closure	78

TABLE OF CONTENTS (continued)

	Page
PROPOSED MATHEMATICAL MODEL	82
Overall Compressibility Model	82
Borehole Expansion	84
Fracture Induction Model	87
Vertical Fracture Initiation	93
Horizontal Fracture Initiation	94
Biot's Constant.....	95
Poisson's Ratio	97
Overburden Stress	99
General Assumptions	100
Fracture Expansion Model	102
Fluid-Loss Rate	105
Fracture Area.....	105
Differential Equation.....	105
No-Fluid-Loss Solution.....	107
Large-Fluid-Loss Solution.....	110
Numerical Solution.....	111
Fracture Width Variation With Distance.....	112
Proposed Solution	114
Elastic Constants	116
Fracture Closure Model	117
Fluid-Loss Coefficient	125
COMPUTER MODEL	128
Features	128
Input Parameters.....	134
Output Parameters	136
Data File Organization	136
Curve-Matching Technique	136
Leak-Off Test Design	138
Introduction	138
Example Design	139

TABLE OF CONTENTS (continued)

	Page
Recommendations	200
NOMENCLATURE	201
REFERENCES	204
APPENDIX A: DERIVATION OF FRACTURE-INDUCTION EQUATIONS	209
APPENDIX B: DERIVATION OF THE OVERBURDEN STRESS EQUATION	216
APPENDIX C: FLOW RATE THROUGH AN ELLIPTICAL CROSS SECTIONAL AREA	219
APPENDIX D: FRACTURE AREA	224
APPENDIX E: SOLUTION FOR LARGE FLUID-LOSS RATE	225
APPENDIX F: DESCRIPTION OF THE DATAFILE FOR THE COMPUTER PROGRAM LEAK	228
APPENDIX G: ELASTIC-PLASTIC SOLUTION OF A HOLLOW CYLINDER	233
APPENDIX H: FRACTURE-CLOSURE PRESSURE.....	237

LIST OF FIGURES

Figure		Page
1	Schematic showing the formation with the lowest fracture pressure just below the last casing seat and the formation with the highest pore pressure formation at the hole bottom.....	2
2	Example plot of pressure gradients versus depth.....	3
3	Typical leak-off pressure plot for a well with a short open hole section.....	6
4	Stress distribution in relatively young deltaic sediments.....	14
5	Schematic showing the fracture initiation mechanism.....	17
6	Stress states around a borehole for regional-stress ratios σ_y/σ_x of 1.4, 2.0, 3.0, and 1.0.....	19
7	Effect of wall thickness on internal bursting pressure of hollow rock cylinders.....	22
8	Overburden stress gradient versus depth for normally compacted Gulf Coast formations.....	24
9	Example of offshore fracture gradients.....	26
10	Possible distribution of pore fluid pressure around the borehole.....	28
11	Graph of bursting pressure versus hole diameter for thick-walled hollow cylinders of limestones.....	31
12	Fracture pressure versus radial confining stress for Bandera sandstone.....	33
13	Matthews and Kelly matrix stress coefficient for normally pressured formations.....	39

Figure		Page
14	K function versus depth used in estimating fracture gradients.....	41
15	Variation in overburden gradients with geologic age.....	42
16	Variations of Poisson ratio with depth.....	43
17	Stress ratio versus rock density.....	45
18	Poisson ratio versus shale index.....	47
19	Correlation of the effective horizontal stress gradient versus the effective vertical stress gradient for the western and central Gulf of Mexico.....	48
20	Two simplified possibilities for the geometry of a hydraulic fracture.....	50
21	Pressure data versus time.....	56
22	Examples showing different characteristic slopes.....	58
23	Example of a three-dimensional fracture profile.....	60
24	Typical well configuration during a leak-off test.....	62
25	Typical stress-strain diagram for steel.....	66
26	Example of bonding between casing cement and formation.....	70
27	Example of a leak-off test performed in a well drilled in the Louisiana Gulf Coast area.....	73
28	Typical pressure-flow rate response for the flow of drilling fluids.....	76
29	Illustration of pressure terms used for pressure decline analysis.....	81
30	Partial yielding of a thick walled cylinder.....	86

Figure		Page
31	Variation of the Poisson ratio with depth.....	98
32	Fracture geometry for the proposed computer Model.....	103
33	Dimensionless solutions for the maximum fracture width as a function of time.....	108
34	Dimensionless solutions for the fracture length as a function of time.....	109
35	Variation of maximum fracture width with distance from well.....	113
36	Function $f_1(\delta)$ and $f_2(\delta)$ versus the dimensionless time parameters.....	123
37	Flow chart of the computer program LEAK.....	129
38	Example output of a simulated leak-off test plot.....	131
39	The effect of trapped air on a leak-off test.....	132
40	The menu display of the program.....	133
41	Example well configuration.....	140
42	Porosity versus depth for the EI-215-D-1 well drilled in Louisiana Gulf Coast area.....	146
43	User's menu for an example. Formation integrity test at a 9-5/8" casing seat.....	149
44	Expected pressure versus time curve for in the example leak-off test design at 0.25 BPM.....	151
45	Expected pressure versus time curve in the example leak-off test design at 0.50 BPM.....	152
46	Porosity versus depth in well VR 75 # 3.....	165
47	Lithology information for well used in example leak-off test design.....	167

Figure		Page
48	Pressure versus time for various flow rate.....	177
49	Pressure versus time for various Poisson's ratio.....	179
50	Pressure versus time for various bulk shear moduli.....	181
51	Pressure versus time for different fracture height.....	182
52	Pressure versus time for various ratios between the elastic-plastic transition radius and the well-bore radius.....	184
53	Pressure versus time for various pore pressure gradients.....	185
54	Pressure versus time for various mud viscosities.....	187
55	Pressure versus time for various well diameters.....	188
56	Pressure versus time for various lengths of casing cement....	189
57	Pressure versus time for various micro-annulus clearances...	191
58	Cumulative filtrate volume versus total time of exposure.....	192
59	Pressure versus time for various API water loss values.....	193

Appendix A

A.1	State of stress around the borehole well.....	210
-----	---	-----

Appendix C

C.1	Free body diagram for fluid element in a narrow slot.....	220
-----	---	-----

Appendix F

F.1	Data file organization used to produce the output example of Figure 38.....	232
-----	--	-----

Figure

Page

Appendix H

H.1 - Pump-in/Flow-back test	238
H.2 - Pressure decline after shut-in.....	239

LIST OF TABLES

	Page
TABLE 1 - Effect of fluid intrusion on the rupturing pressure of sandstone.....	29
TABLE 2 - Measured fracture parameters.....	55
TABLE 3 - Ratio R/R_1 determination using wellbore enlargement data.....	88
TABLE 4 - Field data for the example design of a leak-off test.....	141
TABLE 5 - Interval transit time and correspondent porosity values versus depth (Well EC 215 D-1).....	144
TABLE 6 - Drilling fluid data.....	157
TABLE 7 - Well Geometry.....	158
TABLE 8 - Drilling string data.....	159
TABLE 9 - Open-hole formation data.....	160
TABLE 10- Computed parameters for the field data analysis....	162
TABLE 11- Interval transit time and correspondent porosity values versus depth (Well VR 75 #3).....	164

ABSTRACT

Formation pressure-integrity tests or leak-off tests have been increasingly performed throughout the world. The test is performed primarily to verify how much pressure can be applied to the formation below the bottom of casing, and to test the cement job sheath around the outside of the casing. The initial design of the various casing strings to be cemented in the well depends heavily on the predicted fracture-pressure curve. If this predicted curve is not verified by the test, the casing plan will have to be changed. Thus, verifying formation fracture-pressure during drilling is of great importance. However, the lack of a standard leak-off test procedure and standard interpretation technique for data analysis generally cause the results obtained by different well operators to vary significantly.

In this study, the development of a computer simulation model for leak-off tests has been accomplished. This model is more realistic than the one currently used, but is sufficiently simple that it can be applied with data normally available during leak-off test operations in the field. The model includes the many factors that affect pressure behavior during the test, and can predict with reasonable accuracy what the pressure curve will look like. In addition, test interpretation using the computer model is easily achieved using a curve matching technique.

The first step toward the development of the computer model was to subdivide the leak-off test into four phases: (1) pressure increase due to overall compressibility of the system, (2) fracture

initiation, (3) fracture expansion, and (4) pressure decline and fracture closure after the pump is shut-in. The second step was the development of mathematical models for each phase separately. The mathematical model that predicts pressure increase before fracture initiation includes the most important variables affecting overall compressibility of the system. The modelling of fracture initiation is based on the classical elasticity theory. The modelling of fracture expansion and closure is based on the solution of the continuity equation for flow into a vertical-elliptical fracture with constant height. Having the modelling of each phase done, a computer program that predicts the pressure behavior during the leak-off test was written. An example showing how the computer model can be used for leak-off test design was then presented.

The computer model was verified using field data furnished by Tenneco Oil Company. The data analysis was performed using a curve-matching technique with the computer model. Also a sensitivity analysis was performed to determine the effect of several well and formation characteristics on the shape of the pressure versus time curve obtained during a formation integrity test.

INTRODUCTION

Planning today's modern deep wells requires knowledge of how to predict formation pore pressures and fracture-pressure gradients. The design of the casing strings to be cemented in the well is of primary importance in well planning, especially when abnormal pressure zones are encountered. In general, casing must be set when the mud density required to overcome formation pore pressure at the bottom of a section of borehole is greater than the maximum mud density that can be sustained without fracturing the weakest formation exposed to the mud.

The situation depicted in Figure 1 illustrates this problem. Formation B, just below the last casing seat, has the lowest fracture pressure. Continued drilling will expose formation A, which has the highest pore pressure. However, to prevent the high-pressure fluid contained in formation A from invading the well, drilling personnel should increase the mud density. The mud-density value is limited by the maximum mud density that formation B can sustain without being fractured. If the mud density needed to overcome the high-pressure zone (formation A) is greater than this maximum value, another casing must be set above the high-pressure zone so that drilling can continue safely.

Knowing the fracture-pressure gradients and the formation pore pressures that can be expected enables the engineer to determine the best casing-seat depths. Figure 2 shows the fracture-pressure curve and pore pressure curves as solid lines; the dashed line represents the mud-density design for this particular

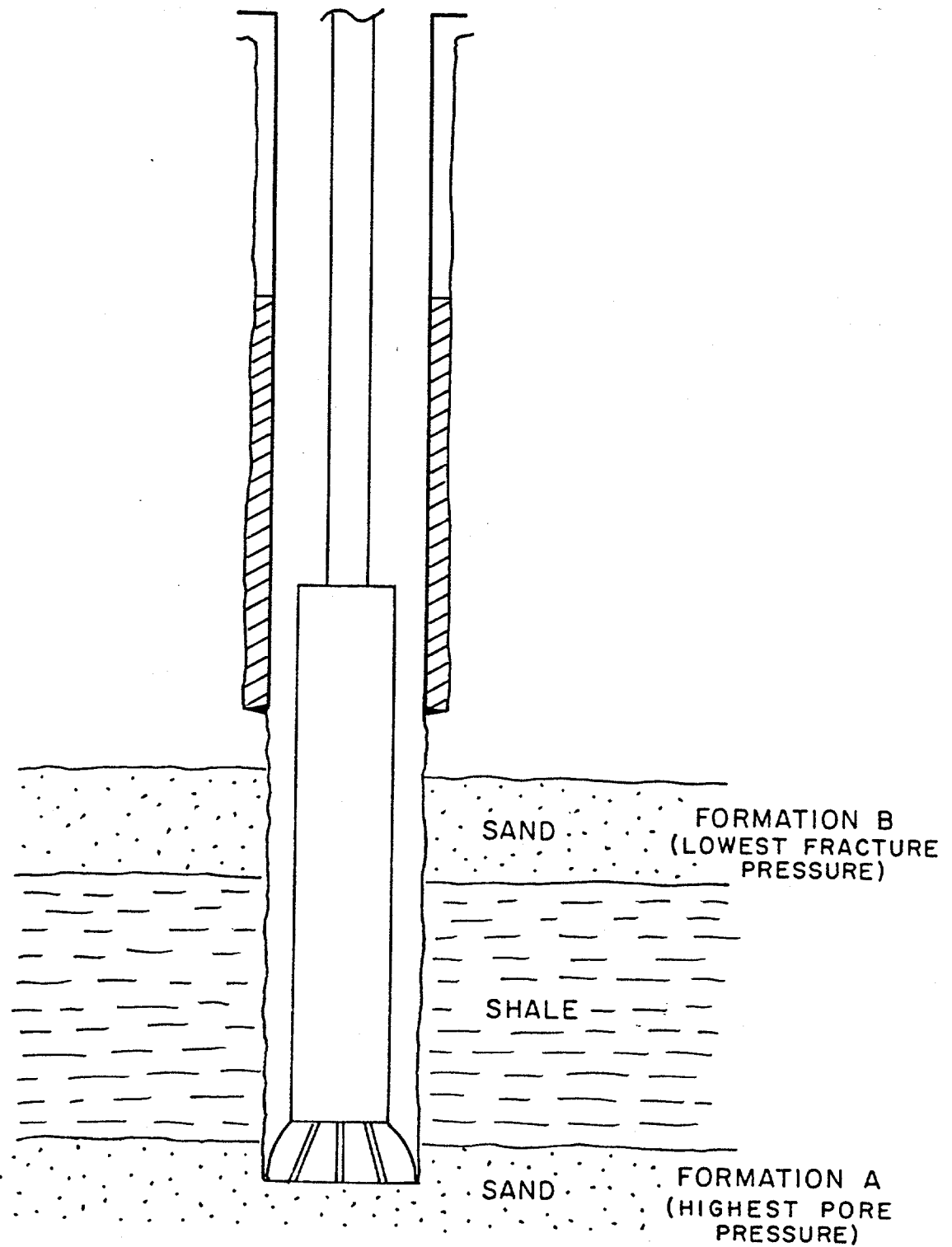


FIGURE 1 - Schematic showing the formation with the lowest fracture pressure just below the last casing seat and the formation with the highest pore pressure formation at the hole bottom.

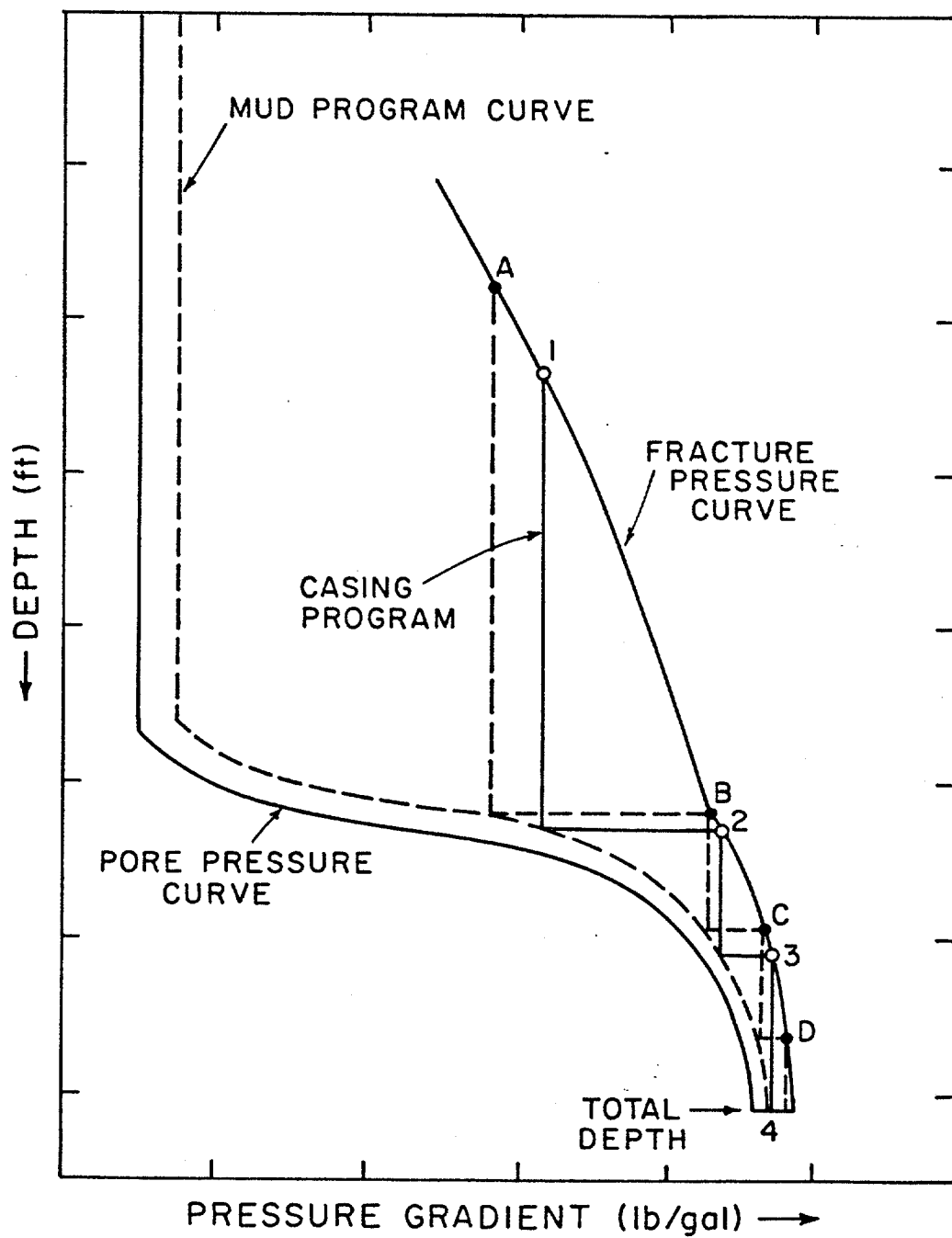


FIGURE 2 - Example plot of pressure gradients versus depth.

case. Pore pressure and fracture gradient are usually expressed as equivalent mud density in lb/gal. As shown, the mud density should always be higher than the expected pore pressure to avoid flow of formation fluids into the well. Point 4 in Figure 2 represents the maximum mud density to be used in the well. However, this value will fracture the exposed formation at point 3, and consequently, to reach point 4, a casing must be set to cover the exposed formations above point 3. The same principle is used to determine the casing-seat depth at point 2. So that point 3 can be reached, the formations exposed above point 2 must be protected by setting a casing, and so on. If the casing at point 1 is set too high, an extra casing will be needed to reach the total depth designated, as shown by the dashed line path A-B-C-D, which usually results in drilling troublesome slim holes. Consequently, the overall cost of the well increases. If the casing setting depth is chosen too low, the well may try to blowout before the casing depth is reached. In many cases, an underground blowout results and there is an uncontrolled flow of formation fluids from the hole bottom to a fractured formation at a more shallow depth. Again, the overall well cost will increase.

The casing plan depends heavily on the predicted fracture-pressure curve, and if drilling operations do not confirm this curve, the casing plan will have to be changed. Thus, verifying fracture-pressure gradients during drilling is of great importance.

Formation fracture pressures are determined with a leak-off test. Leak-off, or open-hole pressure, tests have been performed increasingly throughout the world. They are used to test the cement job sheath around the outside of the casing as well as the fracture gradient in the first sand below the casing shoe.

The leak-off test consists of increasing the well-bore pressure by pulling the bit into the casing, conditioning the mud, closing the BOP valves, and slowly pumping mud down the drill pipe or annulus until well pressure reaches the fracture pressure of the formation being tested. This increase in pressure with time results from the overall compressibility of the system and is represented by line OA in the typical leak-off pressure plot shown in Figure 3. The leak-off, or fracture pressure, occurs at point A when the pressure response deviates from the straight line. After the fracture pressure point is reached, more mud is injected, and the fracture expands until the pump is shut-off at point B. After point B is reached, the well is kept closed and pressure starts to decline owing to filtration of fluids to permeable formations.

Drilling personnel apply a leak-off test primarily to determine how much pressure can be applied to the weaker formation below the actual casing shoe. However, there is currently no standard leak-off test procedure, nor a standard interpretation technique for data analysis. The results of different well operators vary significantly. Drilling problems sometimes occur after the leak-off test because it has been improperly run or improperly interpreted. Analysis of leak-off test data, along with prior knowledge of the formation pressures to be expected, will help the engineer decide on the well depth at which the next casing string should be set to avoid problems associated with lost circulation and underground blowouts. Knowledge of the fracture gradient also permits the engineer to determine the maximum amount of inflow gas that can be allowed into the well. Because knowledge of the fracture gradient is so important, the leak-off test is of unquestionable value. Thus, the design of such a test is also important. Answers to vital questions,

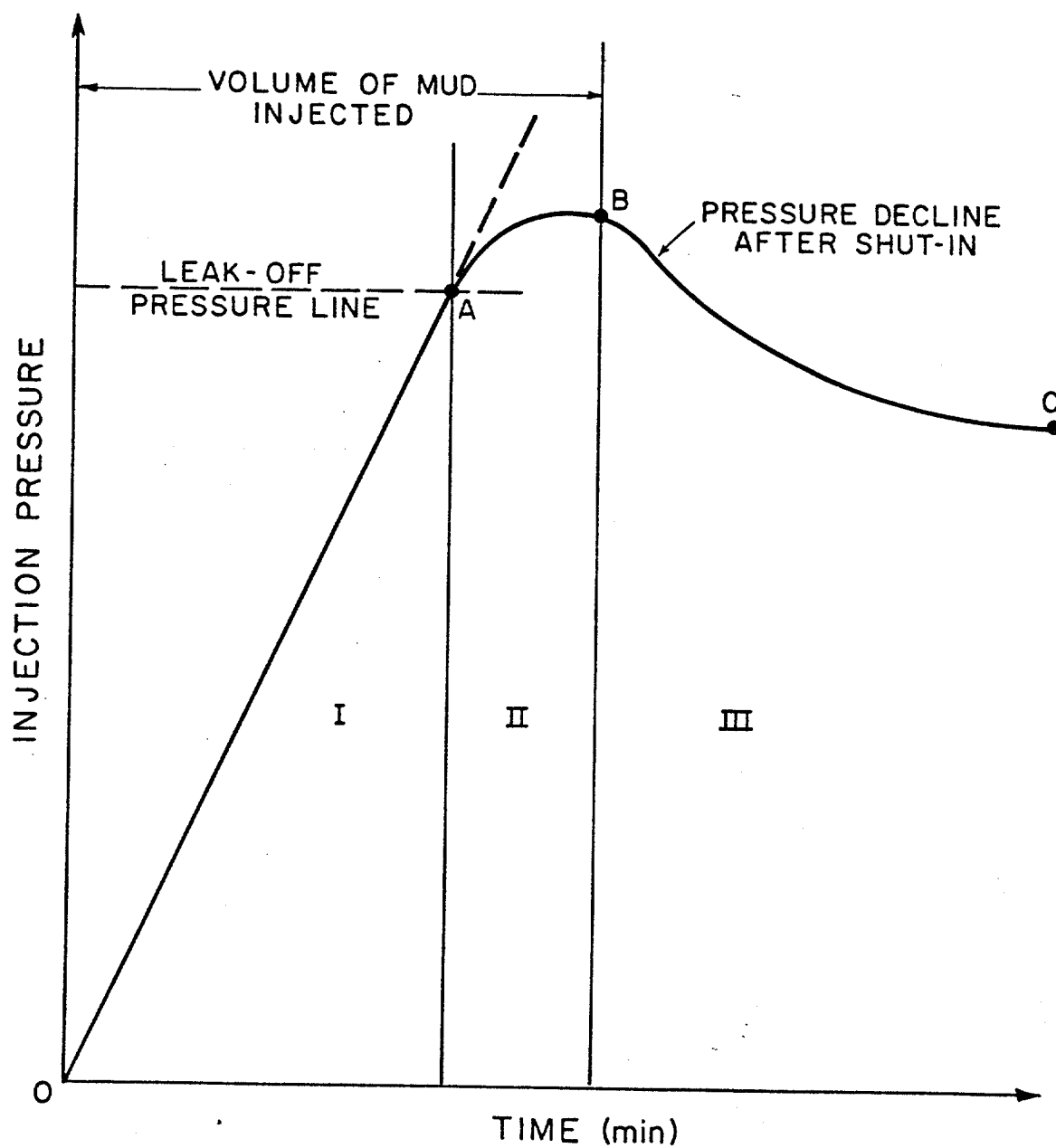


FIGURE 3 - Typical leak-off pressure plot for a well with a short open hole section.

such as how fast the mud should be pumped, what fracture gradient can be expected, how much mud will be injected, how a good pressure-response curve will look, and whether the casing or cement is leaking, can be obtained if a reliable computer simulation model of a leak-off test is available.

A simplified model is currently used to interpret leak-off tests. The fluid is considered to be slightly compressible and pumped into a perfectly rigid container. The injection pressure at the surface is plotted against the volume of mud injected until the observed trend departs from a straight-line. The straight-line fit is obtained by visual inspection of the plotted points. Fracture pressure is determined from the pressure at which first departure from a straight line is seen. The curve is also used to check for leaks. If the pressure departs from a straight line earlier than expected, a leak in the cement behind the casing is suspected. This simplified model relies heavily on the experience of the person interpreting the test. The parameters affecting the fracture and the fracturing process are not analyzed further.

In other areas of petroleum engineering, such as reservoir and production engineering, elaborate models have been used with great success to interpret well-pressure tests. The diffusivity equation, which expresses the mechanism governing fluid flow in a porous medium, has been solved for a wide range of assumed well conditions, permitting pressure data to be used to calculate important parameters, such as formation permeability, skin factors, and the reservoir volume communicating with the well. However, until now only highly simplified equations have been presented for formation fracture-pressure analysis. This work develops a model of

the well system much more realistic than the one presently used. The model can predict with reasonable accuracy what the pressure curve will look like before and after shut-in.

The first part of this study concerns the prediction of the pressure required to initiate a fracture. Fracturing occurs as a result of fluid pressure exerted by the drilling fluid inside the borehole. Theoretical derivation of equations for determining fracture pressure have been developed in the literature. However, these equations are generally too complex, and some of the parameters involved cannot be easily estimated with data normally available in the field. Simplifications of the theoretical equations based on reasonable assumptions make them more usable in the field. However, unresolved conflicts exist in the approaches various authors have taken concerning fundamental issues such as (1) the concept of failure, (2) elasticity versus plasticity, (3) the stress fields present in the earth in the vicinity of the well bore, (4) nonpenetration versus penetration of drilling fluid into formation during the pressure test, (5) homogeneity and isotropy versus heterogeneity, and (6) orientation of the fracture. Consequently, a number of empirical methods of determining the fracture gradient have been used. Approaches range from simple regression analysis of field data to semi-theoretical approaches. In this work, a correlation used to predict formation fracture pressure was selected from the many previously published correlation techniques. The fracture initiation model is used to determine the limit of region I of the typical pressure integrity test shown in Figure 3.

The second part of this study concerns fracture expansion. When pumping of fluid into the well continues after the formation

has been broken, the fracture formed extends. The pressure behavior at borehole conditions, in front of the fracture, is influenced by the fracture geometry. The problem of computing the geometry of a hydraulic fracture during expansion has been studied within two separate disciplines: fluid mechanics and fracture mechanics. These disciplines provide tools for exploring the three-dimensional character of fracture growth and fracture containment. To date, however, the extreme complexity of the general problem has resulted in analyses based on more simplified two-dimensional, linear elasticity solutions of equilibrium cracks. The three-dimensional models include the variations of width, length, and height of the fracture with time, whereas two-dimensional models consider the fracture height to be constant.

The fracture expansion model used in this study has been developed primarily on the basis of detailed study of previously published works written for other applications. The model is the result of the numerical solution of the continuity equation governing the fracture expansion mechanism (region II, Figure 3). The solution includes the assumptions of a vertically closed laterally similar elliptical fracture opening and propagating in a homogeneous, isotropic, and linearly elastic reservoir rock. The fracture expansion model is used to simulate region II of the typical pressure integrity test shown in Figure 3.

The continuity equation for the fracturing expansion mechanism is also solved to determine pressure decline following fracturing, a condition that occurs when the pump is shut-in and pressure begins to decrease while the well is still closed (region III, Figure 3). This pressure decrease is due to filtration of the injected

fluid through the fracture walls. The pressure decline analyses of a leak-off test permit estimation of some important parameters. The most important ones include the fluid loss coefficient, fluid viscosity degradation, formation modulus, fracture closure pressure, and fracture length. Once these parameters are determined through pressure decline analysis, they can be used in the leak-off test simulation of region 1 and 2 in Figure 3.

The third part of this study investigates methods of characterizing the overall compressibility of the system. To precisely predict fracture pressures and surface pump pressure, the computer model should take into account the physical expansion of the casing caused by the increase in pressure, the dynamic filtration of drilling fluid into permeable formations in the open-hole section, open-hole enlargement caused by pressure applied at the borehole walls, and the presence of any air trapped in the system. These factors should be included in the model since they affect overall compressibility. In addition, since mud is pumped into the well, non-Newtonian fluid flow effects will increase the injection pressure at surface and should also be taken into account in the model.

Finally, this work introduces a computer model written for routine simulation of leak-off tests. The model is much more realistic than the one currently used, but is sufficiently simple that it can be applied with data normally available during leak-off test operations in the field.

The program output consists of a plot of surface pressure as a function of time. In addition, computed values of fracture pressure

at surface, fracture gradient, height, length, width, and general data are displayed on the plot.

The model was verified using field data. The model was then used to develop a standard leak-off test interpretation procedure. A sensitivity analysis was made to determine the relative importance of the various formation and wellbore parameters on the interpretation of a formation pressure integrity test.

LITERATURE REVIEW

The mathematical model for the computer simulation of the leak-off test is subdivided into three time periods: (1) the period before the formation fracture pressure has been reached, (2) the period during which fracture expansion takes place, and (3) the period of pressure decline after pumping has stopped. Therefore, this study began with a review of the factors that affect the pressures observed during each of those three periods. All of the previous literature has addressed hydraulic fracturing as a formation stimulation method and has not been directed towards the interpretation of pressure integrity tests. Fortunately, much of the basic fracture mechanics theory will also apply to formation pressure integrity tests. My discussion of previous studies will be limited to those aspects important to the task being undertaken.

Factors Affecting Fracture Initiation Pressure

As discussed previously, the purpose of a pressure integrity, or leak-off, test is to estimate formation fracture pressure. When conducting this test, the engineer needs to know approximately when fracture initiation can be expected. Thus, a means of predicting formation fracture initiation pressure is needed. This section describes the primary parameters known to affect formation fracture initiation pressure.

Subsurface Stress Field

To understand the underground stresses that tend to resist formation fracture, we must consider the geologic processes that have occurred. A simple and common subsurface stress state generally encountered in sedimentary basins containing oil and gas often occurs in a tectonically relaxed area. As the deposition of sediments continues over geologic time, the vertical matrix stress, σ_z , increases owing to the increased loading at the grain-to-grain contacts. Under the influence of this vertical stress, the rock's natural tendency is to expand laterally, but it is prevented from doing so by the surrounding rock. The tendency to expand introduces horizontal stresses. If we designate as principal matrix stresses those stresses that are normal to planes in which no shear occurs, the general state of stress underground can be defined in terms of σ_x , σ_y , and σ_z , as shown in Figure 4.

In tectonically relaxed sediments, far away from intrusive bodies such as salt domes or shale diapirs, the cause of stress is primarily due to only the weight of the overlying mass. In this simplified situation, the horizontal matrix stresses σ_x and σ_y are approximately equal to and smaller than the vertical matrix stress, σ_z . In this case, when the rocks exhibit an elastic behavior the relationship between the vertical stress and the induced horizontal stresses can be expressed by the following equation from elasticity theory

$$\sigma_x = \sigma_y = \sigma_h = [\mu/(1-\mu)] \cdot \sigma_z \dots \dots \dots (1)$$

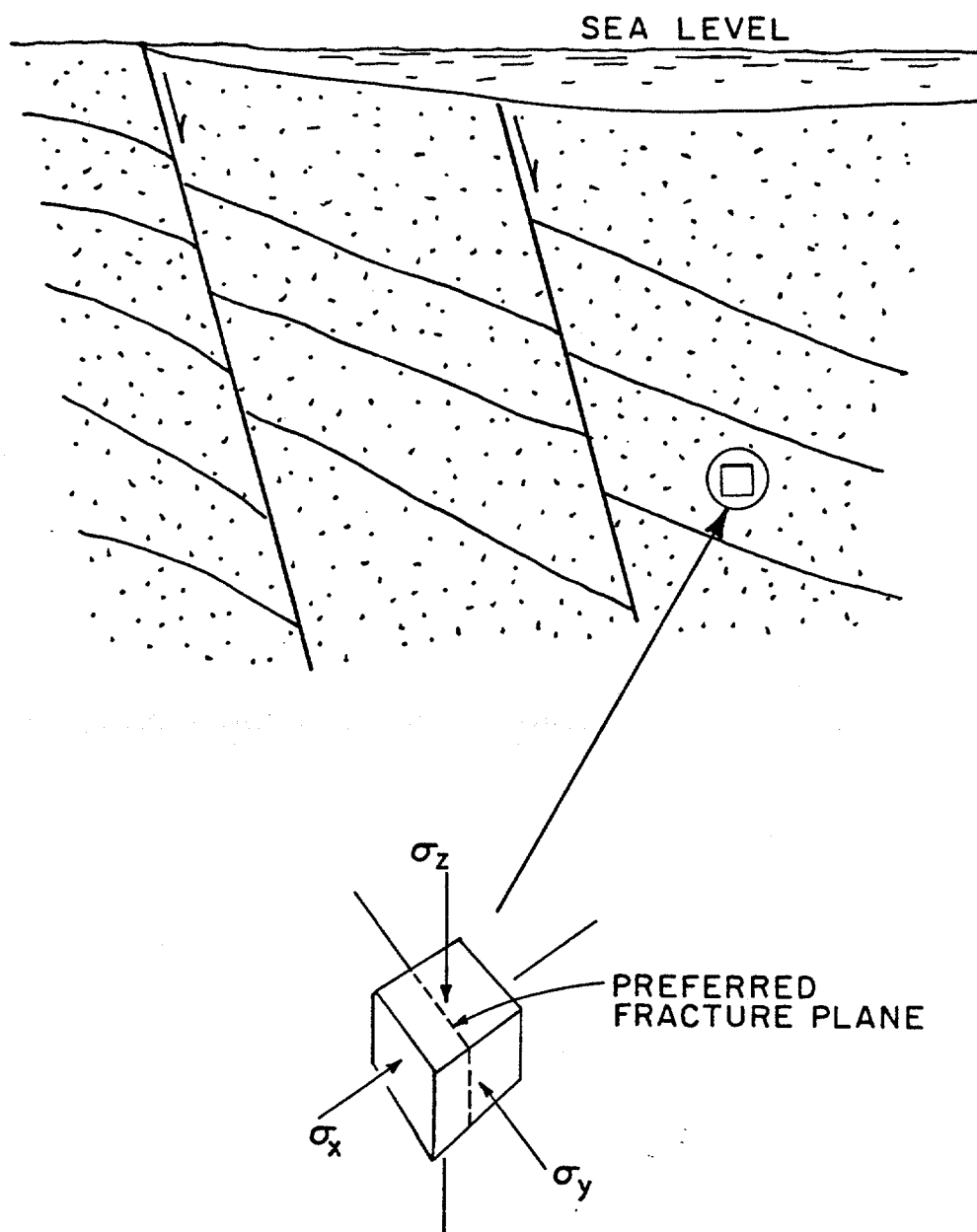


FIGURE 4 - Stress distribution in relatively young deltaic sediments.

where σ_h is the average horizontal stress and μ is Poisson's ratio. Equation (1) also assumes that the horizontal stress is approximately zero in rock being compressed by sedimentation. Since Poisson's ratio, μ , for sedimentary rocks ranges between approximately 0.18 and 0.27 (Birch et al. 1942), the average horizontal compressive stress would be expected to lie within 22-37 percent of the principal vertical matrix stress. If the rocks exhibit plastic behavior, the horizontal and vertical grain stresses would tend to equalize; that is, the horizontal stress would approach 100 percent of the vertical stress due to the weight of the overburden.

Hubbert and Willis (1957) pointed out that over long periods of geologic time the earth has exhibited a high degree of mobility, and rocks have been deformed to the limit of failure by faulting and folding. For this to occur, the principal stresses must be substantially different. Thus, principal stresses in these rocks must have been unequal when folding or faulting occurred (Hubbert and Willis 1957). The conditions for which Equation (1) was derived would tend to apply to a young deltaic depositional environment where normal faulting is common, and the horizontal stresses are less than the vertical stress. In areas where thrust faults and folding are occurring, the horizontal stresses tend to be more than the vertical stresses.

Harrison et al. (1954) found that the earth's crust is stable over a wide range of stress relationships. The stable region is bounded by conditions of faulting. The first condition occurs when one of the unequal horizontal stresses decreases below the lower limit of the stable range normal faulting occurs and continues until the stress

relationship is returned to the lower limit of the stable range. The second condition limiting the stable region is the occurrence of transcurrent and thrust faulting. These types of faulting return the stress conditions to only their respective upper limits of stability; in these instances one or both horizontal stresses would exceed the vertical stress.

Hydraulic Fracturing Mechanism

We can better understand the problem of determining the fracture pressure of a given formation by first considering a very simplified situation in which a fluid is introduced into a small cavity located in the center of the rock element, as shown in Figure 5. For the fracture fluid to enter the cavity, the pressure of the fluid must exceed the pore pressure of the formation. Assuming that the fluid cannot flow a significant distance into the pore spaces, as pressure of the fluid is increased above the formation pore pressure, the rock matrix begins to be compressed. The compression will be greatest in the direction of the minimum matrix stress. The formation will fracture when the fracture fluid pressure exceeds the sum of the minimum principal matrix stress, the pore pressure, and the tensile strength of the formation, S_t .

The preferred fracture orientation will be perpendicular to the least principal stress. Consequently, in regions characterized by normal faulting, according to Equation (1), the least principal stress is horizontal and the fracture orientation should be vertical. In regions characterized by active thrust faulting, however, where the least principal stress is vertical, the fracture orientation should be horizontal. This simplified state of stress underground can be altered

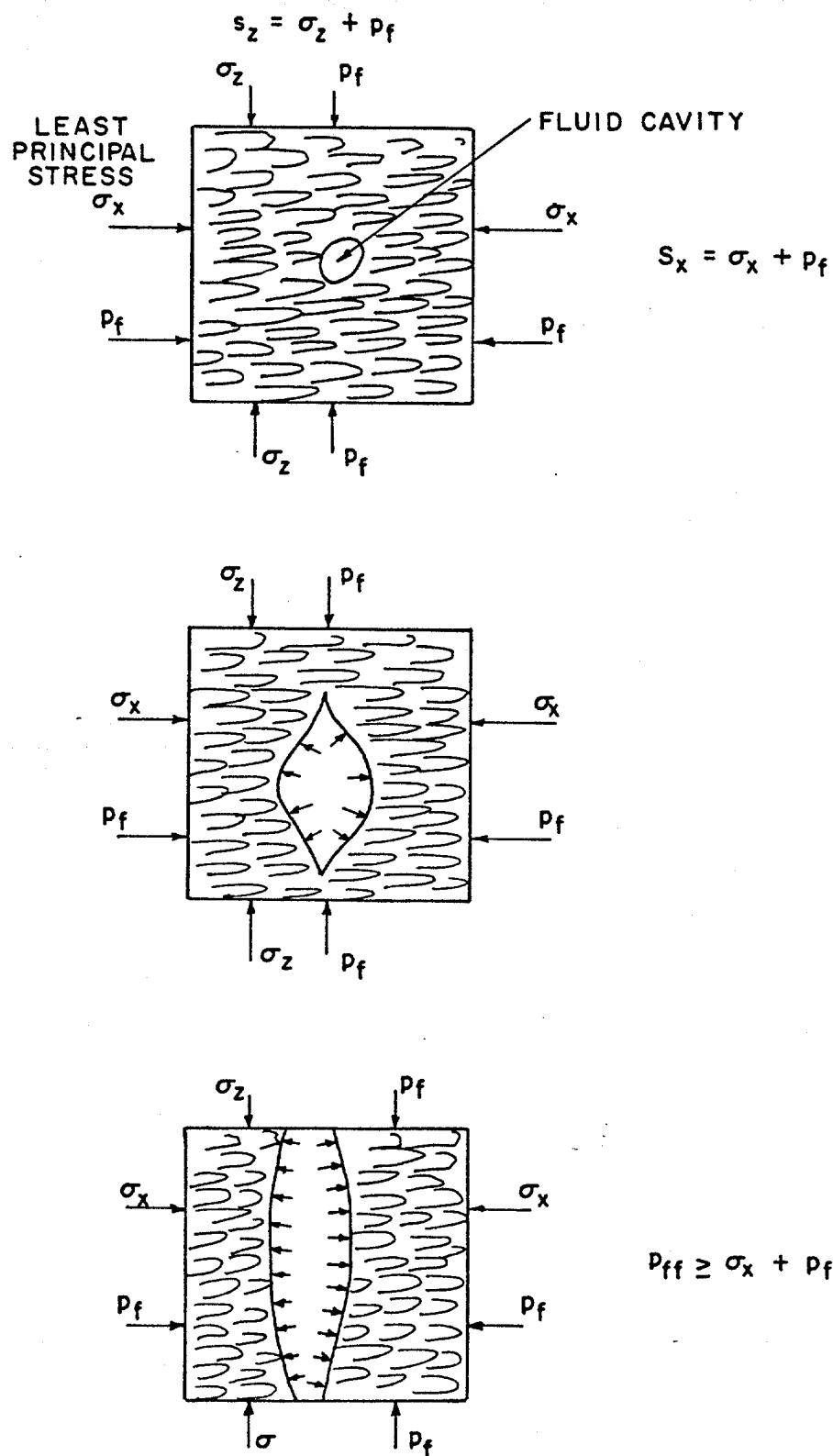


FIGURE 5 - Schematic showing the fracture initiation mechanism.

by various factors that in turn affect the fracture pressure of the formation.

Cylindrical Borehole Effect

The presence of a cylindrical borehole changes the state of stress at its vicinity. Generally this distortion is theoretically calculated by assuming that the rock is elastic, the borehole smooth and cylindrical, and the borehole axis vertical and parallel to one of the pre-existing regional principal stresses.

The vertical borehole creates a local zone of high stress. Hubbert and Willis (1957) pointed out that these stress concentrations are local and that the stresses rapidly approach the undisturbed regional stress area within a few hole diameters. Figure 6 shows values of the horizontal stress across the principal planes in the vicinity of the borehole corresponding to some relative values of the σ_y/σ_x ratio. The distortion of the stress field is not only in the horizontal direction. However, the magnitude of the distortion in the vertical direction, which is a function of the regional horizontal stresses, is very small compared to the concentrations of the horizontal stresses. Stress concentrations rapidly disappear with distance away from the well bore in all directions (Hubbert and Willis 1957).

Since the presence of the borehole affects the state of stress within its vicinity, it also affects the pressure necessary to rupture the formation. It has been shown (Timoshenko and Goodier 1951) that the tangential stress on the periphery of the hole is equal to twice the homogeneous compressive stress of the undisturbed area away

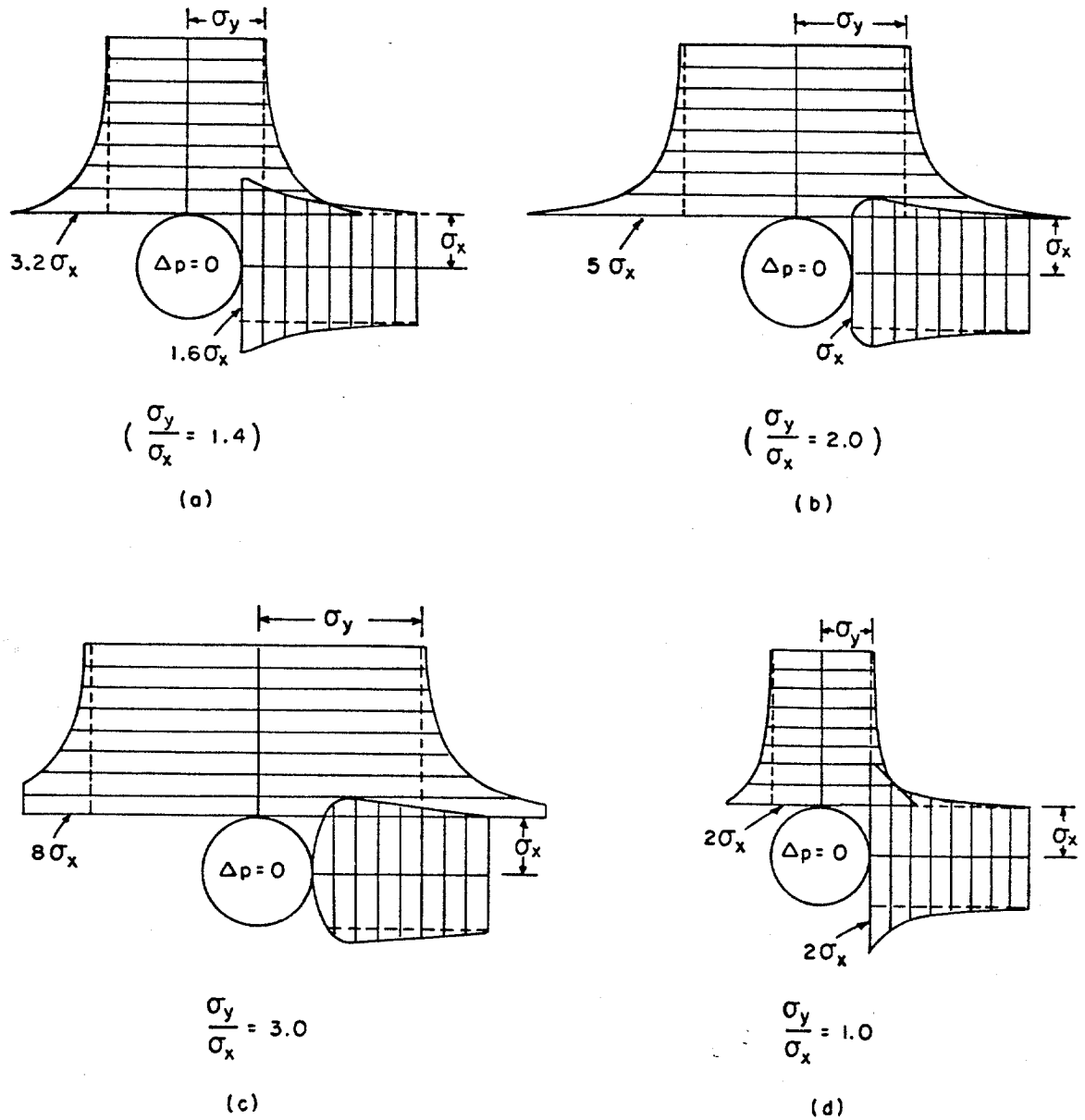


FIGURE 6 - Stress states around a borehole for regional-stress ratios σ_y / σ_x of 1.4, 2.0, 3.0, and 1.0

from the well bore. A vertical plane will fracture only when the effective tangential stress passes from compression to tension. Thus, the pressure required to rupture the borehole vertically is

$$P_f = 2\sigma_h - S_t + P_o \dots\dots\dots (2)$$

where,

P_f = fracture or rupture pressure, psi

S_t = tensile strength of the formation, psi

P_o = formation pore pressure, psi

The convention of signs followed in this work refers to tension as negative and compression as positive. Therefore, the tensile strength of rock, S_t , in Equation (2) should be a negative number.

Equation (2) is derived using elastic theory for the stresses in an infinite plate containing a circular hole, with its axes perpendicular to the plate (Haimson et al. 1967). Equation (2) includes the effect of the stress changes introduced by the well bore and the stresses induced by the borehole fluid pressure.

To determine the effect of well diameter on the rupturing pressure needed to fracture hollow limestone cylinders, Scott et al. (1953) did some experimental work using a fluid that could not penetrate the cylinder walls significantly. They found that little change in the internal rupturing pressure occurred when ratios of outside to inside radii of the cylinder walls were greater than ten

(Figure 7). In experiments performed in shallow wells, no effect on rupturing pressure was observed when the well diameter was varied from 0.19 to 6.0 in., regardless of the type of fluid used.

Overburden Stress

Overburden stress, S_z , is the stress caused in a given point underground by the overburden load or geostatic load of the sediments above this point. This geostatic load is supported at a given depth by the grain-to-grain contact points of the rock material and by the pressure of the fluid inside the pore spaces. The vertical principal matrix stress, σ_z , is the result of this grain-to-grain supported load, and the overburden stress can be expressed by

$$S_z = \sigma_z + P_o \dots \dots \dots (3)$$

The importance of the overburden stress in calculating rupturing pressure is expressed by Equation (3), combined with Equations (1) and (2), which yields

$$P_f = (2 \mu / (1 - \mu)) [S_z - P_o] - S_t + P_o \dots \dots \dots (4)$$

The vertical overburden stress being equal to the geostatic load at a given point is a function of the bulk densities of the materials overlying the point under consideration. The correct value of the vertical overburden stress is therefore the sum of the overlying load of each layer of different formations. However, the total state of stress of the rock at the depth of interest is not always adequately

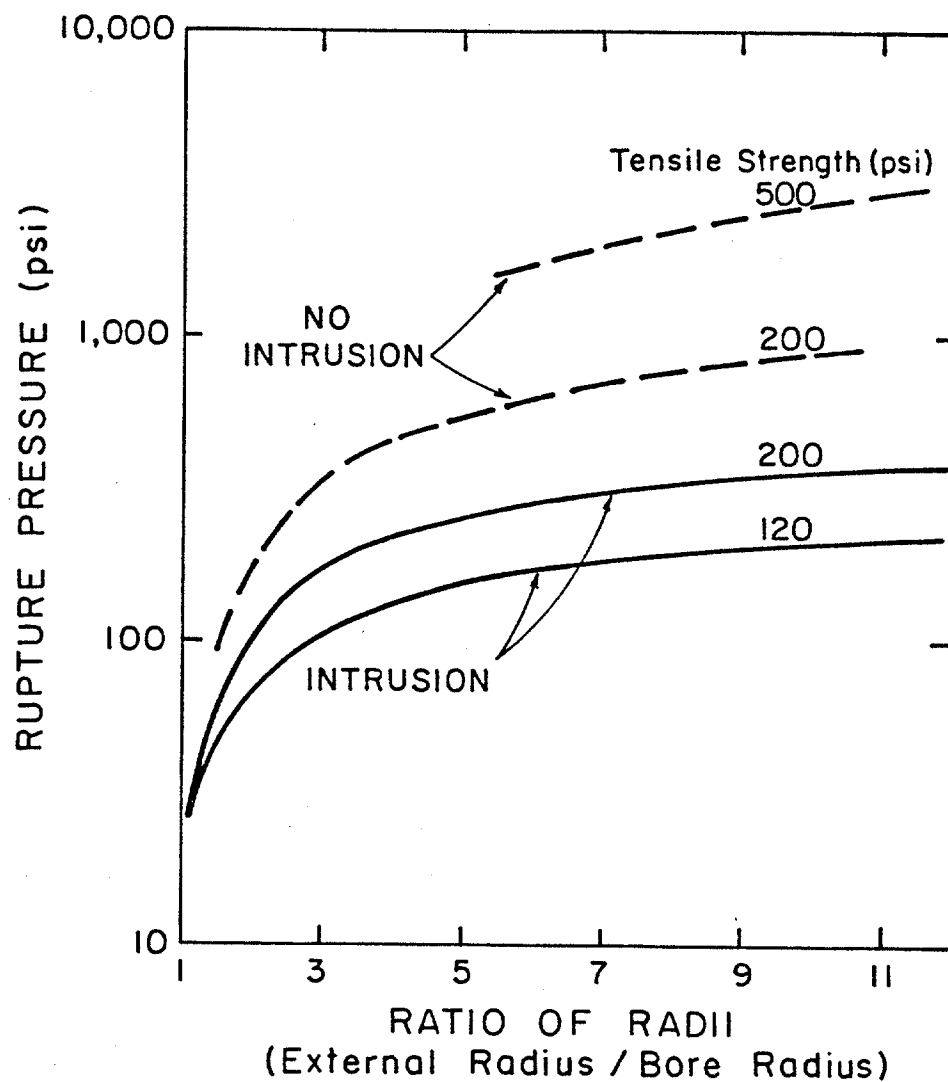


FIGURE 7 - Effect of wall thickness on internal bursting pressure of hollow rock cylinders (from Scott et al. 1953).

described by the vertical overburden stress calculation. Common geologic processes other than simple sedimentation, like the upward movement of low-density salt or plastic shale domes, can alter the vertical state of stress. It is sometimes possible to find the vertical stress state at depth exceeding the geostatic load. In the West Coast area, for example, the continental drift is causing a collision of the North American and Pacific plates, which results in large lateral compressive stresses. This can also be caused by the internal grain friction in sediments immediately above a salt dome. However, rocks generally are quite weak in tension, and faulting will occur, which tends to relieve the buildup of stresses significantly above the geostatic load.

The vertical overburden is often assumed to be equal to 1.0 psi/ft of depth (Harrison et al. 1954; Hubbert and Willis 1957). This is the same as assuming a constant value of bulk density over the entire sediment section. This simplifying assumption can be helpful in some areas when planning wells deeper than 10,000 ft. However, it can lead to significant errors in the computation of overburden stress, especially for shallow sediments beneath deepwater offshore locations. This approximation generally is used when the change in bulk density with respect to depth is not known.

More recent approaches account for variations in overburden pressure and have produced more accurate results. The most accurate estimates of pore pressure and overburden stress gradient can be made using density or porosity data available from well logs. Figure 8 shows an example of variable overburden gradients in the Gulf of Mexico by depth (Eaton 1969). This curve is often used as a

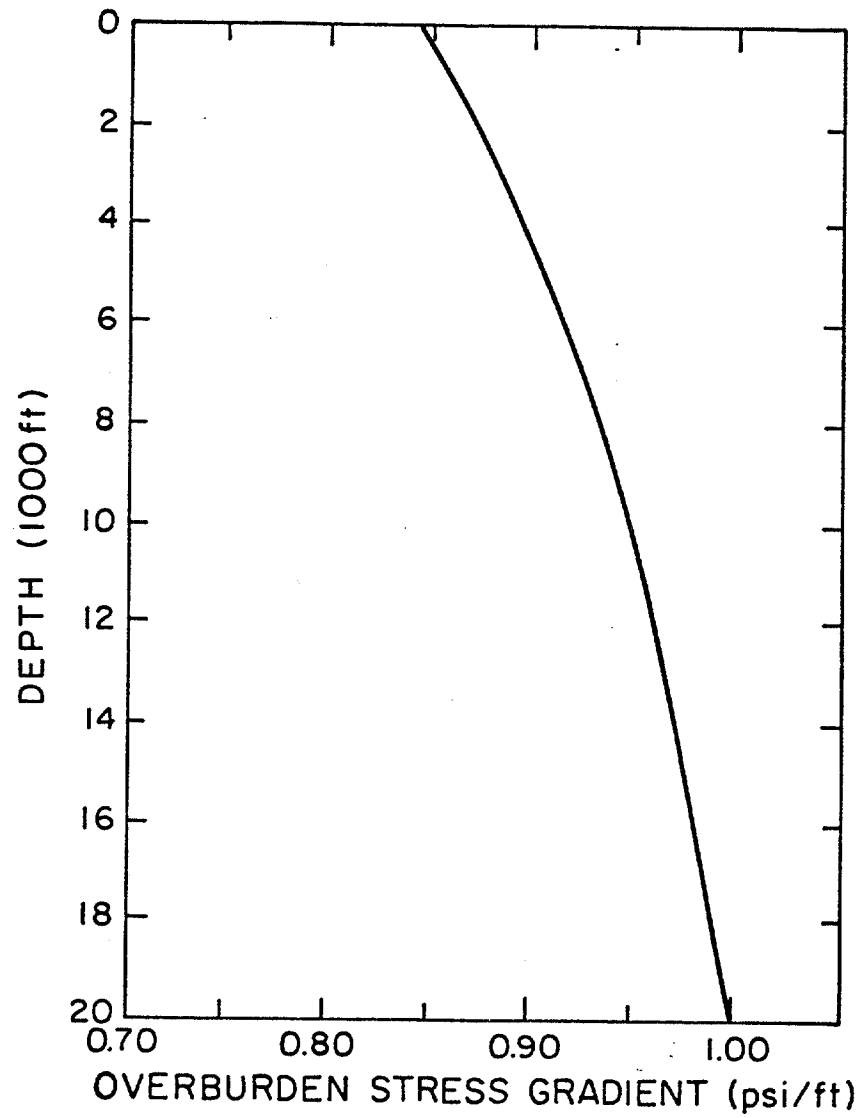


FIGURE 8 - Overburden stress gradient versus depth for normally compacted Gulf Coast formations (after Eaton 1969).

representation of average conditions in this area when well logging data are not available.

Overburden stress gradient also varies significantly with water depth (Christman 1973) in offshore areas, and this variation is responsible for the significant differences in fracture gradients shown in the example presented in Figure 9. Typical onshore fracture gradients are also shown for comparative purposes. The detrimental effect of water depth on fracture pressure is thought to be directly related to the reduction in overburden stress caused by replacing part of the high-density overburden with lower-density seawater.

Penetrating Versus Nonpenetrating Fracturing Fluids

A nonpenetrating fluid is defined in this work as a fluid incapable of permeating a rock formation. Whether a fluid is penetrating or nonpenetrating with respect to a certain rock depends upon the sizes of the interconnected pores and naturally occurring fractures in the rock. An ordinary drilling mud forming a relatively impermeable filter cake on a rock is usually assumed to be a nonpenetrating fluid (Scott et al. 1953), even though there may be small amount of filtration taking place. The rates of any filtration taking place are small enough to be neglected is that they do not have a significant effect on the length or width of the fracture formed.

In the case of a penetrating fluid, the pressure difference between the well-bore fluid, P_w , and the pore fluid in the formation, P_o , will cause an outward radial flow from the well into the

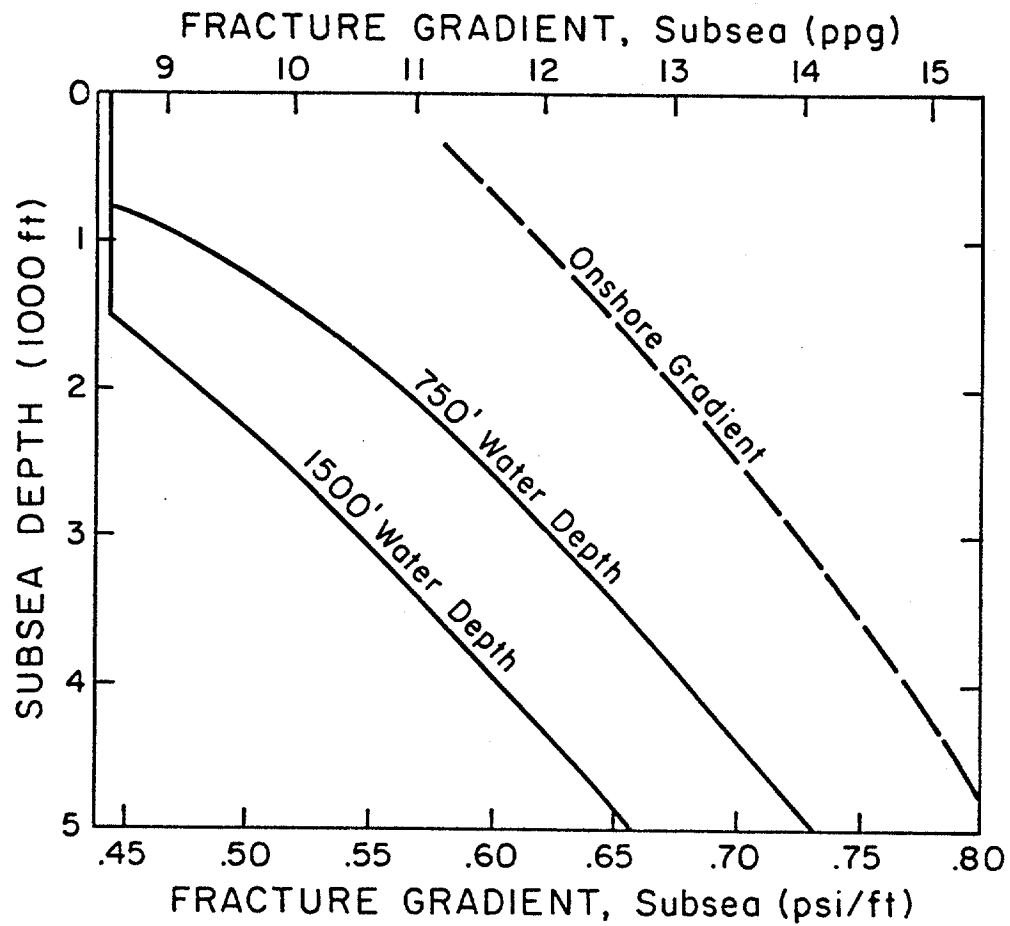
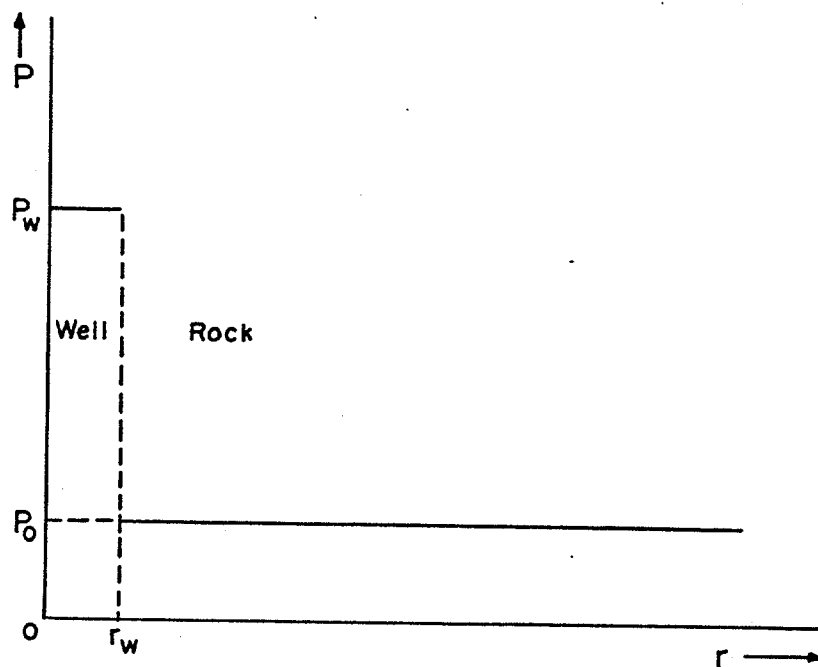


FIGURE 9 - Example of offshore fracture gradients (after Christman 1973).

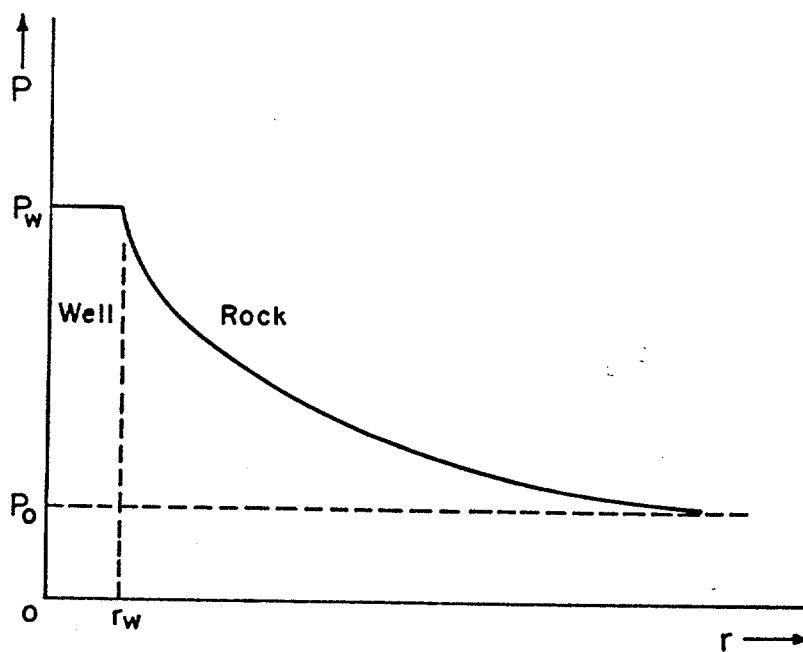
formation. Generally, to simplify the problem being studied, it is assumed that the properties of the penetrating fluid and those of the formation fluid are similar. In addition, the formation is assumed to have uniform permeability so that the fluid flow is axisymmetric.

Figure 10 shows a possible distribution of pressure around the borehole with a penetrating and a nonpenetrating type of fluid. Timoshenko and Goodier (1951) and Geertsma (1957) applied the theory of thermoelasticity, modified to solve problems in elastic material, to show that fluid flow through porous media causes stresses that affect the rupturing pressure of permeable formations. When this happens, the fluid intrusion reduces the breakdown pressure.

This theoretical result was confirmed by the experimental work of Scott et al. (1953) with fracturing cylinders of sandstone rock in the laboratory and shallow wells in a sandstone outcrop. They used mineral oil as the penetrating fluid and drilling mud having very low fluid loss as the nonpenetrating fluid. On the basis of their results, they concluded that the use of penetrating fluids results in a lower rupturing pressure of rock formations than may be expected with nonpenetrating fluids. Their results are presented in Table 1.



(a)
DISTRIBUTION OF PORE FLUID PRESSURE AROUND
WELLBORE (RADIUS r_w) FOR NONPENETRATING
FRACTURING FLUIDS



(b)
POSSIBLE DISTRIBUTION OF PORE FLUID PRESSURE
AROUND WELLBORE (RADIUS r_w) FOR PENETRATING
FRACTURING FLUIDS

FIGURE 10 - Possible distribution of pore fluid pressure around the borehole (from Haimson and Fairhurst 1967).

TABLE 1 - Effect of fluid intrusion on the rupturing pressure of sandstone (from Scott et al. 1953).

Radii (in.)		Rupturing Fluid	Rupturing Pressure (psi)	Type of Fracture
Internal	External			
.19	1.75	drilling mud	2,700	vertical
.19	1.75	drilling mud	2,000	vertical
.19	1.75	drilling mud	2,300	vertical
.19	1.75	mineral oil	1,200	horizontal
.19	1.75	mineral oil	1,400	horizontal
.19	1.75	mineral oil	1,400	horizontal
.19	infinite	drilling mud	4,800	vertical
.19	infinite	drilling mud	4,200	not distinguishable
.19	infinite	drilling mud	4,300	not distinguishable
.19	infinite	drilling mud	3,900	not distinguishable
.19	infinite	mineral oil	1,150	not distinguishable
.19	infinite	mineral oil	600	horizontal
.19	infinite	mineral oil	700	horizontal
.19	infinite	mineral oil	650	not distinguishable

Tensile Strength of Rock

The general trend of the effect of tensile strength on the fracture initiation pressure may be seen in Figure 7, which shows that the greater the strength, the higher the internal rupturing pressure for a given ratio of external to bore radius. However, rocks are seldom isotropic or homogeneous, and they usually vary widely in strength characteristics. Deviations from the assumed isotropy and homogeneity will change the breakdown pressure of the formation. Experimental work (Scott et al. 1953) has indicated that the ratio of internal bursting pressure to tensile strength in cylinders of sandstone and shale may vary from 1.4 for sandstone to 28.6 for shale. These results lead to the conclusion that the difference between the breakdown pressure of two rocks may exceed many times the difference between their tensile strengths.

Weibull's (1952) statistical theory of material strength indicates that the results of standard tensile strength tests that pull the specimens apart, and results of cylinder-rupturing tests, should not be expected to agree unless bore cylinders larger than 1.5 in. are employed. This behavior is supported by the data shown in Figure 11. The value listed in material handbooks for tensile strength of limestone is approximately 500 psi. This value agrees very well with the value given in Figure 11 for hole diameters of thick-walled cylinders of limestone greater than 1.5 in.

Hubbert and Willis (1957), however, pointed out that the tensile strength of flawless specimens can vary from zero, for unconsolidated materials, to hundreds of pounds per square inch for the strongest rocks. But, as observation of any outcrop will demonstrate, flawless

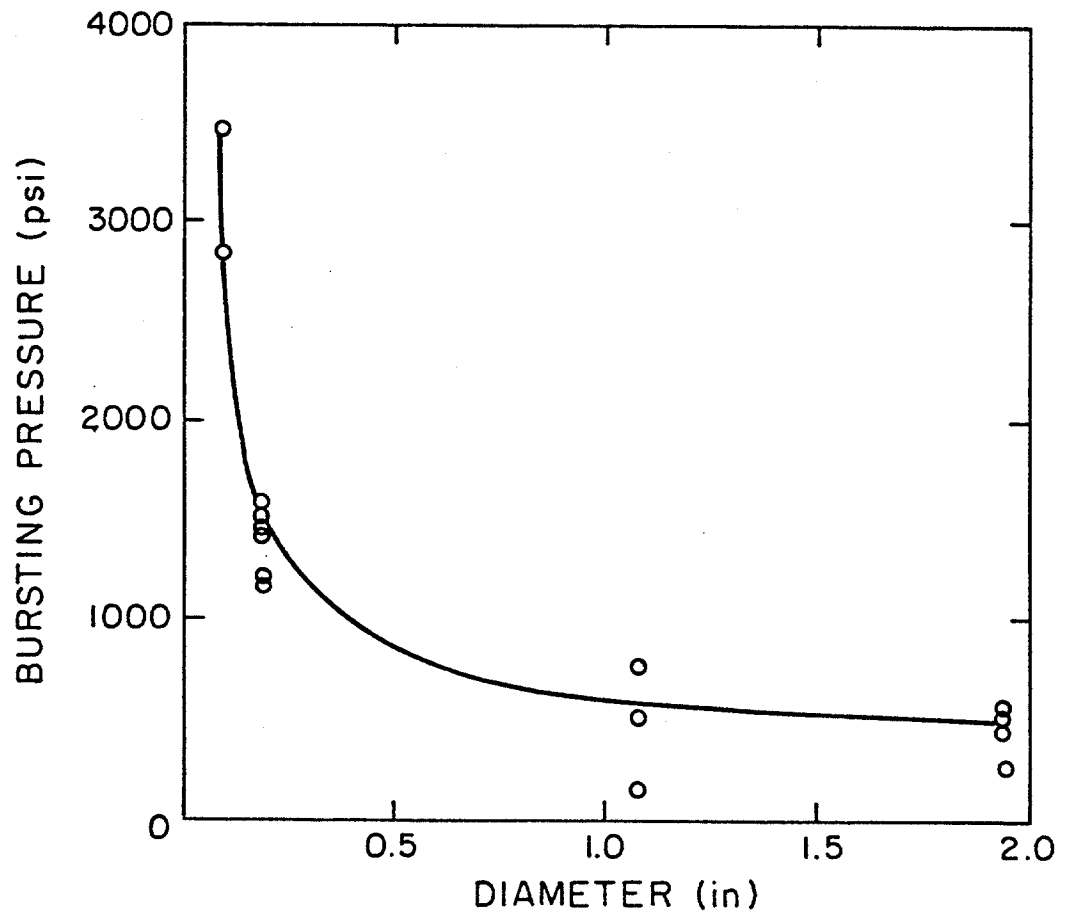


FIGURE 11 - Graph of bursting pressure versus hole diameter for thick-walled hollow cylinders of limestones (Harrison et al. 1954).

specimens of linear dimensions greater than a few feet rarely occur. In addition to the bedding limitations that limit tensile strength to a minimum, the rocks are usually intersected by one or more systems of joints with only slight displacements. Across these joint surfaces the tensile strength is essentially reduced to zero.

Under the idealized conditions of isotropy, homogeneity, and elastic behavior of rocks, the tensile strength will affect the fracture pressure of the formation. Sand and shale occur frequently in the most common lithology; induced hydraulic fractures are expected to occur in sand sections rather than in shale because of the higher tensile strength of shale.

Somerton et al. (1964) have shown that temperature can substantially alter physical properties of rocks. On the bases of plots like the one in Figure 12, they concluded that Young's Moduli and Poisson's ratios, as well as strengths, are decreased by thermal treatment. However, it is interesting to note that the temperature used in their test (1112°F) is excessively high compared to usual borehole temperatures. Scott et al. (1953) in experiments conducted on sandstone cylinders at temperatures between 80°F and 200°F showed no variation in fracture pressure with temperature for either penetrating or nonpenetrating fluids. This range of temperature is much closer to the range of values of bottom-hole temperature encountered during leak-off tests.

Joints and Faults Near the Well Bore

The pressure required to induce hydraulic fracture can be greatly affected if the well bore, instead of being smooth and

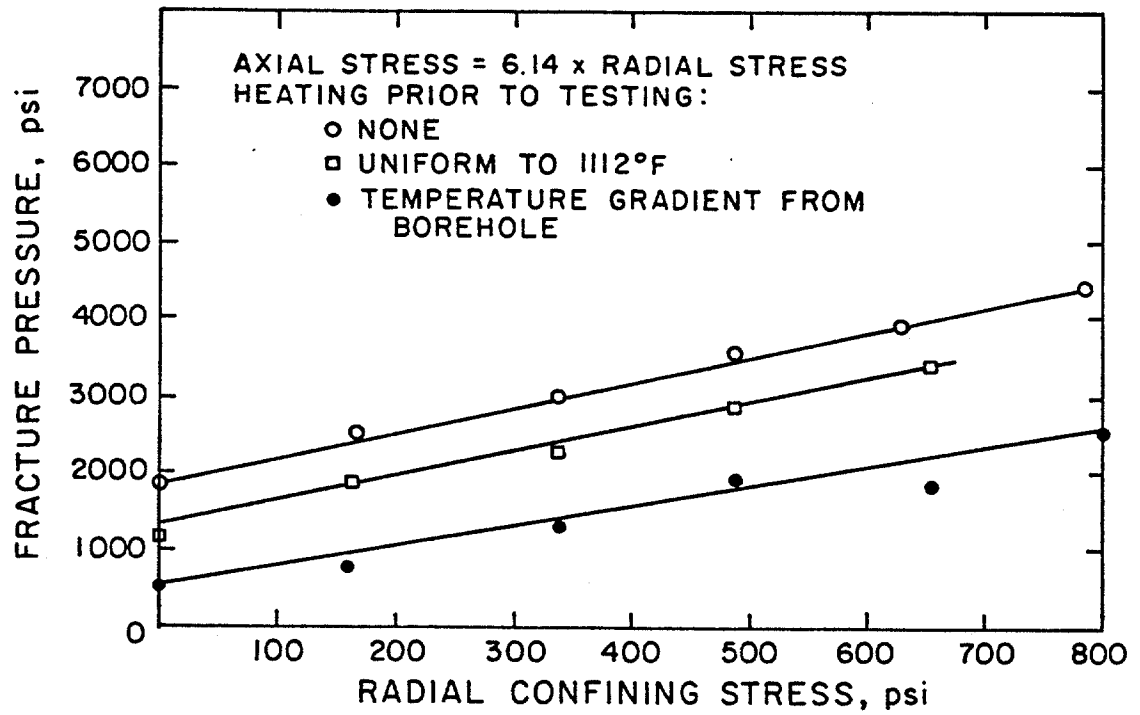


FIGURE 12 - Fracture pressure versus radial confining stress for Bandera sandstone (from Somerton et al. 1964).

cylindrical, as assumed in Equation (4), has the rocks near it intersected by a system of joints and faults. Hubbert and Willis (1957) stated that any section of a well bore a few tens of feet long has probably been intersected. Thus, it appears that the tensile strengths of most rocks subjected to hydraulic fracturing by pressure applied in well bores are effectively zero. Then, according to Equation (4), the pressure required to fracture the formation is only that required to reduce the compressive stresses across some planes in the wall of the hole to zero. The naturally occurring fracture will begin to open when the applied pressure equals the compressive stress normal to it, σ_t . This compressive stress is expressed by

$$\sigma_t = 1/2 \cdot \sigma_z / (1 - \mu) [1 - (1 - 2\mu) \cdot \cos 2\theta] + P_o \dots \dots \dots (5)$$

Harrison et al. (1954) equated this compressive stress normal to an inclined fracture (Equation 5) to the injection pressure required to initiate a vertical fracture in a nonfractured location (Equation 2). They then solved the resultant equation for the fracture inclination angle, θ , and derived the following formula:

$$\theta = 1/2 \cdot \cos^{-1} [(1-4\mu) / (1-2\mu) + (2(1-\mu) / (1-2\mu)) \cdot S_t/\sigma_z] \dots (6)$$

Assuming a nominal value of 0.25 for Poisson's ratio, μ , and -0.1 for the tensile strength to vertical matrix stress ratio, S_t/σ_z , and solving the above equation for the angle θ , at which the existing fracture is as likely to open as is a new vertical fracture, results in a value of approximately 53°. This value indicates that for these

conditions, a naturally occurring fracture will be opened preferentially to a vertical fracture if it makes an angle of about 53° or less with the vertical. In addition, faults that create angles of 30° or less with the vertical fracture, according to Equation (5), should widen at applied pressures equal to $\sigma_z/2$, whereas vertical joints, $\theta=0$, should be $\sigma_z/3$.

Harrison et al. extended their analyses to include cases in which the naturally occurring fracture was tightly closed or filled with secondary deposits, so that, though it possessed a negligible tensile strength, fluid could not be readily injected into it. If we use the same approach as before, but consider that the pressure required to open the fracture is twice the normal compressive stress to widen it, the preexistent fracture would be opened when

$$\theta \leq 1/2 \cdot \cos^{-1} [1 + (1 - \mu) / (1 - 2\mu) \cdot S_t / \sigma_z] \dots \dots \dots (7)$$

As the vertical stress increases with depth, θ approaches zero. For small values of θ , the tightly closed or cemented fracture would not be opened in preference to a new vertical fracture unless it were almost vertical.

Formation Pore Pressure

Just as the effect of overburden variations is important, so also is the effect of formation pore pressure variations. This would be expected from inspection of the theoretical relationships presented in the earlier sections. Correlations for predicting pore pressure are

available in the literature. In this study, it has been assumed that the pore pressure is known.

Correlations for Fracture Pressure Prediction

Hubbert and Willis's (1957) pioneering paper established much of the theoretical basis for subsequent work in fracture-gradient prediction techniques. They described the effect that variations in the three principal stresses can have on fracture gradient and fracture orientation. They pointed out that the pressure to fracture a given formation should overcome the local stress concentration at the borehole wall. This stress concentration was found to be twice the least principal stress of an undisturbed region. In addition, they stated that under conditions of incipient normal faulting, such as those in the Gulf Coast area, the horizontal matrix stress is the least principal stress. If the horizontal matrix stresses in the x and y direction are equal, then the pressure required to initiate fracture in a homogeneous, isotropic formation should be

$$P_f = 2\sigma_h + P_o \dots\dots\dots (8)$$

where $\sigma_x = \sigma_y = \sigma_h$. On the basis of laboratory experiments, Hubbert and Willis concluded that in unconsolidated shallow sediments, the horizontal matrix stress would be approximately one-third the vertical matrix stress. This observation is consistent with Equation (1) if a value of 0.25 is used for Poisson's ratio.

The theoretical treatment used by most authors (Hubbert and Willis 1957; Haimson and Fairhurst 1967; Hagoort et al. 1980; Campos

1983) is to solve the classical problem of stress concentration in a very large rectangular plate with a small circular hole at its center using elasticity theory. The additional stress fields introduced by the fluid being pumped into the well and by borehole fluid movement into the formation are added by the principle of superposition (Hubbert and Willis' 1957). The final solution, which is derived in Appendix A, is

$$P_f = [3\sigma_y - \sigma_x - S_t] / [2 - \alpha \cdot (1-2\mu) / (1-\mu)] + P_o \dots\dots\dots (9)$$

where α is the Biot's constant (Geertsma 1957).

Equation (9) includes the assumptions that rock formation is elastic, porous, isotropic, homogeneous, and has measurable values of Poisson's ratio and Biot's constant. In addition, the well-bore wall is considered to be smooth and circular in cross section, and the principal regional stresses act parallel to the vertical axis of the well bore. The fracturing fluid is considered to penetrate the formation. The theoretical development for a nonpenetrating type of fluid is also given in Appendix A and yields

$$P_f = 3 \cdot \sigma_y - \sigma_x - S_t + P_o \dots\dots\dots (10)$$

It is interesting to note that the assumptions $\sigma_x = \sigma_y = \sigma_h$ and $S_t = 0$ reduce Equation (10) to the Hubbert and Willis formula defined by Equation (8).

Drilling experience has shown that formation fracture gradients generally increase with depth, even in normally pressured formations. Matthews and Kelly (1967) replaced Hubbert and Willis's (1957) assumption that the minimum matrix stress was one-third the overburden with a matrix stress coefficient, K_i , that is a function of depth and can be regarded conceptually as the ratio of horizontal effective stress to vertical effective stress. The coefficient " K_i " was determined empirically from field data collected at the south Texas and Louisiana Gulf Coast, in normally pressured formations only. Figure 13 shows the plot obtained using these field data. The fracture pressure is given by

$$P_f = K_i \cdot \sigma_z + P_o \dots \dots \dots (11)$$

However, for abnormally pressured formations, the matrix stress should be determined at the depth of a normally pressured formation that has the same matrix stress as the abnormally pressured formation. This depth can be found graphically by using a pore pressure versus depth plot or by using the equation

$$(\sigma_{zn} - P_{on}) = (\sigma_z - P_o) \dots \dots \dots (12)$$

where σ_{zn} , P_{on} and σ_z , P_o are the overburden stress and pore pressure evaluated at D_n and D_i , respectively. D_n is the depth of the corresponding normally pressured formation, and D_i is the depth of interest. Equation (12) can be simplified by assuming a fixed value of overburden load gradient.

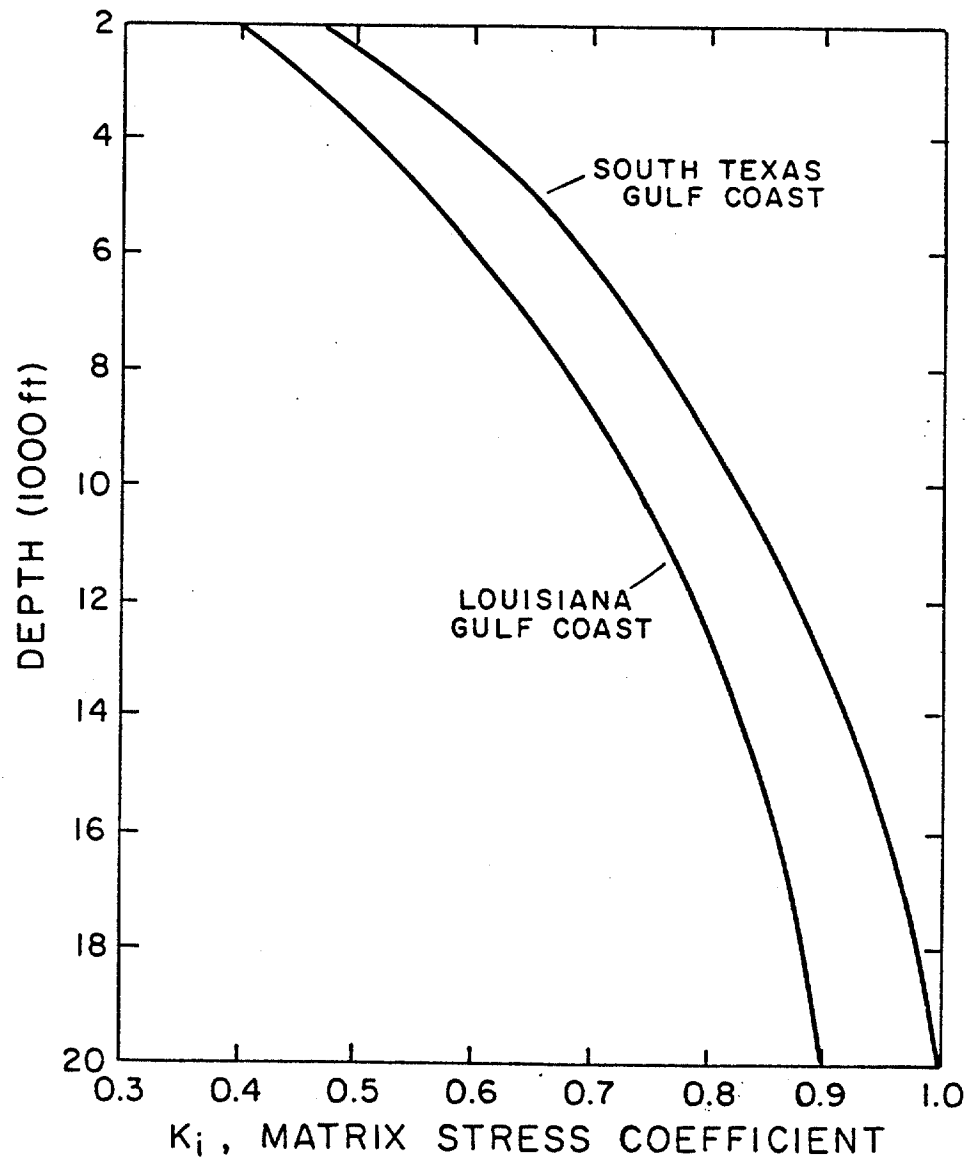


FIGURE 13 - Matthews and Kelly matrix stress coefficient for normally pressured formations (Matthews and Kelly 1967).

In 1968, Pennebaker presented a correlation similar to that of Matthews and Kelly. Pennebaker referred to the coefficient " K_i " as the effective stress ratio and correlated this ratio with depth, regardless of pore pressure ratio. In this case, the actual depth of interest D_i , is used directly in Figure 14 to obtain K_i . In addition, Pennebaker did not assume a constant value of vertical overburden stress. He developed a correlation for determining vertical overburden stress gradient as a function of depth and geologic age for various depths at which the interval transit time obtained from seismic data is 100 μ sec/ft. This correlation is shown in Figure 15.

Eaton (1969) developed a correlation assuming that the relationship between horizontal and vertical matrix stress is accurately described by Equation (1). Using observed fracture-gradient data from western Texas and the Texas and Louisiana Gulf Coast, he computed values of Poisson's ratio as a function of depth, as shown in Figure 16. However, he didn't make any distinction between fracture-pressure gradient and fracture-extension pressure gradient. Consequently, the value of Poisson's ratio obtained in Figure 15 would have been slightly different if the analysis was made using Equation (4). The Gulf Coast data were analyzed by first assuming a constant overburden stress gradient of 1.0 psi/ft and then assuming a variable overburden stress obtained by integration of bulk density logs. Eaton's equation is

$$P_f = [\mu/(1-\mu)] (S_z - P_o) + P_o \dots \dots \dots (13)$$

where Poisson's ratio is obtained as shown in Figure 16.

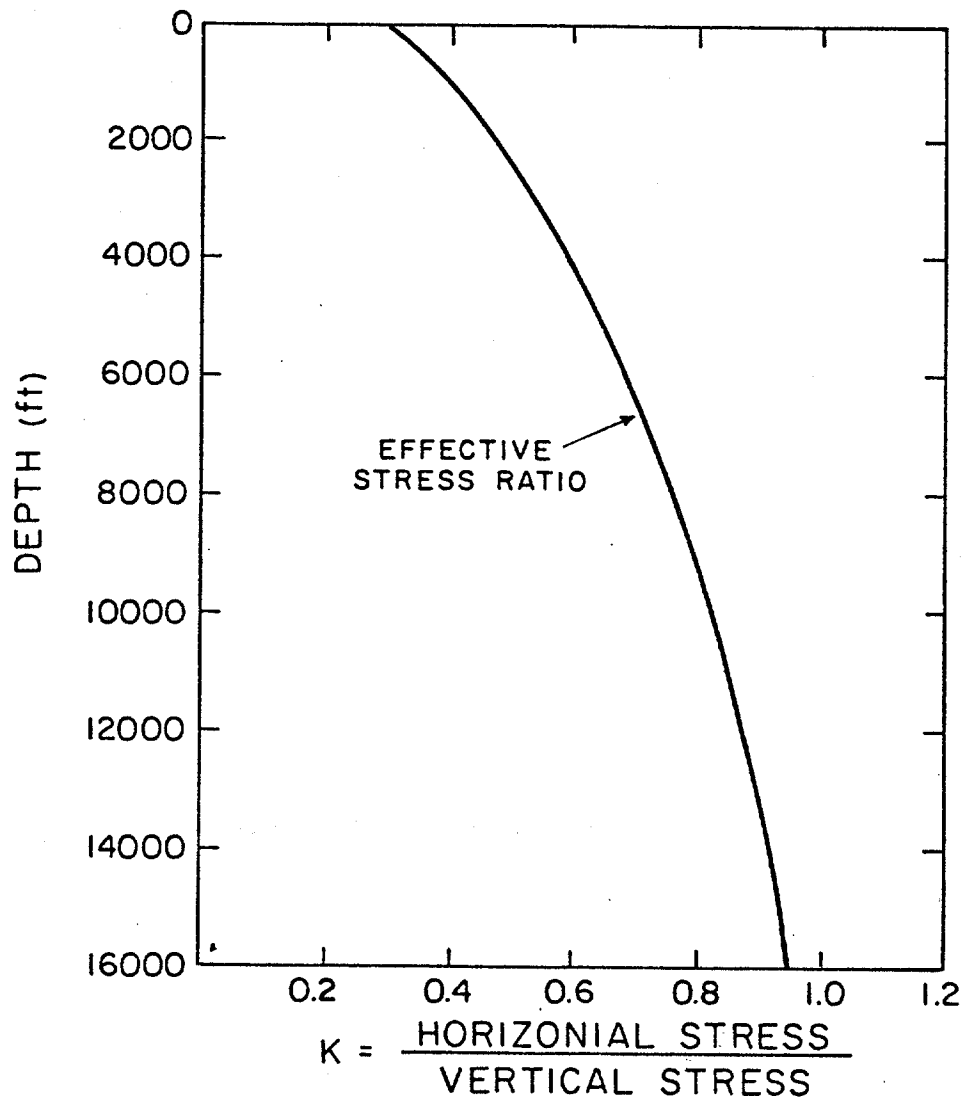


FIGURE 14 -K Function versus depth used in estimating fracture gradients (from Pennebaker 1968).

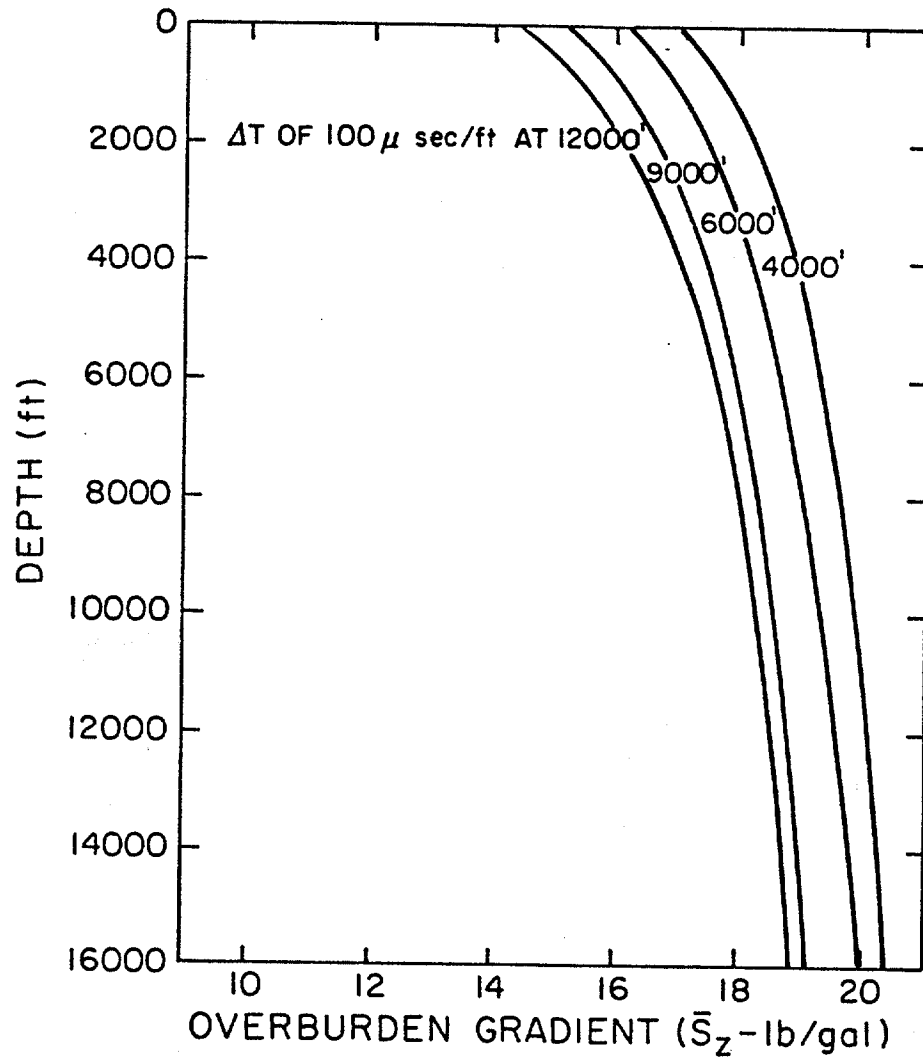


FIGURE 15 - Variation in overburden gradient with geologic age (Pennebaker 1968).

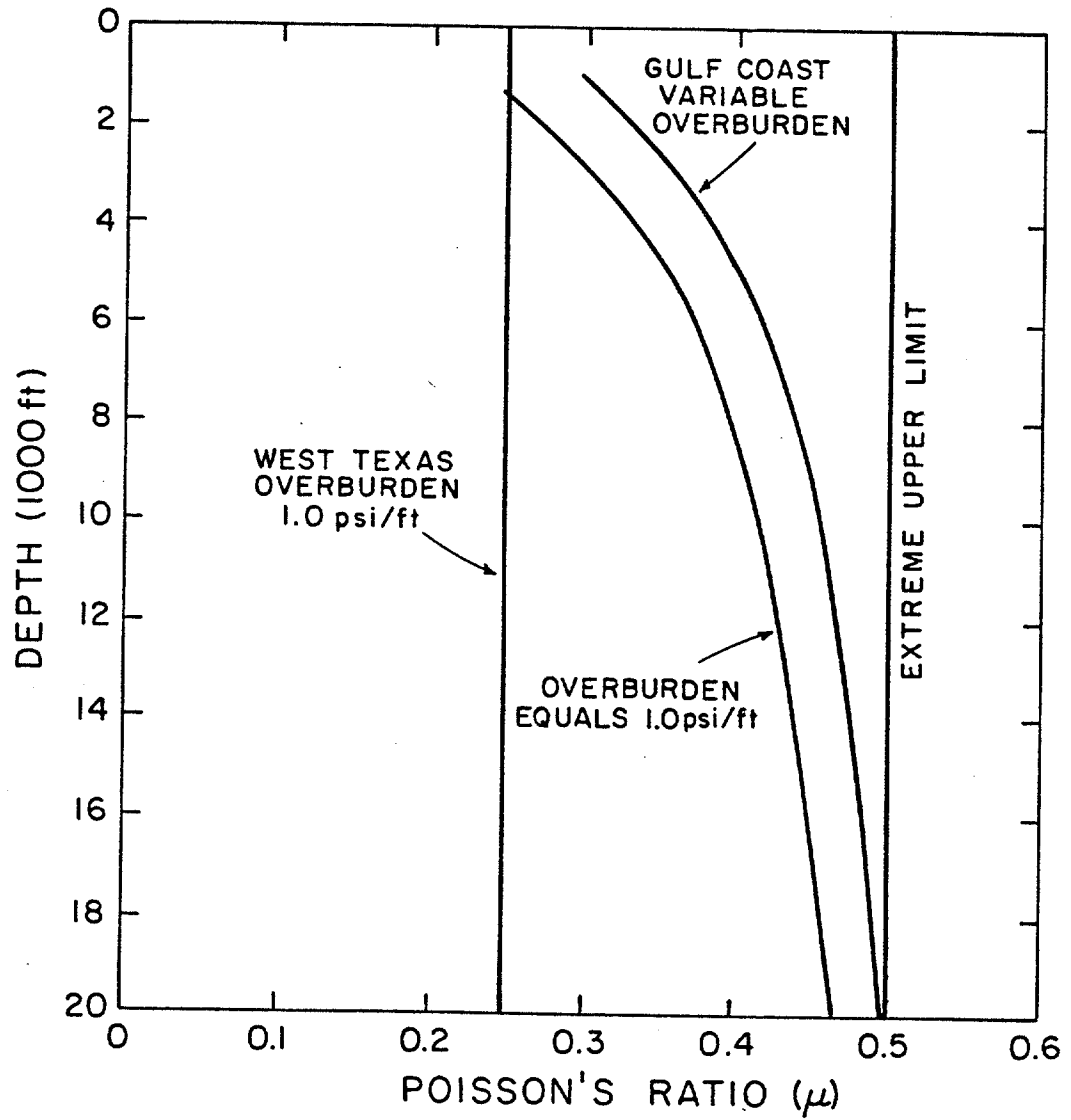


FIGURE 16 - Variations of Poisson ratio with depth (after Eaton 1969).

Christman (1973) examined some bulk density logs of the Santa Barbara channel off the California coast and found that in wells having low fracture pressures zones of unusually low density were exposed in the well bore, and high-fracture gradients were accompanied throughout the well bore by rocks of greater-than-normal density. The finding suggests that formation bulk density correlates with stress ratio and can serve as a measure of the degree of compaction. Fracturing is assumed to be at the depth of highest stress ratio and lowest rock density. The plot of these stress ratios observed in the Santa Barbara channel versus the rock density is shown in Figure 17. The equation to predict formation fracture pressure is

$$P_f = F_T (S_z - P_o) + P_o \dots \dots \dots (14)$$

where,

F_T = stress ratio (Figure 17).

Christman's approach emphasizes that different types of rocks can have different fracture initiation gradients, if all other factors are equal. This then reinforces the concept that the weakest formation is not necessarily at the casing shoe.

Anderson et al. (1973) utilized Biot's (1956) stress-strain relations for elastic porous media and certain other assumptions to develop the following theoretical expression for fracture-gradient prediction:

$$P_f = (2 \cdot \mu / (1 - \mu)) \cdot S_z + ((1 - 3\mu) / (1 - \mu)) \cdot \alpha \cdot P_o \dots \dots \dots (15)$$

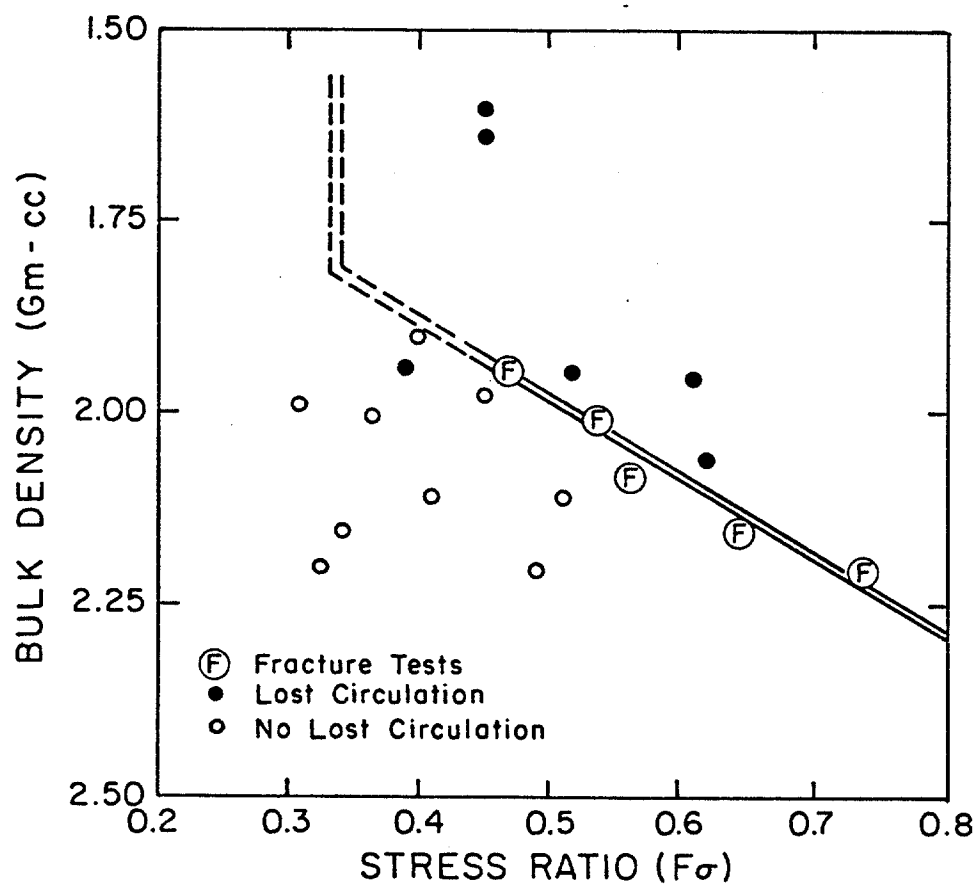


FIGURE 17 - Stress ratio versus rock density (after Christman 1973).

In addition to the fracture-pressure equation, Anderson et al. developed an empirical relationship between Poisson's ratio, μ , and the shale content of sand. The shale content, together with pore and overburden pressures, was estimated by using acoustic and density logging devices. These data were used to develop the fracture-pressure prediction Equation (15) and the plot in Figure 18.

In addition, Anderson et al.'s studies show that fracture gradient varies significantly at a given depth in a geological area and that these variations can be attributed to variable mechanical properties of formations, a finding similar to Christman's (1973).

Brennan and Annis (1984) began their work in the western and central Gulf of Mexico, by first compiling a data base on each well that included overburden pressure, pore pressure, and formation fracture pressures. They then performed an analysis to investigate previously published depth-based correlations. They found that the inadequacy of the results obtained was primarily attributable to the variation from well to well of the top of abnormal pressure and of pore pressure with respect to overburden pressure.

Assuming a variable overburden measured from formation properties and including seawater overburden pressure, Brennan and Annis developed the following equation by curve fitting a plot of $(P_f - P_o)$ versus $(S_z - P_o)$, using 57 leak-off test data. This plot is presented in Figure 19.

$$P_f = P_o + 1.35 (S_z - P_o) - 1.40 (S_z - P_o)^2 \dots\dots\dots (16)$$

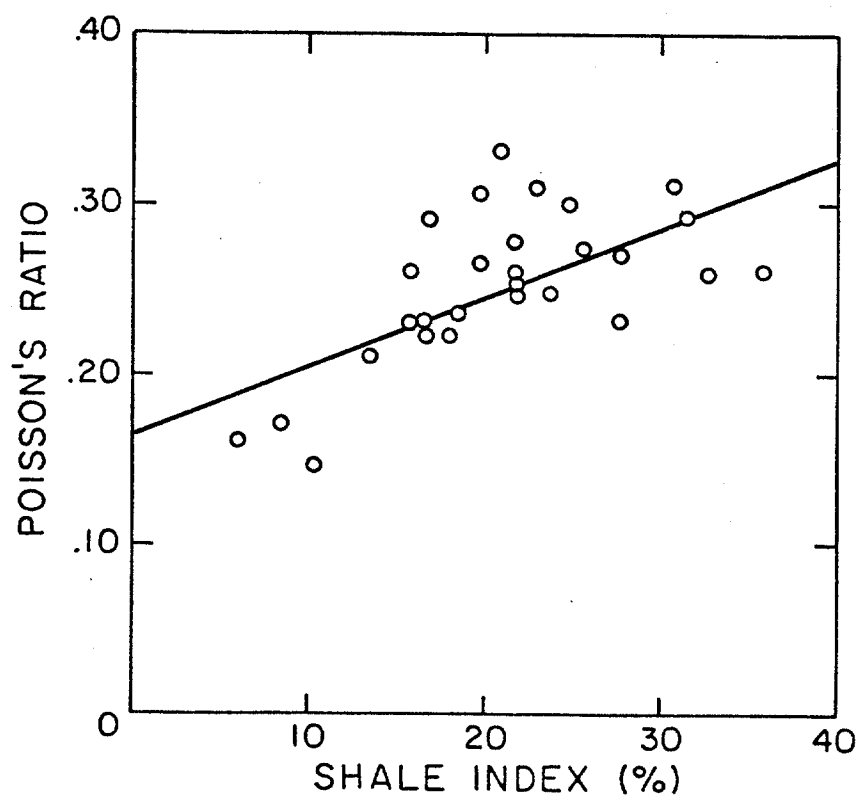


FIGURE 18 - Poisson ratio versus shale index.

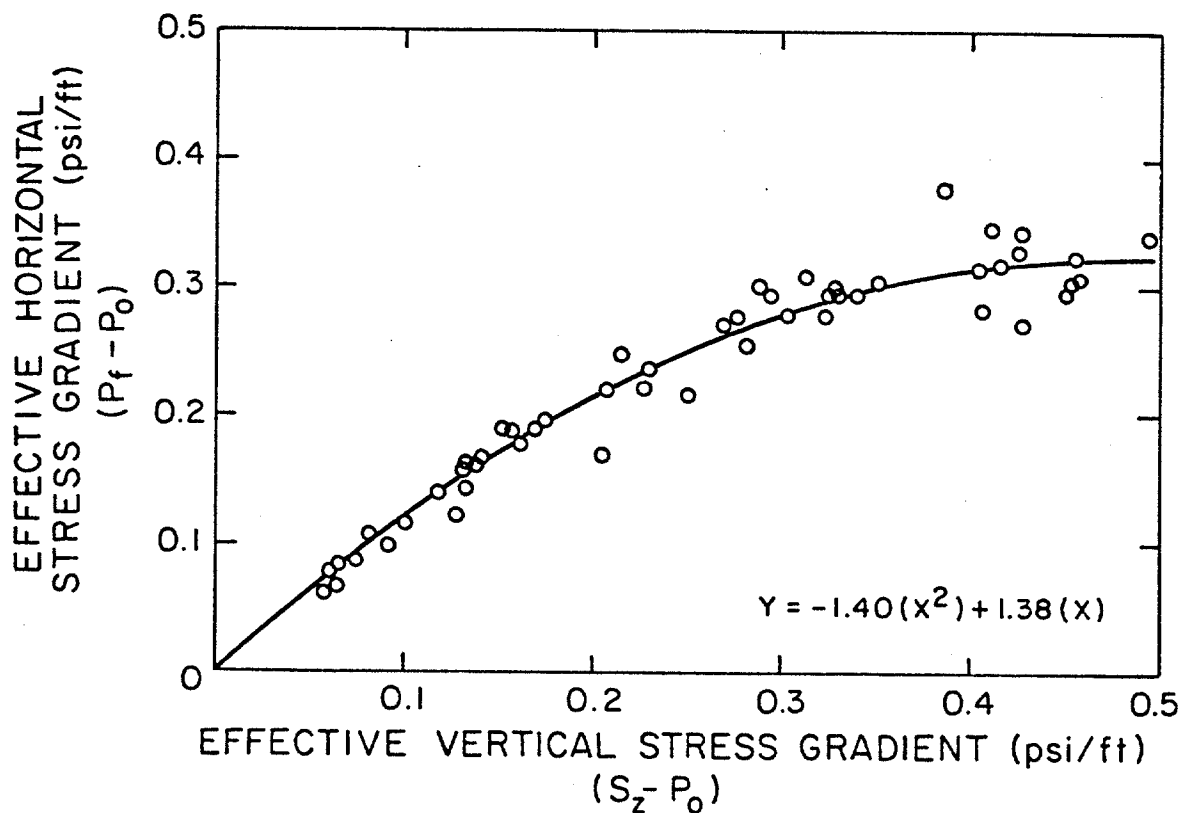


FIGURE 19 - Correlation of the effective horizontal stress gradient versus the effective vertical stress gradient for the western and central Gulf of Mexico (after Brennan and Annis 1984).

Fracture Expansion

The literature on hydraulic fracturing can be divided into two main groups primarily concerned with the geometry of the expanding hydraulic fracture. This literature has evolved from the studies of engineers interested in improving the design of fracture stimulation treatments of oil and gas reservoirs. Authors of the first group use the design methods first proposed by Perkins and Kern (1961) and Nordgren (1972), known as the PKN method after its authors. Basically, authors in this group assume a vertically closed laterally similar elliptical crack. The second group of authors uses the design methods first proposed by Christianovich and Zheltov (1955), Geertsma and DeKlerk (1969), Kiel (1970) and Daneshy (1973), known as the CGDD method after its authors. This second group also assumes a vertically bounded fracture. However, the fracture width is assumed constant across the height of the fracture that forms the shape of a rectangular crack opening. The geometries proposed by these two groups are shown in Figure 20.

The main difference between the PKN method and the CGDD method relates to the potential for bedding plane slip. The CGDD method assumes that the formation bed being fractured is independent of the beds above and below, and consequently the earth would have to slip at the interface between fractured region and overburden and underburden, as illustrated in the detailed view in Figure 20. On the other hand, the PKN group assumes that there is no slip of the boundaries, or only a negligible amount, along the horizontal planes confining the fracture height. They assume that sufficient bonding occurs between the fractured bed and the adjacent strata that the fracture will close at the tips. In addition, the PKN

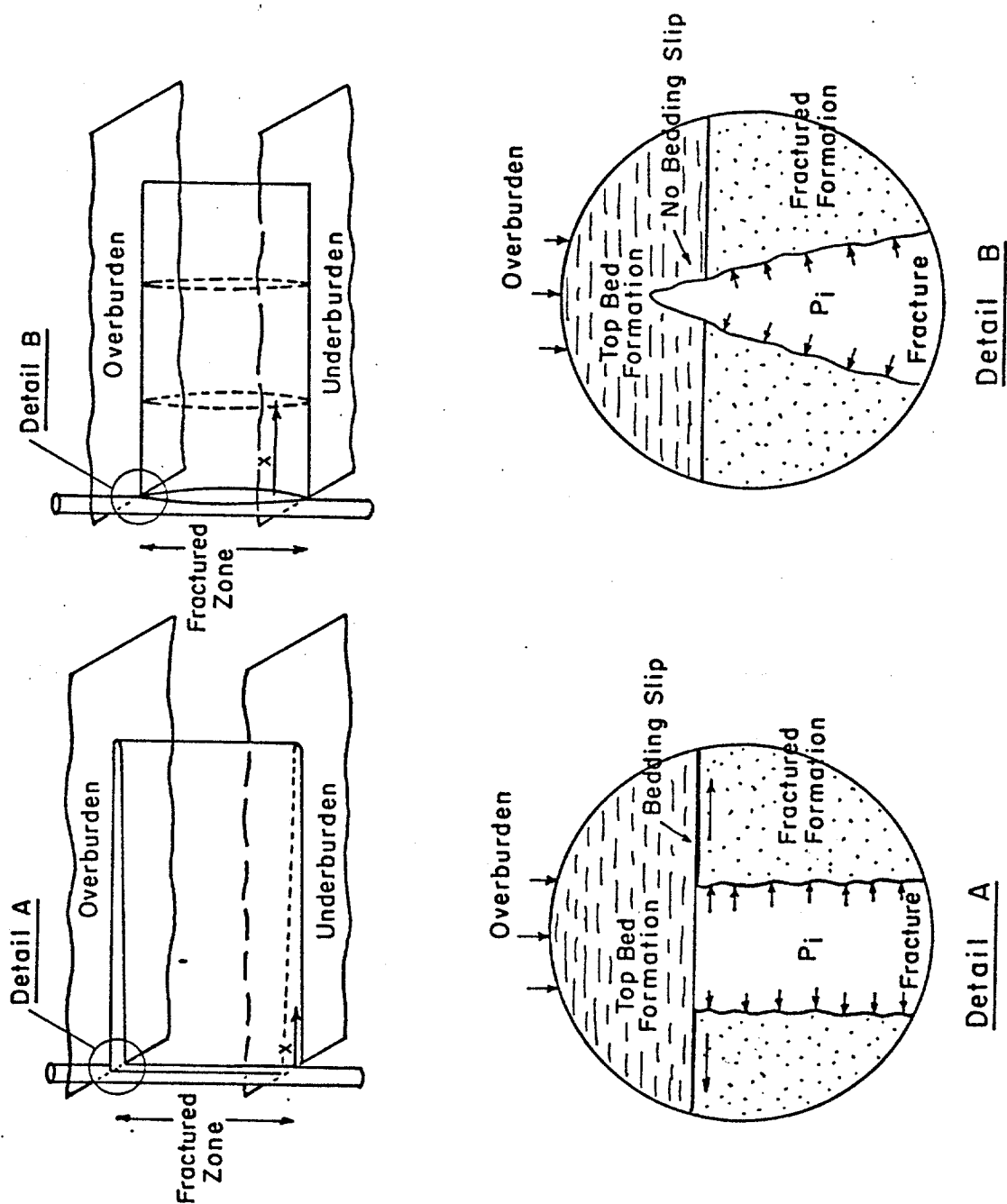


FIGURE 20 -Two simplified possibilities for the geometry of a hydraulic fracture.

group believes that high horizontal stresses at the top and bottom layers limit the height growth of vertical fractures into these zones by tending to close the fracture. These boundary zones can be penetrated until the opposing forces counterbalance one another. If these boundary zones are not thick enough, then the fracture may crack through into other zones. Examples of these higher horizontal stresses can be found sometimes in shale and in limestone reservoirs where non-permeable sections may have higher horizontal stresses than do permeable sections after the reservoir pressure has been drawn down (Perkins and Kern 1961). Figure 20 shows the geometry of these two hypothesis. Also, in areas where the horizontal stress is less than the vertical stress, formations that fail plastically will have a higher horizontal stress than formations that fail elastically.

Nolte (1982) found that bedding planes slip only if the friction between beds can be overcome. This friction is directly proportional to the overburden load acting on the planes where slip occurs. Therefore, it is more likely that bedding planes will slip at shallower depths than at deeper depths because of the difference in overburden.

Various models available in the literature are based on theoretical approaches used to solve the fracture mechanics problem; these approaches are built on certain assumptions that simplify the mathematical solution. These models, according to their fracture geometry and other assumptions, generally fall in one of the two groups, PKN or CGDD. Since they do not incorporate a rigorous mathematical solution they are classified as practical application models. In general, the technical approach is to solve the continuity equation, including the effects of fluid loss to the formation through

the fracture walls and fracture volume change due to the fluid injection into the fracture. The solutions obtained allow width and length of the fracture parameters to be expressed as a function of time. Naturally, pressure distribution along the fracture can also be expressed as a function of time.

The different assumptions made about fracture geometry in a given pressure distribution system will lead to different values of fracture width. In addition, the fluid flow equation describing pressure drop in the fracture will also be different for each case. Basically, the difference depends on the width equation utilized by each model. The CGDD approach utilizes the equation developed by Christianovich and Zheltov (1955) that solved for pressure, has the form

$$\Delta p = W \cdot E / (4 (1 - \mu^2) L \cdot f(x_0/L)) \dots \dots \dots (17)$$

The PKN approach utilizes the Sneddon (1946) equation that, solved for pressure, is

$$\Delta p = W \cdot E / (4 (1 - \mu^2) \cdot h) \dots \dots \dots (18)$$

In Equation (17) the difference between injection pressure and the tectonic stress perpendicular to the fracture wall, Δp , is proportional to the fracture width, W , and inversely proportional to fracture length, L . In Equation (18), Δp is proportional to width and inversely proportional to fracture height, h . Both methods assume constant height, h , and naturally length is a function of time. During the early stage of development of a hydraulic fracture, the

change in length with time is much faster than the change in width with time. Thus, Equation (17) indicates that change in pressure caused by flow along the fracture decreases with time (Daneshy 1973). However, Equation (18) predicts the opposite, since fracture height is constant, pressure will always increase with time.

Investigators (Geerstma and Deklerk 1969; Daneshy 1973) supporting the CGDD method claim that close examination of fracturing pressure charts will show that if the fracturing fluid and injection rates remain constant, the fracturing pressure usually decreases during the fracture expansion. These charts, however, were not included in their papers.

Warpinski (1985) made field measurements of width and pressure in a propagating hydraulic fracture at the U. S. DOE's Nevada test site to investigate pressure drop along the fracture and crack tip arrival time during the normal fracture growth stage. On the basis of these field measurements, Warpinski expressed fracture length as a function of time, t , in the form

$$L = A \cdot t^m \dots\dots\dots (19)$$

They compared the values of the constant, A , and the time exponent, m , obtained for different values of length and time directly with those predicted by the theories of Geertsma and DeKlerk (1969) (CGDD approach), and Nordgren (1972) (PKN approach). Fluid loss to the formation was ignored because it was relatively low. The results showed that Nordgren's exponent for t , when Nordgren's no fluid loss solution was used, matched the data best, and the constant A for both theories was not very different. The measured fracture

parameters obtained by Warpinski are listed in Table 2. Pressure data versus time was plotted for their test #4, and the resulting plot is shown in Figure 21. Pressure continuously increase with time during fracture expansion; this result agrees with the PKN theory.

The single-wing fracture-length equation for Nordgren's model, assuming no fluid loss, yields

$$L = 0.39 [E \cdot q^3 / ((1 - \mu^2) \cdot \nu \cdot h^4)]^{1/5} \cdot t^{4/5} \dots\dots\dots (20)$$

where q is the injection flow rate into the fracture, ν is the fluid viscosity, and the other terms are defined as before. The time exponent, m , mentioned in Warpinski's work is 0.8, and the constant A corresponds to the remaining part of Equation (20). Nordgren also presented the derived equations for well-bore pressure and width as a function of time. For a Newtonian fluid at a constant injection rate, the pressure was also found to increase proportionally to time raised to an exponent. This exponent assumes two different values according to the bounding condition assumed

$$P_e \propto t^{1/5} ; \text{ No fluid loss } \dots\dots\dots (21)$$

$$P_e \propto t^{1/8} ; \text{ Large fluid loss } \dots\dots\dots (22)$$

The net pressure, P_e , in Equations (21) and (22) is the pressure difference between the actual pressure at well bore and the fracture closure pressure, which is defined as the pressure that counteracts the horizontal rock stress perpendicular to the fracture plane.

TABLE 2 - MEASURED FRACTURE PARAMETERS

Test	Theoretical (Nordgren) A			Measured A			Maximum Widths	
	(ft/s ²)	(m/s ²)	m	(ft/s ²)	(m/s ²)	m	(in.)	(mm)
4	2.06	0.63	0.8	0.75	0.23	0.85	0.0223	0.56
5	2.70	0.82	0.8	1.53	0.47	0.85	0.0282	0.72
6	3.40	1.04	0.8	1.98	0.60	0.88	NA	NA
7	3.45	1.05	0.8	3.22	0.98	0.82	0.0350	0.89
9	1.24	0.38	0.8	0.65	0.20	0.91	0.0488	1.24
10	1.85	0.56	0.8	2.56	0.78	0.76	0.0614	1.56
11	1.06	0.32	0.8	1.60	0.49	0.88	0.0626	1.59

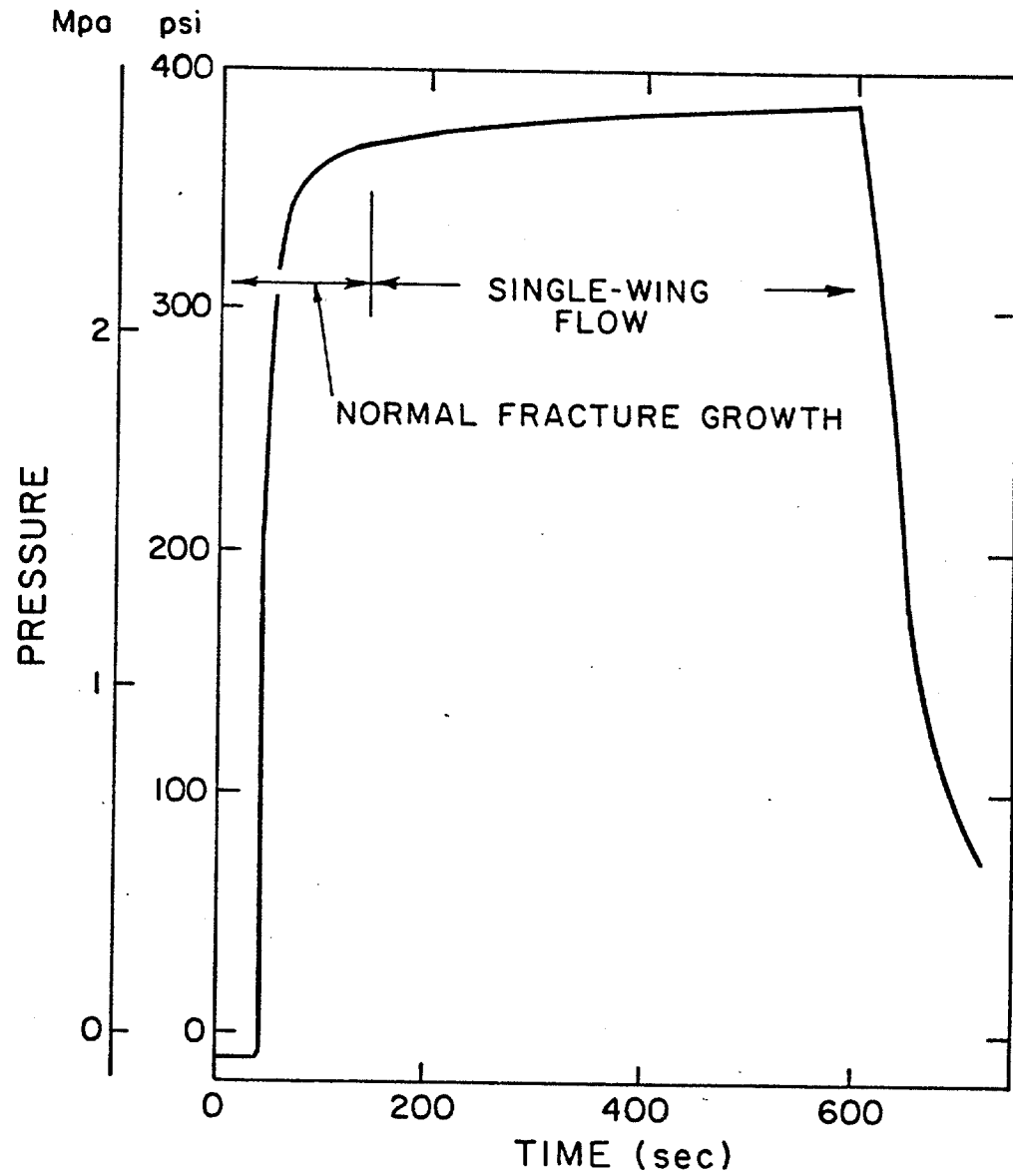


FIGURE 21 - Pressure data versus time (after Warpinski 1985).

Nolte and Smith (1981) discuss how to interpret fracture-pressure response during fracture expansion and conclude that the data presented are consistent with the fracturing assumption of Perkins and Kern (1961) during the initial portion of the treatments called "mode I" in Figure 22. In addition, they noticed that in mode I the slope of each treatment fell within Nordgren bounds (1/8 and 1/5) shown in Equations (21) and (22). Interestingly, the injection period of time above fracture closure in a leak-off test practically never reaches 50 min. Thus, we can conclude, based on Figure 22, that leak-off tests are very likely to fall in the mode I category. In fact, in practice mode II is practically never reached during a leak-off test.

Nolte and Smith (1981) extended the work done by Nordgren (1972) to propose that the time exponent used in Equations (21) and (22) for Newtonian fluid could be represented for a generalized fluid as

$$e = 1 / (2n + 3) \quad ; \quad \text{No fluid loss} \dots\dots\dots (23)$$

$$e = 1 / (4n + 4) \quad ; \quad \text{Large fluid loss} \dots\dots\dots (24)$$

where e is the time exponent, and n is the power-law exponent.

The models derived with CGDD and PKN methods are known as two-dimensional models (2-D models) because of their assumption of constant fracture height. Recently, some researchers have claimed the development of more sophisticated three-dimensional models (3-D models) yielding good results (Williams 1970; Settari and Cleary 1984; Meyer 1985). In the 3-D models, the fracture height, width, and length are allowed to vary with time. The assumption is that the fracture will extend vertically until it reaches the upper and lower

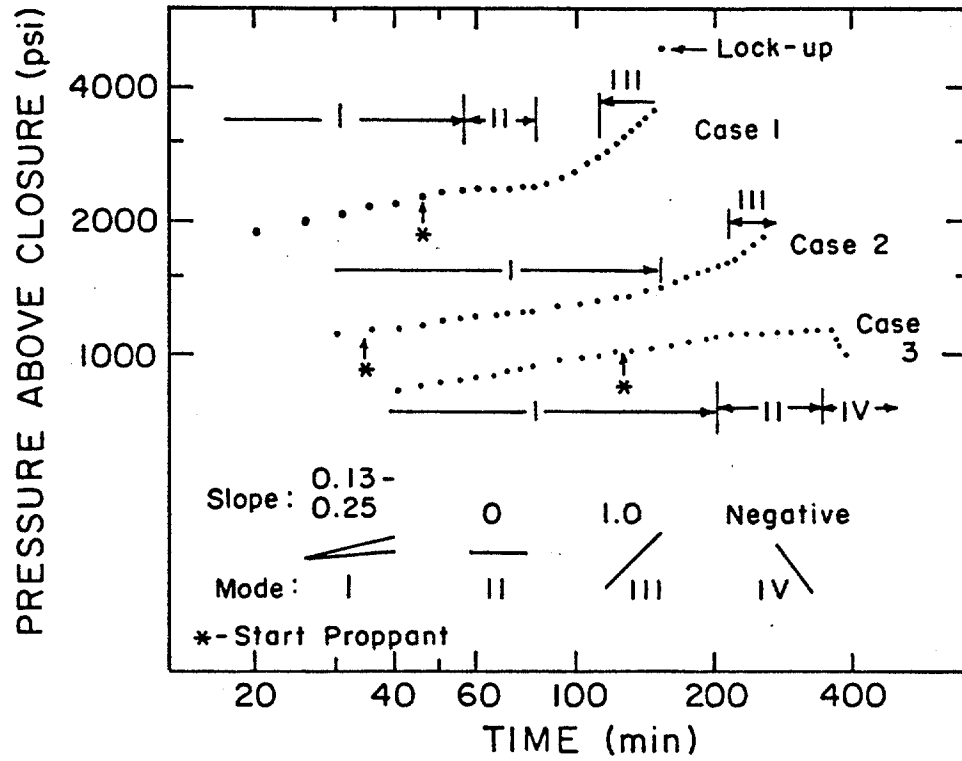


FIGURE 22 - Examples showing different characteristic slopes (after Nolte and Smith 1981).

strata. How deep the fracture penetrates into these strata will depend on the confining stress contrast in the formation being fractured. Figure 23 illustrates how the fracture profile changes with confining stress contrast, ΔT . It shows that as the confining stress contrast increases, the fracture tends to look more like the one predicted by 2-D models with limited height. In general, these 3-D models incorporate the CGDD and PKN methods when confining stress contrast is high. For early stages during fracture expansion or when the length/height ratio is less than or equal to 1, the CGDD method is used; when this ratio is greater than 1, the PKN method is used. For moderate to lower confining stress contrast, the model does not limit the fracture shape to being elliptical or rectangular, but rather allows the width profile to change depending on the overburden/underburden stress and moduli contrast and the fracture height-to-length aspect ratio.

Meyer's (1985) 3-D model, for example, assumes that the pressure profile initially decreases with time (CGDD approach), until it reaches the upper and lower strata. Once it reaches these barriers, the pressure will increase if confining stress contrasts are large, or it will continue to decrease if the barriers are weak.

The 3-D models developed are powerful tools for realistic analysis of fracture treatments because they solve the rock mechanics problem more rigorously than do the 2-D models. However, verification and routine practical application in the full 3-D mode are generally limited by lack of data (Settari and Cleary 1984). Any improvement in accuracy that could be obtained with the mathematical model is generally lost because of the inaccuracy of some of the estimates of the parameters used in the model.

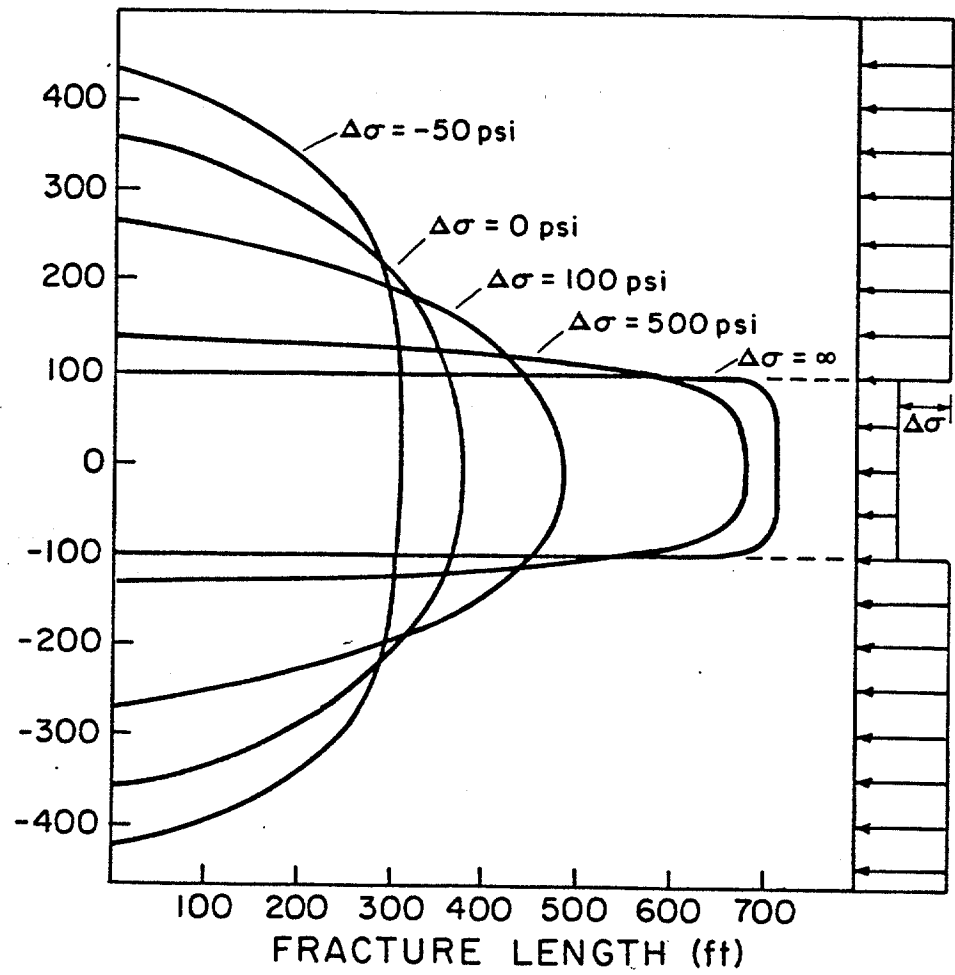


FIGURE 23 - Example of a three-dimensional fracture profile.

System Overall Compressibility

When mud is first slowly pumped into the well during a leak-off test, the Blow-out Preventer (BOP) is closed, the casing is not leaking, and the formation has not been fractured. At this time the well acts as a closed container completely full of mud. The injection of mud into the well bore will increase the annular and the drill pipe pressures because of fluid compressibility. Increasing annular and drill pipe pressures will then cause an increase in stresses in both the drill pipe and casing. The increasing stress will cause the mechanical dimensions of casing and drill pipe to change; this change in dimensions is reflected by a well bore volume and pressure change. In addition, non-Newtonian fluid flow effects such as pressure drop in the drill pipe and open-hole section, as well as effect of gel strength, should also be taken into account when the engineer predicts the relationship between surface pump pressure and pressure at the bottom of the drill pipe. The volume of mud responsible for increasing pressure and for casing and drill pipe expansion is smaller than the total volume injected within a certain period of time since part of it is lost through filtration to permeable formations, if any are present. Figure 24 shows a typical well configuration during a leak-off test.

The basic equation used to calculate the injection pressure response resulting from constant injection flow rate is the definition of isothermal compressibility:

$$C = -1/V (\partial V / \partial p)_T \dots\dots\dots (25)$$

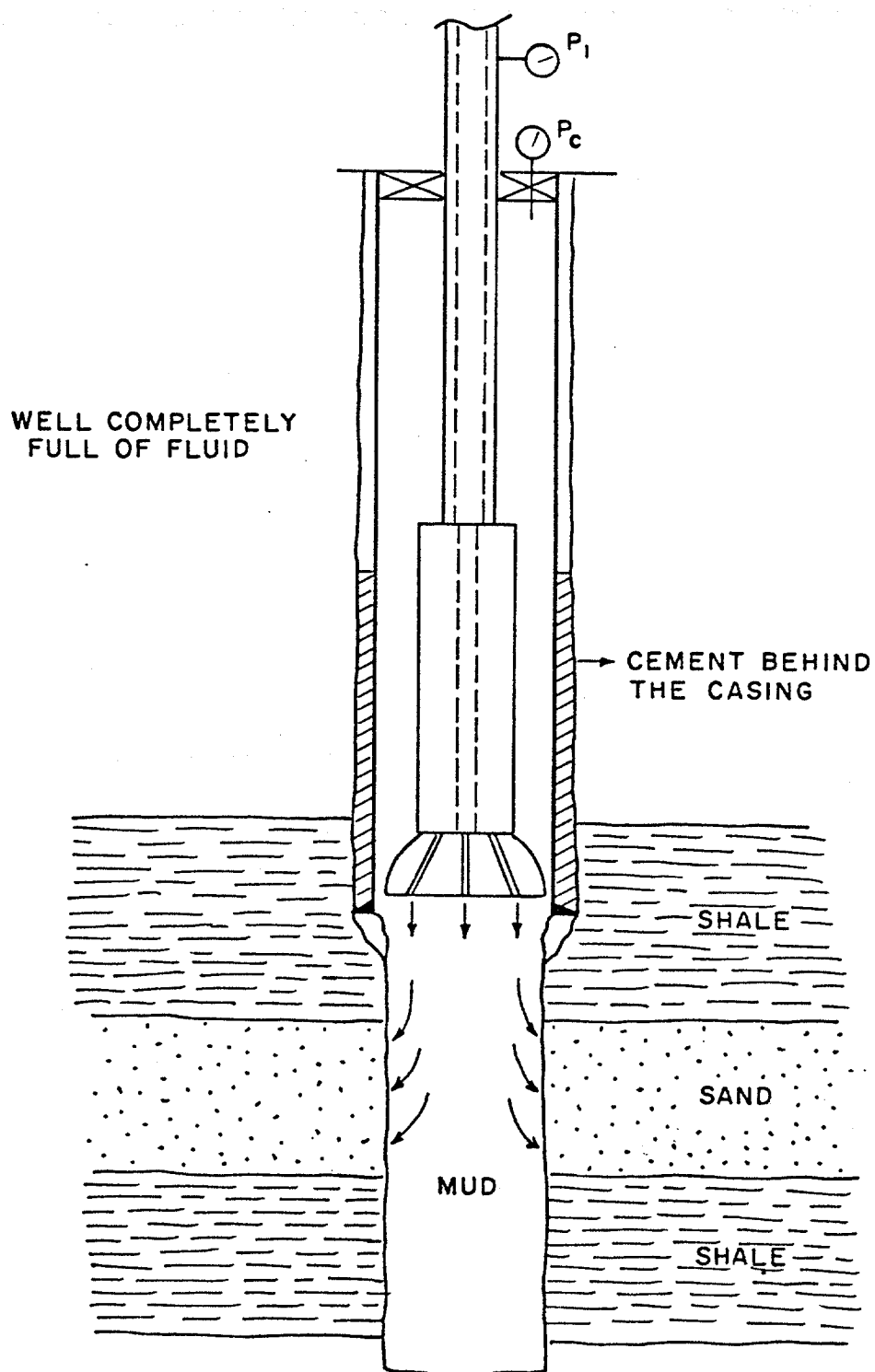


FIGURE 24 - Typical well configuration during a leak-off test.

Equation (25) is generally simplified for small pressure changes and the compressibility closely approximated by using the following equation for average compressibility, C_{avg} :

$$C_{AVG} = -1/V \cdot (\Delta V / \Delta P) \dots \dots \dots (26)$$

or

$$\Delta P = -\Delta V / C_{AVG} \cdot V \dots \dots \dots (27)$$

The total well-bore volume occupied by the mud, V , can be arbitrarily chosen from the original, final, or average volume with no significant change in the numerical answer. For the purposes of this work, the original volume was arbitrarily chosen to be used in the mathematical model.

Mud Compressibility

The effective mud compressibility for water-base muds, C_m , with oil but no gas present can be expressed as

$$C_m = C_w \cdot S_w + C_o \cdot S_o + C_s \cdot S_s \dots \dots \dots (28)$$

C_w, C_o, C_s = water, oil, and solids in the mud compressibilities respectively; psi.

S_w, S_o, S_s = water, oil, and solids in the mud saturations, respectively.

The water compressibility (C_w) is a function of both pressure and temperature. Values for isothermal compressibility of water can be obtained using Tait's empirical equation, which was put into a more useful form by Wilcox (1979):

$$C_w = 0.1368 / (40\,096.1 + 181.27 T - 1.789 T^2 + P) \dots\dots\dots (29)$$

where,

P = pressure, psi

T = temperature, °C

Equation (29) has been verified experimentally within the temperature range of 25°C to 85°C. However, it is believed that Equation (29) can be safely applied within the temperature range of 25°C to 125°C. The solid's compressibility can be found in the literature (Nowacki 1962) and has an average value of $0.2 \times 10^{-6} \text{ psi}^{-1}$. The average compressibility of oil with no gas dissolved in it can be estimated by using the empirical relation of O'Bryan et al. (1986), which is

$$\begin{aligned} C_o = & 6.72 - 0.0522 T + 3.64 \times 10^{-4} T^2 - 6.06 \times 10^{-7} T^3 + \\ & + (3.98 \times 10^{-5} - 4.84 \times 10^{-7} T + 3.16 \times 10^{-9} T^2 - 5.04 \times 10^{-12} T^3) P + \\ & + (2.54 \times 10^{-10} - 3.79 \times 10^{-12} T + 2.42 \times 10^{-14} T^2 - 3.63 \times 10^{-17} T^3) P^2 \\ & \dots\dots\dots (30) \end{aligned}$$

In Equation (30) temperature should be given in °F.

Drill Pipe and Drill Collar Expansion

Drill pipe expansion during a leak-off test is negligible since the difference in internal and external pressures to the pipe is small. This pressure difference corresponds to the frictional pressure loss of the fluid flowing in the pipe ahead of a given point, assuming injection through the pipe. The pressure drop value inside the pipe is small as a result of the low values of injection rate normally used when running a leak-off test.

Casing Expansion

The well-bore volume change, ΔV , caused by a change in surface injection pressure with time, is one of the most difficult parameters to evaluate for Equation (27). With respect to the last casing set, the well can be configured two ways: (1) with the casing cemented up to the surface or (2) with the casing partially cemented and partially backed by old mud. In each case, the strains associated with pressure change will be different. Therefore, these two situations will be considered separately in this section.

The pressure-induced stress is assumed not to exceed the proportionality limit of the elastic region of the stress-strain diagram for the casing material being used. This assumption is valid since casing design practice considers exceeding the yield point of the steel to be equivalent to failure. The elastic region is shown in the typical stress-strain diagram for steel presented in Figure 25. Change in pressure or pressure-induced stress can be used with the change in volume ΔV , rather than the absolute pressure or stress. Hooke's law can be applied to model the stress-strain relationship.

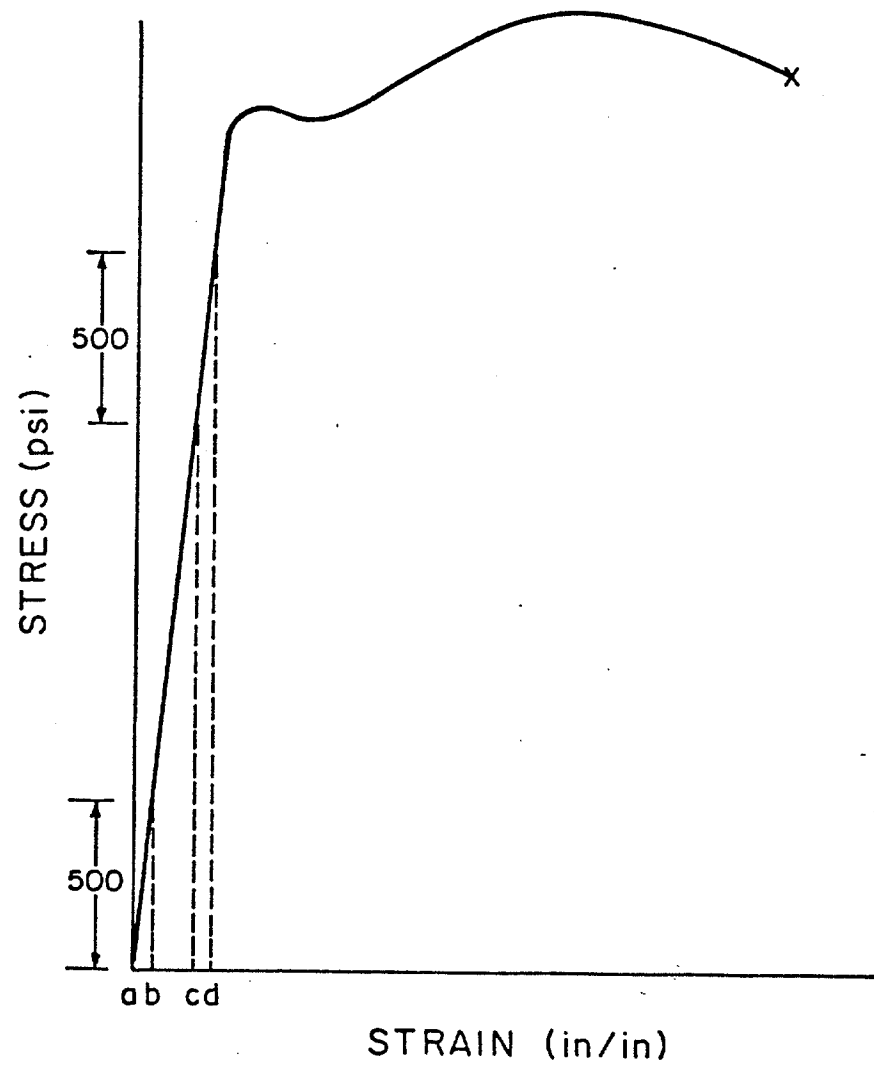


FIGURE 25 - Typical stress-strain diagram for steel.

Casing Not Cemented. For the section of the well in which the casing is not cemented, the pressure of the fluid behind the casing is assumed not to be changed by the expansion of the casing. This is felt to be a valid assumption because of the leak paths generally available to the fluid outside of the casing. In addition, to simplify the stress-strain equations, the casing is considered to be a uniform cylinder. The couplings used to connect the joints of casing are neglected in this analysis since they account for less than 2 percent of the total pipe length.

Hearn (1977) has shown that the diametral strain on a cylinder equals the hoop or circumferential strain. The diametral strain is equal to the change in diameter divided by the unstrained diameter. Combining radial and hoop stress resulting from pressure loading and evaluated by Lamé's equations (Hearn 1977) with Hooke's law (Timoshenko and Goodier 1951) one obtains the following for the change in diameter (Wilcox 1979), ΔD ;

$$\Delta D = D/E_s \left[(1-\mu_s^2) (\Delta P_i R_i - \Delta P_o R_o) / (R_o - R_i) + \mu_s (1 + \mu_s) (\Delta P_i R_i + \Delta P_o R_o) / (R_o + R_i) \right] \dots \dots \dots (31)$$

where,

P_i = variation in pressure inside the cylinder, psi

P_o = variation in pressure outside the cylinder, psi

R_i = internal radius of the cylinder, in.

R_o = external radius of the cylinder, in.

D = original diameter of the cylinder, in.

E_s = Young's modulus for steel, psi

μ_s = Poisson's ratio for steel

Equation (31) includes the reasonable assumption that applied pressure displaces all points of an annular ring of the cylinder wall by the same amount, depending on the radius of the ring. Thus, the cylinder wall maintains its symmetrical radial shape, and no shearing stresses can be set up on transverse planes. In addition, the casing is considered to be anchored by the cemented section; thus, the longitudinal strain due to variation in internal pressure is zero.

Casing cemented. Determining the diametral strain caused by the change in internal pressure of casing in the cemented section necessitates a good knowledge of the bond quality between casing and cement, and between cement and formation. If a great part of the cemented section does not adhere to the formation, but does have a good bond with the casing, internal pressure increases will cause the casing to expand, and tension stresses will be induced in the cement. Since cement has low resistance under tension, it will break. On the other hand, if the bond between the cement and formation is good, the stresses induced by the casing trying to expand will be transmitted through the cement body, which in this case will be under compression, to the formation, which would probably hold the distributed load. If this happens, casing expansion will be negligible.

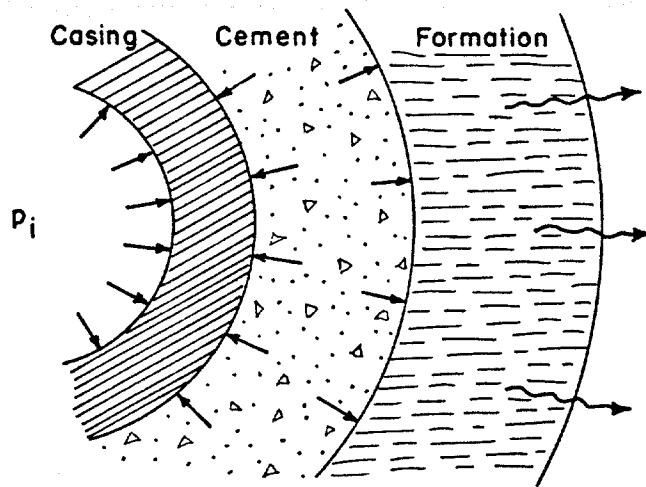
The situation in which casing expansion can be most easily evaluated occurs when there is a space or gap between the casing and the cement behind it along the entire cemented section. This gap

often forms during the cementing job and is called a microannulus. The microannulus can be caused by continued pressure on the casing after cementing, squeezing, or thermal expansion of the casing when the cement is setting up. Normally microannuli have diameter clearances of less than 0.01 in. A cement bond log (CBL) can be used to determine whether a microannulus is present. If the CBL run after cementing shows a good cementing bond along most of the section cemented, and the casing is cemented in a competent formation, the casing expansion will be negligible. However, if a microannulus effect shows up on the logs, the casing will expand until it reaches the cement and then stop. Figure 26 shows the cement behind the casing in the possible situations described above.

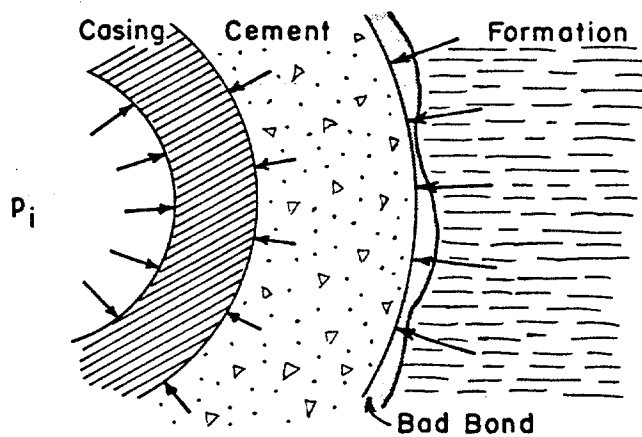
Filtration

During a leak-off test, mud filtration to a permeable formation occurs. The volume of mud (filtrate) lost to the formation will affect the overall pressure behavior of the well bore for a constant injection rate. Filtration first occurs in permeable formations exposed to the mud in the open-hole section. Later, when the formation is fractured, fluid loss will also occur through the walls of the opened fracture.

Static and dynamic filtration have been the subject of several laboratory studies (Howard and Fast 1957; Outmans 1963; Penny et al. 1985). The expression of elementary filtration theory, which assumes static conditions of filtration, steady state, and incompressibility of the mud cake is

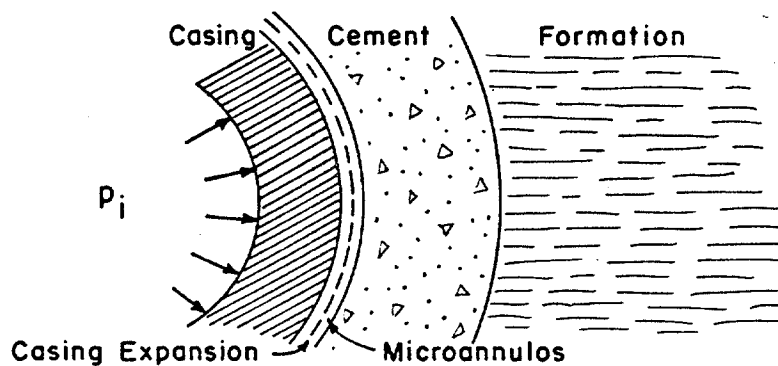


a - Good bond - casing expansion is negligible



Casing under compression
Cement under tension

b - Bad bond between cement and formation - Casing will expand only by breaking the cement



c - Bad bond between casing and cement - microannulus effect

FIGURE 26 - Example of bonding between casing, cement and formation.

$$V_f = A/5.615 \sqrt{\underbrace{[(\Delta P K) / 144.51 \nu] \{(f_{sc} - f_{sm}) / f_{sm}\}}_{2c}} \sqrt{t} + V_{sp} \dots (32)$$

where,

V_f = cummulative filtrate volume, bbl

V_{sp} = spurt loss volume, bbl

ΔP = pressure drop across the cake, psi

K = filter cake permeability, darcies

ν = filtrate viscosity, cp

t = time, min

A = permeable area in contact with the fluid, ft²

f_{sc} = volume fraction of solids in the cake

f_{sm} = volume fraction of solids in the mud

C = fluid loss coefficient ft/ $\sqrt{\text{min}}$

The permeability of the mud cake tends to decrease with increasing pressure and the term under the square root in Equation (32) remains essentially constant. Consequently, the cummulative filtrate volume becomes rather insensitive to changes in the filtration pressure.

Outmans (1963) suggested that the dynamic filtration process in the borehole has three stages while the bit is creating new borehole wall. During the first stage, solids deposited in front of the porous formation build up the filter cake. This buildup continues until the shear stress exerted on the filter cake by the circulating drilling fluid overcomes the maximum shear stress of the surface layer of the filter cake being formed. During the second stage, filtration takes

place through a filter cake of constant thickness in steady-state condition. The third stage begins when the filtration rate becomes constant and independent of the cake thickness.

During the drilling of a well, the filter cake is not deposited by either dynamic or static filtration alone, but by both. Whenever the circulation stops, static filter cake is deposited on the dynamic cake, and the rate of filtration decreases. If circulation is restarted after deposition of static cake on the dynamic cake, erosion will remove the top layer to the point where the rate of solids deposition is equal to the rate of erosion. During this time, the rate of filtration will increase slightly.

Borehole Expansion

An enlargement of the diameter of an open-hole section of the borehole caused by an increase in internal pressure will affect the overall compressibility of the system. This enlargement is practically negligible for most competent rocks exhibiting elastic behavior. However, in highly stressed regions plastic behavior may be expected from rocks such as limestone, clays, salt, shale, and unconsolidated sands. Teplitz and Hassebroek (1946) suggested well-bore expansion due to plastic deformation of shales as a possible explanation for cement lost during squeeze operations because of squeeze cementing pressures.

The plastic behavior of some unconsolidated shales in the Louisiana Gulf Coast area could be the cause of the great difference between the pressure responses of casing tests and formation tests observed during leak-off tests. Figure 27 shows an example of this

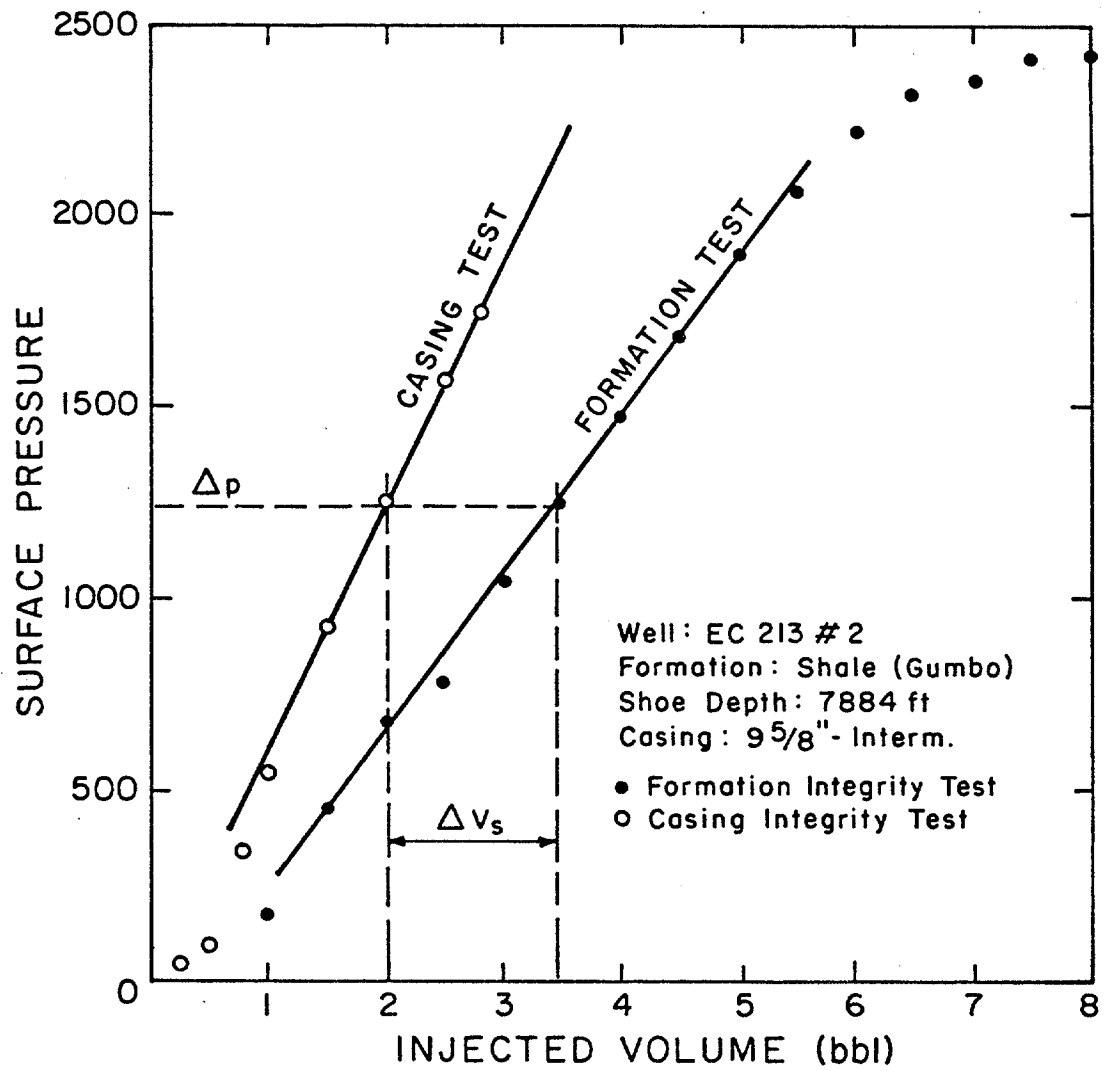


FIGURE 27 - Example of a leak-off test performed in a well drilled in the Louisiana Gulf Coast area.

problem that was seen in a well drilled in the Louisiana Gulf Coast area. The open-hole formation exposed during the test is unconsolidated shale. The casing test curve includes the effect of casing expansion only, whereas the formation test curve also includes filtration and borehole expansion effects. The difference in slope between these two curves cannot be explained by a high fluid loss to the formation during the formation test because a very large fluid loss rate would be required to compensate the difference shown. A large fluid loss rate is not likely to occur in front of impermeable shale. Hence, relatively high borehole expansion should be due to the plastic behavior of the exposed shale formation is the most plausible explanation.

Non-Newtonian Fluid Flow Effects

During a leak-off test the mud is flowing through the drill pipe, drill collars, and out of the drilling column through the bit jets. The open-hole section is sometimes very long, and a pressure loss in this section may occur. However, the total pressure loss caused by the fluid flow is small compared to the pressure required to break the gel strength and initiate circulation. Chenevert and McClure (1970) suggest that this so-called gelification effect can be evaluated by using the following equation:

$$P_g = \tau_g D_1 / 300 [1/d + 1/(d_h - d_p)] \dots\dots\dots (33)$$

where,

P_g = pressure required to break the gel, psi

τ_g = gel strength, lbs/100 ft²

D_i = depth, ft

d = internal pipe diameter, in.

d_h = hole diameter, in.

d_p = outside drill pipe diameter, in.

If the pressure required to initiate well circulation for a given flow rate is recorded prior to the leak-off test, then the corresponding gel strength can be evaluated with Equation (33). Chenevert and McClure (1978) suggests that the pressure drop through the drill string during a leak-off test will be approximately equal to the pressure required to break the gel in the drill pipe.

Drilling mud usually exhibits a thixotropic behavior when circulation begins. Figure 28 shows a typical pressure response observed as a function of increasing pump rate with time. If the well has not recently been circulated, then when circulation is restarted, the injection pressure at surface will rise until it reaches the pressure required to break the gel, p_g . This pressure is sometimes much greater than the pressure required to sustain circulation at the desired flow rate. However, after circulation is established, the injection pressure will fall to the steady frictional pressure loss due to the flow. Some authors have recommended using the pressure required to break the gel as an approximate estimate of the frictional pressure losses at the low pump rates used in a leak-off test. However as shown in Figure 28, for high gel strength, this may result in an inaccurately high value for frictional pressure loss after pumping begins. Therefore, in this study, this simplifying assumption was not made, and frictional pressure loss

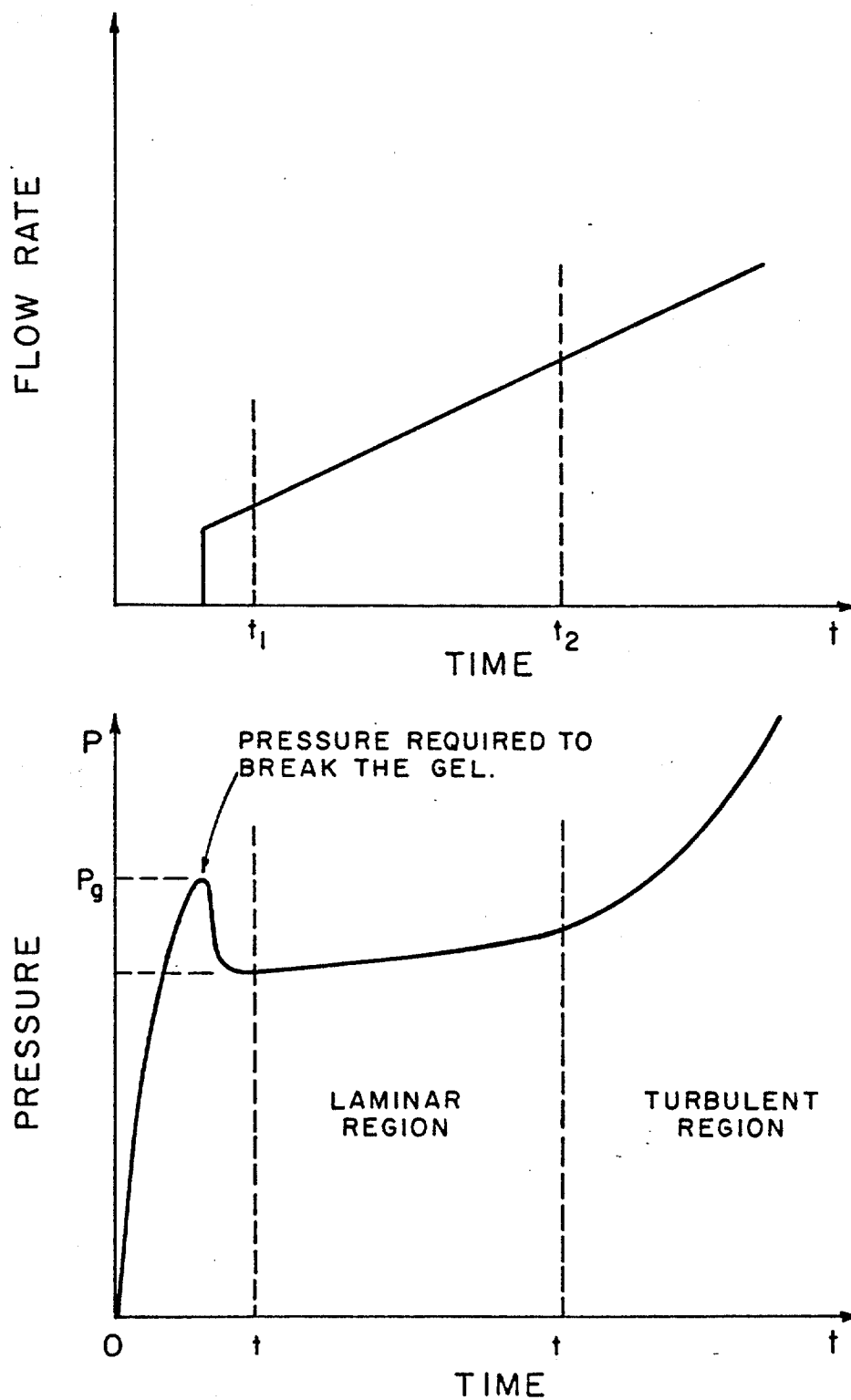


FIGURE 28 - Typical pressure-flow rate response for the flow of drilling fluids.

was computed using conventional equations as the total pressure drop in the drill pipe, drill collars, and bit.

Langlinais et al. (1985) compared experimental data collected in two 6000-ft wells using the various prediction techniques for the fluid pressure losses in a single-phase flow and concluded that accurate results can be obtained with both the Bingham plastic and the power-law rheological models. However, for the data taken from the annulus 4.892 in. by 2.875 in. at laminar flow conditions, the power-law model, which utilizes a slot-approximation equivalent diameter and low viscosities, was marginally better. When data were compared for common range of flow rates (0.25 to 1.50 bbl/min), annulus dimensions, and viscosities used in leak-off tests, the power-law model seemed to show better results than the Bingham plastic model, especially for flow rates between 0.67 and 1.07 bbl/min.

Another pressure drop to be considered is that which occurs at the bit. The pressure loss through the bit, ΔP_b , can be expressed as

$$\Delta P_b = (q^2 \rho_m) / (6.82 A_N^2 C_d) \dots \dots \dots (34)$$

where,

ρ_m = mud density, lb/gal

A_N = total nozzle area, in².

C_d = discharge coefficient = 0.95

q = injection flow rate, bbl/min

For the common flow-rate range used during a leak-off test (0.25 to 1.50 bbl/min) with three nozzles of 12/32 in. in diameter and 10 lb/gal mud density, the pressure loss through the bit varies from 0.84 to 31.63 psi. Chenevert and McClure (1978) neglect the pressure drop caused by flow in the drill string and bit. They consider only the pressure needed to break the gel strength in determining the anticipated leak-off pressure.

Fracture Closure

During a leak-off test, the pump is stopped after the fracture is induced and while it still is expanding. This moment marks the beginning of the shut-in period during which pressure declines in the well bore. This pressure decline is a consequence of the mud filtration through the open fracture walls. Since injection has stopped, the pressure in the fracture will continue to decline, and consequently the fracture will gradually close. Analyzing the rate of pressure decline permits estimation of some of the parameters that quantify a fracture and the fracturing process. Among the most important parameters that can be related to the shape of the pressure-decline curve are the fluid loss coefficient, fluid viscosity degradation, formation modulus, fracture closure pressure, and fracture length. These parameters are generally assumed during the simulation process; after the leak-off test they can be determined on the basis of the pressure decline data, which increases the reliability of the simulation for the next test. Multiple leak off tests are commonly performed to check for test repeatability.

Nolte (1982) presented theoretical analyses permitting those parameters mentioned above to be estimated from the pressure

decline following a fracture treatment of a producing well. On the basis of primary assumptions of a vertical fracture of essentially constant height propagating through a quasi-elastic formation with continuous displacements (i.e., no slip) at planes bounding the top and bottom of the fracture, he derived the following equation:

$$d_p/d_t (\Delta t/t_0) = [(4 C.h_p.E) / (\pi(1-\mu).h^2 \beta_s \sqrt{t_0})] f (\Delta t/t_0) \dots (35)$$

where,

d_p/d_t = rate of pressure decline at time $t = t_0 + \Delta t$, psi/min

h_p = fluid loss height, ft

β_s = ratio of average along the fracture and well-bore
pressure at shut -in

Δt = time since pumping stopped (shut-in), min

t_0 = pumping time prior to shut-in, min

The function $f (\Delta t/t_0)$ is defined by the bounds

$$2 (\sqrt{1 + \Delta t/t_0} - \sqrt{\Delta t/t_0}) > f (\Delta t/t_0) > \sin^{-1} (1 + \Delta t/t_0)^{-1/2}$$

A more useful equation was derived from Equation (35) to determine the difference in the decline pressure between times

δ_1 and δ_2 :

$$\Delta P (\delta_1, \delta_2) = [(C.h_p.E \sqrt{t_0}) / ((1-\mu).h^2 \beta_s)] . G.(\delta_2 \delta_1) \dots (36)$$

The function $G(\delta_2, \delta_1)$ is defined by

$$G(\delta_2, \delta_1) = (16/3\pi) [(1 + \delta_2)^{3/2} - (1 + \delta_1)^{3/2} - (\delta_2^{3/2} - \delta_1^{3/2})] \dots (37)$$

and $\delta = \Delta t / t_0$ which implies $\delta_1 = \Delta t_1 / t_0$ and $\delta_2 = \Delta t_2 / t_0$.

Figure 29 illustrates pressure terms that could be used for decline analysis in a typical pressure response plot of a leak-off test. It is interesting to note that these equations are independent of the fracture length. The parameters in Equations (35) and (36) were derived in this study assuming that the fluid would obey the power-law model. The equation is

$$\beta_s = (2n + 2) / (2n + a + 3) \dots \dots \dots (38)$$

The parameter "a" reflects the decrease in fluid viscosity down the fracture due to temperature, shear, and time degradation of the fluid system. The value of "a" ranges from 0 for a Newtonian fluid of constant viscosity to about 2 for fracturing fluids exhibiting a strong viscosity degradation as the fluid moves out into the fracture. The parameter "n" is the power-law exponent.

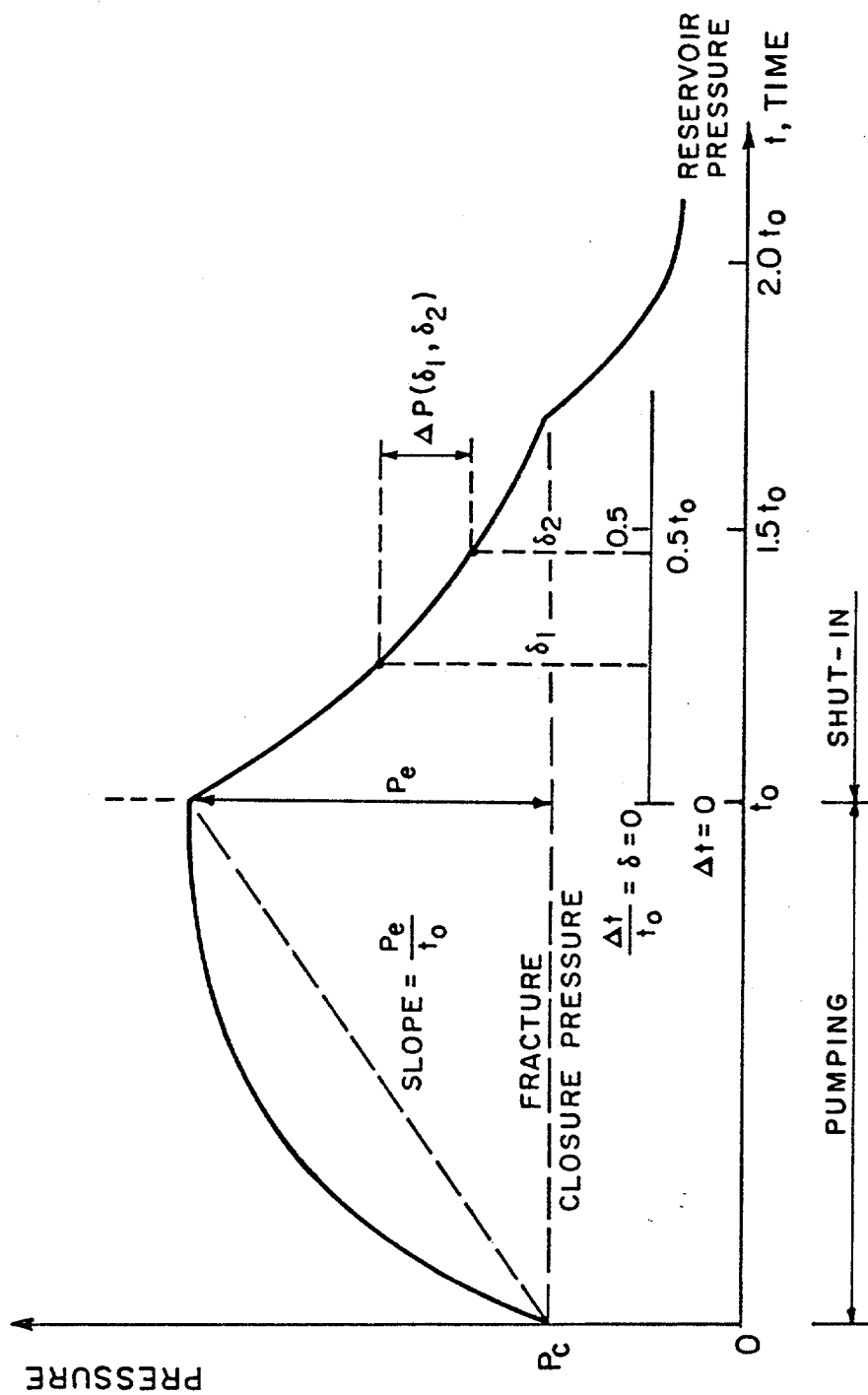


FIGURE 29 - Illustration of pressure terms used for pressure decline analysis (Nolte 1982).

PROPOSED MATHEMATICAL MODEL

Overall Compressibility Model

The increase in injection pressure at surface as a function of volume of mud injected before the formation is broken down is determined by the computer model with an interactive procedure. For a given small additional volume of mud injected at the surface, Equation (27) can be used to calculate the change in pressure as a function of the average compressibility of mud and the total mud volume of the system. However, part of the mud injected is lost through filtration to permeable layers of the formation; part is used to fill the clearance created by the casing expansion; part will occupy the volume of air trapped in the system that shrinks with pressure increase; and part will occupy the clearance created by the borehole expansion.

The increase in pressure during a short interval of time, Δt , is calculated iteratively by first estimating a small volume of mud, ΔV_g , that must be smaller than the volume, ΔV_i , injected during the time, Δt . Using Equation (27) and the volume estimated, the corresponding pressure increase is calculated. This pressure-increase value is then used to determine the volume of filtrate lost to permeable formations, ΔV_f , the volume increase of the system due to casing expansion, ΔV_{csg} , the volume change of any air trapped in the system, ΔV_{air} , and the borehole expansion volume, ΔV_s . These three changes in volume should satisfy the following material balance equation:

$$\Delta V_G = \Delta V_i - (\Delta V_f + \Delta V_{CSG} + \Delta V_{AIR} + \Delta V_S) \dots \dots \dots (39)$$

The right-hand side of Equation (39), which is the calculated volume of mud responsible for the pressure increase, should be approximately equal to the estimated value or left-hand side of Equation (39). If the values disagree, a new estimate is made, and an interval halving technique used to continue the iterative process until agreement is reached.

The volume of filtrate lost to the formation, ΔV_f , during a given period of time, Δt , is calculated with the following equation:

$$\Delta V_F = (C.A./5.615) [\sqrt{t+\Delta t} - \sqrt{t}] \dots \dots \dots (40)$$

where

A = total area of permeable formations exposed, ft^2

t = total time of filtration, min

Δt = increment of time, min

ΔV_f = volume of mud lost during Δt , bbl

In Equation (40) it is assumed that the increase in the difference in pressure between the borehole and the formation is compensated by the decrease in the permeability of the mud cake being formed. The fluid loss coefficient, C , can be determined with the results obtained from a standard API fluid loss test combined with the following simplified equation:

$$C = [(V_f - V_{sp}) / 15029] \dots \dots \dots (41)$$

Equation (41) already includes the filter paper area (45 cm^2) and the time of filtration for standard API tests (30 min). The filtrate volume V_f , and the spurt volume, V_{sp} , are given in cm^3 and the fluid loss coefficient in $\text{ft}/\text{min}^{1/2}$.

The volume increase of the system due to casing expansion, ΔV_{csg} , is calculated by determining the change in diameter, ΔD , of the inside diameter of the casing with Equation (31) and substituting it in the following equation:

$$\Delta V_{csg} = ((D + \Delta D)^2 - D^2) / 1029.5 \cdot L_0 \dots \dots \dots (42)$$

where

D = inside diameter of the casing, in

L_0 = total length of the casing, ft

The change in volume of air trapped in the system ΔV_{air} , is calculated with Equation (27).

Borehole Expansion

The plasticity theory is applied here in an attempt to model the plastic behavior of some unconsolidated shales found in the Louisiana Gulf Coast. The plastic behavior of these shales is believed to cause significant borehole expansion and consequently affect the overall compressibility of the system.

Initially, the case we'll consider is that of a hollow cylinder, $R_1 < r < R_2$, in plane-strain with pressure P_1 applied at R_1 and pressure P_2 applied at R_2 (Figure 30). The assumption is that the rock material may yield only partially so that there is a plastic region surrounded by a region stressed below the limit of plasticity. In the outer portion of the cylinder, $R < r < R_2$, the equations must satisfy the conditions of stress and strain of a perfectly elastic body. In the inner ring, $R_1 < r < R$, plastic theory must be used.

The total strain, ϵ_r , at a given radius, r , is calculated with the following equation:

$$\epsilon_r = \left\{ P_2 + (R/R_2)^2 (P_1 - P_2) / ((R/R_2)^2 - \ln (R/R_1)^2 - 1) \right\} \\ \left[1/(2(\lambda + G)) \right] - [R^2/(2G r^2)] \left[(P_1 - P_2) / ((R/R_2)^2 - \ln (R/R_1)^2 - 1) \right] \dots\dots\dots (43)$$

Detailed derivation of Equation (43) is presented in Appendix G. The well bore can be considered a hole in the middle of an infinite plate, which implies $R_2 \rightarrow \infty$ in Equation (43). The total strain at the well bore, $r = R_1$, caused by an increase in interval pressure, Δp_1 , according to Equation (43) is

$$\epsilon_{R_1} = (1 + \mu) \Delta P_1 / [E (1 + \ln (R/R_1)^2) (R/R_1)^2 \dots\dots (44)$$

In Equation (44), it is assumed that the increase in pressure, Δp , won't cause an increase in pressure far away from the well bore

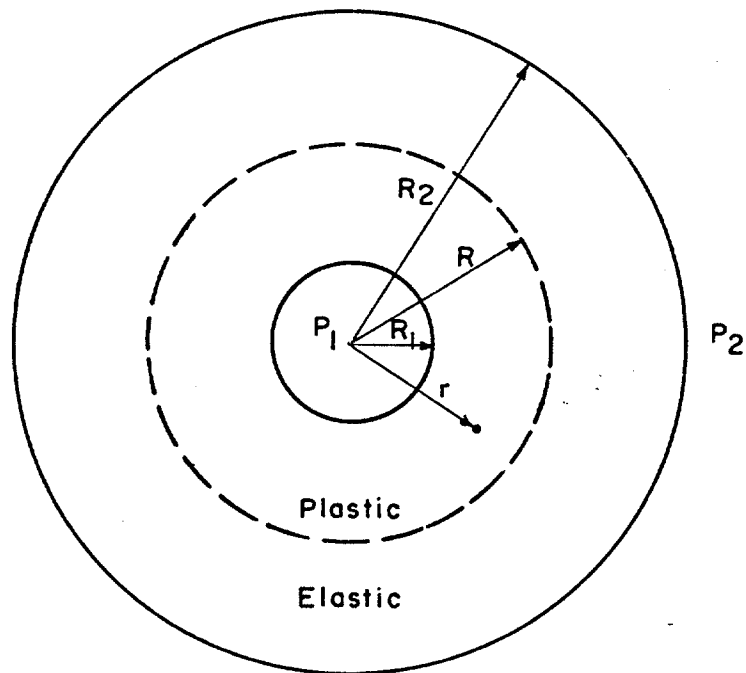
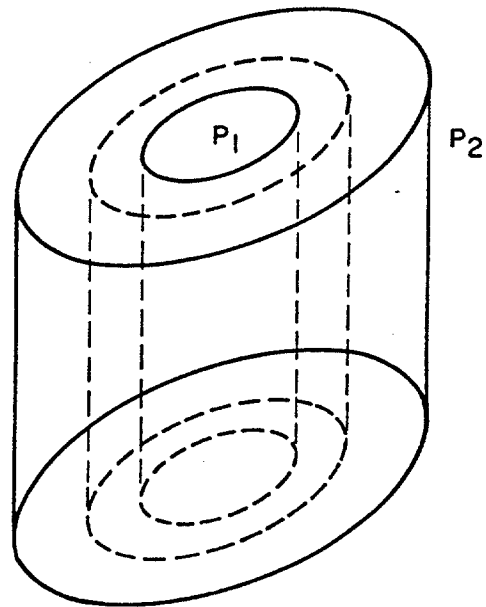


FIGURE 30 - Partial yielding of a thick walled cylinder.

which implies that $\Delta p_2 = 0$. However, Equation (44) cannot be used unless the ratio between the plastic limit radius and well-bore radius, R/R_1 , is known. Based on casing and formation integrity test data from unconsolidated shale in the Gulf Coast area, an average value of $R/R_1 = 20$ was obtained. This value was obtained by reading the enlargement volume of the well for different values of pressure increase, Δp_1 . Figure 27 shows how the enlargement volume, ΔV_s , is obtained for a given, Δp_1 . The values of total strain can be easily calculated using the initial well diameter and the enlargement volume. Table 3 shows the parameters used in Equation (44) and the corresponding values of R/R_1 determined for five different wells. The ratio $R/R_1 = 20$ should be used only for unconsolidated shale encountered in the Louisiana Gulf Coast area. For other areas or different plastic formations, the ratio R/R_1 should be reevaluated using the technique illustrated by Table 3.

If the rock material does not exhibit a plastic behavior, the value of R/R_1 to be used in Equation (44) is 1. This value reduces Equation (44) to the strain equation of a perfectly elastic material.

Fracture Induction Model

The fracture induction model selected for use in this computer model is based on the assumption of an infinite plate with a circular hole in it. This classical solution leads to equations that include formation properties such as Poisson's ratio and Biot's constant, and state-of-stress components such as horizontal matrix stresses and

TABLE 3

WELL: SMI 160 A-3

(13 3/8" SURFACE CASING AT 5166 FT (MD))

ΔV_s (bbl)	Δd (in)	ϵ	Δp (psi)	R/R_1	OTHER INFORMATION
0.30	0.14175	0.00810	200	18.0	$E = 1.5 \times 10^6$ psi
0.62	0.29171	0.01667	400	18.4	$\mu = 0.255$
0.94	0.44042	0.02517	600	18.6	
1.26	0.58790	0.03359	800	18.5	
1.58	0.73419	0.04195	1000	18.5	
				AVG: 18.40	

TABLE 3 (cont.)

WELL: SMI 275 #1

(7 5/8" CASING AT 15040 FT (MD) and 12939 FT (TVD))

ΔV_s (bbl)	Δd (in)	ϵ	Δp (psi)	R/R_1	OTHER INFORMATION
0.35	0.0762	0.0090	200	26.5	E - 2.75×10^6 psi $\mu = 0.313$ H - 277 ft
0.75	0.1624	0.0191	400	27.5	
1.15	0.2478	0.0292	600	27.7	
1.55	0.3324	0.0391	800	28.0	
1.95	0.4161	0.0490	1000	28.0	
2.35	0.4991	0.0587	1200	28.0	
AVG: 27.6					

TABLE 3 (cont.)

WELL: EC 213 #2

(9 5/8" 7884 FT)

ΔV_g (bbl)	Δd (in)	ϵ	Δp (psi)		OTHER INFORMATION
0.10	0.7357	0.00633	250	16.6	Shale: 80-90%
0.20	0.14667	0.01262	500	16.6	Sand: 20-10%
0.30	0.21933	0.01887	750	16.6	E - 2.10×10^6
0.40	0.29154	0.02508	1000	16.5	μ - 0.28
0.50	0.36332	0.03125	1250	16.4	
0.60	0.43467	0.03739	1500	16.3	
AVG: 16.5					

TABLE 3 (cont.)

WELL: VR 232 #1

(9 5/8" INTERM CASING AT 10137 FT (MD))

ΔV_s (bbl)	Δd (in)	ϵ	Δp (psi)	R/R_1	OTHER INFORMATION
0.100	0.07903	0.00647	250	18.5	E - 2.3×10^6 psi μ - 0.295
0.225	0.17711	0.01446	500	18.5	
0.350	0.27442	0.02240	750	18.6	
0.475	0.37098	0.3028	1000	19.5	
0.600	0.46681	0.3811	1250	19.5	
AVG: 18.92					

TABLE 3 (cont.)

WELL: GC 135 #1

(20" AT 2300 FT)

ΔV_g (bbl)	Δd (in)	ϵ	Δp (psi)	OTHER INFORMATION	
0.11	0.05060	0.00195	50	15.5	$E = 1.20 \times 10^6$
0.20	0.09192	0.00354	100	15.0	$\mu = 0.21$
0.30	0.13776	0.00530	150	15.0	
0.40	0.18352	0.00706	200	15.0	
				AVG: 15.13	

vertical matrix stresses, which are sometimes difficult to measure. In the model, these parameters are considered best determined by extrapolation. With this technique, fracture gradients of the various formations can be computed after the first hole is drilled in a given area. These fracture gradients are then used to estimate the fracture gradient in the second hole, while such variables as changes in depth and fluid pressure are taken into consideration. As the second hole is drilled, information gained is used to update and improve data obtained from the first hole, and the process is continued with subsequent drilling.

The equations used in this work are explained in Appendix A; compression is represented as positive and tension as negative. Tensile strength of the formation, S_t , which appears in all the equations in Appendix A, is thus a negative number.

Vertical Fracture Initiation

Vertical fracturing begins when the maximum effective tangential stress exceeds the tensile strength of the formation. In the case of a penetrating type of fluid, the pressure at well bore necessary to induce fracturing of the formation, P_f , can be determined by

$$P_f = [(2\mu / (1-\mu)) \cdot [S_z - P_o] - S_t] / [2 - \alpha(1-2\mu)/(1-\mu)] + P_o \dots (45)$$

Equation (45) can be used only for a penetrating fluid. This characteristic of the fluid for a certain formation is highly dependent on rock permeability and naturally occurring fractures in the

formation. Drilling mud, which is the fracturing fluid most commonly used during leak-off tests, can be considered either a penetrating or a nonpenetrating type of fluid, depending only on its fluid loss capability. For example, an ordinary drilling mud forming a relatively impermeable filter cake on a permeable rock is classified as a nonpenetrating fluid. In this situation, the pressure at well bore necessary to fracture the formation is higher and can be determined by

$$P_f = (2\mu / (1 - \mu)) \cdot [S_z - P_o] + P_o - S_t \dots \dots \dots (46)$$

Derivation of Equations (45) and (46) is presented in Appendix A. The equations show that under the assumed conditions, fracture pressure, P_f , can be estimated from the overburden stress, S_z , and the formation properties, which are the Poisson's ratio, μ , and the elasticity constant or Biot's constant, α .

Horizontal Fracture Initiation

To initiate a horizontal fracture around the borehole, the vertical principal stress, σ_z , acting on the formation must exceed the tensile strength of the formation. The fracture is assumed to occur all the way around the hole. In the case of a penetrating fluid, the pressure at well bore needed to fracture the formation horizontally can be estimated by

$$P_f = (S_z - P_o - S_t) / (1 - \alpha (1 - 2\mu) / (1 - \mu)) + P_o \dots \dots \dots (47)$$

As indicated in Appendix A, horizontal fracturing can be induced with a nonpenetrating fluid only if end effects occur at the well bottom or if joints have separated sufficiently to allow the entrance of flow. In addition, the pressure at the well bore should be at least that of the overburden, which yields

$$P_f = S_z - S_t \dots\dots\dots (48)$$

The derivation of Equations (47) and (48) are also included in Appendix A. Equations (45), (46), (47), and (48) constitute the fracture-induction criteria used in the leak-off test simulator.

Equations (45) through (48) give the initiation criteria for vertical and horizontal fractures. Whether the actual fracture is horizontal or vertical is determined in the computer model by analysis of the fracture-pressure values calculated, P_f . After the type of fluid is defined, the fracture pressures, p_f , for initiation of vertical and horizontal fractures are calculated. The fracture associated with the smaller P_f is the one initiated.

Biot's Constant

Biot's elastic constant, α , is a property of the rock, and assuming that the rock is homogeneous, isotropic, and linearly elastic, Biot's constant can be expressed as

$$\alpha = 1 - C_{ma} / C_b \dots\dots\dots (49)$$

The compressibility of the material of the rock, C_{ma} can be measured from core samples or obtained from published tables of physical properties of rocks (Carmichael 1982). The bulk rock compressibility, C_b , can also be determined experimentally by first measuring the compressional wave travel time of the rock, Δ_{tc} , with a sonic logging tool, and the bulk density of the rock ρ_b , and using the following relationship:

$$1/C_b = 1.34 \times 10^{10} (\rho_b / \Delta t_c^2) (1 + \mu) / (3(1 - \mu)) \dots (50)$$

The value of Biot's constant is needed in the computer model only when a penetrating type of fluid has been used to fracture the formation. However, drilling fluids are generally designed to be nonpenetrating to promote well-bore stability and limit formation damage.

The value of α is within the range $0 < \alpha < 1$, where 0 is the porosity of the rock formation. The best technique for determining α is to test representative formation cores in the laboratory. Common values of α reported in the literature for sandstone are within the range of 0.70 to 0.90.

Poisson's Ratio

Poisson's ratio, μ , used in the preceding equations, is a rock property that can also be determined experimentally from acoustic logs through the following equation:

$$\mu = [2 - (\Delta t_s / \Delta t_c)^2] / [2 [1 - (\Delta t_s / \Delta t_c)^2]] \dots \dots \dots (51)$$

In Equation (51) the shear wave travel time, Δt_s , should be measured from an acoustic log. Poisson's ratio can also be evaluated by plotting the effective horizontal stress gradient versus the effective vertical stress gradient from Equation (21); this yields

$$2\mu / (1 - \mu) = [P_f - P_o + S_t] / [S_z - P_o] \dots \dots \dots (52)$$

Equation (52) assumes a nonpenetrating type of fluid and a variable overburden stress with depth. The term can be evaluated for a given area of drilling activity as a function of depth, which will allow the establishment of a correlation between Poisson's ratio and depth for that area. Figure 31 shows the variation of Poisson's ratio with depth for the Gulf Coast area based on Eaton's (1969) data. The curve shown in Figure 31 is used in the simulator to determine the proper value of Poisson's ratio to be used in Equations (45), (46), and (50) for the Gulf Coast area. To provide appropriate input for the computer, the curve shown in Figure 31 was fitted using an equation suggested by Constant and Bourgoyne (1986). The resulting equation is

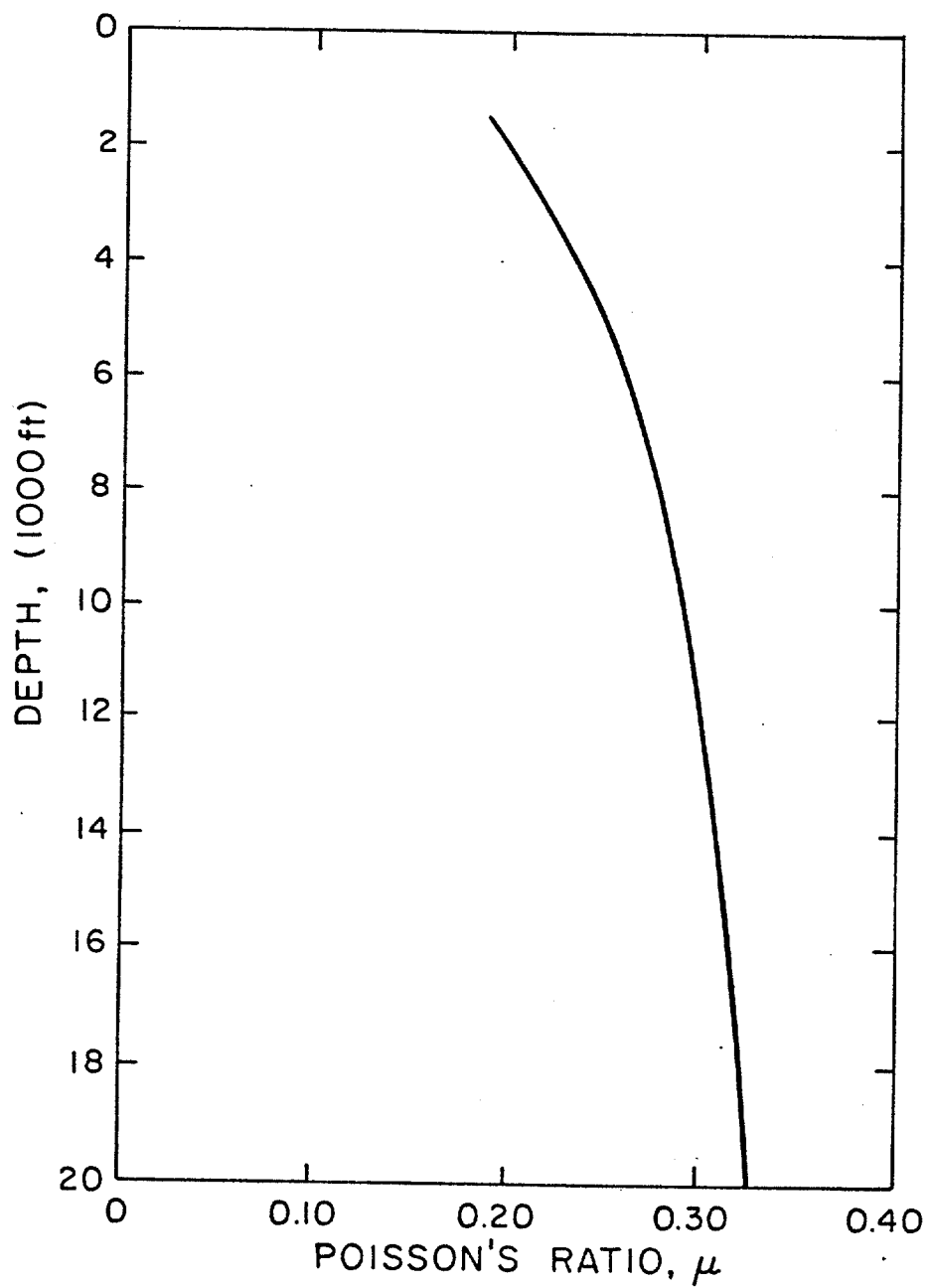


FIGURE 31 - Variation of the Poisson ratio with depth.

$$\mu = [1 - 0.629 e^{-1.28 \times 10^{-4} D}] / [3 - 0.629 e^{-1.28 \times 10^{-4} D}] \dots (53)$$

The fracture induction model presented here can always be reduced to one single equation, providing that in the same area of drilling activity, the values of Poisson's ratio versus depth are obtained without distinguishing penetrating from nonpenetrating fluid types. In this approach, Equations (42) and (44), which are independent of Biot's constant, α , can be used to develop the correlation.

Overburden Stress

The overburden stress, S_z , which appears in all the fracture-pressure equations, should be determined from density logs. The density logs allow the evaluation of the surface porosity, ϕ_0 , and the porosity decline constant, K , by the method shown in Appendix B. These parameters should be evaluated for a given area of drilling activity. The overburden stress is calculated with the following equation:

$$S_z = 0.052 \{ \rho_{sw} D_w + \rho_g D - ((\rho_g - \rho_f) \phi_0 / K) [1 - e^{-KD}] \} \dots (54)$$

where

ρ_{sw} = seawater density, lb/gal

D_w = water depth, ft

ρ_g = grain density, lb/gal

ρ_f = pore fluid density, lb/gal

The accuracy of Equation (54) for evaluating overburden stress as a function of depth depends heavily upon how accurately the parameters K and σ_0 are evaluated for a given area.

General Assumptions

The assumptions made in the derivation of the fracture-pressure equations deal primarily with principal stresses present near the borehole, rock homogeneity, rock isotropy, and elastic behavior of rocks.

Derivations of Equations (45) through (48) were based on the assumption that one principal stress is parallel to the borehole axis, which does not always hold true. However, the derivation of equations that can handle any orientation of the principal stresses, can be obtained using a similar procedure. In practice, the orientation of the principal stresses is unknown, but is generally assumed to be in the vertical and horizontal directions. Thus, a non-parallel orientation of the borehole and a principal stress would be of interest only for directional boreholes.

The equation for breakdown pressure is shown in Appendix A to depend on both of the horizontal principal matrix stresses, σ_x and σ_y . These matrix stresses were considered equal, which is true only in tectonically relaxed areas, where the only active force is that of gravity. When the difference between σ_x and σ_y increases, the breakdown pressure decreases. Thus, if the assumption $\sigma_x = \sigma_y$ does not hold, the fracture pressure obtained in the field will be smaller

than that predicted by the equations, assuming that all other assumptions are not violated.

Rock homogeneity and isotropy are assumptions introduced in the derivation mainly for mathematical simplification. However, rocks are seldom homogeneous or isotropic. Deviations from these assumed conditions will affect the breakdown pressure of the formation. These mathematical simplifications must be made if useful equations are to be obtained. Sufficient data are generally not available to enable us to take this inhomogeneity and anisotropy into account.

The equations developed are for horizontal and vertical fracture induction. Inclined fractures seldom begin as inclined fractures; they usually start as vertical and reorient themselves away from the well bore to become inclined. It is assumed in this model that the vertical fracture initiation criteria of Equations (45) and (46) provide an accurate estimation of the fracture-pressure value for inclined fractures. This simplification avoids the use of lengthy and impractical equations for induction of inclined fractures. This assumption is reasonable because inclined fractures, as mentioned above, generally start as vertical fractures.

Among the theories available for the study of reservoir rocks, elasticity often best fits the rock behavior before failure occurs. The assumption of elastic behavior for rocks holds true for most competent rocks. However, the inelastic behavior of some rocks, such as unconsolidated shales, will affect the principal rock stresses and consequently affect the breakdown pressure. Fracture gradients in soft plastic shales are expected to be greater than those in

sandstones. This is because the cohesive resistance or internal friction is less in plastic shales than in sandstones which permits less difference between the horizontal and vertical matrix stresses. The fracture-pressure prediction for plastic shales, obtained with equations derived from elasticity theories, generally yields conservative values.

Fracture Expansion Model

The fracture expansion model selected for use in this study is basen on Nordgren's (1972) work. The model is based on the solution of the continuity equation for flow of an incompressible fluid through an already-initiated fracture. The assumption of incompressibility of the fluid will cause only small errors in the case of leak-off tests that use water-base drilling muds. In addition, total pressure variation is relatively small during fracture expansion, which also justifies the assumption of incompressibility. The model cannot, however, be used for highly compressible fluids such as foams.

The fracture geometry assumed is shown in Figure 32. The fracture expansion model is limited to a vertical fracture considered to propagate in a straight line away from the well. The vertical height, h , is limited to the thickness of the formation being fractured. These assumptions define the model as a 2-D model of the type included in the PKN method. In addition, it is assumed that an isotropic, homogeneous material surrounds the fracture.

The continuity equation for flow of an incompressible fluid through a cross section of the fracture shown in Figure 32 is

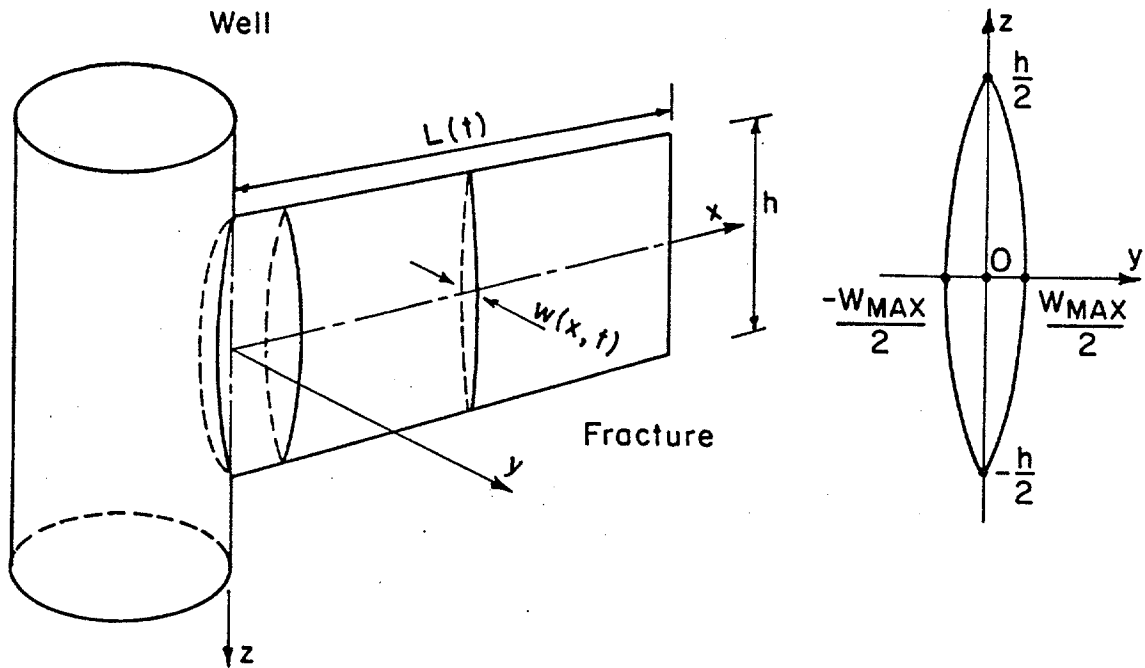


FIGURE 32 - Fracture geometry for the proposed computer Model.

$$\partial q / \partial x + q_L + \partial A / \partial t = 0 \dots\dots\dots (55)$$

where

$q(x,t)$ = volume rate of flow through a cross-sectional
(x = constant) area of the fracture

$q_L(x,t)$ = volume rate of fluid loss to formation per unit of length
of fracture

$A(x,t)$ = cross-sectional area of the fracture

The volume rate of flow through a cross-sectional area of the fracture can be assumed to be related to the pressure gradient along the fracture according to the solution shown in Appendix C for laminar flow of a Newtonian viscous fluid in an elliptical tube of semi-axes $\frac{1}{2} h$ and $\frac{1}{2} W_{\max}$ with $h \gg W_{\max}$. The flow rate is given by

$$q = - [\pi \cdot w^3 \cdot h / 64 \nu] \partial (\Delta P) / \partial x \dots\dots\dots (56)$$

where

$W = W_{\max}$ at $x = 0$ Figure 32

Equation (56) is valid for laminar fluid flow within the fracture. The laminar flow regime occurs when the Reynolds number, N_{Re} , is smaller than or equal to 2500. It can be calculated using the following classical equation:

$$N_{Re} = 7.81 \times 10^{-3} [(q \cdot \gamma) / h \nu]$$

When γ = the specific gravity of the fluid.

Fluid-Loss Rate

The following equation can be used to relate fluid-loss rate per unit of length of fracture, q_L , to the fluid-loss coefficient, C , the fracture height, h , and time at which the fracture area at position x is exposed:

$$q_L = (2 C h) / \sqrt{t - T(x)} \dots \dots \dots (58)$$

Fracture Area

The cross-sectional area, A , of the elliptical fracture with width, w , and height, h , is

$$A = (\pi/4) w h \dots \dots \dots (59)$$

The derivation of Equation (59) is presented in Appendix D. Taking the partial derivative of a A with respect to the time, t , yields

$$\partial A / \partial t = (\pi / 4) h \partial w / \partial t \dots \dots \dots (60)$$

Differential Equation

If we substitute Equations (56), (58), and (60) into Equation (55) and use the vertical plane-strain solution, Equation (18), for a fracture under constant pressure, we have

$$G / (64(1-\mu) \nu h)) \partial^2 (W^4) / \partial x^2 = [8C / \pi \sqrt{t - T(x)}] + (\partial W / \partial t) \dots (61)$$

The differential Equation (61) can be simplified to a dimensionless form with the following equations:

$$x = 0.0238 \pi [(1-\mu) \nu q^5 / (256 C^8 G h^4)]^{1/5} x_D \dots (62)$$

$$L = 0.0238 \pi [(1-\mu) \nu q^5 / (256 C^8 G h^4)]^{1/5} t_D \dots (63)$$

$$t = 1.798 \times 10^{-5} \pi^2 [(1-\mu) \nu q^2 / (32 C^5 h G)]^{2/5} t_D \dots (64)$$

$$W = 0.00424 [16 (1-\mu) \nu q^2 / (C^2 G h)]^{1/5} W_D \dots (65)$$

$$\partial^2 (W_D^4) / \partial x_D^2 = (1 / \sqrt{t_D - \tau_D(x_D)}) + (\partial W_D / \partial t_D) \dots (66)$$

The derivation of Equation (66) is presented in Appendix E, along with its boundary conditions, which in dimensionless form are

$$- (\partial (W_D^4) / \partial x_D) |_{x_D=0} = 1 \dots (67)$$

$$W_D(x_D, 0) = 0 \dots (68)$$

$$W_D(x_D, t_D) = 0 \quad \text{for } x_D \geq L_D \dots (69)$$

$$\tau_D(L_D(t'_D)) = t'_D \quad \text{for } 0 \leq t'_D \leq t_D \dots\dots\dots (70)$$

The nonlinear partial differential Equation (61) cannot be solved analytically. However, Nordgren's (1972) approximate numerical solutions for conditions of no fluid loss and large fluid loss to the formation are given in dimensionless form in Figure 33. These solutions are for the width of the fracture at the borehole wall, W_D (0, t_D), where maximum width occurs.

The dimensionless solutions for the total length of the fracture as a function of the dimensionless time, t_D , for both no fluid loss and large fluid loss are shown in Figure 34.

No-Fluid-Loss Solution

The no-fluid-loss solution is obtained by neglecting the fluid-loss term, q_L , in Equation (55) and integrating the resulting equation as shown in Appendix E. This solution is realistic for the case of negligible fluid loss out of the fracture. Fluid loss will be negligible when drilling fluids with a very low water loss are used for a sufficiently short time. This solution would also apply if the rock being fractured is impermeable.

The equations for dimensionless fracture width at well bore and fracture length are

$$W_D(0, t_D) = 1.00 t_D^{1/5} \dots\dots\dots (71)$$

and

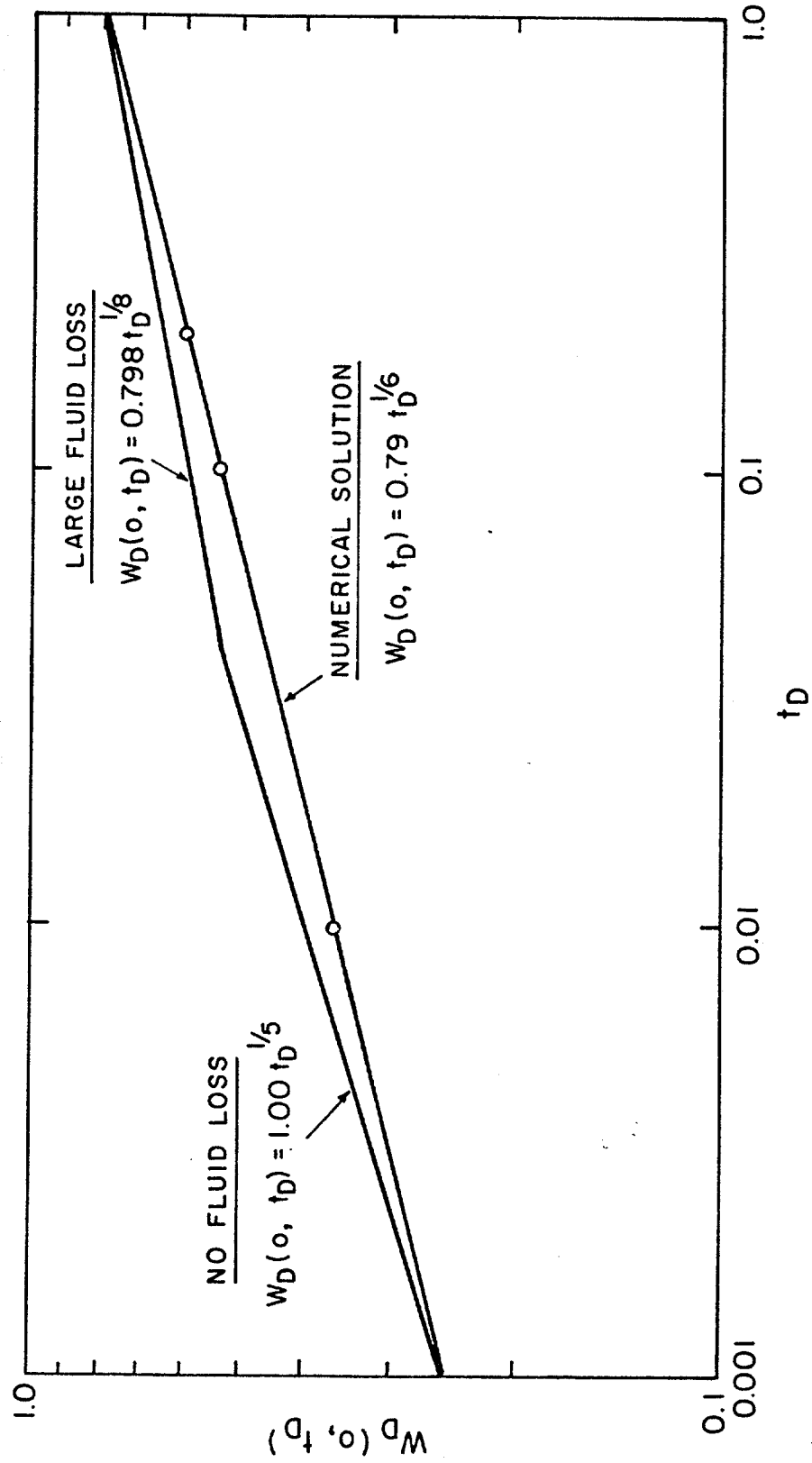


FIGURE 33 - Dimensionless solutions for the maximum fracture width as a function of time.

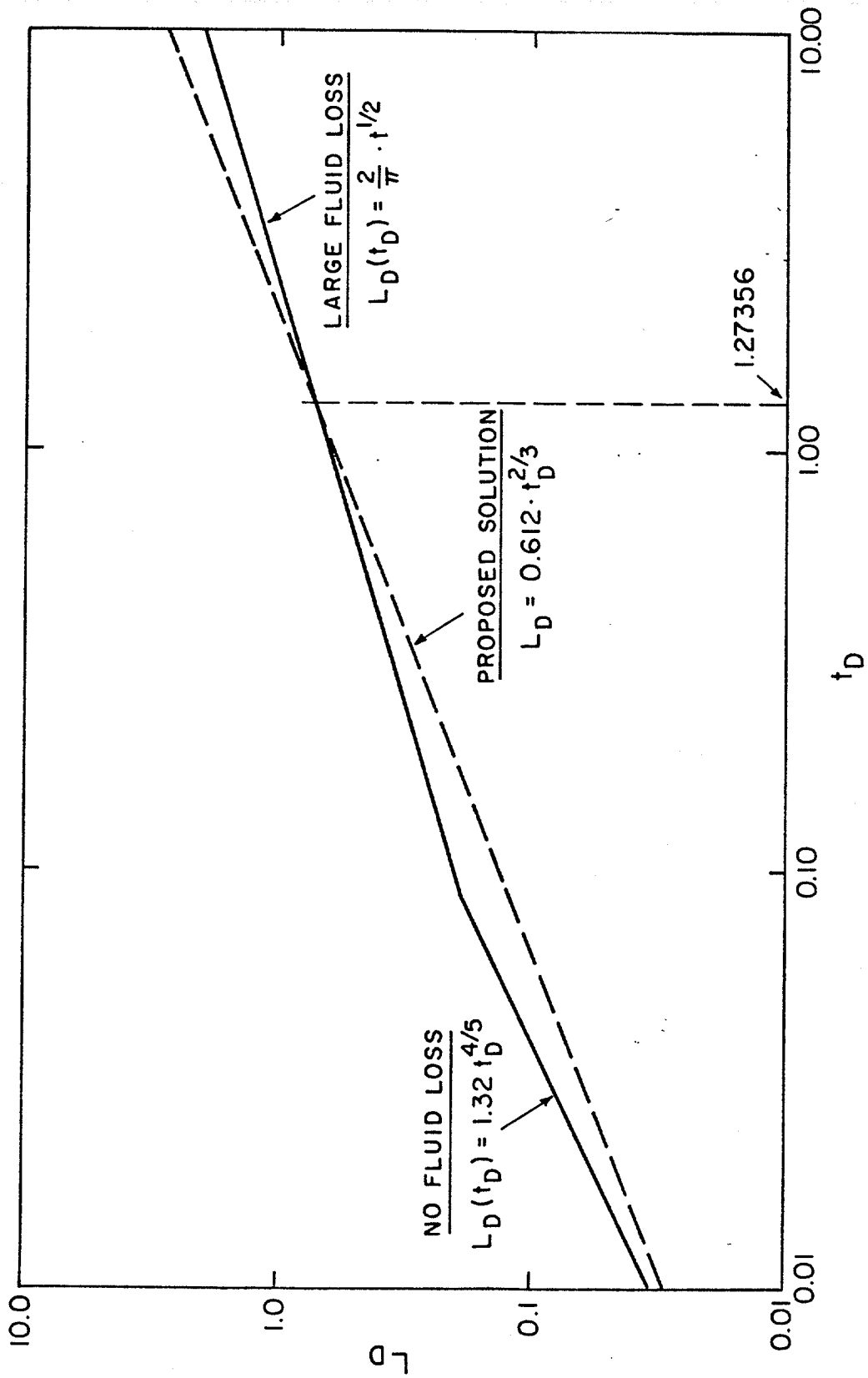


FIGURE 34 - Dimensionless solutions for the fracture length as a function of time.

$$L_D(t_D) = 1.32 t_D^{4/5} \dots\dots\dots (72)$$

The fracture width is obtained from the dimensionless solution of Figure 33 for a given dimensionless time, t_D , in combination with Equations (64) and (65). The pressure expansion at the fracture entrance can then be determined by substituting the width obtained in Equation (18). The resulting equation is

$$P(0, t) = \sigma_h + W(0, t).G / ((1-\mu).h) \dots\dots\dots (73)$$

In Equation (73), σ_h is the matrix stress acting perpendicular to the fracture wall, given in psi. This stress is equal to the normal compressive stress on the fracture plane before fracturing occurs, and it is also known as fracture-closure pressure. A method for measuring fracture-closure pressure from pressure-decline data is presented in Appendix H.

Large-Fluid-Loss Solution

The large-fluid-loss or large-time solution is based on the assumption that for large time, the term corresponding to the change in cross-sectional area of the fracture with time, $\partial A / \partial t$, can be neglected in comparisons with the fluid-loss term, q_L , in Equation (55). The resulting partial differential equation can be easily integrated, as shown in Appendix C. The large-fluid-loss assumption is realistic only if the fracture wall is exposed for a long period of time to a drilling fluid with a moderate to high water loss, and a permeable formation is present. The validation of this

approximation of large time is confirmed by comparison with numerical results in Figures 33 and 34. The equations for dimensionless fracture width at well bore and fracture length are

$$W_D(0, t_D) = (\sqrt{2/\pi}) \cdot t_D^{1/8} \dots\dots\dots (74)$$

and,

$$L_D(t_D) = (2/\pi) t_D^{1/2} \dots\dots\dots (75)$$

Numerical Solution

The numerical solution of Equation (55) was obtained using a finite difference method, and the results for the dimensionless width and length of fracture are shown in Figures 33 and 34, respectively. The curve fitting of the numerical solution for dimensionless fracture width in Figure 33 yields

$$W_D(0, t_D) = 0.79 t_D^{1/6} \dots\dots\dots (76)$$

The curve fitting expressed by Equation (76) accurately represents the numerical solution obtained, as shown by the plot of some points calculated with Equation (76), in Figure 33. Values of fracture width can be obtained by first calculating the dimensionless time, t_D , for a given time of expansion, t , with Equation (64). Then a dimensionless width value can be obtained using Equation (76) and converted to an actual width value with Equation (65).

The substitution of Equations (64) and (65) into Equation (76) produces the following equation for fracture width:

$$W(0, t) = 0.076643 [((1-\mu) \nu q^2) / (\pi^{3/2} G h C^{1/2})]^{2/9} t^{1/6} \dots (77)$$

Pressure expansion as a function of time can be calculated by substituting the value of fracture width obtained from Equation (77) into Equation (73).

Fracture Width Variation With Distance

The variation of maximum fracture width with distance, x , away from the well bore is shown in Figure 35 for conditions of no fluid loss and large fluid loss. The curves are very similar, which suggests that the ratio $W(x, t) / W(0, t)$ is not dependent on the fluid-loss coefficient, C . In this case, the real solution can be approximated by a combination of the numerical solution for fracture width at the borehole, $W_D(0, x_D)$, Equation (72), and the solution for the variation of maximum fracture width for a large fluid-loss rate (Equation E.11, Appendix E), which yields

$$W_D(x_D, t_D) = 0.79 [(x_D / L_D) \sin^{-1}(x_D / L_D) + (1 - x_D^2 / L_D^2)^{1/2} - (\pi/2) (x_D / L_D)]^{1/4} t_D^{1/6} \dots (78)$$

Equation (78) is not a solution for the nonlinear partial differential Equation (66). However, it is a fairly close approximation since it satisfies all the boundary conditions represented by Equations (67) through (70) and includes an approximation of the numerical solution of Equation (66). For Equation (78) to satisfy the boundary condition of Equation (67), the dimensionless fracture length, L_D , must be

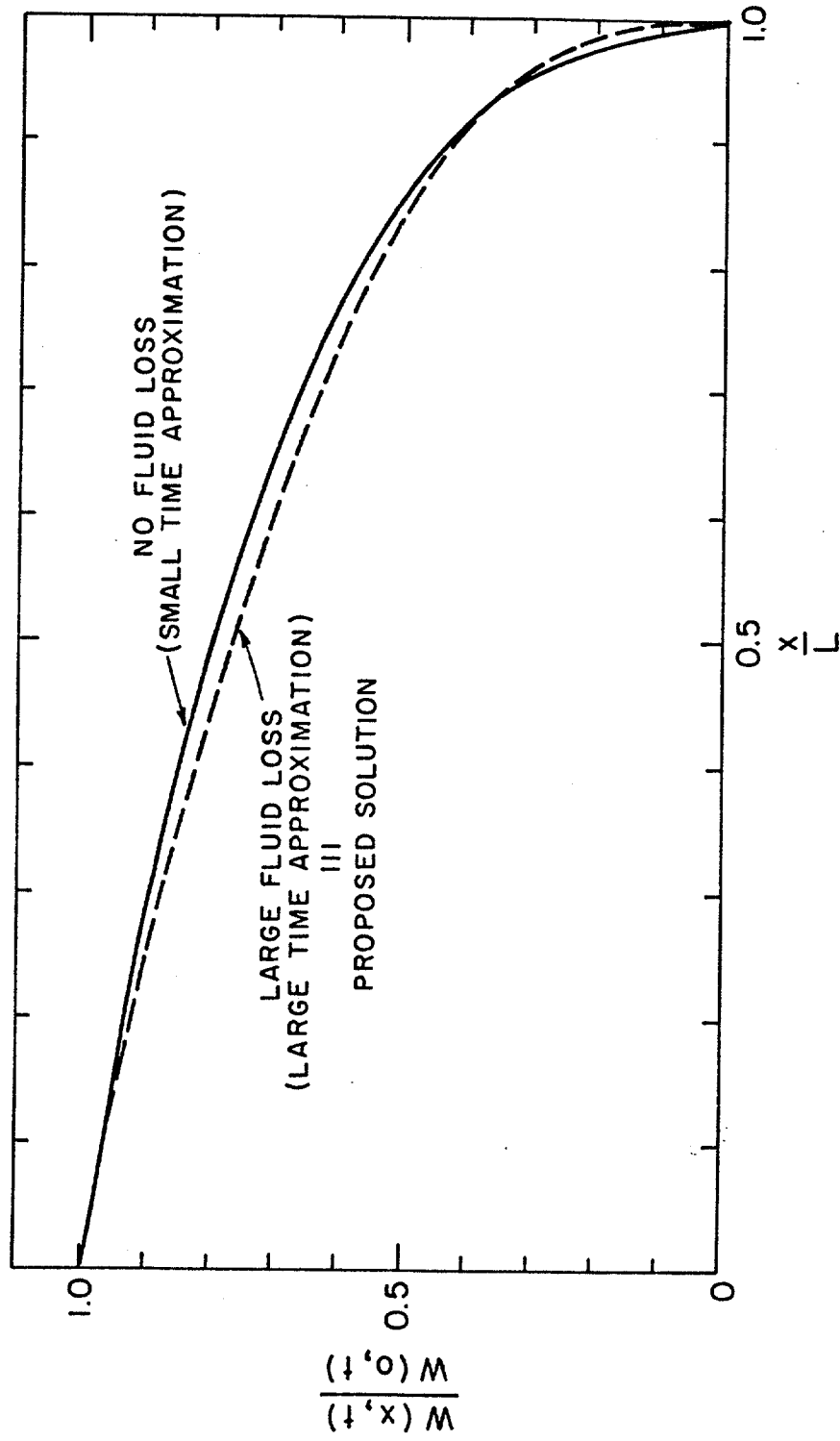


FIGURE 35 - Variation of maximum fracture width with distance from well.

$$L_D = 0.612 t_D^{2/3} \dots \dots \dots (79)$$

Equation (79) is plotted on Figure 34 as dashed lines. This approximated solution is close enough to the numerical solution obtained by Nordgren (1972) for the needed application. Thus, comparison further justifies the proposed solution for fracture-width variation with distance represented by Equation (78).

The fracture length can be determined directly by substituting Equations (63) and (64) into Equation (79), which yields

$$L(t) = 14.491 [(G.q^7) / (16(1-\mu).v.C^4.h^8)]^{1/9} . t^{2/3} \dots \dots \dots (80)$$

Proposed Solution

The solution used in the computer model for the propagation problem includes the three approximate solutions previously presented and shown in Figures 33, 34, and 35. The appropriate approximation is determined by the value of dimensionless time, t_D . The three dimensionless solutions for fracture width, represented by the straight lines in Figure 33, intersect the numerical solution line at $t_D = 0.000849$, and the numerical solution line intersects the large-fluid-loss line at $t_D = 1.27356$. Therefore, the no-fluid-loss approximation is applied for the small time, $t_D < 0.000849$, and the large-fluid-loss solution is applied for the large time, $t_D > 1.27356$.

The API fluid loss will greatly affect the determination of the proper interval to be applied for a given set of test parameters. The

lower the API value, the smaller the t_D obtained, and the larger the fracture width produced. Naturally, for very small times the model will also approximate the no-fluid-loss solution.

The fracture-width equations for conditions of no fluid loss and large fluid loss are derived in the same manner as was Equation (77) for numerical solution; they are

-No Fluid Loss

$$W(0, t) = 0.094265 [((1-\mu) \cdot v \cdot q^2) / (G \cdot h)]^{1/5} \cdot t^{1/5} \dots\dots\dots (81)$$

-Large Fluid Loss

$$W(0, t) = 0.066462 [(2 (1-\mu) \cdot v \cdot q^2) / (\pi^3 \cdot G \cdot C \cdot h)]^{1/4} t^{1/8} \dots\dots (82)$$

The equations for fracture length are

-No Fluid Loss

$$L(t) = 101.26 [(G \cdot q^3) / ((1-\mu) \cdot v \cdot h^4)]^{1/5} \cdot t^{4/5} \dots\dots\dots (83)$$

-Large Fluid Loss

$$L(t) = [(5.615 \cdot q) / (\pi \cdot h \cdot C)] t^{1/2} \dots\dots\dots (84)$$

From Equation (84) it can be seen that the fluid-loss coefficient, C , cannot be equal to zero. Equations (77), (80), (81), (82), (83), and (84), combined with Equation (73), constitute the basic mathematical modeling of fracture expansion assumed in this work.

Elastic Constants

Young's modulus, E, and the shear bulk modulus, G, which are the elastic constants of the rock being fractured, may be determined from a core sample of the rock under load in a testing machine; they are usually referred to as static elastic constants. If these constants are determined using wave-propagation relationships from measured elastic-wave velocities, they are usually referred to as dynamic constants. Rocks are not ideally elastic, and the dynamic constants for rocks are consistently higher than the elastic constants (Tixier et al. 1975).

Ideally, the elastic constants should be measured dynamically using well logging tools. It is easier to make logging measurements than to recover an unaltered core that is presumably representative of the formation and restore the core to an in-situ stress state. The dynamic measurements from well logs provide continuous curves that reveal changes and trends and are based on a larger radius of investigation.

The following equation represents the relationship between the elastic constants and Poisson's ratio, bulk density, and compressional transit times from acoustic logs:

Young's Modulus: E

$$E = 1.34 \times 10^{10} (\rho_b / \Delta t_c^2) [(1+\mu).(1 - 2\mu) / (1-\mu)] \dots\dots (85)$$

In Equation (85) the bulk density, ρ_b , is obtained from a density log in g/cm^3 . The compressional transit time, Δt_c , is measured from a sonic log in $\mu \text{ sec/ft}$. Young's modulus is given in psi.

Bulk Shear Modulus: G

Once Young's modulus has been calculated for the rock, the bulk shear modulus, G, is calculated using the following equation:

$$G = E / (2 (1+\mu)) \dots\dots\dots (86)$$

The other two elastic constants, Poisson's ratio and Biot's constant, are determined as discussed earlier in this chapter.

Fracture Closure Model

The fracture-closure model to be used in the mathematical model for leak-off test simulation is based on the solution of the continuity equation governing the fluid flow into the fracture. Since flow rate during fracture closure is zero, because the pump has been shut in, the corresponding term that includes flow rate is set to zero after integration of the differential equation over the length of the fracture.

Equation (55), the general continuity equation governing the fracture phenomena, combines with Equation (58) to yield

$$\partial q / \partial x + ((2 C h_p) / \sqrt{t - T(x)}) + \partial A / \partial t = 0 \dots\dots\dots (87)$$

The fracture height, h , in the fluid-loss term in Equation (55) is replaced by the permeable fraction of the total height of the fracture, h_p in Equation (87). In the fracture-expansion model, h and h_p were made equal for mathematical simplification and this assumption was found to have a negligible effect on the final answer. During fracture closure, however, the pressure decline is caused only by the filtration or fluid loss through the fracture wall, and the h_p/h ratio can significantly affect the pressure-decline gradient. If h_p cannot be evaluated from logs before the leak-off test, then it can be set equal to the total fracture height, h , for simulation purposes and evaluated later from logs or the leak-off test data obtained.

The cross-sectional area of the elliptical crack is given by Equation (59); the derivation for this equation is given in Appendix D. The maximum fracture width for a fracture under constant pressure is represented as

$$W = ((1-\mu) / G) h \Delta P \dots\dots\dots (88)$$

By substituting Equation (88) into (59) and deriving with respect to t , one obtains

$$\partial A / \partial t = (\pi (1-\mu) / 4G) h^2 (\partial P / \partial t) \dots\dots\dots (89)$$

Equation (89) contains the reasonable assumption that the bulk shear modulus of the formation, G , and the total fracture height, h , do not change significantly with time. Now, combining Equations (89) and (87) yields

$$\partial q / \partial x = ((2.C.h_p) / \sqrt{t - T(x)}) + [\pi (1-\mu) h^2 / (4.G)]. \partial P / \partial t \dots (90)$$

The method followed to solve Equation (90) is the same as that used by Nolte (1982). Since the theoretical approach used here is the same as that used to solve the fracture-expansion problem, the assumptions are the same, and consequently the discussion of the assumptions made in the fracture-expansion model also applies here.

The following equation is obtained by integrating Equation (90) over the length of the fracture and making the boundary conditions of flow rate equal to zero at the borehole ($x=0$) and at the fracture tip ($x=L$):

$$[2 C h_p L / \sqrt{t_0}] . f(t) = - (\pi/4) ((1-\mu) h^2) / G \int_0^L (\partial P / \partial t) dx \dots (91)$$

where

$$f(t) = (\sqrt{t_0} / L) \int_0^L d_x / \sqrt{t - T(x)} \dots \dots \dots (92)$$

and,

t_0 = injection time prior to shut-in, min

L = fracture length measured from the borehole, ft

To obtain a general solution for the pressure-decline problem, we must handle the integral terms in Equations (91) and (92) separately because no direct integration is possible. The time at which fluid loss begins at a distance, x , from the well, $T(x)$, is a function of x . This function must be determined before the integral term in Equation (92) can be evaluated. The x function can be

obtained by combining the equation for the length of an expanding fracture, x , with the equation of the fracture length at shut-in given in the previous section. These equations have the form

$$x(t) = \text{Const.} \cdot t^e \dots\dots\dots (93)$$

and

$$L = \text{Const.} \cdot t_0^e \dots\dots\dots (94)$$

Dividing Equation (93) by (94) and simplifying yields

$$t = T_0 [x(t) / L]^{1/e} \dots\dots\dots (95)$$

Combining Equation (70) with (95) yields

$$T(x) = t_0 [x(t) / L]^{1/e} \dots\dots\dots (96)$$

The substitution of Equation (96) into Equation (92) yields

$$f(t) = (\sqrt{t_0} / L) \int_0^L dx / \sqrt{t - t_0 [x/L]^{1/e}} \dots\dots\dots (97)$$

However, direct integration of Equation (97) is only possible if the value of the exponent "e" is 1 or ½. Based on numerical solution, the exponent "e" for the proposed fracture-expansion model is 2/3, which eliminates the possibility of direct integration of Equation (97). The value of ½ for "e" was determined to be the lower bound of the rate of fracture extension when fluid loss dominates, as discussed in the last section. This lower bound indicates that the second term in

Equation (87) dominates the third term to the extent that this third term, which controls fluid storage, can be neglected. The exponent "e" equals $\frac{1}{2}$ in Equation (97), allows the following solution after integration:

$$f_1(t) = \sin^{-1} [(1 + (t - t_0) / t_0)^{-\frac{1}{2}}] ; \text{ Lower bound} \dots\dots\dots (98)$$

The value of "e" for the upper bound is obtained by assuming a no-fluid-loss rate. In this case, q_L can be neglected in Equation (84), as explained in the previous section. The corresponding exponent is $e = 4/5$, which also does not allow direct integration of (97). However, the upper-bound exponent can be set equal to 1, a more conservative value to allow integration. This assumption will prove to be reasonable when the solution is obtained. The exponent $e=1$ in Equation (97) allows the following solution:

$$f_2(t) = 2 [\sqrt{1 + (t - t_0) / t_0} - \sqrt{(t - t_0) / t_0}] ; \text{ upper bound} \dots\dots (99)$$

The actual value of exponent e in the proposed fracture-expansion model is $2/3$, which is exactly halfway between the upper- and lower-bound exponents $\frac{1}{2}$ and 1. Then, the solution found for $f(t)$ using the exponent $2/3$ should be in the interval

$$f_1(t) < f(t) < f_2(t) \dots\dots\dots (100)$$

For simplification, the term $\delta = (t - t_0) / t_0$ is introduced in Equations (98) and (99) and yields

$$f_1(\delta) = \sin^{-1} [1 + \delta]^{-1/2} \dots \dots \dots (101)$$

and

$$f_2(\delta) = 2 [\sqrt{1 + \delta} - \sqrt{\delta}] \dots \dots \dots (102)$$

The functions $f_1(\delta)$ and $f_2(\delta)$ are plotted in Figure 36. The difference between the two curves is very small, especially for values of $\delta > 1.5$, which represent the common range found in leak-off test operations. Even for smaller values of δ , the bounds are still very close, and as a result, either of the two bounds can be used as an approximated solution for Equation (92) without compromising the accuracy since the proposed solution falls in between the bounded solutions, and since other parameters in Equation (91) cannot be estimated with any certainty.

Therefore, picking the upper bound as the approximate solution for $f(t)$, substituting it in Equation (91), and solving for the integral term yields

$$\int_0^L (\partial p / \partial t) dx = (16.G.C.h_p.L) / (\pi \sqrt{t_0} (1-\mu).h^2) [\sqrt{1 + \delta} - \sqrt{\delta}] \dots (103)$$

If we let \bar{p} be the average pressure along the fracture length, L , \bar{p} can be expressed as

$$\bar{p} = 1/L \int_0^L p.d x \dots \dots \dots (104)$$

Derivation of Equation (104) with respect to time yields

$$\partial \bar{p} / \partial t = 1/L \int_0^L \partial p / \partial t dx \dots \dots \dots (105)$$

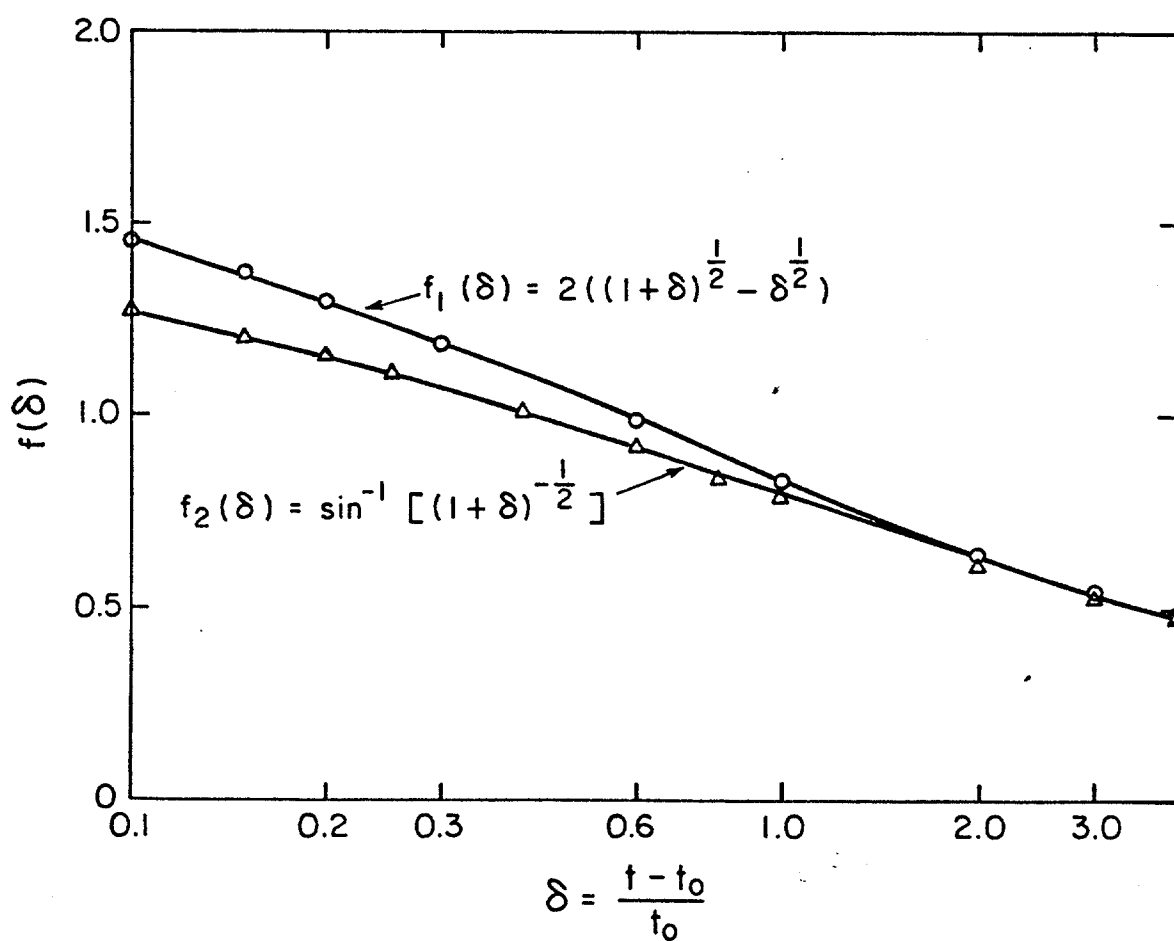


FIGURE 36 - Function $f_1(\delta)$ and $f_2(\delta)$ versus the dimensionless time parameters.

Substituting (105) into (103), and substituting the partial derivative, since \bar{p} is a function of time only, gives

$$d\bar{p}/dt = [(16.C.h_p.G) / (\pi \sqrt{t_0}(1-\mu)h^2)] \{ \sqrt{1+\delta} - \sqrt{\delta} \} \dots\dots (106)$$

Since $\delta = (t - t_0) / t_0$, the derivation of this expression with respect to time yields

$$dt = t_0.d\delta \dots\dots\dots (107)$$

To determine the partial derivative of \bar{p} with respect to time in Equation (106), we must first evaluate \bar{p} by means of Equation (104) as a function of the well-bore pressure, p . This pressure decreases from p at the well bore to p_L at the tip of the crack as a continuous function. Since the flow gradient is not linear an arithmetic average is not appropriate. Then, assuming a quadratic form yields

$$P(x) = P - (P - P_L)(x/L)^2 \dots\dots\dots (108)$$

Substitution of (108) into (104) and integration yields

$$\bar{p} = (2P + P_L) / 3 \dots\dots\dots (109)$$

Finally, after Equation (109) is expressed with respect to time, t , and the resulting equation and Equation (107) are substituted into

(106), the resulting equation is integrated over the ratio of time, δ , in the interval δ_0 to δ , which yields

$$\Delta P(\delta_0, \delta) = \left((16.C.h_p.G.\sqrt{t_0}) / (\pi.(1-\mu).h^2) \right) [(1+\delta)^{3/2} - \delta^{3/2} - 1] \dots (110)$$

where,

$$\Delta P(\delta_0, \delta) = P(\delta_0) - P(\delta) \dots (111)$$

and

$$G(\delta, \delta_0) = [(1+\delta)^{3/2} - \delta^{3/2} - 1] - [(1+\delta_0)^{3/2} - \delta_0^{3/2} - 1] \dots (112)$$

Fluid-Loss Coefficient

The fluid-loss coefficient, C , can be graphically determined in the laboratory with a standard API fluid-loss test. The procedure consists of plotting cumulative filtrate volume, V_f , versus the square root of the corresponding time. As shown by Equation (32) for wall cake building fluids, this yields a linear relationship with the slope, m . The relationship between the fracturing fluid or fluid-loss coefficient and the slope, m , for this case is obtained by differentiating Equation (32) with respect to time, t , and dividing the result by the cross-sectional area, A , of the media through which the flow rate, q , takes place. It yields

$$(dV_f / dt) (1/A) = (q/A) = v = (m/2 A) (1/\sqrt{t}) \dots (113)$$

The fluid-loss coefficient is defined as

$$C = v \sqrt{t} \dots \dots \dots (114)$$

Finally, if we combine Equations (113) and (114), and convert to field units, the fluid-loss coefficient becomes

$$C = 0.0164 \cdot m/A \dots \dots \dots (115)$$

Equation (115) expresses the fluid-loss coefficient in field units of $\text{ft}/\sqrt{\text{min}}$, the area, A , in cm^2 , and the slope, m , in $\text{cm}^3/\sqrt{\text{min}}$. The slope, m , obtained from Equation (32) can be substituted into Equation (115), yielding

$$C = 0.0164 \left((V_f - V_{sp}) / A \sqrt{t} \right) \dots \dots \dots (116)$$

The value of C can be obtained through an API fluid-loss test. The straight line plotted determines the spurt loss, V_{sp} , which is the intercept with the y-axis, and the slope, m . The spurt loss of drilling fluids is usually negligible.

The fluid-loss coefficient can also be determined by using pressure-decline data from leak-off tests. Equation (112) indicates that if two points are selected on the pressure-decline data, the function $G(\delta, \delta_0)$ can be evaluated. The two corresponding values of pressure are used to also evaluate $\Delta P(\delta_0, \delta)$. If the remaining variables are known, Equation (110) can be used to determine the

fluid-loss coefficient. This procedure can be repeated for various data points to obtain an average value of fluid-loss coefficient. Curve-matching techniques can also be used to obtain this average. Nolte (1982) shows this technique in detail.

COMPUTER MODEL

The successful planning of future wells requires a good knowledge of how to predict fracture-pressure gradients and properly verify them during drilling. Leak-off tests are used to verify the fracture-pressure gradient of the weaker formation below the actual casing shoe. However, a standard leak-off test procedure has not yet been formulated, nor has a standard interpretation technique for data analysis. Consequently, these data cannot be fully utilized. A computer simulation of a leak-off test has been developed to aid in designing the test before it is actually conducted and also to allow interpretation of the data collected after the test is run. This chapter will show the steps taken to develop the software necessary to accomplish this task. In addition, the program configuration and necessary data file organization will also be discussed here. The program follows the steps shown in the flow chart in Figure 37.

Features

The computer model developed to simulate leak-off tests predicts with reasonable accuracy the shape of the pressure curve on the basis of certain number of input parameters commonly available in the field. The computer model incorporates four mathematical models that simulate each individual phase that occurs during a leak-off test. These phases are (1) pressure increase due to change in overall compressibility of the well system, (2) formation breakdown and the consequent creation of a fracture, (3) expansion of this fracture to an elliptical shape, and (4) closure of the fracture by fluid filtration after the pump is stopped. These four

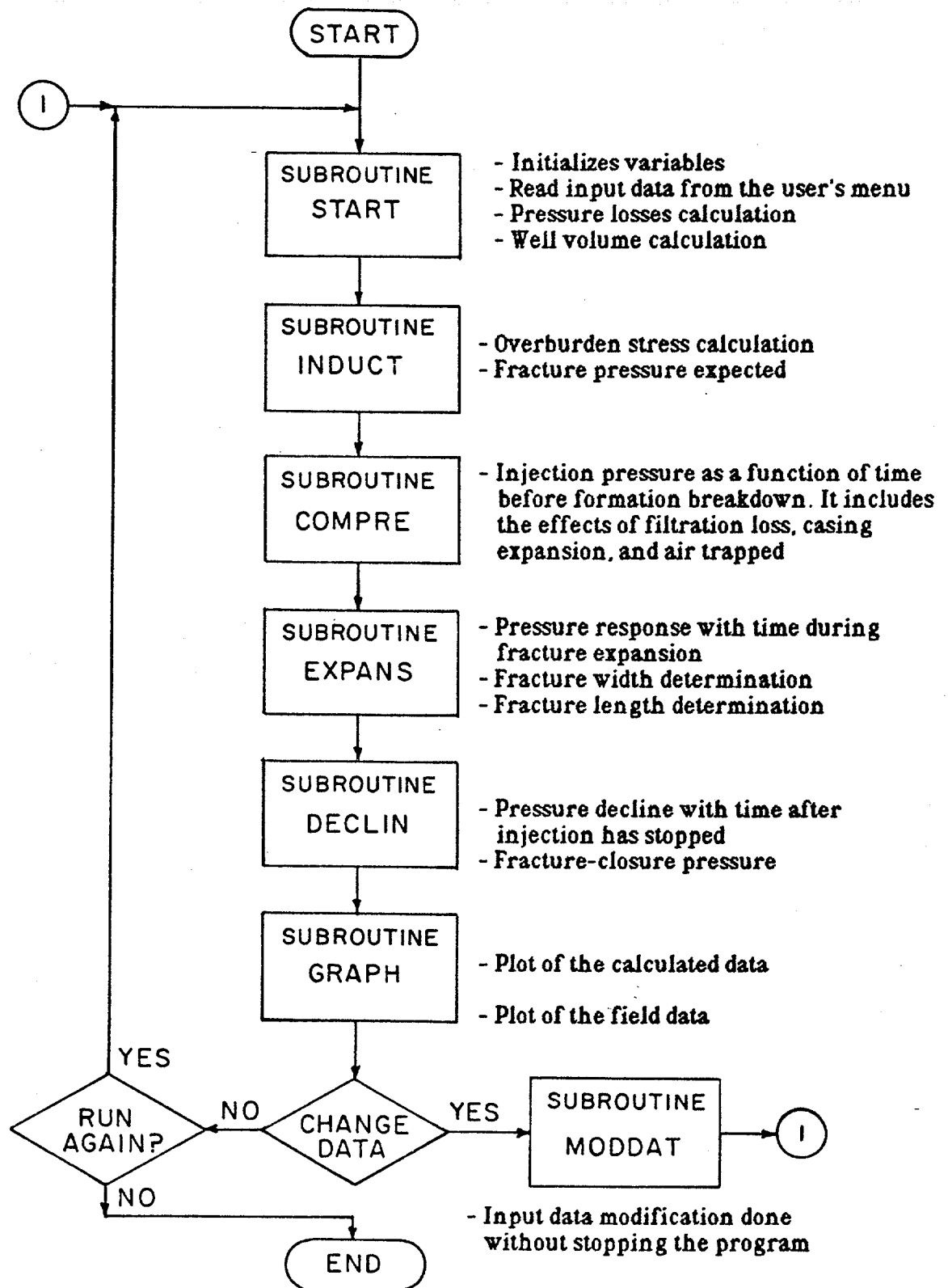
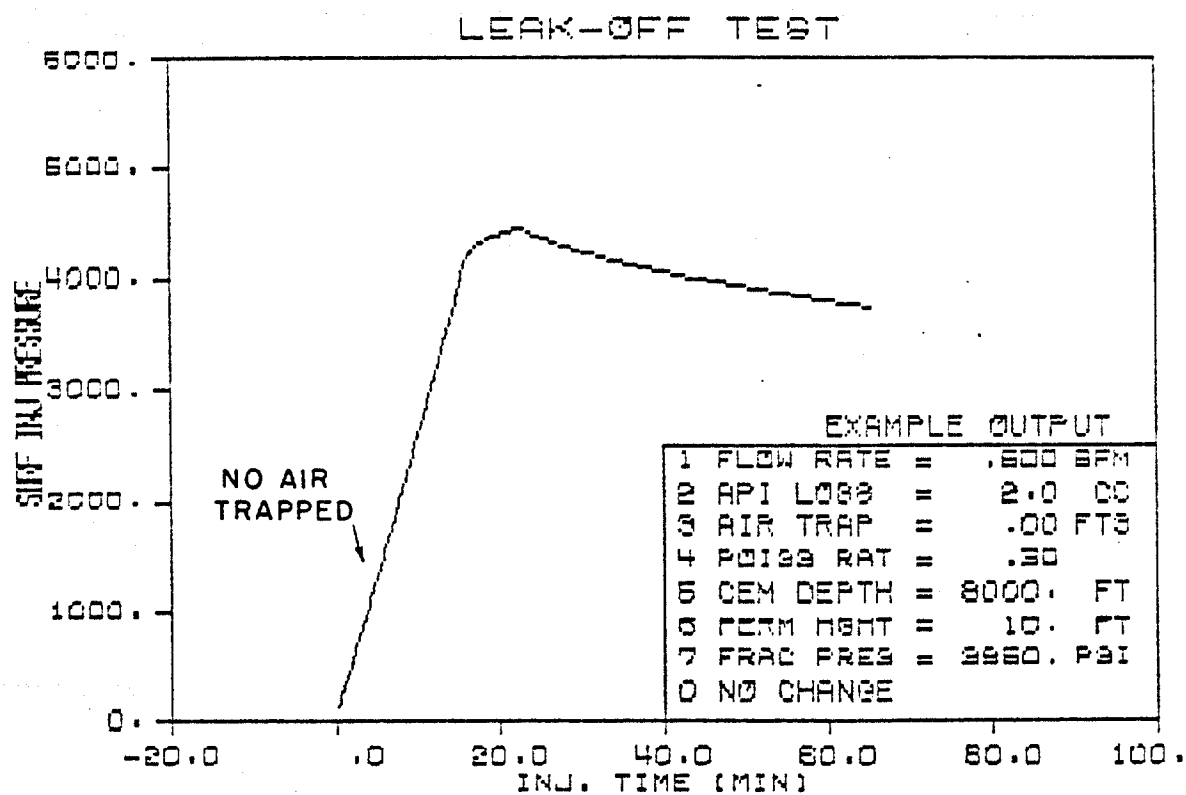


FIGURE 37 - Flow chart of the computer program LEAK.

models are explained in the previous chapter. The input data needed for the model are stored in a data file in the format shown in Appendix F to be used by the computer program LEAK. The program plots injection pressure at surface against time. Since flow rate is approximately constant throughout the test, this time scale is directly proportional to the volume of mud injected for the portion of the test during which the pumps are used. In addition, input test parameters important in the simulation process are shown on the right-hand corner of the plot, as depicted in the example output in Figure 38. The list of input/output parameters shown in Figure 38 can also be printed at the end of a run.

An additional feature of the computer model developed in its ability to simulate the injection pressure curve of a leak-off test for any volume of air trapped. Figure 39 shows an example of this type of simulation; in this example, air trapped is assumed to be zero initially, and then changed to 3.5 ft^3 , with other conditions kept constant. The curvature occurring at early times is caused by the presence of air in the closed-well system.

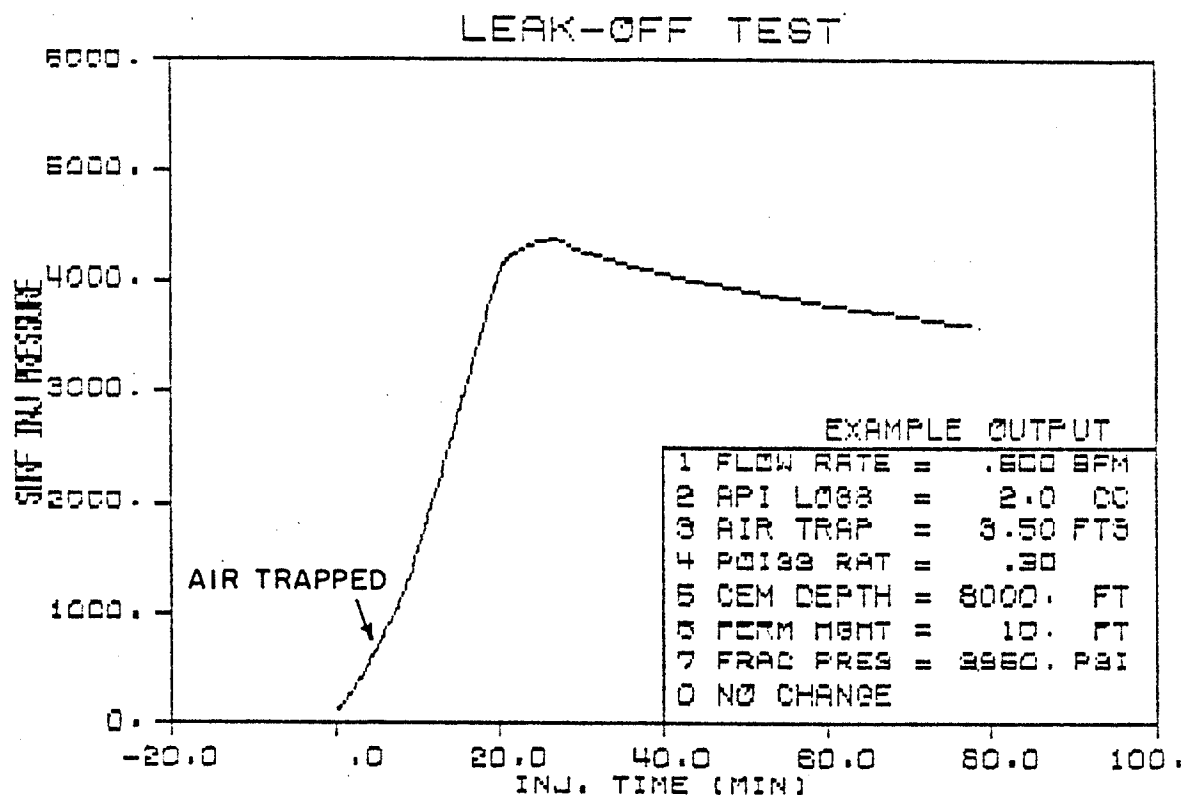
The computer program LEAK is written in FORTRAN computer language and designed to be user friendly. The input data needed for the program are stored in a data file formatted as shown in Appendix F. The most important alterable data are displayed on the screen in the format of a menu (Figure 40). The code shown in the left-hand corner is used to change the corresponding pair of parameters. The 26 parameters displayed can be changed as often as needed during a leak-off test simulation or interpretation.



INPUT/OUTPUT PARAMETERS

MUD DENSITY = 10.80 LB/GAL
 FLOW RATE = .50 BPM
 PORE PRESSURE = 9.20 LB/GAL
 CSG SHOE DEPTH = 12941. FT
 SECT FRAC : 12342.- 12352. FT
 FRAC GRAD EXP = 16.76 LB/GAL
 FRAC PRESS SURF = 3950.4 PSI
 VOL INJ SHUT-IN = 11.40 BBL
 FRACT HEIGHT = 10.00 FT
 FRACT WIDTH = .06758 IN
 FRACT LENGTH = 633.5 FT

FIGURE 38 - Example output of a simulated leak-off test plot.



INPUT/OUTPUT PARAMETERS

MUD DENSITY = 10.80 LB/GAL
 FLOW RATE = .50 BPM
 PORE PRESSURE = 9.20 LB/GAL
 CSG SHOE DEPTH = 12941. FT
 SECT FRAC : 12342.- 12352. FT
 FRAC GRAD EXP = 16.76 LB/GAL
 FRAC PRESS SURF = 3950.4 PSI
 VOL INJ SHUT-IN = 13.50 BBL
 FRACT HEIGHT = 10.00 FT
 FRACT WIDTH = .06769 IN
 FRACT LENGTH = 637.6 FT

FIGURE 39 -The effect of trapped air on a leak-off test.

MENU

1 MUD DENSITY / MUD VISCOSITY	:	10.00	LB/GAL	/	25.00	CP
2 MUD YIELD PT / MUD 10 MIN GEL	:	8.00	*/100 FT2	/	9.00	*/100FT2
3 MUD SPURT LOSS/API FLUID LOSS	:	.0	CM3	/	2.0	CM3
4 FLOW RATE/TOTAL DEPTH	:	.50	BBL/MIN	/	12951	FT
5 PORE PRESS/TENSILE STRENGTH	:	:5900	PSI	/	0	PSI
6 SURF POROS/POROS DECL CONST	:	.42		/	.000073	
7 VOL INJ SHUT-IN/TOT PERM HGHT	:	2.00	BBL	/	10	FT
8 TOP AND/BOTTOM OF FORM INTER	:	12342	FT	/	12352	FT
9 HOLE DIAM / MICROANNULUS	:	13.00	IN	/	.0000	IN
10 BIOT CONST/POISSON RATIO	:	.79		/	.30	
11 AIR GAP/WATER DEPTH(OFFSHORE)	:	108	FT	/	95.	FT
12 DRILLING TIME / CIRCULAT TIME	:	20.0	MIN	/	120.0	MIN
13 TOP CEMENT DEPTH/AIR TRAPPED	:	6000	FT	/	0.00	FT3
14 TO CONTINUE THE PROGRAM						

ENTER PROPER CODE TO CHANGE ANY PARAMETER/S ?

FIGURE 40 - The menu display of the program.

When the injection pressure is calculated, a smaller menu is added in the lower right-hand corner, as shown in Figure 38. This menu includes the input/output parameters that the user will most likely want to vary. These variables can also be changed by using the corresponding code on the left. These parameters are shown on the plot so that the user can visually associate the most important parameters with the curve shape produced.

Input Parameters

The information necessary for a leak-off test simulation can be obtained directly from field observations and fed into the computer. This information includes

1. Flow rate
2. Drilling fluid information
 - a. Mud density
 - b. mud viscosity
 - c. 10-min gel
 - d. yield point
 - e. percentage oil
 - f. percentage solids
 - g. API fluid loss
 - h. spurt loss
3. Well geometry
 - a. Total well depth
 - b. Casing shoe depth of last casing
 - c. Top of cement outside last casing
 - d. Casing OD, ID, grade
 - e. Drill collars OD, ID, length

- f. Drilling pipes OD, ID, length
- g. Heavy-weight drill pipes OD, ID, length
- h. Bit size
- i. Bit jets size
- j. Water depth (if offshore)
- 4. Lithology (open-hole section only)
 - a. Type
 - b. Depth interval of each formation
 - c. Pore pressure
 - d. Formation age
 - e. Surface porosity decline constant (Appendix B)
- 5. Amount of time that the formations are exposed to the drilling fluid
- 6. Volume of air trapped during the test

During the drilling personnel's preparations for a leak-off test air can become trapped in the mud-injection lines between the top of the mud level in the drill string itself and the outlet of the mud pump to be used during the test. Another place where air becomes trapped is between the annular BOP valve and the mud level inside the annular space in the casing. At the beginning of the leak-off test, when mud is first slowly injected into the well, the well is completely closed; the air trapped is thus compressed and injection pressure increases very slowly with time. As the volume of air trapped diminishes, due to pressure increase, the injection pressure increases more rapidly because of the change in the overall compressibility of the system.

7. Air gap between the kelly bushing and the floor (or water surface if offshore)
8. Temperature at surface and temperature gradient

Output Parameters

The program output consists primarily of a plot of injection pressure at surface versus injection time, which also includes the surface injection pressure needed to fracture the formation for the given input conditions. The output also includes the fracture gradient expected, total injected volume of mud at shut-in, the maximum fracture width obtained, and the total fracture length.

Data File Organization

With the information listed in the previous section, the data file for the program can be added in the format shown in Appendix F. The data file used to obtain the output example shown in Figure 38 is also shown in Appendix F.

Curve-Matching Technique

Once the input data is defined for a given area and stored in the data file, the model will produce a simulated leak-off test plot similar to the one in Figure 38. During the leak-off test, the actual data measured to plot pressure versus time are stored in the data file (see Appendix F), and the program will read data from the data file and plot it on top of the simulated plot. The user can then easily observe whether a match occurs between the predicted plot and the field data plot. The computer model is assumed to

accurately simulate the behavior of a pressure curve for the input parameters given. A match of the data indicates that all the input parameters agree with the field conditions, and the parameters then represent the leak-off test design criteria for that specific well depth and the formations it penetrates. These parameters may also be used for future wells drilled in the same area.

When a good match between the predicted and observed leak-off test curves is obtained, the observed leak-off test can be interpreted with confidence. When a mismatch occurs, input data can be varied over the possible range to see whether the observed data can be explained. Failure to obtain a match indicates a poor cement job. A mismatch between the predicted curve and the one produced by field data means that some input parameters should be changed so that they fit the field data. For example, if the fracture pressure predicted by the model is higher than the actual fracture pressure observed, the parameters involved in fracture pressure determination, such as Poisson's ratio, depth, overburden stress, pore pressure, and tensile strength, should be reevaluated until a match is obtained. If variation of these parameters over a likely range of values does not produce a match, then a leaking cement is indicated. In large open-hole sections, different formations are sometimes exposed, and the weakest one may not be at the casing seat. If it is not a smaller fracture-pressure gradient will be observed.

Changing certain parameters will affect the whole shape of the simulated pressure curve because they appear in each stage of the fracturing mechanism, which includes fracture creation, expansion, and closure. For example, if the fracture-expansion portion of the simulated curve is similar to the one shown by the field data, but

the fracture pressure does not match, the Poisson's ratio should not be changed because it will affect both the fracture pressure and the fracture-expansion curve. In this case, such parameters as overburden stress, tensile strength, and pore pressure should be examined first.

The next section illustrates this curve-matching technique with a series of leak-off test data obtained in the field.

Leak-Off Test Design

Introduction

The computer model for leak-off test simulation can be used not only for interpreting tests, but also for designing leak-off tests. Before drilling personnel conduct the test, it is very important for them to know the flow rate to be used during the test, what fracture gradient is expected, the total volume of mud to be injected during the test, and what a good pressure response curve looks like. To better describe the steps that should be taken to design a leak-off test with the software developed, this section uses an example to illustrate the process.

The well chosen for this example is located in the Louisiana Gulf Coast area. Most of the information needed to design the leak-off comes from drilling-morning reports and mud logs, which were generously furnished by Teneco Oil Company. The leak-off test can be designed after all the necessary well information is collected. The test can also be designed before the well is drilled on

the basis of expected data from the well-planning design, or while the casing is set, which provides the most up-to-date information.

Example Design

The example design of the leak-off test presented here incorporates data from a well drilled in the Gulf of Mexico area by Tenneco Oil Company. The well, located in Eugene Island block #215, is named OCS-G-0580 No. D-1. The design presented here is for the predominantly shale formation immediately below the casing seat of the 9 - 5/8" intermediary casing set at 12,342 ft (true vertical depth). The well is directional, and the configuration at the time of the test is shown in Figure 41.

The general information needed for the test design is listed in Table 4. Other information needed and not available at the time of the test will be presented during the development of the example.

Open-hole section. After the casing is cemented and the float collar equipment, cement, and shoe drilled, 10-20 ft of formation should be drilled (rathole). In the present case, the rathole should be drilled to 12,951 ft (MD), which includes 10 ft of open-hole section. The formation below the casing shoe is predominantly shale mixed with sand, as shown in Figure 41. The 10 ft of open-hole section will expose this lithology to the test.

Bit depth, drilling time, and circulation time. The drilling time spent to drill the rathole should be recorded so that the cumulative water loss to permeable formations can be calculated. After the rathole is drilled, the bit should be positioned at 12,940 ft, which is

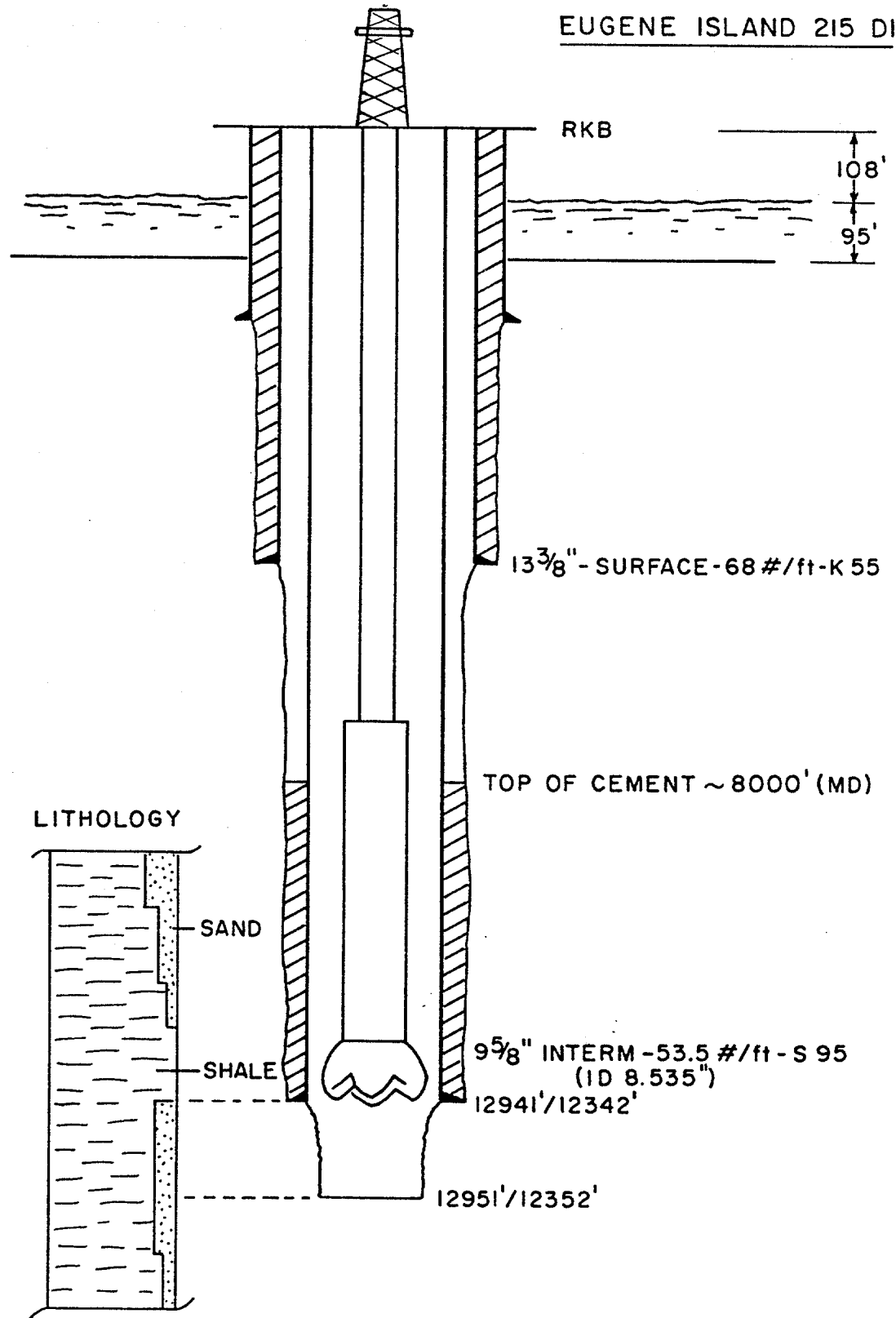


FIGURE 41 - Example well configuration.

TABLE 4
FIELD DATA FOR THE EXAMPLE DESIGN OF A LEAK-OFF TEST
(WELL EI 215 DI)

Drilling Fluid Data

Well Identif.	Mud Density (lb/gal)	Plastic Viscosity (CP)	Yield Point (LBF/100 ft ²)	10 Min GEL (LBF/100 ft ²)	API Fluid Loss (cm ³)	Solids Concent (%)	Oil Concent (%)	Flow Rate (BPM)	Drig Time (MIN)	Circul. Time (MIN)
EI 215 D-1	10.8	25.0	8.0	9.0	16.0	26	2.		20.0	120.0

Well Geometry

Well Identif.	Last CSG (*)	CASING OD (in.)	(Top) ID (in.)	Length (ft)	CASING (Bottom) OD (in.)	ID (in.)	Length (ft)	Total Depth (ft)	Water Depth (ft)	AIR GAP (ft)	Top Cement Depth (ft)	Shoe Depth MD/TVD (ft)
EI 215 D-1	1	9.625	8.535	12941	-	-	-	12951	95.0	108.2	8000	12941
								12352				12342

Drilling string data

Well Identif.	Last CSG (*)	DRILL PIPES			HEAVY-WEGHT DP			DRILL COLLARS			Bit Diam (in)	Jets Size (32nd.in)	Bit Depth (ft)
		OD (in.)	ID (in.)	Length (ft)	OD (in)	ID (in)	Length (ft)	OD (in)	ID (in)	Length (ft)			
EI 215 D-1	I	5.	4.276	8778	5.0	4.0	2700	6.25	2.813	1463	8.5	11 11 11	12940

Open-hole formation data.

Well Identification	FORMATION TESTED OR BEING TESTED			OPEN-HOLE		
	TVD TOP (FT)	TVD BOTTOM (FT)	TYPE	PORE PRESS. (LB/GAL)	TEMPERATURE (°F)	TOTAL PERM. HEIGHT (FT)
EI 215 DI	12342	12352	SHALE	9.2	211	10

(*) C - Conductor; S - Surface; I - Intermediary; L - Liner

inside the casing. The well should be circulated with a mud volume of at least 1.5 times the total volume of mud in the well. This will clean the annulus and obtain a uniform mud weight of 10.8 lb/gal throughout the well. In our example, the values of drilling time and circulating time were estimated to be 20 min and 120 min, respectively.

Surface porosity and porosity-decline constant. Surface porosity (ϕ_0) and the porosity-decline constant (K) are determined as discussed in Appendix B. According to this method, a porosity log of the area should be used to plot porosity as a function of depth. The porosity log available for the example well is an acoustic log; the values of formation transit time versus depth obtained from this log are listed in Table 5. The values were averaged over 500-ft depth intervals. The corresponding porosities, listed in the same table, were calculated using the following equation for the Gulf Coast area:

$$\Delta t_0 = 50 + (130 + \Delta t_f) \phi - 180\phi^2 \dots\dots\dots (116)$$

where

Δt_0 = measured interval transit time, μ sec/ft

Δt_f = Interval transit time of the porous fluid, μ sec/ft

Equation (116) includes the variation of interval transit time of the rock matrix, Δt_m , with porosity for the Gulf Coast area (Bourgoyne 1986).

TABLE 5

Interval transit time and correspondent porosity values versus depth.

DEPTH INTERVAL	INTERVAL TRANSIT TIME Δt	POROSITY \emptyset
1000 - 1500	156.4	0.398
1500 - 2000	150.8	0.370
2000 - 2500	143.4	0.336
2500 - 3000	141.0	0.324
3000 - 3500	141.6	0.327
3500 - 4000	141.0	0.324
4000 - 4500	136.4	0.304
4500 - 5000	139.2	0.316
5000 - 5500	134.8	0.297
5500 - 6000	135.4	0.299
6000 - 6500	128.2	0.269
6500 - 7000	125.8	0.259
7000 - 7500	119.8	0.235
7500 - 8000	121.8	0.243
8000 - 8500	116.2	0.221
8500 - 9000	112.4	0.207
9000 - 9500	111.0	0.202
9500 - 10000	108.4	0.192
10000 - 10500	105.8	0.182
10500 - 11000	101.2	0.166
11000 - 11500	96.8	0.150
11500 - 12000	98.2	0.155
12000 - 12500	96.4	0.148

The plot of porosity versus depth can be approximated by a straight line on semi-log paper, as shown in Figure 42. The porosity-decline constant, K , and the surface porosity, ϕ_0 , are 0.0000731 and 0.42 respectively.

Pore pressure. The pore pressure information was obtained from an offset well drilled in the same area. The average true vertical depth at the formation to be tested below the casing seat is 12,347 ft. The corresponding pore pressure is 5900 psi (equivalent to 9.2 lb/gal mud density).

Elastic constants of rock. The elastic constants of the formation that must be input to the computer model are Poisson's ratio, Biot's constant, and Young's modulus. The Poisson's ratio for the Gulf Coast area can be obtained from Figure 31 by entering the true vertical depth of the formation of interest, which is 12,347 ft. A Poisson's ratio of 0.30 is obtained.

The Young's modulus of the formation is obtained using Equation (85). A density log of the well is used to determine the average value of bulk density at the casing-seat depth, which is 2.36 g/cm³. The bulk density value could also be obtained using the porosity data in Table 5 and Equation (B.3) in Appendix B. The value from the density log, however, is more precise. Equation (116) yields a compressional wave travel time, Δt_c , of 96.4 μ sec/ft. Added to Equation (85), these data yields

$$E = 1.34 \times 10^{10} (2.36/96.4^2) \{ (1 + 0.3) (1 - 2 (0.3)) / (1 - 0.3) \} \\ = 2.524 \times 10^6 \text{ psi}$$

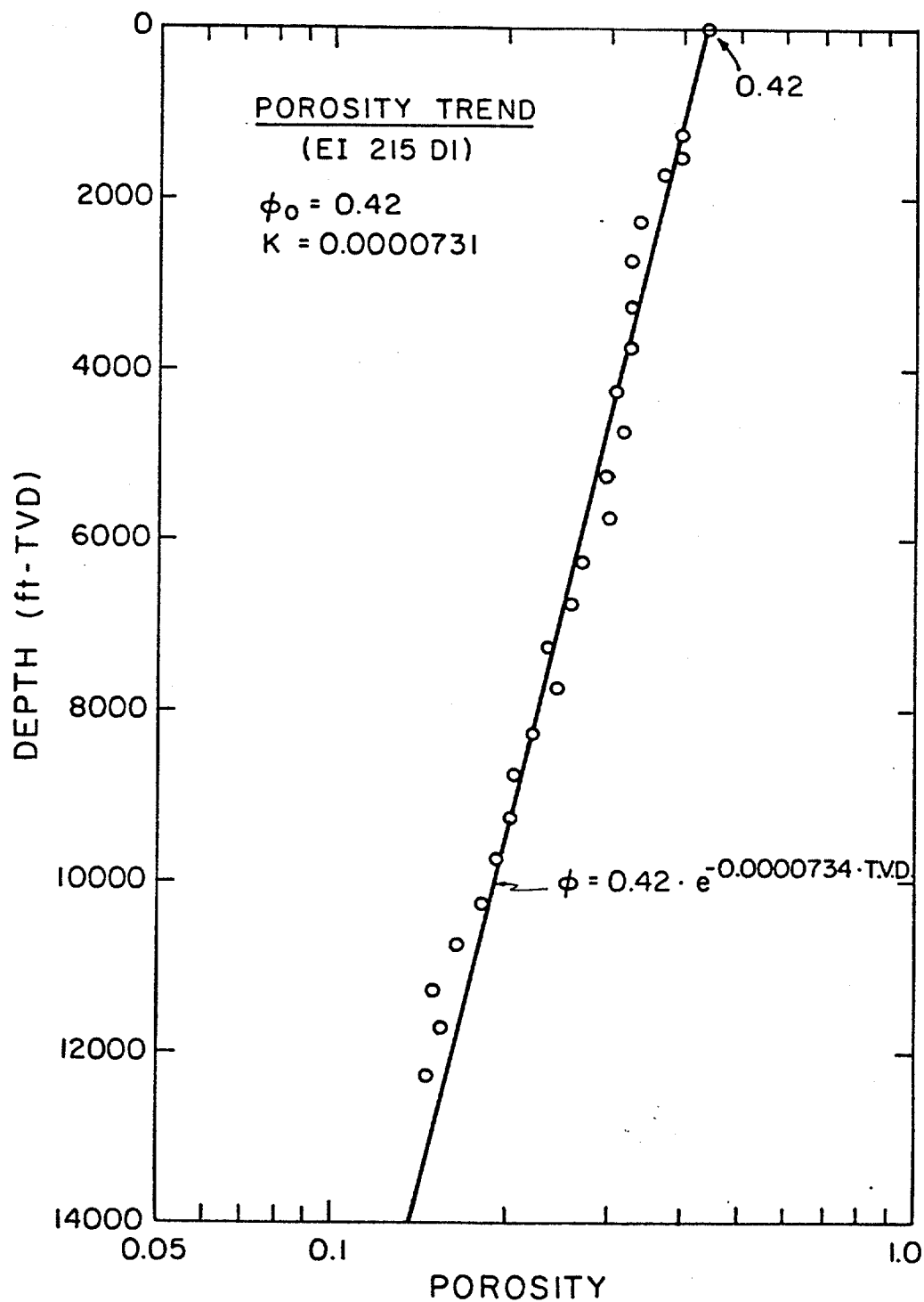


FIGURE 42 - Porosity versus depth for the EI-215-D-1 well drilled in Louisiana Gulf Coast area.

If we assume the compressibility of the rock matrix, C_{ma} , to be equal to $0.1 \times 10^{-6} \text{ psi}^{-1}$; calculate the bulk rock compressibility from Equation (50); and substitute the results in Equation (49), we get

$$\alpha = 1 - (0.1 \times 10^{-6}) / (2.1 \times 10^{-6}) = 0.79$$

Cementing job. Two input data related to the cement outside the intermediate casing are needed. The first is the quality of the cementing job, which can indicate the existence of a microannulus between the casing and the cement. This information can be obtained if a CBL-VDL log is run after the cement sets. The microannulus, if it occurs, cannot be larger than 0.01 in., the maximum size normally encountered. In the present example, no CBL-VDL logs were run, but information gathered from other wells indicates that the quality of the cementing job is generally very good, and no microannulus problems have been noticed.

The second piece of information needed is the depth of the top of the cement outside the casing. This information can also be obtained from the CBL-VDL log. Also, it can be calculated on the basis of the volume of cement displaced and the well geometry. In our example well, the top of the cement is at approximately 8000 ft of measured depth.

Total injected volume. The total volume of drilling fluid injected before shutting-in the pump and after fracturing the formation must be entered into the program. During the simulation process this value tells the program when to stop simulating the fracture expansion and start simulating the pressure-decline period. About

pressure has been reached. In the example well, 2 bbl of mud will be injected after the formation has been fractured.

Pressure-decline period. After the pump is stopped, the well should be kept closed, and pressure and time should be recorded until the pressure falls to the fracture-closure pressure. Sometimes this point is indicated by a break in the rate of decline. In any case, the pressure during the decline period should be recorded so that parameters affecting the pressure decline rate can be estimated by a history matching technique using the computer model.

Drilling fluid. The drilling-fluid properties can be determined from the mud program planned for the well or by direct measurement. Directly measuring the mud properties is preferable. However, mud properties can be measured only immediately before the test begins. In the present example, the well is already drilled, and the mud properties were measured immediately before the test started. They appear on the output menu shown in Figure 43. The most important input data the model uses are shown on the output in Figure 43.

Flow rate selection. Initially, the selection of flow rate should be based on pump limitations, mud volume in the hole, and open-hole conditions. Normally, the flow rate for a leak-off test should fall in the range of 0.25-1.50 bbl/min. The range for very short open-hole sections that do not expose any sandstone formations should be 0.25-0.50 bbl/min. If sandstone formations are present, the range should be 0.75-1.50 bbl/min, depending on the length of the open-hole section. Also, the total time of the test should be considered. For low flow rates and great mud volume in the hole, the test will take longer than for high flow rates.

MENU

1 MUD DENSITY / MUD VISCOSITY	:	10.80	LB/GAL / 25.00	CP
2 MUD YIELD PT / MUD 10 MIN GEL	:	8.00	*/100 FT2/ 9.00	*/100 FT2
3 MUD SPURT LOSS/API FLUID LOSS	:	0.0	CM3 / 16.0	CM3
4 FLOW RATE/TOTAL DEPTH	:	.25	BBL/MIN/ 12951	FT
5 PORE PRESS/TENSILE STRENGTH	:	5900	PSI / 0	PSI
6 SURF POROS/POROS DECL CONST	:	.42	/ .000073	
7 VOL INJ SHUT-IN/TOT PERM HGHT	:	2.00	BBL / 10	FT
8 TOP AND/BOTTOM OF FORM INTER	:	12342	FT / 12352.	FT
9 HOLE DIAM / MICROANNULUS	:	13.00	IN / .0000	IN
10 BIOT CONST/POISSON RATIO	:	.79	/ .30	
11 AIR GAP/WATER DEPTH(OFFSHORE)	:	108	FT / 95.	FT
12 DRILLING TIME / CIRCULAT TIME	:	20.0	MIN / 120.0	MIN
13 TOP CEMENT DEPTH/AIR TRAPPED	:	8000	FT / .00	FT3
14 TO CONTINUE THE PROGRAM				

ENTER PROPER CODE TO CHANGE ANY PARAMETER/S ?

FIGURE 43 - User's menu for an example formation integrity test at a 9-5/8" casing seat.

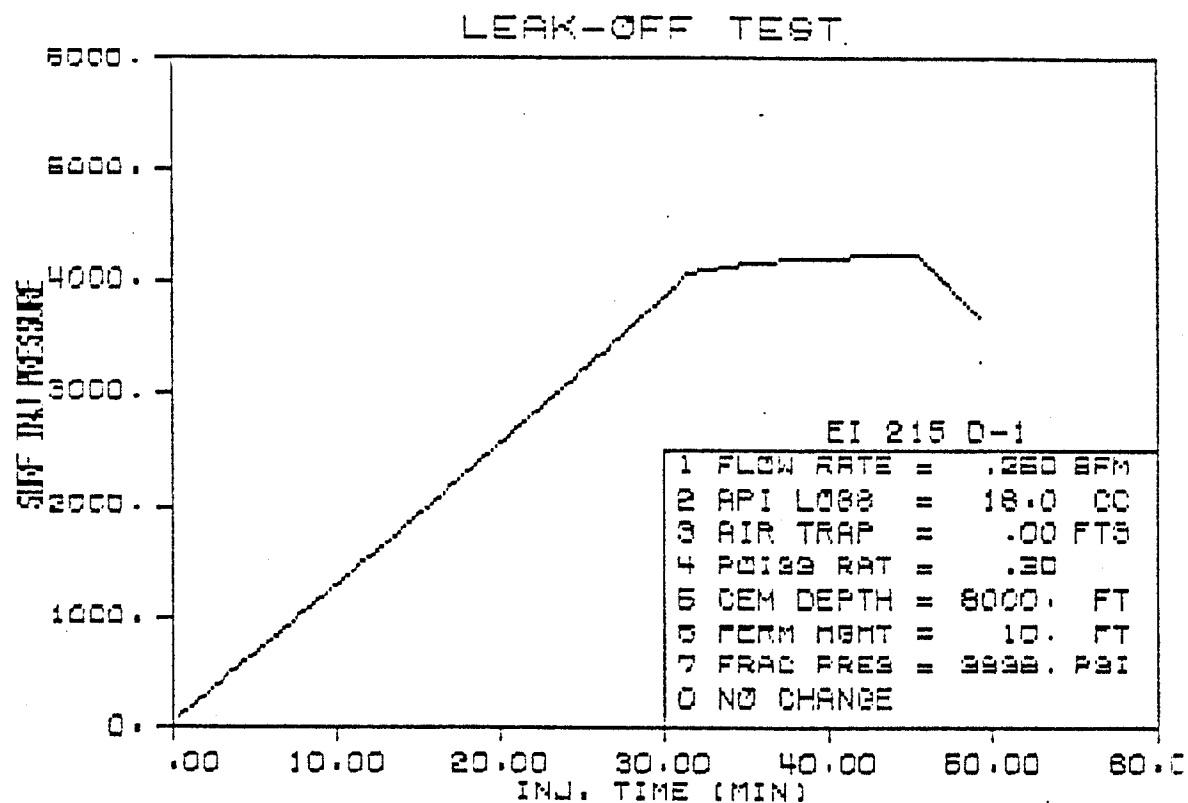
In the example, the open-hole section is very short (10 ft), and only shale is present; therefore, the initial flow rate chosen is 0.25 bbl/min.

Expected curve. All the information described above is next entered into the computer model. The program output is the expected pump pressure versus time curve for the leak-off test. This curve is shown in Figure 44, along with other important input and output parameters.

The prediction shown in Figure 44 of the time needed to reach breakdown pressure is approximately 32 min or a total of 8 bbl injected at 0.25 bbl/min. Increasing the flow rate to 0.50 bbl/min (Figure 45) will reduce the time to approximately 16 min. The increase in flow rate reduce the total time of the test and increase the maximum fracture width and length.

Test Procedures

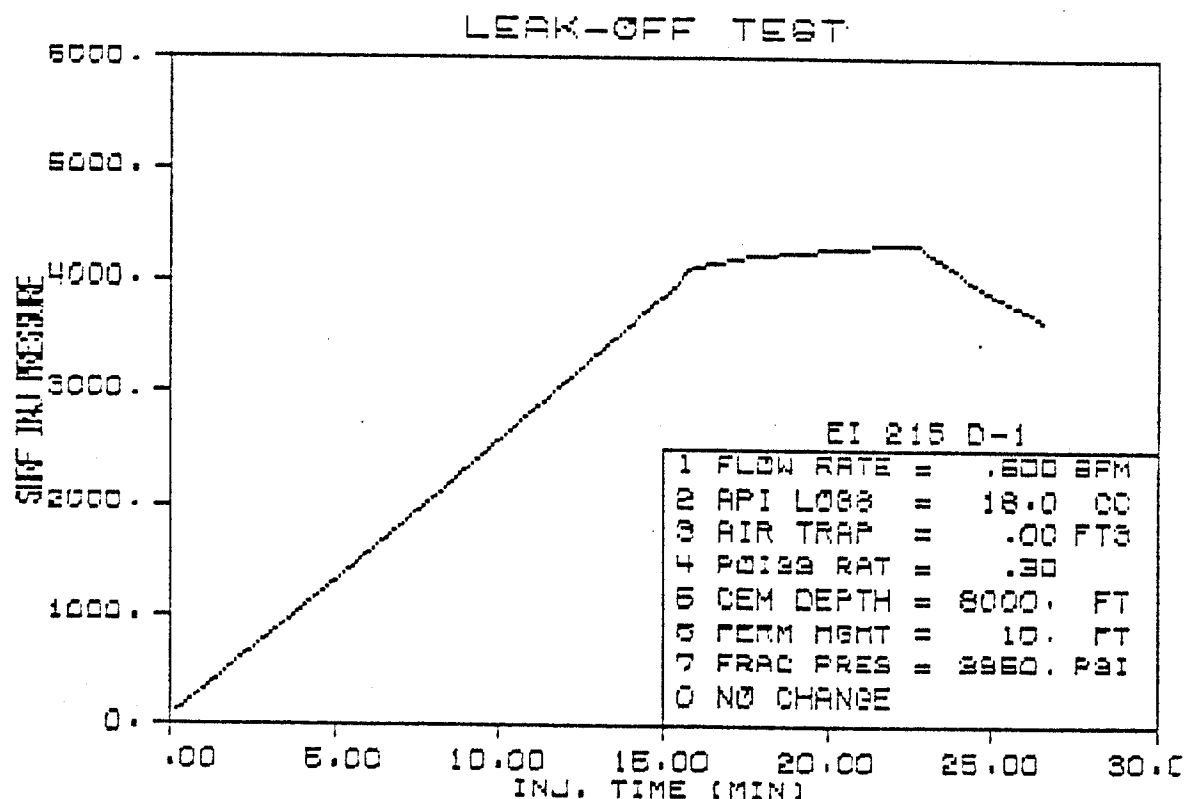
1. After the cement and float equipment are drilled, a rathole should be drilled 10 ft below the casing seat. If geologic information indicates that a formation weaker than those exposed is present within close range, then this formation should be drilled through and the test repeated.
2. After the rathole is drilled, the bit should be positioned in the casing immediately above the shoe to reduce the risk of the drill pipe becoming stuck during the test.



INPUT/OUTPUT PARAMETERS

MUD DENSITY = 10.80 LB/GAL
 FLOW RATE = .25 BPM
 PORE PRESSURE = 9.20 LB/GAL
 CSG SHOE DEPTH = 12941. FT
 SECT FRAC : 12342.- 12352. FT
 FRAC GRAD EXP = 16.76 LB/GAL
 FRAC PRESS SURF = 3938.5 PSI
 VOL INJ SHUT-IN = 11.40 BBL
 FRACT HEIGHT = 10.00 FT
 FRACT WIDTH = .04437 IN
 FRACT LENGTH = 235.4 FT

FIGURE 44 - Expected pressure versus time curve for the flow rate in the example leak-off test design at 0.25 BPM.



INPUT/OUTPUT PARAMETERS

MUD DENSITY = 10.80 LB/GAL
 FLOW RATE = .50 BPM
 PORE PRESSURE = 9.20 LB/GAL
 CSG SHOE DEPTH = 12941. FT
 SECT FRAC : 12342. - 12352. FT
 FRAC GRAD EXP = 16.76 LB/GAL
 FRAC PRESS SURF = 3950.4 PSI
 VOL INJ SHUT-IN = 11.40 BBL
 FRACT HEIGHT = 10.00 FT
 FRACT WIDTH = .05592 IN
 FRACT LENGTH = 297.0 FT

FIGURE 45 - Expected pressure versus time curve in the example leak-off test design at 0.50 BPM.

3. The well should be circulated using the mud pump until the mud density returning from the annulus is the same as the mud density being pumped down the drill pipe. The drilled cuttings or any injected slugs should be circulated to the surface.

4. The smaller cementing pump, rather than the mud pump, should be used to conduct the leak-off test. After switching to the cementing pump, circulate first through the bypass in the standpipe manifold to remove air from the pump piping.

5. When the hole is full of mud, a blowout preventer should be closed above the drilling spool.

6. Returns through the choke manifold should be circulated down the drill pipe to remove any air trapped below the annular preventer and in the choke manifold.

7. The pump rate should be set at the desired value for the test. A rate of 0.25 bbl/min was used in the example test.

8. The choke should be closed and the stroke counter and timer reset.

9. Pumping down the drill pipe should continue at a constant pump rate and both drill pipe and choke pressure recorded as a function of time or volume injected.

10. When the pump is stopped, the well should be kept closed and the drill pipe and casing pressures should be continuously recorded as a function of time.

11. The well should be bled-off and the amount of mud recovered in the trip tank recorded. This volume should be compared to that predicted by the computer model. If a leak in the cement is present, the observed volume recovered will be less than that predicted.

12. The two graphs, that predicted by the model and the real data one, should be compared to see if the test was accurate.

VERIFICATION OF COMPUTER MODEL USING FIELD DATA

This chapter explains how the model has been verified with field data from wells drilled offshore of the Louisiana Gulf Coast. All data were generously furnished by the offshore division of Tenneco Oil Company. Data from four wells were used to verify the pressure response predicted by the computer model. Data from an additional eight wells were used to provide some of the needed information concerning sediment density, lithology, porosity, bulk shear modulus, etc. When these data were unavailable for a well, average values for the area were used.

Once the parameters necessary to run the computer model were all defined, they were entered into the model. The output produced by the model includes the simulated leak-off pressure curve and a plot of the observed pressure data points. The predicted curve and the field data points plotted were then checked for a match. After a match was obtained, the fracture pressure and fracture dimensions were computed and a summary of the calculated results printed. This interpretation procedure was automatically performed by the computer model.

When the curves did not match, the parameters that could be causing the mismatch were varied over a range of values considered normal for those parameters in an effort to match the observed data. Once a match of the two curves were obtained, this process was stopped, and the results were printed.

After the computer model has been verified with field data, a sensitivity analysis is performed for the main parameters involved in the computer model. The sensitivity analysis is particularly important if a parameter's relationship to pressure at surface is not easily identifiable. The sensitivity analysis is performed by varying the parameter being analyzed while keeping the other variables constant. The different curve outputs produced are then compared to determine the effect of the parameter variation.

Selected Wells

The casing-seat integrity test data obtained from four different wells drilled in the Louisiana Gulf Coast area are listed in Tables 6, 7, 8, and 9. These wells are identified as follows:

Field	Block *	Well *	Abbreviation Used
East Cameron	213	2	EC 213 * 2
Vermilion	75	3	VR 75 * 3
Eugene Island	151	1	EI 151 * 1
South Marsh Island	160	A-3	SMI 160 A-3

Unfortunately, in some cases the test was stopped immediately after the leak-off, and pressure data were not recorded during the fracture-expansion period. In these cases, the well was bled-off immediately after the pump was shut off, and no pressure-decline data were recorded.

TABLE 6

1- Drilling Fluid Data

Well Identif.	Last CSG (^x)	Mud Density (lb/gal)	Plastic Viscosity (CP)	Yield Point (LBF/100 ft ²)	10 Min GEL (LBF/100 ft ²)	API Fluid Loss (cm ³)	Solids Concent (%)	Oil Concent (%)	Flow Rate (BPM)	Drig Time (MIN)	Circul. Time (MIN)
EC 213*2	I	11.8	27.0	12.0	6.00	2.8	19	2	0.50	60.	0.
VR 75 *3	S	9.5	9.0	25.0	44.00	20.0	8	0	0.25	60.	60.
EI 151 *1	I	10.1	10.0	6.0	3.00	5.6	10	0	0.25	30.	30.
SMI-160-A3	S	9.6	7.0	13.0	15.0	20.2	8	0	0.50	30.	180.

TABLE 7**2- Well Geometry**

Well Identif.	Last CSG (*)	CASING (Top)			CASING (Bottom)			Total Depth (ft)	Water Depth (ft)	AIR GPA (ft)	Top Cement Depth (ft)	Shoe Depth MD/TVD (ft)
		OD (in.)	ID (in.)	Length (ft)	OD (in.)	ID (in.)	Length (ft)					
EC 213 #2	I	9 5/8	8.535	7884.	-	-	-	7944	111.	201.	4600	7884 7884
VR 75 #3	S	13 3/8	12.347	4510.	-	-	-	4564 4554	21.	201.	222	4510 4500
BI 151 #1	I	9 5/8	8.535	14284.	-	-	-	14351 14351	280.	116.	12000	14284 14284
SMI-160-A3	S	13 3/8	12.347	5166.	-	-	-	5228 4828	280.	201.	312	5166 4175

(*) S - surface

I - intermediary

L- liner

TABLE 8

3 - Drilling string data

Well Identif.	Last CSG (*)	DRILL PIPES			HEAVY-WEGHT DP			DRILL COLLARS			Bit Diam (in)	Jets Size (32nd.in)	Bit Depth (ft)
		OD (in.)	ID (in.)	Length (ft)	OD (in)	ID (in)	Length (ft)	OD (in)	ID (in)	Length (ft)			
EC 213 #2	I	5	3.750	6377.	5	3	420	6 1/2	2.813	1087.	8 1/2	14 14 14	7884
VR 75 #3	S	4 1/2	3.286	2447.	4 1/2	2.750	917	8	2.812	1146.	12 1/4	15 15 15	4510
EI 151 #1	I	5	3.750	12064.	5	3	882	9	2.813	1338.	8 1/2	12 12 11	14284
SMI-160-A3	S	4 1/2	3.286	3078	4 1/2	2.750	912	7 3/4	3.0	1238.	12 1/4	16 16 16	5166

(*) S - surface

I - intermediary

L- liner

TABLE 9**4 - Open-hole formation data.**

Well Identification	Last CSG (*)	FORMATION TESTED OR BEING TESTED				OPEN-HOLE	
		TVD TOP (FT)	TVD BOTTOM (FT)	TYPE	PORE PRESS. (LB/GAL)	TEMPERATURE (°F)	TOTAL PERM. HEIGHT (FT)
EC 213*2	I	7884.	7915.	Shale ~ 80% Sand ~ 20%	9.40	157	31.0
VR 75 *3	S	4510.	4520.	Shaly Sand	9.40	125	54.0(*)
EI 151*1	I	14284.	14351.	Shale	9.60	256	67.0
SMI-160-A3	S	4775.	4805	Shale-Gumbo	8.95	127	0.

(*) Not confirmed

Computation of the calculated parameters entered into the model is explained in the following section for all the wells tested. The data listed in Tables 6, 7, 8, and 9, along with the calculated parameters, were input into the model using the data file organization described in Appendix F.

Computed Parameters

The parameters that must be computed before they can be entered into the model are Biot's constant, Poisson's ratio, surface porosity, porosity-decline constant, and Young's modulus.

Biot's Constant

Biot's constant, which generally varies from 0.7 to 0.9, is used only when the fracturing fluid is of the penetrating type. As discussed earlier, drilling muds are designed to be nonpenetrating fluids; therefore, the model doesn't use Biot's constant for drilling muds.

Poisson's Ratio

Poisson's ratio is calculated with Equation (53) as a function of depth. The depth to be used is the average true vertical depth between the top and the bottom of the formation to be fractured. This depth information is obtained by looking for the weakest formation exposed in the open-hole section. These depths are given in Table 9, and the computed Poisson's ratios are listed in Table 10.

TABLE 10

WELL IDENTIFICATION	(D _i) DEPTH OF INTEREST (ft)	(μ) POISSON'S RATIO	(θ _o) SURFACE POROSITY	(K) POROSITY DECLINE (Constant)	(E) YOUNG'S MODULUS (psi x 10 ⁶)
EC 213 #2	7890.	0.29	0.415	0.0000886	2.100
VR 75 #3	4515.	0.26	0.415	0.0000886	1.452
EI 151 #1	14318.	0.31	0.420	0.0000731	3.000
SMI-160-A3	5170.	0.24	0.415	0.0000886	1.460

Surface Porosity and the Porosity-Decline Constant

The surface porosity ϕ_0 , and porosity-decline constant, K , are obtained by the procedure explained in Appendix B and exemplified in the preceding chapter. The values of ϕ_0 and K are obtained for the well EI 215 D-1 was also used for the well EI 151 #1 since no logs are available for this well. This was felt to be a reasonable assumption because both wells were in the same general area.

The sonic log available for the well VR 75 #3 provided the data on interval transit time versus depth interval given in Table 11. The corresponding porosities were calculated using Equation (116) and are plotted as a function of depth in Figure 46. The values of ϕ_0 and K are listed in Table 10. Since no logs are available for the well EC 213 #2, the values of ϕ_0 and K were assumed to be equal to those of the well VR 75 #3.

Young's Modulus

To calculate Young's modulus with Equation (85), the engineer must know the bulk density, interval transit time, and Poisson's ratio at the depth of interest. The values of Poisson's ratio for each well are listed in Table 10. The interval transit time for the well VR 75 #3 is given in Table 11; the bulk density was obtained by combining Equations (116) and (B.3) from Appendix B. For the well EI 151 #1, the value of bulk density was obtained from the density log and interval transit time from the sonic log of the well EI 215 D-1. The Young's modulus for the well SMI 160 A-3 was calculated using

TABLE 11

DEPTH INTERVAL (ft)	INTERVAL TRANSIT TIME μ sec/ft	POROSITY	DEPTH INTERVAL (ft)	INTERVAL TRANSIT TIME μ sec/ft	POROSITY
6600-6700	117.4	0.226	9300- 9500	104.7	0.178
6700-6800	113.2	0.210	9500- 9700	102.0	0.169
6800-6900	118.0	0.229	9700- 9900	102.5	0.171
6900-7100	117.3	0.226	9900-10100	100.3	0.163
7100-7300	115.8	0.220	10100-10300	102.2	0.170
7300-7500	114.8	0.216	10300-10500	97.5	0.153
7500-7700	111.6	0.204	10500-10700	97.5	0.154
7700-7900	113.1	0.210	10700-10900	101.5	0.166
7900-8100	111.0	0.202	10900-11100	101.0	0.166
8100-8300	109.3	0.196	11100-11300	95.8	0.147
8300-8500	107.5	0.189	11300-11500	95.5	0.146
8500-8700	110.1	0.199	11500-11700	103.5	0.174
8700-8900	105.6	0.182	11700-11900	103.3	0.173
8900-9100	107.4	0.188	11900-12100	108.6	0.188
9100-9300	107.3	0.188	12100-12300	100.8	0.165
			12300-12500	98.6	0.157
			12500-12700	100.9	0.166
			12700-12900	108.5	0.193
			12900-13100	114.0	0.212
			13100-13300	125.7	0.259
			13300-13500	132.1	0.285

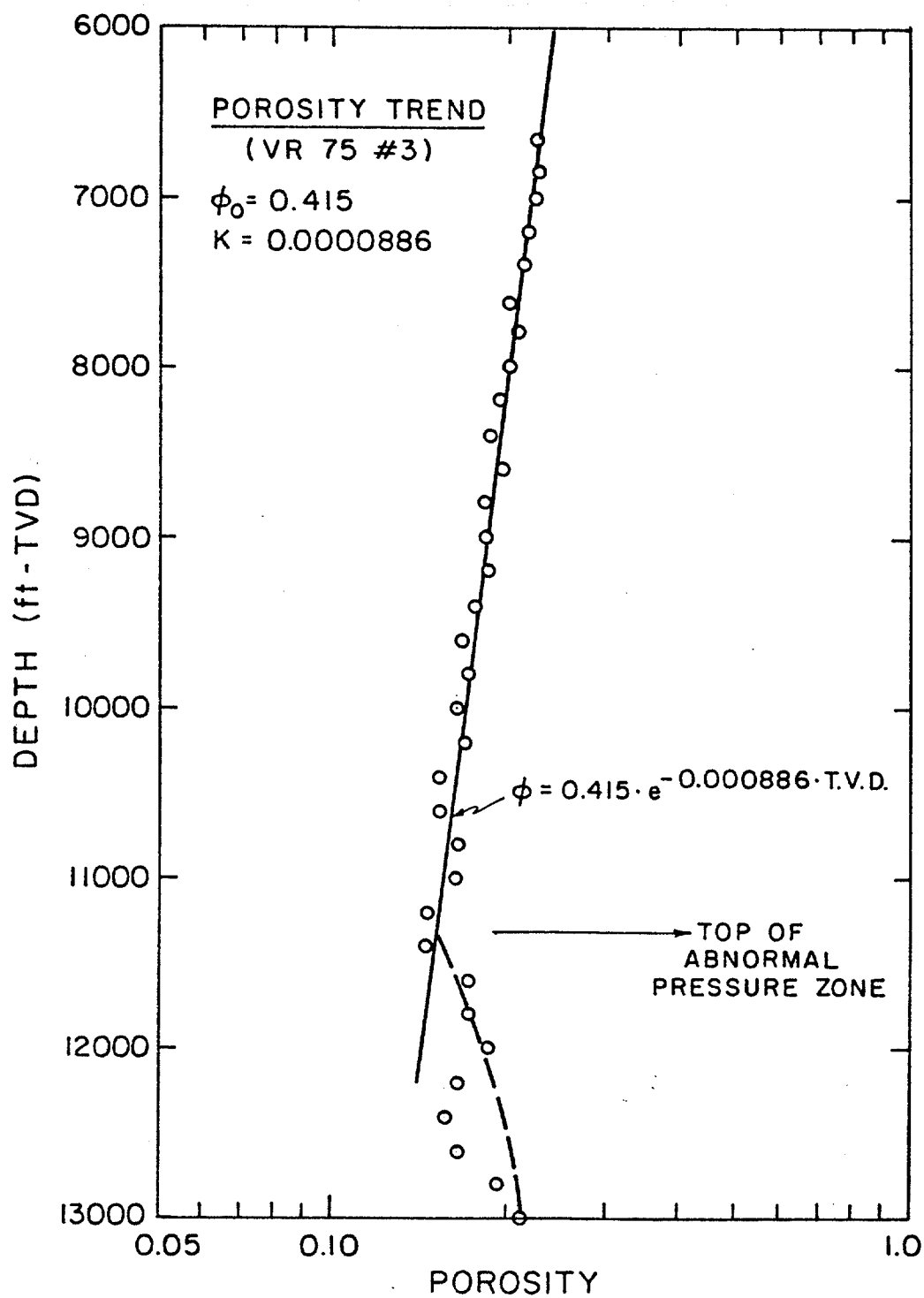


FIGURE 46 - Porosity versus depth in well VR 75 # 3.

the available log information from the well VR 75 #3. Table 10 summarizes the Young's modulus calculated for each well.

Field Data Analysis

The results of the field data analysis performed using the computer model are compared to the observed pump pressure response for each well. In the outputs presented, the solid line represents the curve simulated by the model and will be referred to as the "predicted curve"; asterisks represent the curve based on the field data points, which will be referred to as the "field data curve."

Well EC 213 #2

The computer model was run using the available data for this well to produce the output shown as RUN # 1. The lithology information available for the open-hole section of this well, 7884-7944 ft, is shown in Figure 47. It indicates that the section is predominantly composed of shale. Since the formation has a high shale content, the tensile strength was considered initially 350 psi. In addition, because of the plastic behavior of this unconsolidated shale, the borehole is expected to expand, and this expansion was accounted for in RUN # 1.

Data obtained from the drilling-morning report indicate that the well had not been circulated before the test (Table 6). Therefore, the pressure necessary to break the gel was considered more representative of pressure losses than the pressure losses due to flow. However, an examination of the straight-line trend seems to indicate that a much higher pressure was necessary to break the mud gel,

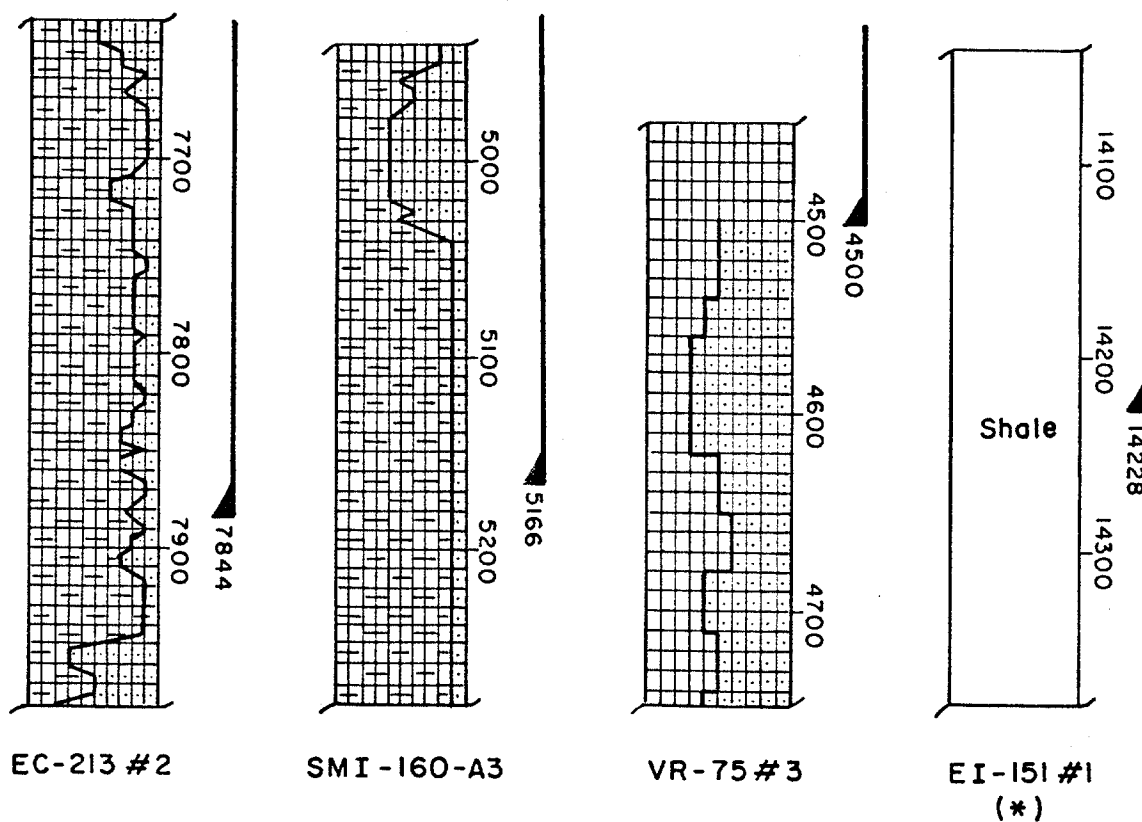
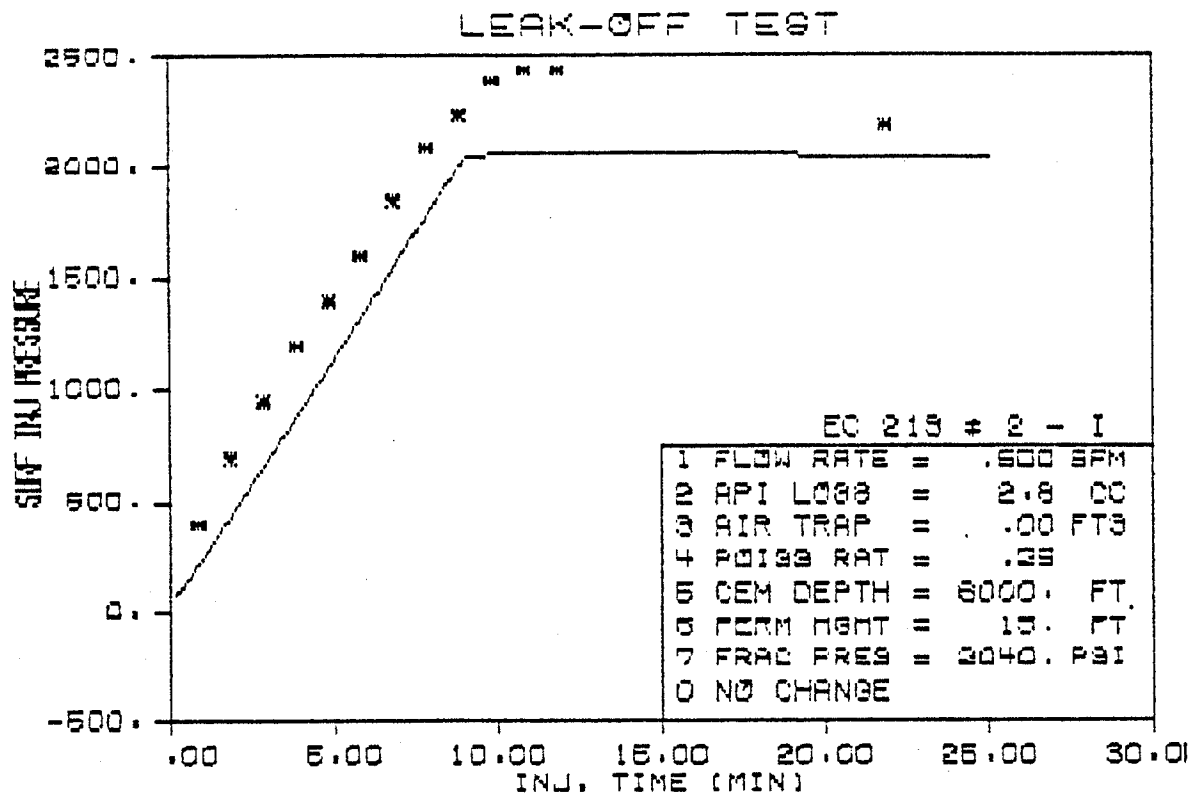


FIGURE 47 - Lithology information for well used in example leak-off test design.



INPUT/OUTPUT PARAMETERS

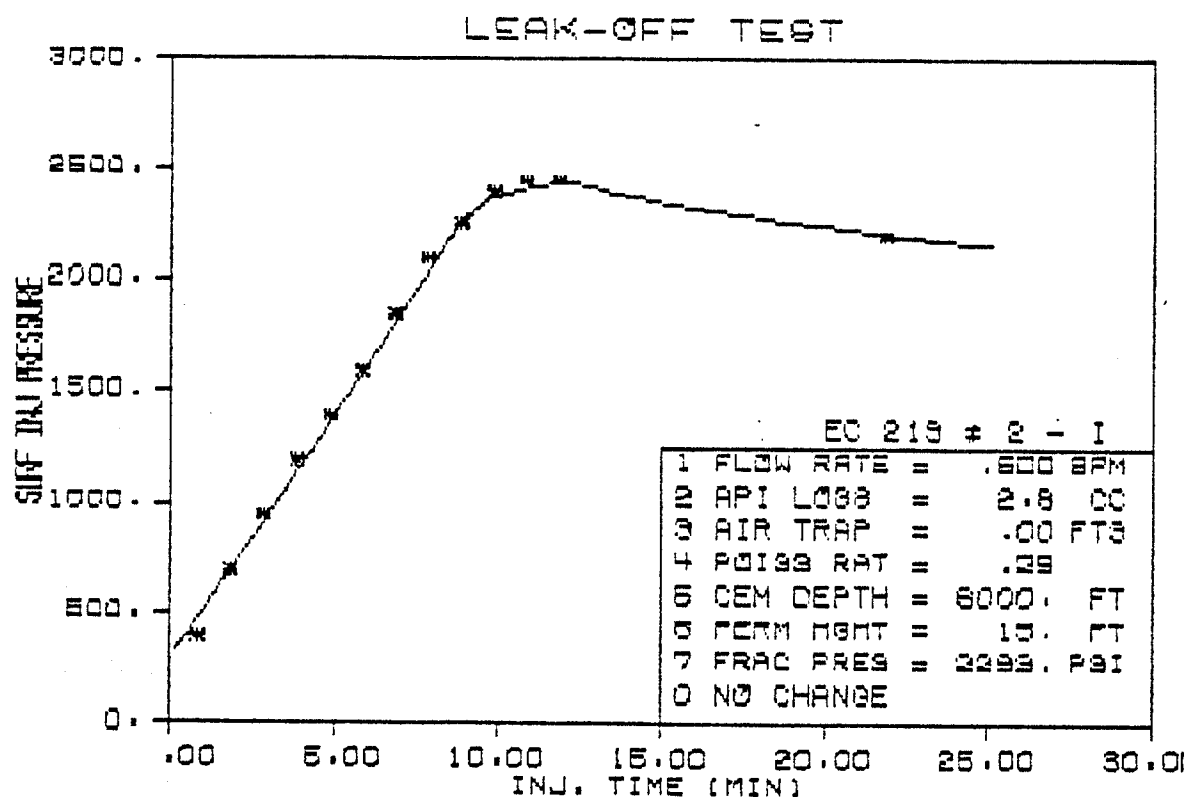
MUD DENSITY = 11.80 LB/GAL
 FLOW RATE = .50 BPM
 PORE PRESSURE = 9.00 LB/GAL
 CSG SHOE DEPTH = 7884. FT
 SECT FRAC : 7884.- 7944. FT
 FRAC GRAD EXP = 16.58 LB/GAL
 FRAC PRESS SURF = 2040.0 PSI
 VOL INJ SHUT-IN = 6.15 BBL
 FRACT HEIGHT = 60.00 FT
 FRACT WIDTH = .04044 IN
 FRACT LENGTH = 62.1 FT

RUN # 1

which suggests that the gel strength should have been much higher than that reported 6 lbf/100 ft². Another significant mismatch occurs on the fracture-expansion portion of the two curves. The predicted curve has a flat shape during the fracture expansion, whereas the field data curve has a well-defined curvature. The flat shape occurs only when the fluid loss rate through the fracture walls is high, or the fracture is of great height. A high fluid loss rate is not possible because the formation is practically impermeable, and consequently, the fracture height initially assumed, 60 ft, should be much smaller.

The fracture height was reduced to 15 ft, which corresponds to the height of a section exactly below the casing seat that has the highest sand content in the open-hole section, approximately 30 percent, as shown in Figure 47. In fact, because of the high sand content, this section should be the weakest one exposed. The effects of the changes discussed above are shown in RUN # 2. The curves show a good match, especially in the fracture-expansion portion of the curve. Interestingly, fracture pressures were matched without any variable being changed specifically for this purpose. In addition, the only field data point recorded during the pressure-decline period falls exactly on the predicted pressure-decline line. This indicates the correctness of the fluid-loss coefficient and permeable height entered into the model.

The fracture pressure obtained is 2293 psi, which corresponds to the fracture gradient of 16.58 lb/gal. The fracture geometry, after the injection of approximately 6.15 bbl of drilling mud, appears on the output plot RUN # 2 along with other important information.



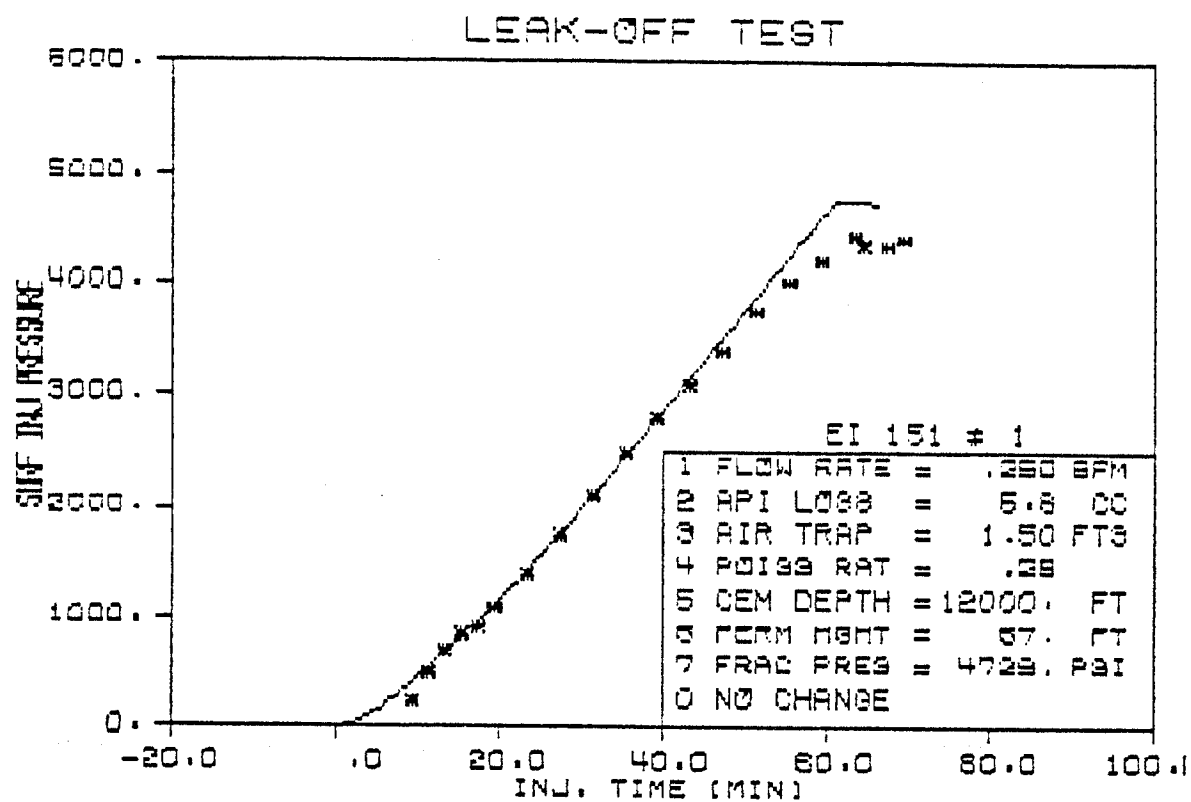
INPUT/OUTPUT PARAMETERS

MUD DENSITY = 11.80 LB/GAL
 FLOW RATE = .50 BPM
 PORE PRESSURE = 9.03 LB/GAL
 CSG SHOE DEPTH = 7884. FT
 SECT FRAC : 7884.- 7899. FT
 FRAC GRAD EXP = 16.58 LB/GAL
 FRAC PRESS SURF = 2293.2 PSI
 VOL INJ SHUT-IN = 6.15 BBL
 FRACT HEIGHT = 15.00 FT
 FRACT WIDTH = .05508 IN
 FRACT LENGTH = 213.9 FT

Well EI 151 # 1

Field data were analyzed with the computer model to produce the curve match shown as RUN # 3. At the beginning of the test the field data curve shows a slight curvature, which suggests that some air was trapped in the system during the test. This portion of the curve was matched by the predicted curve when a volume of 1.5 ft³ of air was entered as trapped in the system. Lithology information for the open-hole section indicates the presence of unconsolidated shale of the type shown in the field as shale gumbo. This type of formation is characterized by a plastic behavior, which is confirmed in RUN # 3 by the match obtained on the straight-line portion of the curve. This match was obtained when the borehole expansion due to plastic formations in the model was considered.

However, the upper part of the field data curve could not be matched. The predicted curve shown in RUN # 3 was obtained when Poisson's ratio was decreased from 0.30 to 0.28. Poisson's ratio could have been decreased until the fracture pressures matched. But a Poisson's ratio lower than 0.28 would be out of the common range for the area and depth being considered. The curves indicate that the upper field data points do not follow the straight-line trend of the predicted curve, but depart from it at about 3500 psi. The fact that this pressure could not be matched by varying the parameters over a reasonable range suggests that a leak in the cement occurred and that more shallow, weaker formations might have been fractured by mud channeling through the cement.



INPUT/OUTPUT PARAMETERS

MUD DENSITY = 10.10 LB/GAL
 FLOW RATE = .25 BPM
 PORE PRESSURE = 9.55 LB/GAL
 CSG SHOE DEPTH = 14284. FT
 SECT FRAC : 14284.- 14351. FT
 FRAC GRAD EXP = 16.44 LB/GAL
 FRAC PRESS SURF = 4729.4 PSI
 VOL INJ SHUT-IN = 16.10 BBL
 FRACT HEIGHT = 67.00 FT
 FRACT WIDTH = .02000 IN
 FRACT LENGTH = 29.8 FT

RUN # 3

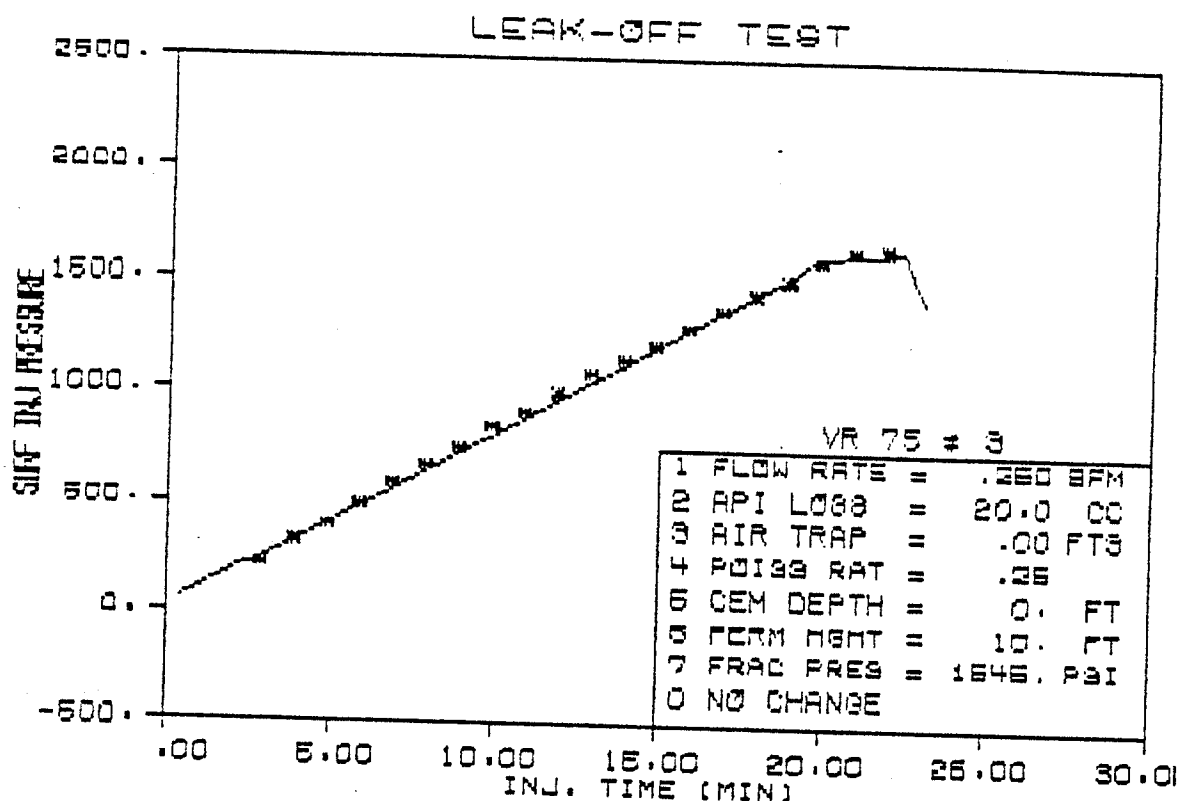
Well VR 75 # 3

The curve match obtained between the predicted pressure curve and the field data curve is shown in RUN # 4. The lithology information available for this well indicates that the open-hole section is composed of shaly-sand. The intervals from 4510 to 4520 ft and from 4548 to 4564 ft show cleaner sands than occur in the rest of the interval. The straight-line trend of the pressure curve was matched by adjusting for an enlargement of the well-bore section due to the presence of plastic formations. In this case, a portion of the open hole section was assumed to have a high shale content with a tensile strength of 350 psi. This value lies within the common range for shale (0-500 psi).

The fracture was assumed to occur in the cleanest sand situated in the interval between 4510 and 4520 ft, right below the casing seat. The good match obtained for the fracture-expansion portion of the curve, approximately 19-22 min, confirms the assumption. The fracture pressure at surface in RUN # 4 is 1545 psi, which corresponds to a fracture gradient of 15.85 lb/gal. Other important information is also printed in RUN # 4.

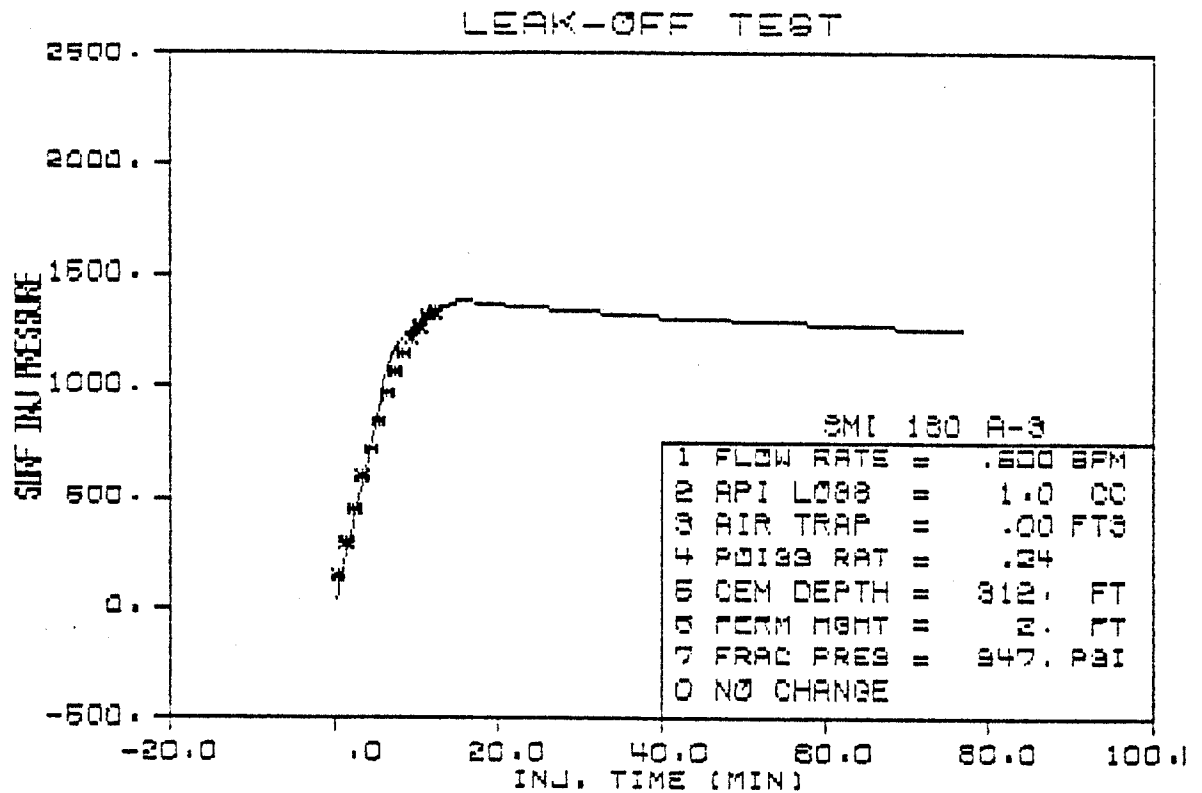
Well SMI 160 A-3

RUN # 5 shows the match obtained for the field data of the well SMI 160 A-3. The match was obtained by assuming a fracture height of 6 ft right below the casing seat. In addition, since the formation is practically 100 percent shale gumbo, the fluid loss to the formation was considered negligible and the API water loss was set equal to 1 cm^3 . The fracture pressure obtained at surface is 947 psi,



INPUT/OUTPUT PARAMETERS

MUD DENSITY = 9.50 LB/GAL
 FLOW RATE = .25 BPM
 PORE PRESSURE = 9.38 LB/GAL
 CSG SHOE DEPTH = 4510. FT
 SECT FRAC : 4510.- 4520. FT
 FRAC GRAD EXP = 15.85 LB/GAL
 FRAC PRESS SURF = 1544.9 PSI
 VOL INJ SHUT-IN = 5.60 BBL
 FRACT HEIGHT = 10.00 FT
 FRACT WIDTH = .02825 IN
 FRACT LENGTH = 60.3 FT



INPUT/OUTPUT PARAMETERS

MUD DENSITY = 9.60 LB/GAL
 FLOW RATE = .50 BPM
 PORE PRESSURE = 8.38 LB/GAL
 CSG SHOE DEPTH = 5166. FT
 SECT FRAC : 4775.- 4781. FT
 FRAC GRAD EXP = 13.25 LB/GAL
 FRAC PRESS SURF = 946.6 PSI
 VOL INJ SHUT-IN = 7.70 88L
 FRACT HEIGHT = 6.00 FT
 FRACT WIDTH = .07109 IN
 FRACT LENGTH = 1290.5 FT

which corresponds to a fracture gradient of 13.25 lb/gal. The fracture width at the well bore is 0.07109 in. Other information is printed in the output RUN #5.

Sensitivity Analysis of the Model

The sensitivity analysis presented in this section was performed with the data available from the wells EC 213 # 2 and EI 151 # 1. The effect of changing one variable in the computer model, while keeping the others constant, will be discussed in this section. The main variables included in the sensitivity analysis are (1) flow rate, (2) Poisson's ratio, (3) bulk shear modulus, (4) fracture height, (5) rock mechanics behavior, (6) pore pressure, (7) mud viscosity, (8) well diameter, (9) cement-top depth, (10) microannulus width, and (11) API water loss. Other parameters that affect the pressure behavior at surface during a leak-off test are also included in the model. Most of these parameters are included in the fracture geometry of the well, mud properties, and drill-string geometry and therefore are known to a high degree of accuracy. A sensitivity analysis was performed only for those parameters that cannot be easily defined or selected.

Flow Rate

The effects of flow-rate changes on pressure behavior at surface are shown in Figure 48. Increasing the flow rate causes the fracture pressure of the formation to be reached sooner, which consequently increases the slope of the straight-line trend. The increase in flow rate also causes an increase in pressure during fracture expansion. This is due to the increase in pressure drop in

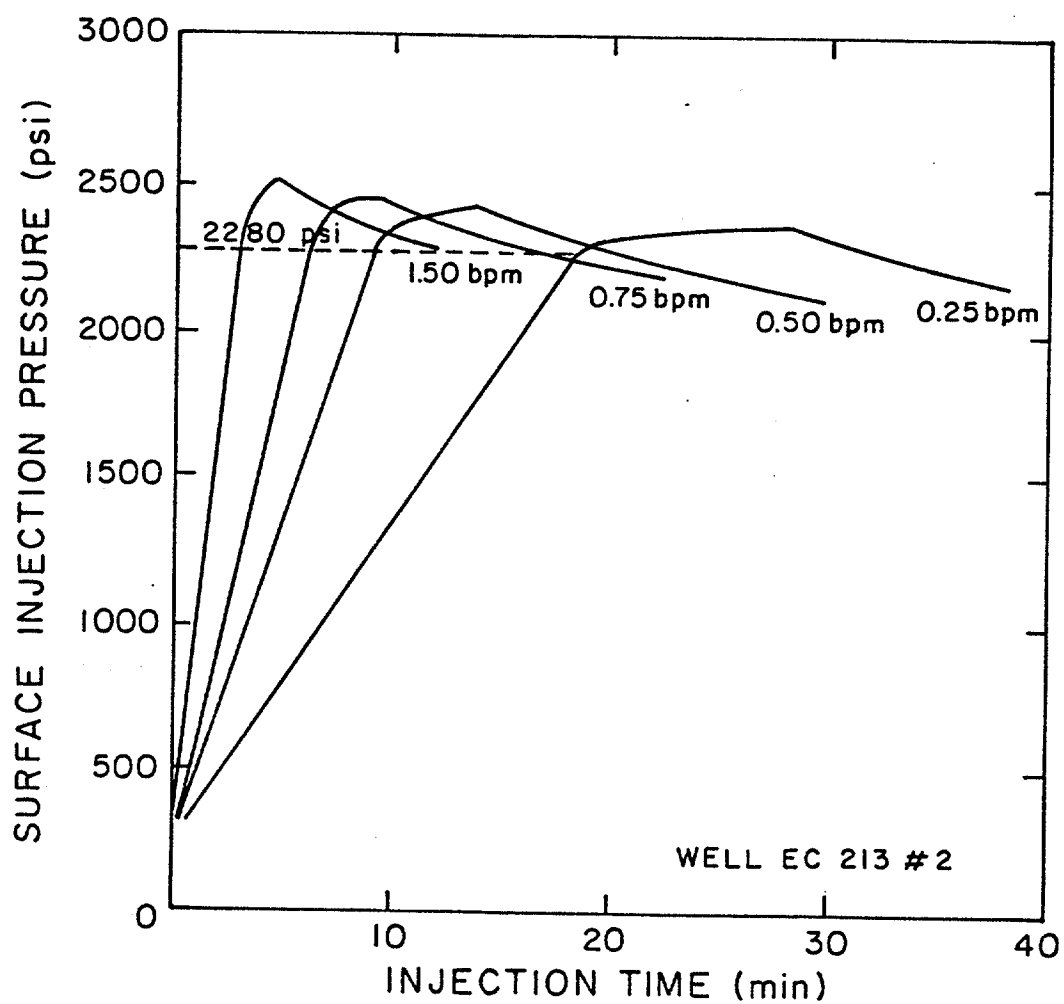


FIGURE 48 - Pressure versus time for various flow rate.

the fracture. The pressure-decline curve is also affected by flow rate, as expected, since during this period the pump is shut off.

Poisson's Ratio

Figure 49 shows how changing Poisson's ratio affects the pressure behavior of the curve. Fracture pressure is very sensitive to variations in Poisson's ratio. An increase in Poisson's ratio from 0.24 to 0.28 in this example causes the fracture pressure to increase by approximately 450 psi.

Equation (73) relates pressure during fracture expansion to Poisson's ratio. According to that equation, an increase in Poisson's ratio causes an increase in pressure. However, this pressure increase is small, as shown by the plot in Figure 49. Pressure decline is not very sensitive to changes in Poisson's ratio; according to Equation (110), an increase in Poisson's ratio causes a slight increase in the rate of pressure decline.

Bulk Shear Modulus

Equation (86) directly relates the bulk shear modulus to Young's modulus. Thus, the sensitivity analyses are the same for both parameters. Young's modulus is related to the overall compressibility of the system through the stress-strain relations for elastic, plastic, and elastic-plastic rock behavior. These relations are given in Appendix G. An increase in Young's modulus will cause a decrease in strain in the open-hole section. This decrease in strain is translated into less expansion of the borehole and consequently

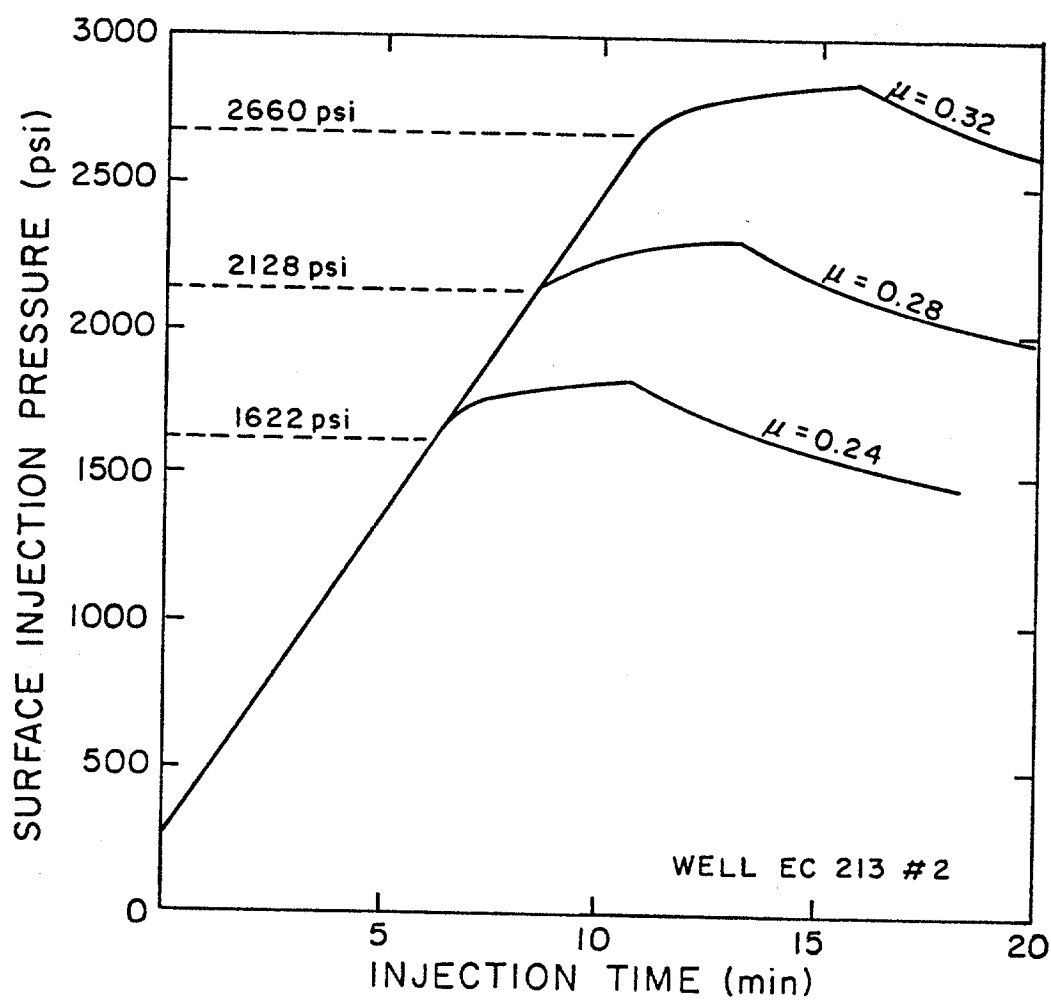


FIGURE 49 - Pressure versus time for various Poisson's ratio.

implies a higher rate of pressure increase before fracture initiation (Figure 50).

During fracture expansion, the pressure is directly related to the bulk shear modulus. However, in the proposed model, the exponent of the bulk shear modulus is always less than 1. Therefore, the rate of pressure increase is not very sensitive to changes in the bulk shear modulus.

On the other hand, during the pressure-decline period, pressure is very sensitive to changes in the bulk shear modulus. The exponent of the bulk shear modulus is 1 during this period. Figure 50 shows how changing the bulk shear modulus effects pressure behavior.

Fracture Height

The fracture height, h , naturally does not affect pressure behavior before fracture initiation or the fracture-pressure value itself. During fracture expansion, however, changes in fracture height greatly affect pressure behavior. Figure 51 shows that this is especially true when the fracture height is small. During the pressure-decline period, the ratio between the permeable portion of the total fracture height and the fracture height itself greatly influences the pressure behavior of the curve. In Figure 51, the permeable height is fixed to equal 5 ft. As fracture height decreases, the ratio between the two heights increases, and consequently the pressure declines faster. This can also be deduced by examining Equation (110).

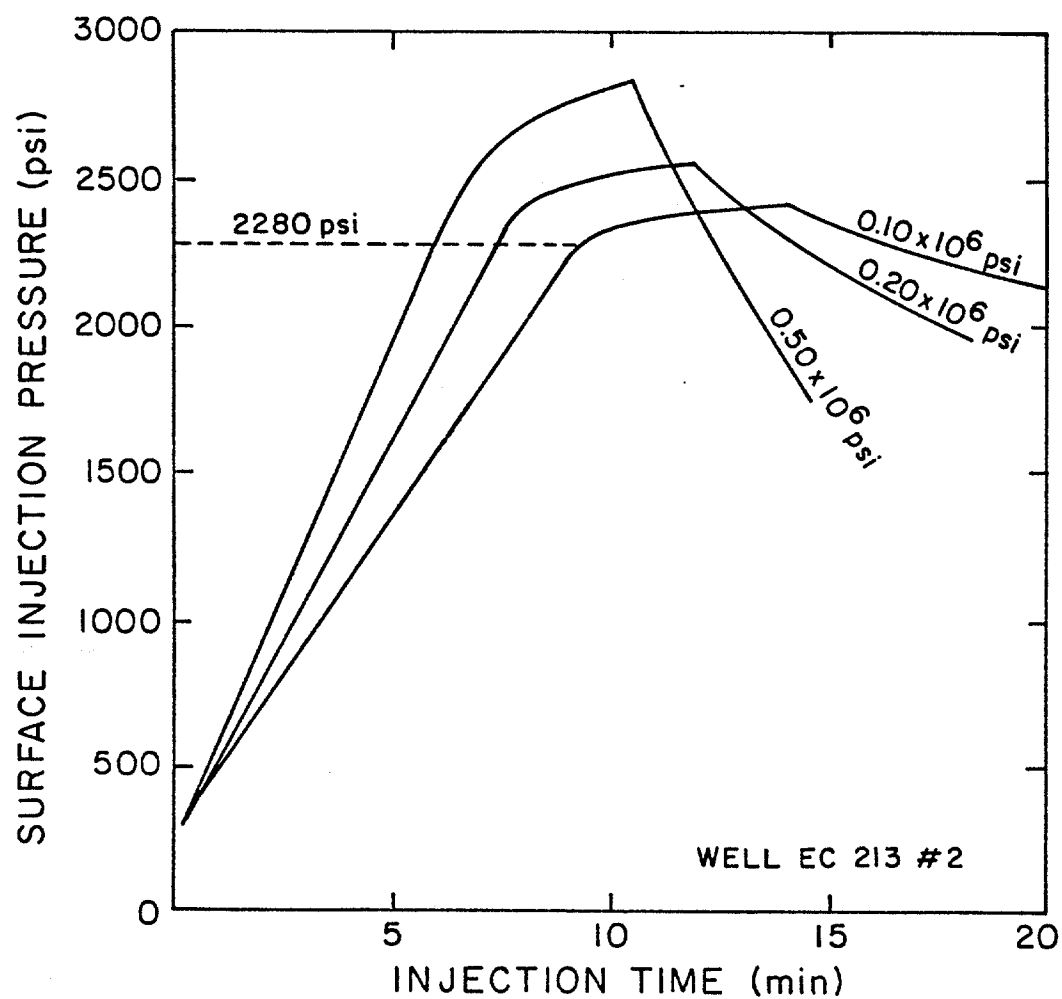


FIGURE 50 - Pressure versus time for various bulk shear moduli.

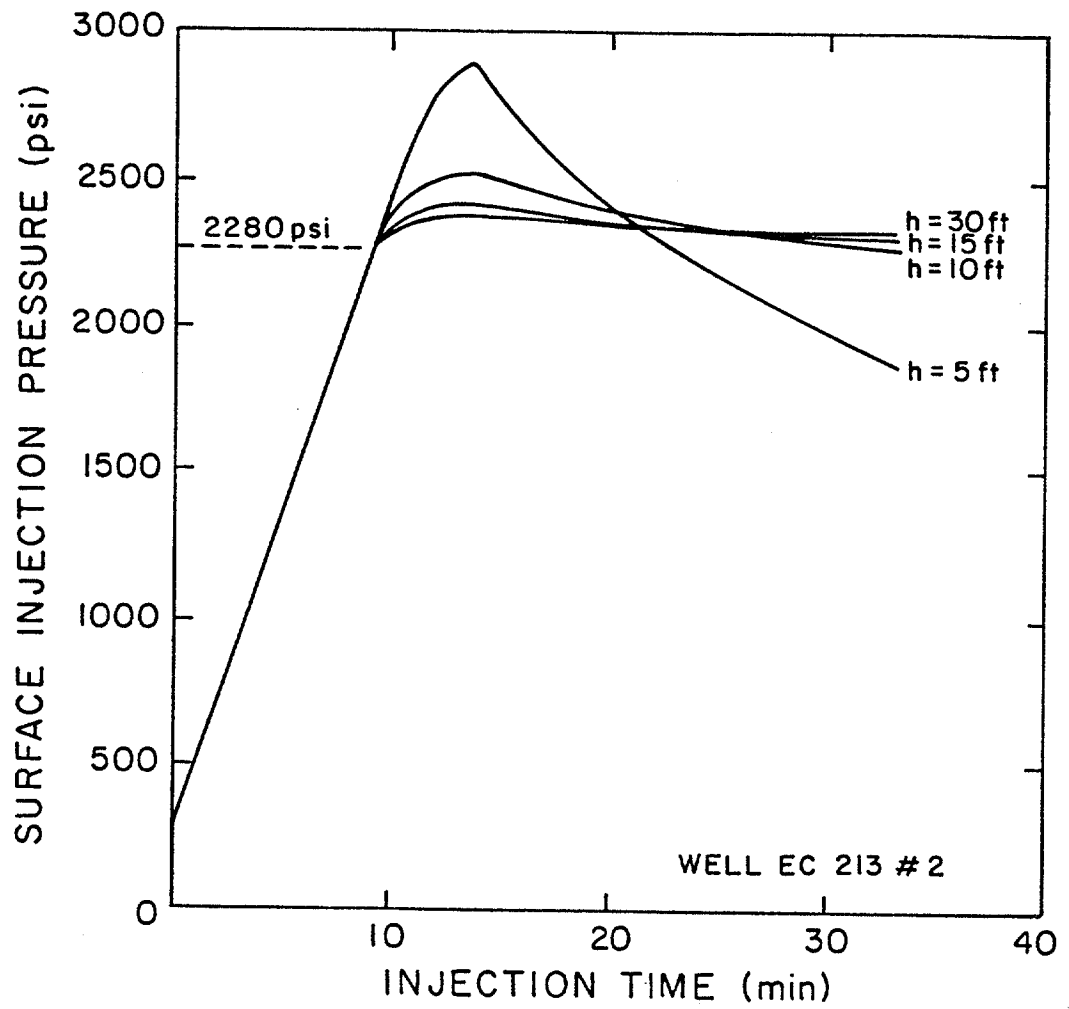


FIGURE 51 - Pressure versus time for different fracture heights.

Borehole Expansion Model

Figure 52 shows the effects of the borehole expansion model on surface injection pressure during a leak-off test. In Figure 52, R/R_1 is the ratio between the radius of the transition from the zone of plastic behavior to the zone of elastic behavior and the well-bore radius, R_1 . These two radii are shown in Figure 30, the overall compressibility model. This ratio determines how far the plastic region extends from the well bore. The perfect elastic state of stress exists throughout the formation when $R/R_1 = 1$. Increasing the plastic region (increasing R/R_1) reduces the rate of pressure increase before fracture initiation. This occurs because the enlargement of the borehole affects the overall compressibility of the system.

Pore Pressure

Pore pressure affects only the fracture pressure obtained. An increase in pore pressure causes an increase in fracture pressure and vice-versa. Figure 53 shows how varying the pore pressure gradient affects the pressure behavior of the curve.

Mud Viscosity

Mud viscosity affects the surface injection pressure during fracture expansion. In the proposed model, pressure is directly related to mud viscosity raised to an exponent much smaller than unity. Therefore, variations in mud viscosity essentially do not affect the shape of the pressure curve predicted by the computer model.

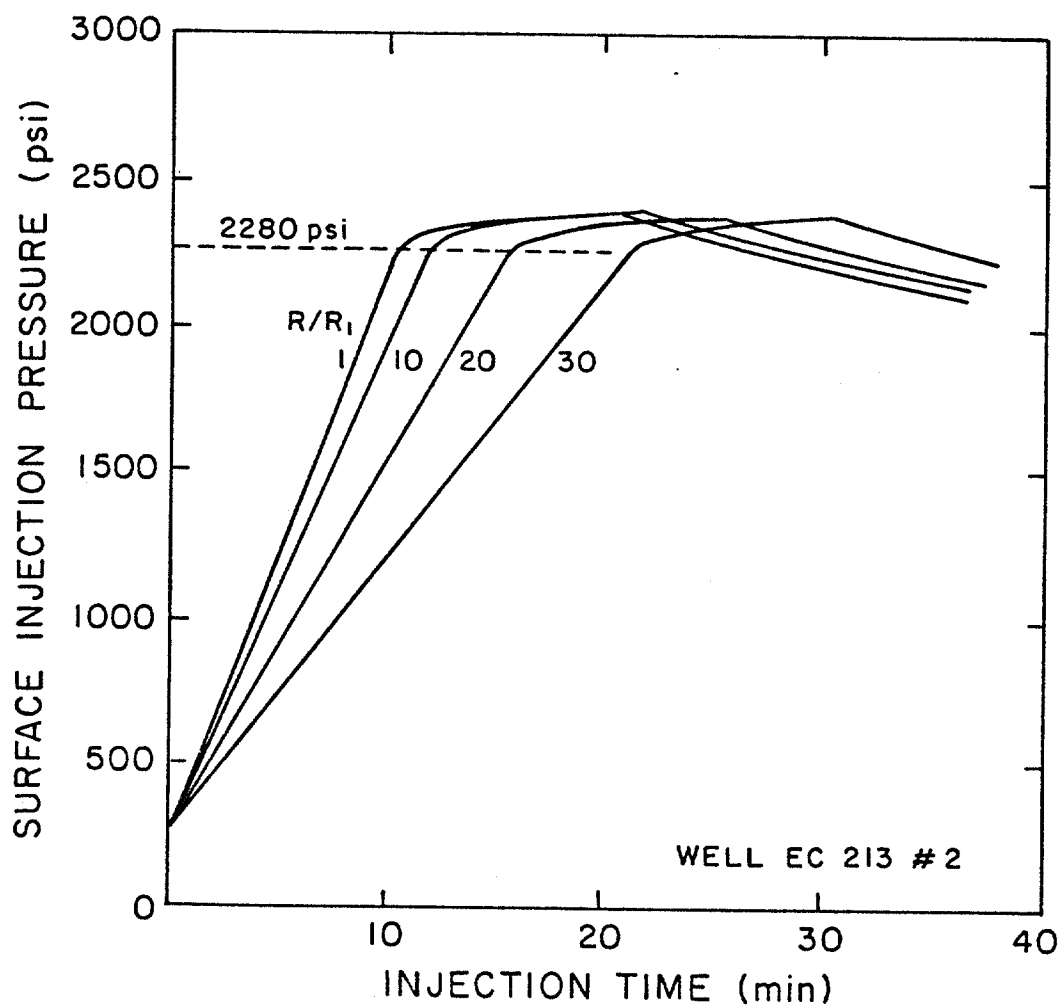


FIGURE 52 - Pressure versus time for various ratios between the elastic-plastic transition radius and the well-bore radius.

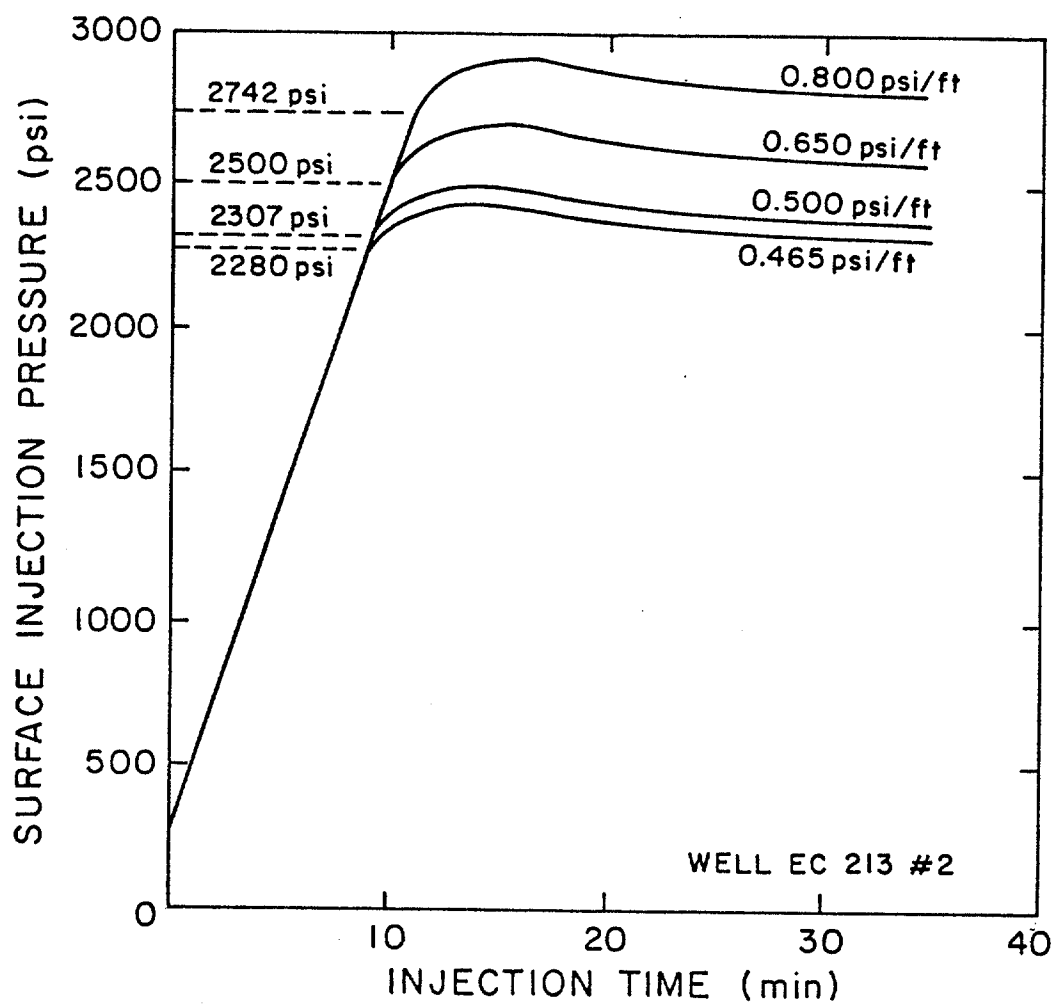


FIGURE 53 - Pressure versus time for various pore pressure gradients.

During the pressure-decline period, the mud filtrate viscosity is assumed to be equal to the pore fluid viscosity; therefore the mud filtrate viscosity does not affect the rate of pressure decline. Figure 54 shows how a change in mud viscosity from 10 to 30 cp affects the pressure behavior of the predicted curve.

Well Diameter

As shown by Figure 55, the well diameter only affects the portion of the curve recording the period before fracture initiation. This was expected, since well diameter is included in the equation of the rock strain, which was shown to greatly affect that part of the predicted pressure curve. For a given diametral strain (the ratio between the enlarged and the original diameter), an increase in diameter is expected to increase the hole enlargement volume, which causes a lower rate of pressure increase. This is confirmed by the plot in Figure 55.

Top-of-Cement Depth

The plot in Figure 56 shows that for the depth of the top of the cement outside the last casing to affect the pressure predicted by the model, the noncemented sections must be greater than about 7000 ft. The effect shown for a 14,000-ft noncemented section, an unusually long one, is very small. Therefore, neglecting this effect in the model would not cause major errors.

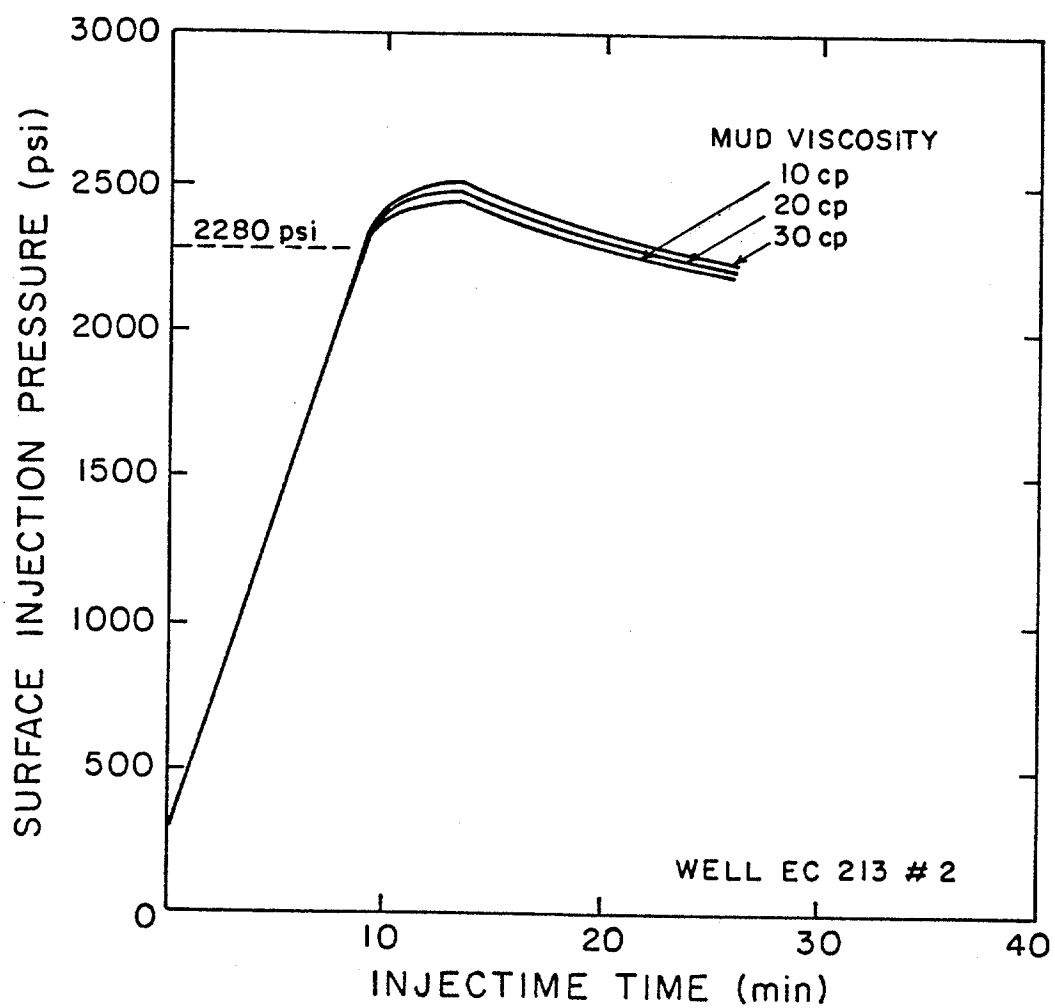


FIGURE 54 - Pressure versus time for various mud viscosities.

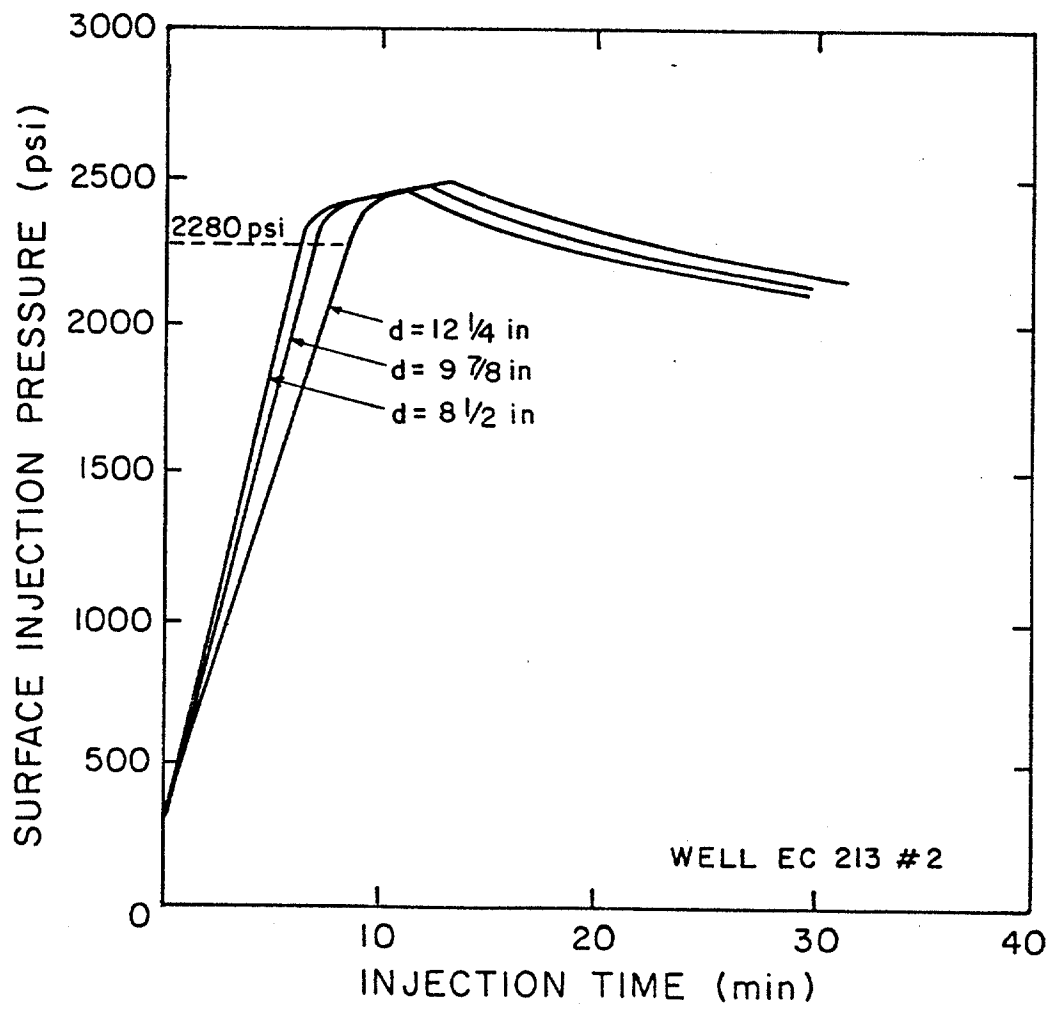


FIGURE 55 - Pressure versus time for various well diameters.

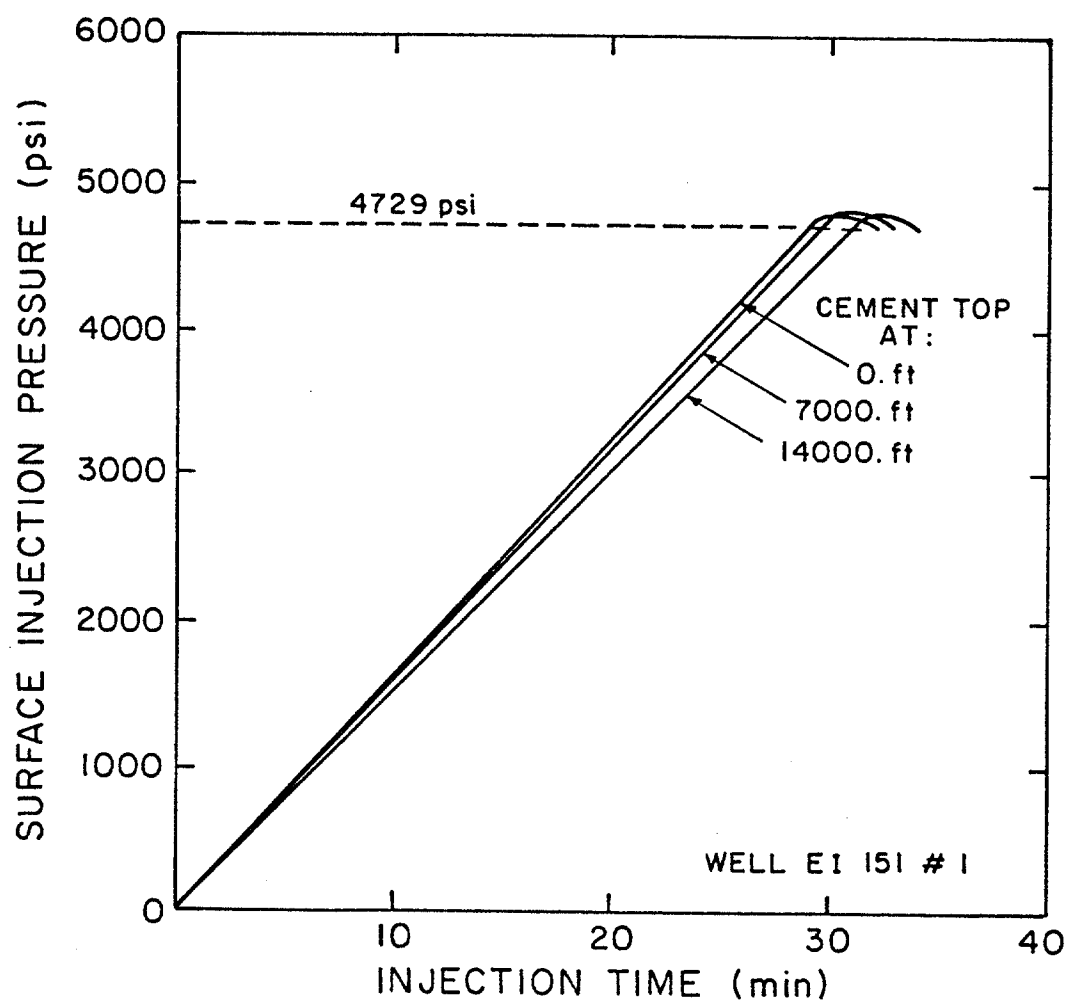


FIGURE 56 - Pressure versus time for various lengths of casing cement.

Microannulus

The effect of a microannulus on the pressure behavior of the predicted curve is shown in Figure 57 for a casing completely cemented up to the surface. The casing is 7884 ft long, and normally microannuli provide less than 0.01 in. of diameter clearance. Figure 57 shows the two extremes in terms of clearance for this situation. It can be seen from the figure that a microannulus can significantly affect pressure behavior if the microannulus occurs in a long cemented section of casing, and the clearance is very large.

Water Loss

Figure 58 shows how cumulative filtrate varies with time for different API water loss values. The fluid loss to the formation within a given period of time is great during the early stage of filtration. After the mud cake has been built, a lower filtration rate is observed. In fact, Figure 58 shows that for an API of 10 cm^3 , approximately 0.0074 bbl of fluid will be lost between 60 and 70 min after filtration is started. For a 10-min interval at the beginning of filtration, however, the volume lost is approximately 0.036 bbl, which is five times greater than the loss 60 min after filtration has begun. During a leak-off test, the permeable formations have been exposed for longer than 60 min because of drilling and circulation time. Therefore, the additional filtrate volume lost during the test is expected to be very low. The practically negligible decrease in pressure before fracture initiation shown in Figure 59, which is caused by an increase in API water loss, confirms this.

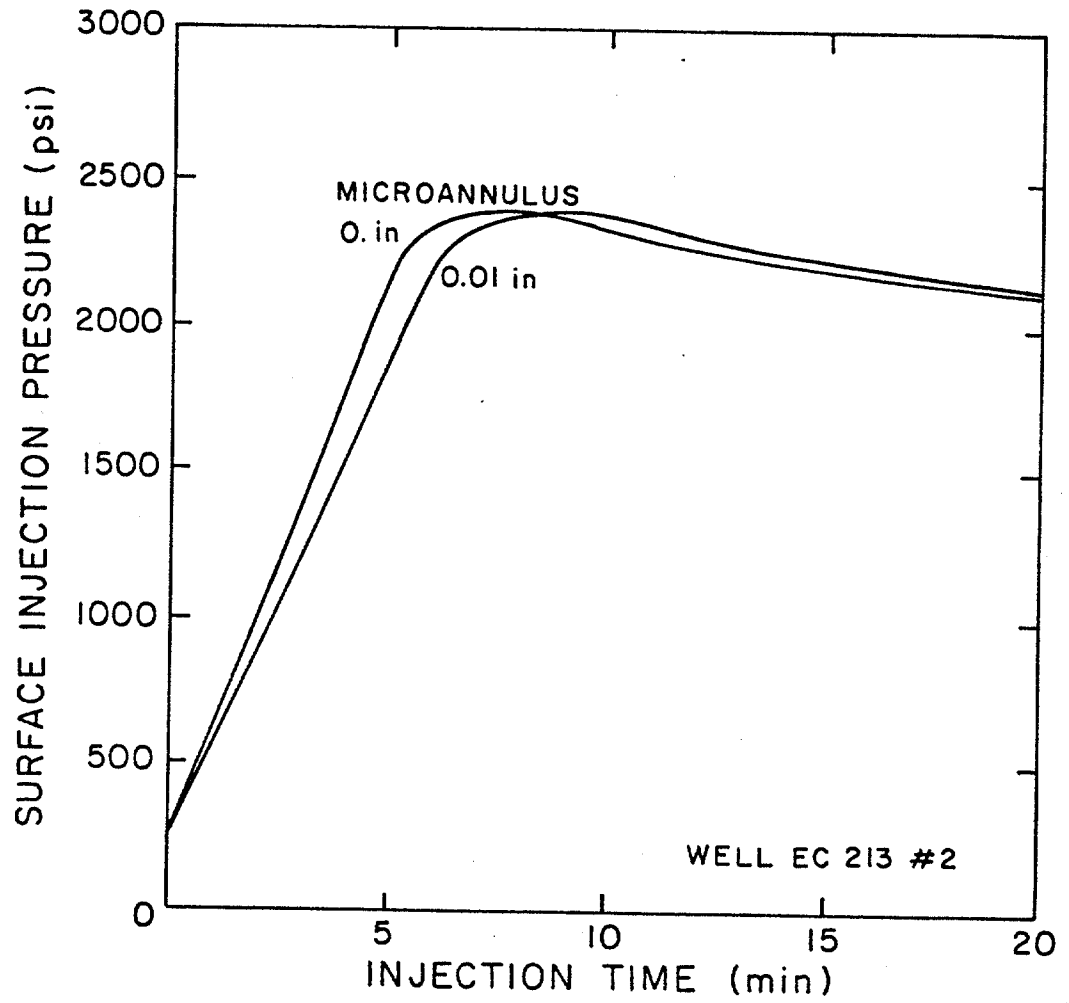


FIGURE 57 - Pressure versus time for various micro-annulus clearances.

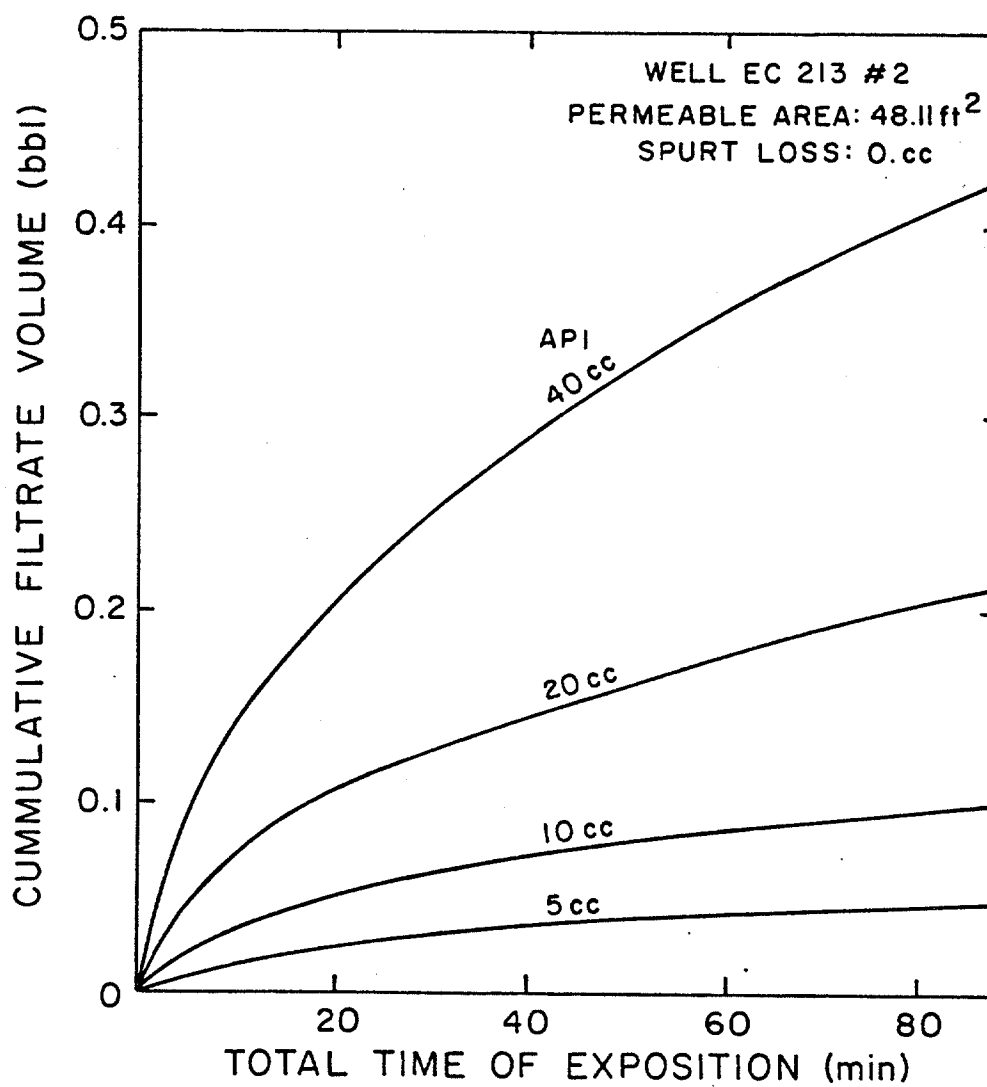


FIGURE 58 - Cumulative filtrate volume versus total time of exposure.

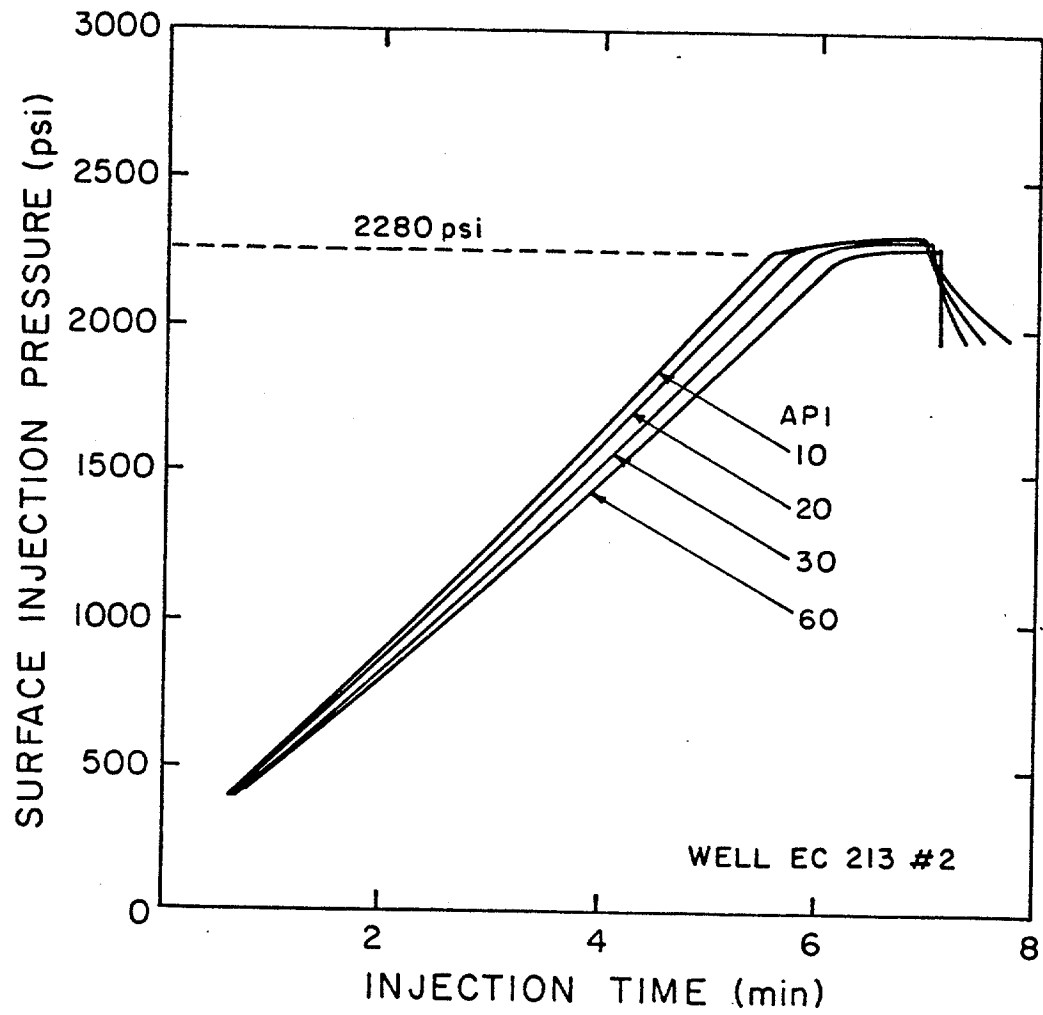


FIGURE 59 - Pressure versus time for various API water loss values.

During fracture expansion the effect of changing API water loss on pressure is not very significant. This is because the pressure is related to API water loss raised to an exponent between 0 and -1. Figure 59 shows that an increase in API water loss practically does not affect the fracture-expansion portion of the curve. However, this increase will greatly affect the fracture width and length obtained, as indicated by Equations (77) and (80).

During the pressure-decline period, the effect of changing API water loss is more significant. The rate of pressure decline is directly proportional to API water loss. Thus, if the API water loss value doubles, the rate of pressure decline also doubles.

SUMMARY AND CONCLUSIONS

A reliable computer simulation model for formation pressure-integrity tests has been developed. The computer model is based on a mathematical model that takes into account the many factors that affect pressure behavior. The model was developed by subdividing the formation pressure-integrity test, or leak-off test into four phases: (1) pressure increase due to change in the overall compressibility of the system, (2) formation breakdown when the fracture is initiated, (3) fracture expansion, and (4) pressure decline and fracture closure after the pump is shut in.

The mathematical model for predicting injection pressure before fracturing includes the most important variables affecting overall compressibility of the system: mud compressibility, casing expansion, well-bore expansion, fluid loss to permeable formations, and volume of air accidentally trapped in the system. The fracture pressure is determined with the equations derived from the elasticity and plasticity theory for a hole in the middle of an infinite plate.

A fracture-expansion model for an elliptical crack propagating in an elastic, isotropic, homogeneous formation has been proposed for use in modeling pressure variation with time during the fracture-expansion period. This model is based on three different approximated solutions for the continuity equation of flow: (1) large fluid-loss approximation, (2) no fluid-loss approximation, and (3)

numerical solution approximation. Each solution is used according to its dimensionless time range of validity.

The solution of the continuity equation for flow has also been used to model the pressure-decline period after the pump is shut in. The computer simulation program was written on the basis of these four mathematical models.

The computer model was verified using field data from offshore of the Louisiana Gulf Coast furnished by the offshore division of Tenneco Oil Company. A curve-matching technique was applied to analyze the field data with the computer model. An example showing how the computer model can be used for leak-off test design was also presented.

Conclusions

The following conclusions are made on the basis of the sensitivity tests conducted:

1. The most important parameters affecting fracture-initiation pressure are Poisson's ratio, tensile strength, overburden stress, pore pressure, and fluid type (penetrating or nonpenetrating).
2. The most important parameters affecting the pressure-time slope of a pressure-integrity test are flow rate, API water loss, volume of air accidentally trapped in the system, top-of-

cement depth, well diameter, and rock mechanics behavior of the formation (expressed by the ratio R/R_1).

3. The least important parameter affecting the pressure-time slope is the microannulus.

4. The most important parameters affecting the pressure-time relationship during fracture expansion are fracture height, bulk shear modulus, flow rate, and Poisson's ratio.

5. The mud viscosity and the API water loss parameters do not affect the pressure-time relationship significantly during the fracture-expansion period.

6. The most important parameters affecting the pressure-time relationship during the fracture-closure period are API water loss, bulk shear modulus, Poisson's ratio, and the ratio between the fracture permeable height and fracture height.

The following conclusions are made on the basis of the field data analysis:

1. The low pressure-time slope shown by pressure-integrity tests performed in predominantly unconsolidated shale lithology can be explained by the enlargement of the well bore due to the plastic behavior of this formation.

2. The well-bore enlargement, calculated using the stress-strain relations from the elasticity theory, is always smaller than the enlargement calculated using the elastic-plastic stress-strain relationship. The rock strain equation derived for the elastic-plastic case is a function of the ratio between the extension radius of the plastic region and the well-bore radius, R/R_1 .

3. The ratio R/R_1 for the relatively shallow gumbo-shale lithology encountered in the Gulf Coast area was found to vary between 15 and 28. This range was found using the available leak-off test data from the range of 2300-13000 ft. A ratio equal to 1 should be used for rocks having a purely elastic behavior.

4. A pressure-integrity test that has an early concave upward pressure-time relationship indicates the presence of air trapped in the piping system connected to the pump outlet or in the annular below the kelly-bushing.

5. A pressure-integrity test that has a concave upward pressure-time relationship all the way up to the fracture-initiation pressure indicates that the fluid-loss rate to permeable formations is very high.

6. A pressure-integrity test that in which a concave downward pressure-time relationship occurs much earlier than the

fracture pressure predicted indicates a cement leak or a casing leak.

7. A pressure-integrity test showing a constant pressure as a function of time after the pump has been shut in indicates that only impermeable formations are present in the open-hole section.

8. A pressure-integrity test showing the pressure-time curve displaced upward from the origin indicates that this displacement corresponds to the pressure losses in the system. The pressure losses in the system can be representative of the pressure required to break the mud gel strength if the well has not been circulated before the test, or they can be an indication of pressure losses due to the flow of the drilling fluid.

Recommendations

1. Among the many factors affecting the pressure behavior during a formation pressure-integrity test, the microannulus effect was proved by the sensitivity analysis to be negligible. In future work, the model can be simplified by eliminating the microannulus effect.

2. The tensile strength of rocks has been neglected in most of the fracture-pressure correlations developed in the past. In the fracture-pressure prediction equations derived in this work, however, the tensile strength significantly affects the fracture pressure obtained. Although it is almost impossible to measure this parameter under well conditions, an attempt should be made to estimate it by the history matching technique presented in this work for different formations and depths within a given area of drilling activity.

NOMENCLATURE

English

C	=	Fluid-loss coefficient, $\text{ft}/\text{min}^{1/2}$
C_{AVG}	=	average compressibility (constant temperature), psi^{-1}
c_m	=	mud compressibility, psi^{-1}
c_o	=	oil compressibility, psi^{-1}
c_s	=	solids compressibility, psi^{-1}
c_w	=	water compressibility, psi^{-1}
d	=	well-bore diameter, in
D	=	depth, ft
E	=	Young's Modulus, psi
G	=	Bulk-shear Modulus, psi
h	=	fracture height, ft
h_p	=	fracture-permeable height, ft
K	=	porosity-decline constant
L	=	total or final fracture length, ft
m	=	time exponent, dimensionless
n	=	Power-law exponent, dimensionless
N_{Re}	=	Reynolds number, dimensionless
P	=	pressure at fracture entrance, psi
P_e	=	pressure above closure pressure, psi
P_f	=	fracture pressure, psi
P_g	=	pressure to break the gel, psi

- P_o = original formation pore pressure, psi
 P_p = pore-fluid pressure, psi
 P_w = well-bore pressure, psi
 q = total flow rate, bpm
 q_i = flow rate at the fracture entrance, bpm
 q_L = fluid loss rate per unit of area, bbl/ft²
 R, r = radius, in
 S_{xx}, S_{yy}, S_{zz} = total principal stresses, psi
 S_t = formation-tensile strength, psi
 S_o = oil concentration, dimensionless
 S_s = solids concentration, dimensionless
 S_w = water concentration, dimensionless
 S_z = overburden stress, psi
 T = temperature, °C or °F as noted
 t = time, min
 t_o = total time at shut-in, min
 V = total mud volume, bbl
 V_f = volume of mud filtrate, bbl
 V_{sp} = spurt-loss volume, bbl
 W = fracture width, ft
 x = distance from the fracture entrance to a point in the fracture, ft
 x_o = distance from the fracture entrance to the tip of the fracture, ft
 ΔD = change in borehole diameter, in
 ΔP = change in pressure, psi

Greek

- δ = $\Delta t/t_0$
 \emptyset = porosity, dimensionless
 \emptyset_0 = surface porosity, dimensionless
 μ = Poisson's ratio, dimensionless
 ν = mud viscosity, cp
 T = stress, psi
 T_h = average horizontal stress
 T_g = gel strength, lbf/100 ft²
 ϵ = strain, in/in
 π = constant (3.14159)
 ρ_b = bulk density, g/cm³
 ρ_g = grain density, g/cm³
 α = Blot's constant, dimensionless

Subscripts

- D = dimensionless
 i = initial or interest
 n = normal
 x,y,z = general orientations
 o = outside
 w = well bore

REFERENCES

- Anderson, R. A., Ingram, D. S., and Zanier, A. M.: "Determining Fracture Pressure Gradients from Well Logs," Journal of Petroleum Technology Reprint Volume: Acoustic Logging (Nov. 1973) 1259-1268.
- Barenblatt, G. I.: "Mathematical Theory of Equilibrium Cracks," Advances in Applied Mechanics (1962) 55-129.
- Biot, M. A.: "Theory of Propagation of Elastic Waves in a Fluid-Saturated Porous Solid: 1-Low Frequency Range, 2- High Frequency Range," Journal of the Acoustical Soc. of America (1956), vol. 28, 168-191.
- Birch, F., Schairer, J. F., and Spicer, H. C.: "Handbook of Physical Constants," Geological Society of America Special Papers 36 (Jan. 1942).
- Bourgoyne, A. T., Jr.: "Applied Drilling Engineering," Society of Petroleum Engineering, Dallas, TX. (1986).
- Brennan, R. M., and Annis, M. R.: "A New Fracture Prediction Technique That Shows Good Results in Gulf of Mexico Abnormal Pressure," SPE paper # 13210 (1984).
- Campos, Joao C. B.: "Tensoes Na Parede de um POCO Circular Segundo a Teoria da Elasticidade," Boletim Tecnico, published by PETROBRAS the Brazilian oil company (1983) 209-216.
- Carmichael, R. S.: Handbook of Physical Properties of Rocks, CRC Press (1982) Vol. I, II, III.
- Chenevert, M. E., and McClure, L. J.: "How to Run Casing and Open-Hole Pressure Tests," Oil and Gas Journal (March 1978) 66-76.
- Christianovich, S. A., and Zeltov, Y. P.: "Formation of Vertical Fractures by Means of Highly Viscous Liquid," Proc. Fourth World Petroleum Congress (1955) II, 579-586.

- Christman, S. A.: "Offshore Fracture Gradients," Journal of Petroleum Technology (Aug. 1973) 910-914.
- Conoco Inc. "Conoco Internal Cement Bond Logging School," Chapter 8, pp. 81 and 82. Unpublished material.
- Constant, W. D., and Bourgoyne, A. T., Jr.: "Fracture Gradient Prediction for Offshore Wells," SPE paper # 15105 (1986), 127.
- Daneshy, A. A.: "On The Design of Vertical Hydraulic Fractures," Trans., AIME (Jan. 1973) vol. 255, 83-97.
- Eaton, B. A.: "Fracture Gradient Prediction and Its Application in Oil Field Operations," Journal of Petroleum Technology (Oct. 1969) 1353-1360.
- Geertsma, J., and DeKlerk, F.: "A Rapid Method of Predicting Width and Extent of Hydraulically Induced Fractures," Journal of Petroleum Technology (Dec. 1969) 1571-1581.
- Geertsma, J.: "The Effect of Fluid Pressure Decline on Volumetric Changes in Porous Rock," Trans., AIME (1957), vol. 210, 331-340.
- Hagoort, J., Weatherhill, B. D., and Settari, A.: "Modeling The Propagation of Waterflood-Induced Hydraulic Fractures," Soc. of Petroleum Engineers Journal (Aug. 1980) 293-303.
- Haimson, Bezalel, and Fairhurst, Charles: "Initiation and Extension of Hydraulic Fractures in Rocks," Soc. of Petroleum Engineers Journal (Sept. 1967) 310-318.
- Harrison, E., Kleschnick, W. F., Jr., and McGuire, W.J.: "The Mechanics of Fracture Induction and Extension," Trans., AIME (1954), vol. 201, 252-263.
- Hearn, E. J.: Mechanics of Materials: An Introduction to the Mechanics of Elastic and Plastic Deformations of Solids and Structural Components, Pergamon Press Ltd., Oxford (1977) 179-180, 195-196.
- Howard, G. C., and Fast, C. R.: "Optimum Fluid Characteristics for Fracture Extension," Drilling and Production Practice (1957) 261-270.

- Hubbert, M. K., and Willis, D. G.: "Mechanics of Hydraulic Fracturing," Trans., AIME (1957), vol. 210, 153-166.
- Jaeger, J. C., and Cook, N. G.: Fundamentals of Rock Mechanics, Chapman and Hall, London (1979) 3rd. Edition.
- Kiel, O. M.: "A New Hydraulic Fracturing Process," Journal of Petroleum Technology (Jan. 1970) 89-96.
- Lamb, H.: Hydrodynamics, Dover Publications Inc., New York (1932), 6th. Edition.
- Langlinais, J. P., Bourgoyne, A. T., Jr., and Holden, W. R.: "Frictional Pressure Losses for the Flow of Drilling Mud and Mud/Gas Mixtures," SPE paper # 11993 (1985).
- Matthews, W. R., and Kelly, J.: "How to Predict Formation Pore Pressure and Fracture Gradient From Electric and Sonic Logs," Oil and Gas Journal (Feb. 20, 1967).
- Meyer, B. R.: "New Simulator Makes Fracture Design Routine," Oil and Gas Journal (June 1985) 87-92.
- Nolte, K. G.: "Determination of Fracture Parameters from Fracturing Pressure Decline," SPE paper # 8342 presented at 54th Annual Tech. Conf., Las Vegas (Sept. 1982).
- Nolte, K. G.: "Fracture Design Considerations Based on Pressure Analysis," SPE paper # 10911 (1982).
- Nolte, K. G., and Smith, M. B.: "Interpretation of Fracturing Pressures," Journal of Petroleum Technology (Sept. 1981) 1767-1775.
- Nordgren, R. P.: "Propagation of a Vertical Hydraulic Fracture," Trans., AIME (1971) vol. 253.
- Norwacki, W.: Thermoelasticity, Addison-Wesley (1962).
- O'Bryan, P. L., Bourgoyne, A. T., Jr., Monger, T. G., and Kopcsó, Debra: "The Compressibility of Oil-Base Drilling Fluids," Louisiana State University, Baton Rouge (1986).

- Outmans H. D.: "Mechanics of Static and Dynamic Filtration in the Borehole," SPE paper # 491 (1963).
- Pennebaker, S. E.: "An Engineering Interpretation of Seismic Data," SPE paper # 2165 (1968).
- Penny, G. S., Conway, M. W., and Lee, W.: "Control and Modeling of Fluid Leak-Off During Hydraulic Fracturing," Journal of Petroleum Technology (1985) 937-949.
- Perkins, T. K., and Kern, L. R.: "Widths of Hydraulic Fractures," Journal of Petroleum Technology (1961) 937-949.
- Scott, P. P., Jr., Bearden, W. G., and Howard, G. C.: "Rock Rupture as Affected by Fluid Properties," Trans., AIME (1953) vol. 198 111-124.
- Settari, A.: "Simulation of Hydraulic Fracturing Processes," Soc. of Petroleum Engineers Journal (Dec. 1980) 487-500.
- Settari, A.: "A New General Model of Fluid Loss in Hydraulic Fracturing," Soc. of Petroleum Engineers Journal (Aug. 1985) 491-501.
- Settari, A., and Cleary, M. P.: "Three-Dimensional Simulation of Hydraulic Fracturing," Journal of Petroleum Technology (July 1984) 1177-1190.
- Sneddon, I. N.: "The Distribution of Stress in the Neighborhood of a Crack in an Elastic Solid," Proc. Royal Society of London (Oct.-Dec. 1946), series A, 187, 229-260.
- Somerton, W. H., Mehtam M. M., and Dean, G. W.: "Thermal Alteration of Sandstones," SPE paper # 907 (Oct. 1964)
- Teplitz, A. J., and Hassebroek, W. E.: "An Investigation of Oil Well Cementing," Drilling Production Practice, API (1946) 76.
- Timoshenko, S. P. and Goodier, J. N.: Theory of Elasticity, McGraw Hill Publishing Co., New York (1951).
- Tixier, M. P., Loveless, G. W., and Anderson, R. A.: "Estimation of Formation Strength from the Mechanical Properties Log," Journal of Petroleum Technology Reprint Volume: Acoustic Logging (March 1975) 283-293.

Warpinski, N. R.: "Measurement of Width and Pressure in a Propagating Hydraulic Fracture," Soc. of Petroleum Engineers Journal (Feb. 1985) 46-54.

Weibull, W.: "A Survey of Statistical Effects in the Field of Material Failure," Applied Mechanics Review (Nov. 1952) 5 and 449.

Wilcox, T. C.: "Mechanical Integrity Testing of Injection Wells," M. S. thesis, Louisiana State University, Baton Rouge (1979).

Williams, B. B.: "Fluid Loss From Hydraulically Induced Fractures," Journal of Petroleum Technology (July 1970) 882-888.

APPENDIX A

APPENDIX A DERIVATION OF FRACTURE-INDUCTION EQUATIONS

The stress field due to the two horizontal total principal stresses S_{xx} and S_{yy} acting on the edges of a very large rectangular plate with a small circular hole (radius r_w) at its center is given by (Haimson and Fairhurst 1967).

$$\sigma_{rr1} = [((\sigma_x + \sigma_y) / 2) (1 - r_w^2 / r^2) - ((\sigma_x - \sigma_y) / 2) (1 + 3 r_w^4 / r^4 - 4 r_w^2 / r^2) \cos 2 \theta]$$

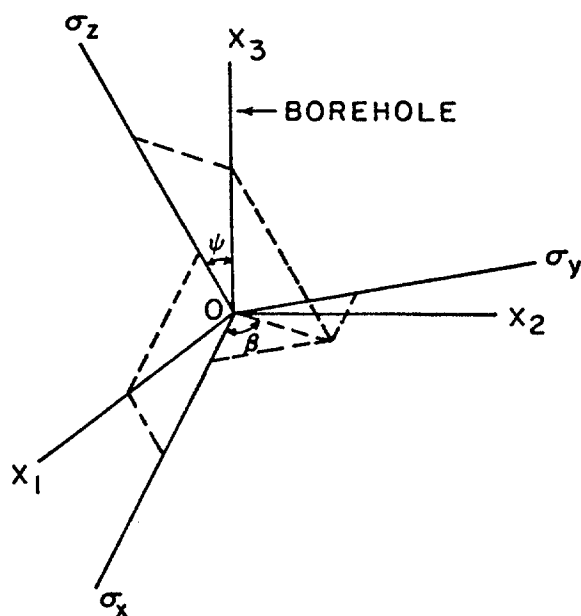
$$\sigma_{\theta\theta1} = [((\sigma_x + \sigma_y) / 2) (1 + r_w^2 / r^2) + ((\sigma_x - \sigma_y) / 2) (1 + 3 r_w^4 / r^4) \cos 2 \theta]$$

$$\sigma_{r\theta1} = [((\sigma_y - \sigma_x) / 2) (1 - 3 r_w^4 / r^4) + 2 r_w^4 / r^4) \sin 2 \theta]$$

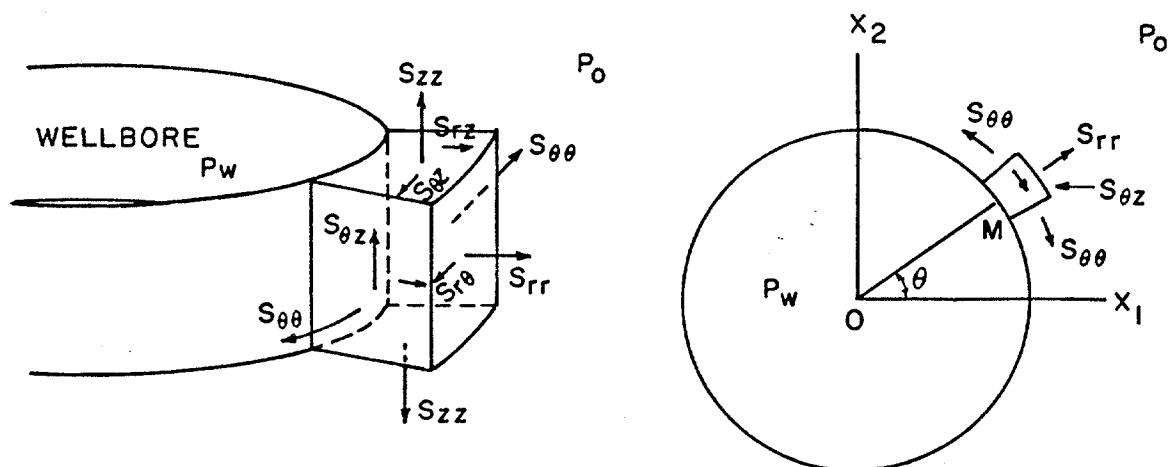
$$\sigma_{zz1} = \sigma_z - r [2 (\sigma_y - \sigma_x) r_w^2 / r^2 \cos 2 \theta]$$

$$\sigma_{\theta z1} = \sigma_{rz1} = 0 \dots\dots\dots (A-1)$$

Equations (A-1) assume that the borehole axis is parallel to the principal stress, σ_z , as shown in Figure A.1. The resulting stress distribution in terms of total stresses ($S_{ij} = \sigma_{ij} + P_p$) at the well-bore radius ($r = r_w$) in the polar coordinates shown in Figure (A.1) is



a) ORIENTATION OF OX_1, OX_2, OX_3 WITH RESPECT TO THE IN SITU PRINCIPAL STRESSES (GENERAL CASE)



b) TOTAL STRESS COMPONENTS ON THE BOREHOLE WALL
IN POLAR COORDINATES

FIGURE A.1 - State of stress around the borehole well.

$$S_{rr1} = P_0$$

$$S_{\theta\theta1} = \sigma_x + \sigma_y + 2(\sigma_x - \sigma_y) \cos 2\theta + P_0$$

$$S_{zz1} = \sigma_z - 2r(\sigma_x - \sigma_y) \cos 2\theta + P_0$$

$$S_{r\theta1} = S_{\theta z1} = S_{rz1} = 0 \dots\dots\dots (A.2)$$

The stresses induced by the borehole fluid pressure, p_w , at the depth under consideration, and at the wellbore (Campos 1983) are

$$S_{rr2} = P_w - P_0$$

$$S_{\theta\theta2} = -(P_w - P_0)$$

$$S_{zz2} = S_{r\theta2} = S_{\theta z2} = S_{rz2} = 0 \dots\dots\dots (A.3)$$

When fluid penetrates the formation from the well bore, assuming that the penetrating fluid has the same viscosity as the formation fluid and the formation has the same permeability in all directions, the induced stresses at the wall of the borehole are

$$S_{rr3} = 0$$

$$S_{\theta\theta3} = \alpha [(1 - 2\mu) / (1 - \mu)] (P_p - P_0)$$

$$S_{zz3} = \alpha [(1 - 2\mu) / (1 - \mu)] (P_p - P_0)$$

$$S_{r\theta3} = S_{\theta z3} = S_{rz3} = 0 \dots\dots\dots (A.4)$$

The complete state of stress underground at the borehole wall is determined by the principle of superposition (Timoshenko and

Goodier 1951), which consists of the components σ_{ij1} , σ_{ij2} , σ_{ij3} . This yields

$$\begin{aligned} S_{rr} &= P_0 + P_w - P_0 = P_w \\ S_{\theta\theta} &= \sigma_x + \sigma_y + 2(\sigma_x - \sigma_y) \cos 2\theta + 2P_0 - P_w + \alpha [(1-2\mu)/(1-\mu)] (P_p - P_0) \\ S_{zz} &= \sigma_z - 2r(\sigma_y - \sigma_x) \cos 2\theta + P_0 + \alpha [(1-2\mu)/(1-\mu)] (P_p - P_0) \\ S_{r\theta} &= S_{\theta z} = S_{rz} = 0 \dots\dots\dots (A.5) \end{aligned}$$

Equation series (A.5) shows that all shear stresses are zero at the borehole wall, and therefore S_{rr} , $S_{\theta\theta}$, and S_{zz} are the three secondary principal stresses at the borehole wall. The maximum stresses occur at $\theta = 0$ and π . Substituting any of these values in Equations (A.5) yields

$$\begin{aligned} S_{rr} &= P_w \\ S_{\theta\theta} &= 3\sigma_x - \sigma_y + 2P_0 - P_w + \alpha [(1-2\mu)/(1-\mu)] (P_p - P_0) \\ S_{zz} &= \sigma_z - 2\mu(\sigma_y - \sigma_x) + P_0 + \alpha [(1-2\mu)/(1-\mu)] (P_p - P_0) \dots\dots (A.6) \end{aligned}$$

If the area under consideration is tectonically relaxed, Equation (1) from the text can be substituted in Equations (A.6) to yield

$$\begin{aligned} S_{rr} &= P_w \\ S_{\theta\theta} &= (2\mu/(1-\mu))\sigma_z + 2P_0 - P_w + \alpha [(1-2\mu)/(1-\mu)] (P_p - P_0) \\ S_{zz} &= \sigma_z + P_0 + \alpha [(1-2\mu)/(1-\mu)] (P_p - P_0) \dots\dots\dots (A.7) \end{aligned}$$

Vertical Fracture Initiation

Vertical fractures begin when the maximum effective tangential stress, $\sigma_{\theta\theta}$, exceeds the tensile strength of the formation, S_t . Then, fracture initiation occurs when $\sigma_{\theta\theta} = S_t$, which substitutes in Equations A.7 (remember that $S_{\theta\theta} = \sigma_{\theta\theta} + P_p$) to yield

$$S_t = (2\mu / (1 - \mu)) \sigma_z + 2P_o - P_w + \alpha [(1 - 2\mu) / (1 - \mu)] (P_p - P_o) - P_p \quad \text{..... (A.8)}$$

For a penetrating type of fluid, the pore pressure, P_p , at the borehole wall is $P_p = P_w$ (see Figure 10). Substituting this equality in (A.8) and solving for the well-bore pressure, yields

$$P_w = [(2\mu / (1 - \mu)) \sigma_z - S_t] / (2 - \alpha (1 - 2\mu) / (1 - r)) + P_o \quad \text{..... (A.9)}$$

For a nonpenetrating type of fluid, the pore pressure, P_p , at the borehole wall is the original formation pore pressure, or $P_p = P_o$. Therefore, the well-bore pressure becomes from Equation (A.8)

$$P_w = [2\mu / (1 - \mu)] \sigma_z - S_t + P_o \quad \text{..... (A.10)}$$

Horizontal Fracture Initiation

Horizontal fractures begin when the maximum effective vertical stress, σ_{zz} , exceeds the tensile strength of the formation, S_t . Thus, fracture initiation occurs when the maximum effective vertical stress, σ_{zz} , exceeds the tensile strength of the formation, S_t ; that is, fracture initiation occurs when $\sigma_{zz} = S_t$, which substitutes in Equation (A.7) to yield

$$S_t = \sigma_z + P_o - P_p + \alpha [(1 - 2\mu) / (1 - \mu)] (P_p - P_o) \dots \dots \dots (A.11)$$

For a penetrating fluid $P_p = P_w$, then, P_w can be expressed as

$$P_w = (\sigma_z - S_t) / [1 - \alpha (1 - 2\mu) / (1 - \mu)] + P_o \dots \dots \dots (A.12)$$

Substituting for a nonpenetrating fluid, $P_p = P_o$, then in Equation B.11 yields

$$S_t = \sigma_z \dots \dots \dots (A.13)$$

Equation (A.13) indicates the impossibility of obtaining a horizontal fracture with a nonpenetrating fluid. However, end effects should occur at the well bottom in which axial forces equal to the pressure times the area of the cross section of the hole would be exerted upon the ends of the interval. Another way of producing horizontal fracture with a nonpenetrating fluid is to introduce points that are separated sufficiently to allow the entrance of the fluid.

Then, it is only necessary to apply sufficient pressure to hold the fracture open.

The pressure at the well bore in any case should be at least that of the overburden, and then

$$P_w = S_z \dots\dots\dots (A.14)$$

APPENDIX B

APPENDIX B

DERIVATION OF THE OVERBURDEN STRESS EQUATION

The vertical overburden stress, S_z , originating from geostatic load at a sediment depth, D_s , for sediments having an average bulk density, ρ_b , where g is the gravitational constant, is given by

$$S_z = \int_0^D \rho_b \cdot g \cdot dD \dots\dots\dots (B.1)$$

The value of ρ_b can be expressed as a function of porosity, \emptyset , the grain density, ρ_g , and the pore fluid density, ρ_f , by

$$\rho_b = \rho_g \cdot (1 - \emptyset) + \rho_f \cdot \emptyset \dots\dots\dots (B.2)$$

The change in bulk density with depth of burial is primarily rated to the change in sediment porosity with compaction. Values of bulk density as a function of depth can be obtained from conventional well-logging methods applied in a given area. Since grain density of sedimentary deposits has been found to be approximately constant with depth (Bourgoyne 1986), porosity can be calculated directly by rearranging Equation (B.2) in the form

$$\emptyset = (\rho_g - \rho_b) / (\rho_g - \rho_f) \dots\dots\dots (B.3)$$

This equation allows average bulk density data read from well logs to be easily expressed in terms of an average porosity for any

assumed values of grain density and pore fluid density. The plot of the depth of these average porosity values in a semi-log paper can generally be approximated by a straight-line trend. The equation of this straight line is given by

$$\emptyset = \emptyset_0 \cdot e^{-K \cdot D} \dots\dots\dots (B.4)$$

The surface porosity \emptyset_0 , is the porosity at a depth of zero, and K is the porosity-decline constant. For the Gulf Coast area, for example, these values are $\emptyset_0 = 0.41$ and $K = 0.000085$, and

$$\emptyset = 0.41 e^{-0.000085 D} \dots\dots\dots (B.5)$$

The substitution of Equation (B.2) in (B.1) yields

$$S_z = \int_0^D [\rho_g \cdot (1 - \emptyset) + \rho_f \cdot \emptyset] g \cdot dD$$

or rearranging

$$S_z = \int_0^D [\rho_g - (\rho_g - \rho_f) \cdot \emptyset] g \cdot dD \dots\dots\dots (B.6)$$

Substituting (B.4) in (B.6) yields

$$S_z = \int_0^D [\rho_g - (\rho_g - \rho_f) \emptyset_0 e^{-K \cdot D}] g \cdot dD \dots\dots\dots (B.7)$$

For offshore areas, Equation (B.7) must be integrated in two parts. From the surface to the ocean bottom, which in this case is

represented by $\emptyset = 1$, and from the mud line to the depth of interest, D_i . Using Equation (B.6) for the first integral, one obtains

$$S_z = \int_0^{D_W} \rho_{sw} g \cdot d \cdot D + \int_0^{D_i} [\rho_g - (\rho_g - \rho_f) \cdot \emptyset_0 \cdot e^{-K D}] g \cdot d D \dots (B.8)$$

Integrating (B.8) for field units yields

$$S_z = 0.052 [\rho_{sw} D_W + \rho_g D_i - ((\rho_g - \rho_f) \cdot \emptyset_0 / K) (1 - e^{-K D_i})] \dots (B.9)$$

where,

ρ_{sw} = seawater density, lb/gal

D_W = water depth, ft

Equation (B.8) can be used for normal and abnormal pressure formations. The values of \emptyset_0 and K should be evaluated for a given area of drilling activity.

APPENDIX C

APPENDIX C

FLOW RATE THROUGH AN ELLIPTICAL CROSS-SECTIONAL AREA

Lamb (1932) has shown that the pressure gradient for flowing Newtonian fluids in an elliptical conduit of essentially zero excentricity is 16 times as great as the pressure gradient for the same fluid flowing between parallel plates under the same condition of height, h , maximum width, w , and flow rate. Then, the pressure drop along an elliptical vertical fracture, $(d_p/d_l)_e$, is

$$(d_p / d_x)_e = (16/3\pi) [d_p / d_x]_{\text{SLOT}} \dots\dots\dots (C.1)$$

Pressure Drop in a Slot

For an element of fluid having height, h , and thickness, Δy , as shown in the slot representation of Figure C.1, the forces acting on the fluid element are:

-Force applied by the fluid at point 1; F_1

$$F_1 = P \cdot h \cdot \Delta y \dots\dots\dots (C.2)$$

- Force applied by the fluid pressure at point 2; F_2

$$F_2 = (P - (d_p/d_x)_f \Delta x) h \Delta y \dots\dots\dots (C.3)$$

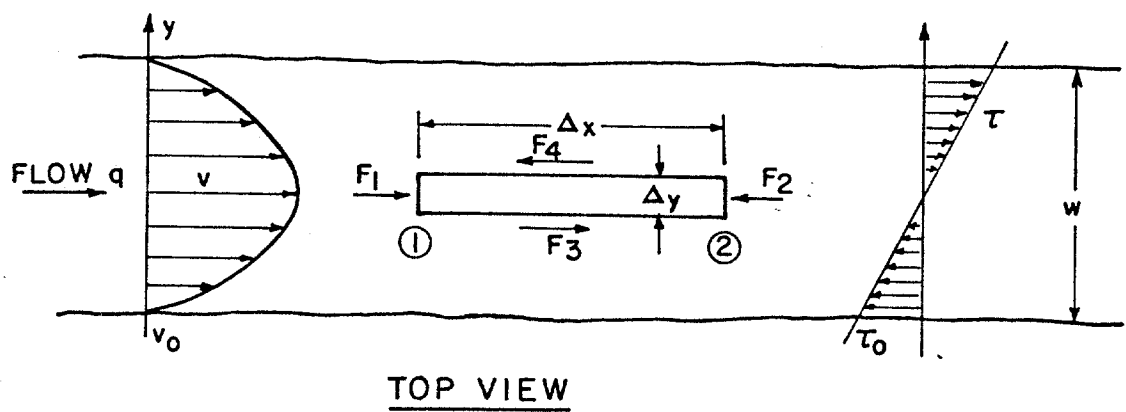
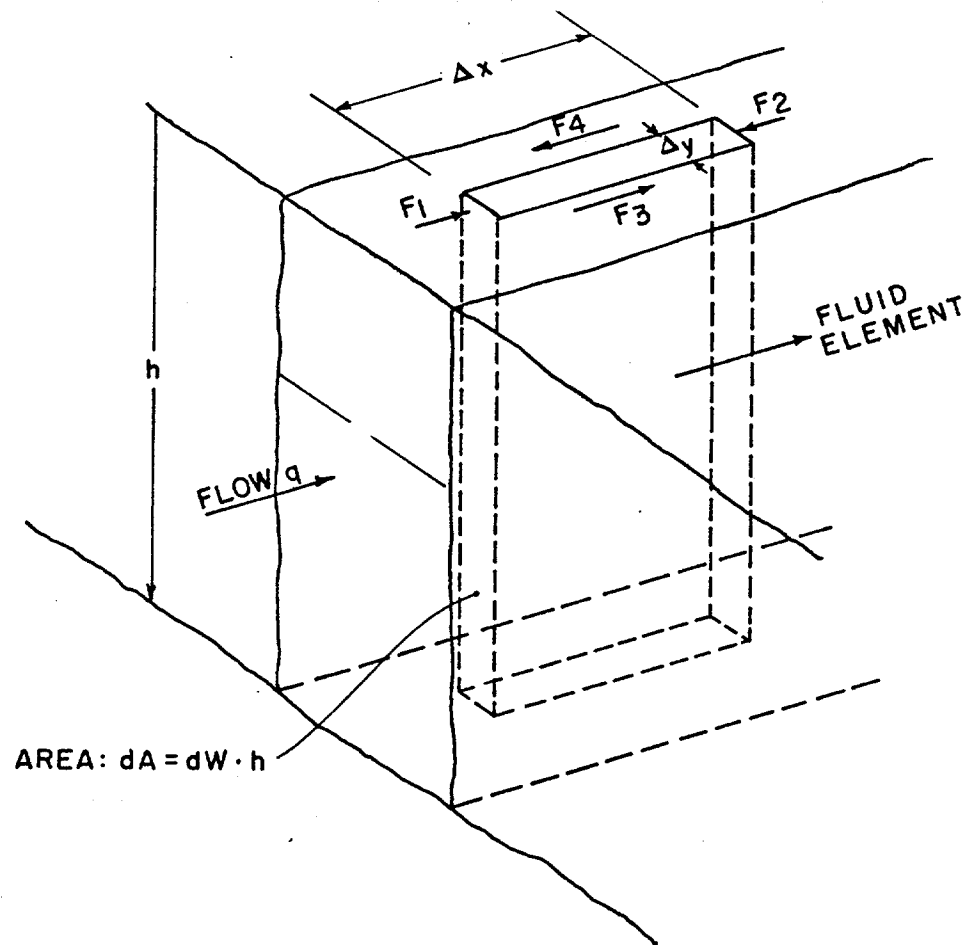


FIGURE C.1 - Free body diagram for fluid element in a narrow slot.

- Frictional force exerted by the adjacent layer of fluid below the fluid element; F_3

$$F_3 = \tau \cdot h \cdot \Delta x \dots\dots\dots (C.4)$$

- Frictional force exerted by the adjacent layer of fluid above the fluid element; F_4

$$F_4 = \tau_{w+\Delta y} h \Delta x = (\tau + (d\tau/dy) \Delta y) \cdot h \cdot \Delta x \dots\dots\dots (C.5)$$

For a steady-state flow, the sum of the forces acting in the fluid element must be zero, then

$$P \cdot h \cdot \Delta y - (P - (d_p/d_x) f \cdot \Delta x) h \cdot \Delta y + \tau h \Delta x - (\tau + (d\tau/d_y \Delta y)) \cdot h \cdot \Delta x = 0 \dots (C.6)$$

Dividing the equation by $h \cdot \Delta y \cdot \Delta x$ yields

$$(d_p/d_x) f \cdot \Delta x - (d\tau/d_y) = 0 \dots\dots\dots (C.7)$$

Since $(d_p/d_x)f$ is not a function of w , Equation (C.7) can be integrated with respect to w . Separating variables and integrating gives

$$\tau = w (d_p/d_x) f + \tau_0 \dots\dots\dots (C.8)$$

τ_0 is the constant of integration and corresponds to the shear stress at $w = 0$. The shear rate, $\dot{\gamma}$, is given by

$$\dot{\gamma} = - (d_v/d_y) \dots\dots\dots (C.9)$$

Thus, for the Newtonian model combining (C.8) and (C.9), it yields

$$\tau = \tau \dot{\gamma} = -\tau (d_v/d_y) = \eta \cdot (d_p/d_x)_f + \tau_0 \dots \dots \dots (C.10)$$

Separating variables and integrating gives:

$$v = (-\eta^2/2\eta) (d_p/d_x)_f - (\tau_0 \eta/\eta) + v_0 \dots \dots \dots (C.11)$$

Where v_0 is the second constant of integration, which corresponds to the fluid velocity at $w = 0$. Considering that the fluid wets the slot walls, the velocity, v , is zero for $y = 0$ and for $y = w$. Then, applying these boundary conditions to equation (C.11), it becomes

$$v = (1/2\eta) (d_p/d_x)_f (w \cdot y - y^2) \dots \dots \dots (C.12)$$

The flow rate, q , is given by

$$q = \int v \cdot d_A = \int v \cdot h \cdot dy = (h/2\eta) (d_p/d_x)_f \int_0^w (wy - y^2) dy \dots \dots \dots (C.13)$$

Integrating this equation from $y = 0$ to $y = w$, yields

$$q = (w^3 \cdot h / 12\eta) (d_p/d_x)_f \dots \dots \dots (C.14)$$

Substituting $(d_p/d_x)_f$ for the slot approximation given by Equation (C.14) into Equation (C.1) yields

$$q = [\pi \cdot w^3 \cdot h / (64\nu)] (d_p/d_x)_e \dots\dots\dots (C.15)$$

Where w in Equation (C.15) is the maximum width of the elliptical cross-sectional area of the fracture, and h is the fracture height.

APPENDIX D

APPENDIX D

FRACTURE AREA

The elliptical cross-sectional area of a vertical fracture at any distance, x , from the well bore can be expressed by

$$A = \int_{-h/2}^{h/2} w_{(x,z)} dz \dots\dots\dots (D.1)$$

The fracture width, $w_{(x,z)}$, at any point, z , along the fracture height, h , can be determined as a function of the maximum fracture width, $w_{(x,0)}$ by

$$w_{(x,z)} = w_{(x,0)} \sqrt{1 - (4z^2/h^2)} \dots\dots\dots (D.2)$$

Substituting Equation (D.2) into (D.1) yields

$$A = w_{(x,0)} \cdot \int_{-h/2}^{h/2} (1 - (4z^2/h^2))^{1/2} dz \dots\dots\dots (D.3)$$

Integration of Equation (D.3) is easily accomplished by first making the substitution $Z = h \cdot \theta/2$. The resulting equation for the area of the fracture after integration is

$$A = (\pi/4) \cdot w \cdot h \dots\dots\dots (D.4)$$

APPENDIX E

APPENDIX E SOLUTION FOR LARGE FLUID-LOSS RATE

The term $\partial A/D_t$ is assumed here to be negligible in Equation (55) compared with the fluid-loss rate q_L . Then, when Equation (58) is substituted in (55), Equation (55) becomes

$$\partial q / \partial x + (2.h.C / \sqrt{t - T(x)}) = 0 \dots\dots\dots (E.1)$$

where $T(x)$ depends on x such that

$$T[L(t)] = t, \quad 0 \leq t \leq t \dots\dots\dots (E.2)$$

The flow rate at the fracture entrance q_i is assumed constant, such that

$$q(0, t) = q_i \dots\dots\dots (E.3)$$

Integration of Equation (E.1) from the fracture entrance, $x = 0$, to a generic position, x , yields

$$q(x, t) = q_i - 2.h.C \int_0^x (dx / \sqrt{t - T(x)}) \dots\dots\dots (E.4)$$

The function $T(x)$ in Equation (E.4) can be expressed by the following equation, based on (E.2)

$$T(x) = t.(x/L)^2 \dots\dots\dots (E.5)$$

If we know that $q(L,t) = 0$, the solution of Equation (E.4) with Equation (E.5) in field units is

$$T(x) = [\pi.h.C.x / (5.615.q_i)]^2 \dots\dots\dots (E.6)$$

and

$$L(t) = [5.615 q_i / (\pi.C.h)].t^{1/2} \dots\dots\dots (E.7)$$

If Equations (E.6) and (E.7) are used, Equation (E.4) becomes

$$q(x,t) = q_i [1 - (2/\pi) \sin^{-1} x/L] \dots\dots\dots (E.8)$$

Combining Equations (18) and (56) yields

$$q(x,t) = [\pi G / (256 (1-\mu).\nu)] \partial (w^4(x,t)) / \partial x \dots\dots\dots (E.9)$$

Substitution of Equation (E.9) into (E.8) yields

$$\partial / \partial x [w^4(x,t)] = [256 (1-\mu).\nu / q_i (\pi G)] [(2/\pi) \sin^{-1} (x/L) - 1] \dots\dots (E.10)$$

Integration of Equation (E.10) from 0 to x gives

$$w(x,t) = 4 \left[(2(1-\mu)\nu q_i^2) / (\pi^3 G.C.h) \right]^{1/4} \left[(x/L) \sin^{-1}(x/L) + (1-(x^2/L^2))^{1/2} - (\pi x/2L) \right]^{1/4} t^{1/8} \dots\dots\dots (E.11)$$

The maximum fracture width occurs at $x=0$; therefore, Equation (E.11), used with field units, yields

$$w_{(0,t)} = 0.066463 \left[(2(1-\mu)\nu q_i^2) / (\pi^3 G.C.h) \right]^{1/4} t^{1/8} \dots\dots (E.12)$$

The dimensionless forms for fracture length and width at the well bore are obtained by means of Equations (58):

$$L_D(t_D) = (2/\pi) \cdot t_D^{1/2} \dots\dots\dots (E.13)$$

and

$$w_D(0,t_D) = \sqrt{2/\pi} \cdot t_D^{1/8} \dots\dots\dots (E.14)$$

APPENDIX F

APPENDIX F

DESCRIPTION OF THE DATAFILE FOR THE COMPUTER PROGRAM LEAK

Mud-Related Data

LINE 1 - Mud Properties.

RHOM (LB/GAL) - Mud density.

VISCM (CP) - Mud plastic viscosity.

YP (LB/100 FT²) - Mud yield point.

GEL (LB/100 FT²) - Mud 10-min gel.

API (CM³) - API fluid loss reported at 30 min (standard test).

VSP (CM³) - Spurt loss. If not available enter zero. The spurt loss effect in the model is very small (see chapter 3, "Proposed Mathematical Model").

LINE 2- Mud Composition and other Parameters.

SS (%) - Solids saturation in the mud.

SO (%) - Oil saturation in the mud.

QI (BPM) - Flow rate used or to be used in the leak-off test.

TDRILL (MIN) - Drilling time to drill the open-hole section.

TCIRC (MIN) - Time circulating before the leak-off test begins.

Well Geometry

LINE 3 - Casing-string data

ODCSG (in.) - Casing outside diameter.

DICSG (in.) - Casing inside diameter.

OLCSG (ft) - Casing length.

This line contains nine fields, three for each parameter above. It takes into account that a maximum of three different casing grades can be used in one section.

LINE 4 - Other well data

HOLE (in) - Open-hole diameter. Generally, this value is equal to the bit diameter.

AIRGAP (ft) - Distance between the rotary kelly bushing and the seawater level. In onshore wells it is equal to zero.

DEPBOT (ft) - Actual measured depth (MD) of the well.

DEPCIM (ft) - Approximate top of the cement outside the last casing.

DW (ft) - Water depth. In onshore wells, this value is zero.

OMICR (in.) - Micro-annulus gap estimated, for a good quality cement job, this value is ~ 0.

Drill String

LINE 5 - Pipes information

OD (in.) - Outside diameter.

DI (in.) - Inside diameter.

OL (ft) - Length.

Each piece of information should be provided for the drill pipes, heavy-weight drill pipes, and drill collars, in that order. The total length of the bottom-hole assembly should be included in the drill collar's total length.

LINE 6 - Bit information

BDEP (ft) - Bit depth during the leak-off test.

DBIT (in.) - Bit diameter.

AJ1, AJ2, AJ3 (/32 in.) - Jets size. Sizes for all three jets should be entered.

Open-hole Formation

LINE 7 - Depths and Temperature information

HPERM 1 (ft) - Total permeable height. The sum of the height of each permeable formation in the open-hole section.

HPERM 2 (ft) - Permeable height of the formation to be fractured.

TVDB (ft) - True vertical depth of the well-bottom. In the case of a vertical well: TVDB = DEPBOT.

TVDS (ft) - True vertical depth of the casing shoe.

DEP1 (ft) - True vertical depth of the top of the formation to be fractured. Generally, this value is equal to TVDS.

DEP2 (ft) - True vertical depth of the bottom of the formation to be fractured.

GTEMP (°F/100 ft) - Local temperature gradient.

LINE 8 - Rock related parameters

P (PSI) - Pore pressure of formation to be fractured.

ZFOR - Poisson's ratio of rock (Figure 31).

EFOR - Young's modulus of rock (Equation 85).

ALPHA - Biot's constant.

ST (PSI) - Tensile strength of the formation.

PHI - Surface porosity.

AK - Porosity-decline constant.

RHOGR (LB/GAL) - Average grains density.

RHOFL (LB/GAL) - Formation fluid density.

Figure F.1 shows the data file used to produce the output example of Figure 38, which follows the data file organization described above.

10.8 25.0 8.0 9.0 16.0 5.0
0.26 0.02 0.25 20. 120.
9.625 8.535 12941. 0. 0. 0. 0. 0. 0.
13.0 108. 12951. 8000. 95. 0.
5.0 4.276 8778. 5.0 4.0 2700. 6.25 2.813 1463.
12940. 8.5 11. 11. 11.
10. 10. 12352. 12342. 12342. 12352. 1.14
5900. 0.30 1.524E06 0.79 500. 0.42 0.0000731 21.645 8.94
999. 999.
4.0 1250.
5.0 1610.
5.5 1790.
6.0 1990.
6.5 2175.
7.0 2290.
7.5 2450.
8.0 2690.
9.0 2950.
10.0 3125.
10.25 3200.
10.5 3250.
999. 999.

FIGURE F.1 - Data File Organization Used to Produce the Output

Example of Figure 38.

APPENDIX G

APPENDIX G

ELASTIC-PLASTIC SOLUTION OF A HOLLOW CYLINDER

The hollow cylinder $R_1 < r < R_2$ in plane strain shown in Figure 30 with pressure p_1 applied at R_1 and pressure p_2 applied at R_2 is considered here. There is a plastic region, $R_1 < r < R$, and an elastic region $R < r < R_2$. The radius, R , of the elastic-plastic boundary is determined by the technique described in the chapter "Proposed Mathematical Model" and continuity conditions have to be satisfied there.

Elastic Region

The radial, σ_r , and tangential stresses, σ_θ , for a hollow cylinder are obtained from the elasticity theory (Timoshenko and Goodier 1957), and are expressed by

$$\sigma_r = (\lambda + 2G) (du/dr) + (\lambda u/r) \dots\dots\dots (G.1)$$

$$\sigma_\theta = \lambda (du/dr) + (\lambda + 2G) (u/r) \dots\dots\dots (G.2)$$

where λ is the Lamé's constant and u the displacement at the radius, r . Since the internal, p_1 , and external, p_2 , pressures are independent of r and the vertical direction Z , the stress equation is given by (Jaeger and Cook 1979)

$$\partial \sigma_r / \partial r + (\sigma_r - \sigma_\theta) / r = 0 \dots\dots\dots (G.3)$$

Substitution of Equation (G.1) and (G.2) into (G.3) yields

$$(d^2u/dr^2) + (1/r)(du/dr) - u/r^2 = 0 \dots\dots\dots (G.4)$$

The general solution of (G.4) is

$$u = A \cdot r + B/r \dots\dots\dots (G.5)$$

where A and B are constants of integration that can be determined by the boundary conditions

$$\begin{aligned} \sigma_r &= p_1 & \text{when } r &= R_1 \\ \sigma_r &= p_2 & \text{when } r &= R_2 \\ (\sigma_r)_{\text{plastic}} &= (\sigma_r)_{\text{elastic}} & \text{when } r &= R \\ (\sigma_\theta)_{\text{plastic}} &= (\sigma_\theta)_{\text{elastic}} & \text{when } r &= R \dots\dots\dots (G.6) \end{aligned}$$

Plastic Region

The plasticity theory (Jaeger and Cook 1979) indicates that the yield condition expressed by the following equation

$$\sigma_\theta - \sigma_r = 2K \dots\dots\dots (G.7)$$

must be satisfied. The parameter K is related to the yield stress of the rock, σ_0 , by the expression $K = \sigma_0 / \sqrt{3}$.

Substitution of Equation (G.1) and (G.2) into (G.7) with the boundary conditions (G.6), yields

$$A = [P_2 + (K R^2 / R_2^2)] / 2(\lambda + G) \dots\dots\dots (G.8)$$

$$B = K R^2 / 2G \dots\dots\dots (G.9)$$

The total strain (plastic + elastic), at a distance, r , from the borehole, ϵ_r , is expressed by

$$\epsilon_r = d_u / d_r \dots\dots\dots (G.10)$$

Substitution of Equations (G.8) and (G.9) into (G.5), and derivation of the resulting equation with respect to r , yields

$$d_u / d_r = \epsilon_r = [P_2 + (K R^2 / R_2^2)] / (2(\lambda + G)) - K R^2 / (2 G r^2) \dots\dots\dots (G.11)$$

The value of K can be found by combining Equations (G.3) with (G.7), which yields

$$d\tau_r / d_r = 2 K / r \dots\dots\dots (G.12)$$

Solving Equation (G.12), using the boundary conditions (G.6), gives

$$K = (P_1 - P_2) / ((R/R_2)^2 - \log_e (R/R_1)^2 - 1) \dots\dots\dots (G.13)$$

Finally, substituting Equation G.13 into (G.11) gives

$$\epsilon_r = [P_2 + (R/R_2)^2 (P_1 - P_2) / [(R/R_2)^2 - \log_e (R/R_2)^2]] / (2(\lambda + G)) \\ - [R^2 / (2.G.r^2)] (P_1 - P_2) / [(R/R_2) - \log_e (R/R_2)^2 - 1] \dots \dots \dots (G.14)$$

The strain at the borehole wall, $r = R_1$, if the well is considered as a hole in the middle of an infinitive plate, $R_2 \rightarrow \infty$, according to Equation (G.14), is

$$\epsilon_{R1} = P_2 / (2(\lambda + G)) + (R/R_1)^2 (1/2G) [(P_1 - P_2) / (1 + \log_e (R/R_1)^2)] \\ \dots \dots \dots (G.15)$$

For an increment of pressure, ΔP_1 , at the borehole wall, R_1 , and considering that far from the well bore, $\Delta P_2 = 0$, Equation (G.15) is reduced to

$$\epsilon_{R1} = (R/R_1)^2 / (1 + \log_e (R/R_1)^2) \cdot \Delta P_1 / 2G \dots \dots \dots (G.16)$$

APPENDIX H

APPENDIX H

FRACTURE-CLOSURE PRESSURE

Fracture-closure pressure can be determined by a pump-in/flow-back procedure or by observing the pressure decline after shut-in. If fracture-closure pressure is determined with a pump-in/flow-back procedure, then after the fracture is initiated and an additional volume of mud is pumped into the fracture, the well is backflowed at an appropriate constant rate (e.g., through a surface choke) that varies for different formations. A plot of pressure versus flow-back time will exhibit a characteristic reversal of curvature when the fracture closes (Figure H.1). If fracture pressure is determined by observing the pressure decline after shut in, the closure pressure is determined by observing the ratio of pressure decline to the well shut-in. The same reversal characteristic will be exhibited by the plot when the fracture closes (Figure H.2).

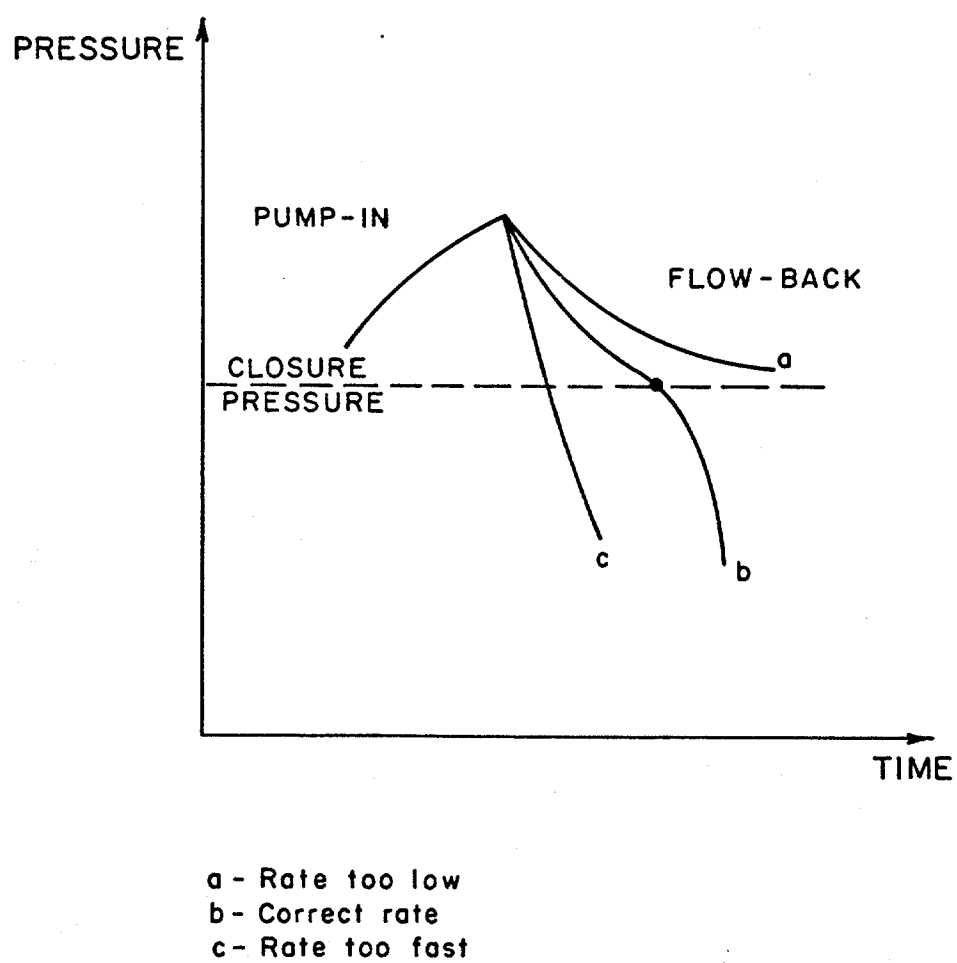


FIGURE H.1 - Pump-in/flow-back test.

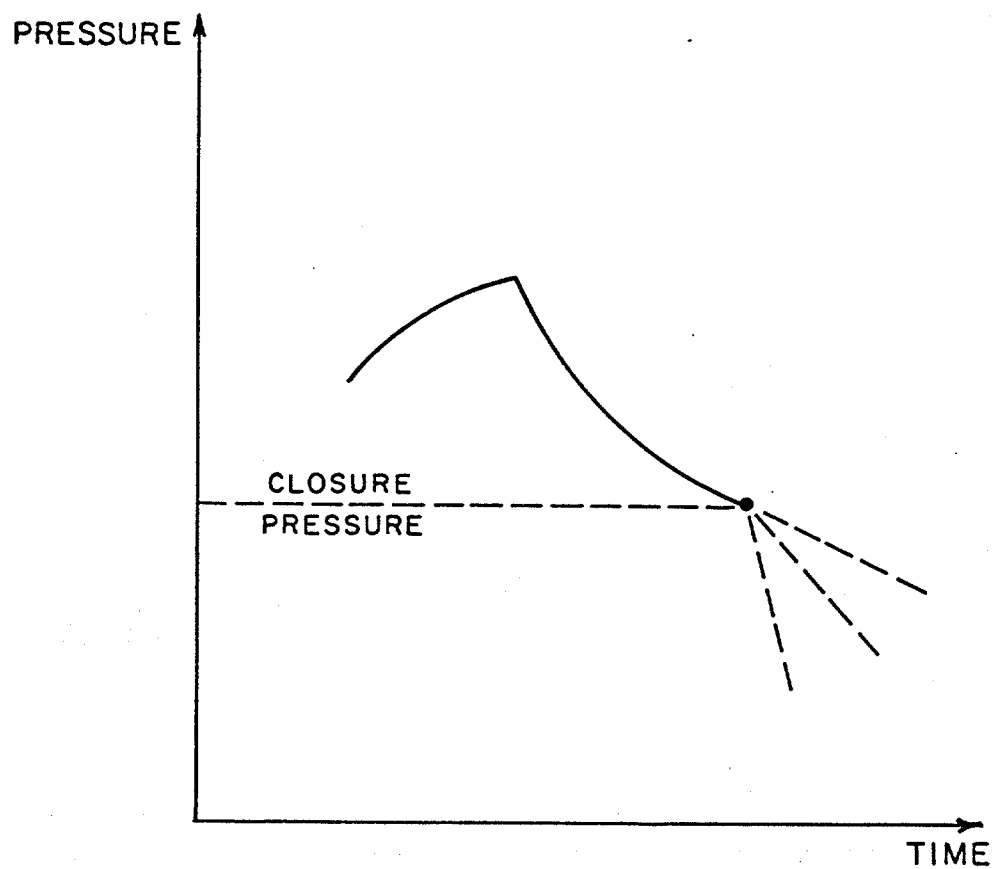


FIGURE H.2 - Pressure decline after shut-in.

VITA

Mauricio de Aguiar Almeida, the son of Manoel de Almeida and Irinea de Aguiar Almeida, was born on April 14, 1956, in Rio de Janeiro, RJ, Brazil. He graduated from Fundação Técnico-Educacional Souza Marques in December 1978, receiving his Bachelor of Science degree in mechanical engineering. After graduation, he joined the petroleum engineer staff of Petroleo Brasileiro S. A. - PETROBRAS in Salvador, Bahia, Brazil, in 1979, where he attended petroleum engineering classes until 1980. After receiving one year of training on oil rigs in the field, he joined the drilling engineer staff of the Petrobras Research Center in Rio de Janeiro, RJ, Brazil. He worked there until August of 1982, when he was selected to enter Louisiana State University to pursue a Master of Science degree in petroleum engineering. After receiving his Master's degree in the summer of 1985, he continued studies in LSU's Ph.D. program. Upon graduation, he will return to work in the PETROBRAS Research Center in Brazil. He married Maria de Fatima Cabral in January, 1979, and has two daughters, Thais and Priscila.